UNIVERSITY OF SOUTHAMPTON

Soil/Structure Interaction of Temporary Roadways

by

Andrew Steven Lees

A thesis submitted for the
degree of Doctor of Philosophy

Department of Civil &
Environmental Engineering

July 2000

Abstract

A series of tests on model temporary military trackway, subject to vehicle loads, on a soft over-consolidated clay was carried out at the London Geotechnical Centrifuge Centre. Two of the tests were conducted under plane strain conditions and analysed the effects of static and cyclic 'whole vehicle loads' on trackway performance. The other two used a rolling vehicle to impose traffic loads on unjointed and jointed trackway respectively, to assess the effects of trackway joints on the underlying soil and to determine the sequence of events involved in the onset of trackway failure.

A series of finite element analyses using the critical state soils program CRISP was undertaken in which it was attempted to model the centrifuge models. Two-dimensional analyses were used to model the plane strain centrifuge tests, and three-dimensional analyses for tests involving the rolling vehicle. A two-dimensional effective stress slip element, and a three-dimensional slip element were developed to assist in re-creating the interface between stiff aluminium trackway and soft clay. The results were in good agreement, allowing further analyses to be carried out with modified soil and trackway properties.

The centrifuge tests and finite element analyses showed that soil/trackway failure is not typically caused by bearing capacity failure of the soil, or by degradation of the soil due to cyclic loading. It is due to very high soil/trackway contact stresses generated by the low-bending-stiffness articulated joints causing immediate failure of a thin surface layer of the soil. Soil/trackway displacements accumulate as degraded soil is driven aside and successively deeper layers of soil are exposed.

Existing trackway performance could be improved significantly by enhancing its stiffness in the direction of vehicle travel: either by increasing the joint interval, restraining panels against rotation or by designing a new, more effective, trackway system.

List of contents

List of figures

List of tables

Acknowledgements

I am grateful to my supervisor, David Richards, for his continuous help, support and guidance over the last three and a half years. Also to William Powrie, Richard Harkness and Stuart Moy for useful advice at crucial times.

Centrifuge testing requires much effort on the part of many individuals and several setbacks before the rewards are gained. I thank, in particular, Harvey Skinner for his expertise and hard work in designing and setting up much of the centrifuge apparatus, operating the centrifuge and, above all, his sense of humour when things did not go to plan. In addition I would like to thank Stephen Wake, Deryk Taylor, Ken Yeates, Ralph Biffin and Dave Bowden for their advice and assistance.

CRISP is a constantly evolving program, but sadly its manuals are not. I am therefore immensely grateful to Amir Rahim of the CRISP Consortium for his regular, and often late-night, assistance and programming, particularly in the development of the new slip element codes.

I am grateful for the financial support of DERA. I would like to thank Karl Phillips for his useful advice on practical military matters and his unfailing enthusiasm.

Definitions and abbreviations

c_u undrained shear strength

e void ratio

e_0 void ratio on critical state line at p' = 1kPa

E Young's modulus

EI bending stiffness

g acceleration due to gravity

G shear modulus

H slope of the Hvorslev line

I second moment of cross sectional area

k (with subscript to denote direction) permeability

K bulk modulus

K earth pressure coefficient

K_0 initial in-situ earth pressure coefficient

M slope of the critical state line

N gravity scaling factor (centrifuge modelling)

N_p v on isotropic virgin compression line when $\ln p' = 0$, $(= \Gamma+\lambda-\kappa)$

OCR over consolidation ratio

p_{cs} p' on the critical state line

p' average effective stress = $(\sigma_1' + \sigma_2' + \sigma_3')/3$

q deviatoric stress invariant

S slope of the no tension cut-off line in q: p' space

u pore water pressure

v specific volume

γ unit weight of soil

γ_w unit weight of water

Γ specific volume on critical state line at p' = 1kPa in υ:ln p' space

κ slope of unload/reload lines in υ:ln p' space

λ slope of one-dimensional compression line in υ:ln p' space

ν Poisson's ratio

σ' normal effective stress

τ shear stress

ϕ internal angle of shearing

ϖ angular velocity

Subscripts

h horizontal

v vertical

Chapter 1

Introduction

1.1 Background

When temporary roadways, that is roads whose life expectancy is measured in hundreds or thousands of axle passes, are required for short periods at several locations, it may be more economical to use a retrievable and re-usable trackway system, rather than to construct a pavement of unbound aggregate (i.e. haul road). Commercial trackway systems are often utilised at open-air sports events and festivals, as well as by the military, where highly concentrated vehicle movements may occur on unmade ground for relatively short durations.

Mobile army units use various aluminium trackway systems whilst on manoeuvres, particularly on the approaches to temporary bridges over rivers where traffic is concentrated and where the ground is soft and susceptible to deep rutting. The trackway is assembled into a roll and transported on a spool on the backs of military vehicles to the required location where it is rolled out onto the ground. Upon completion of manoeuvres, the trackway is then rolled back onto the spool and is available to be transported to its next location.

It has been found in practice that the use of trackway can improve the mobility of military vehicles and allow an increased number of possible vehicle movements at any given location. However, where there is soft ground, soil and trackway deformations can be high and existing trackway systems may fail due to repeated vehicle loading. Trackway failure is due to unacceptable levels of deformation, to a point where it becomes irreversible and may significantly compromise vehicle mobility. With the trend towards heavier military vehicles and the need to continue to utilise the current stock of

trackway, an understanding of soil/structure interaction is required to maximise the effectiveness of and prevent any unnecessary damage to the trackway itself.

1.2 Objective

The main objective of the research described in this dissertation was to develop a finite element model within CRISP to assess the performance of various trackway geometries, on various soils, subjected to military traffic loads. The Defence Evaluation and Research Agency (DERA) funded the development of a slip element within CRISP suitable for use in soil/structure interaction problems, which will assist in the construction of the finite element models. These elements allow accurate modelling of the slippage that occurs between trackway and soil as it bends under loading and allow uplift of the trackway at the ends which occurs in severe transverse rutting (Figure 1.1). Existing slip elements could achieve this but had problems with the differentiation between total and effective stresses across slip elements. The new slip elements overcome this.

Verification of the finite element models is carried out by physical testing and this primarily consists of centrifuge model testing. The aim of the centrifuge model tests was to assess the effect of a number of factors, in isolation, on trackway performance. These factors include the rapid, cyclic movement of the joints (Figure 1.1) and the effect this has on the properties of the underlying soil; the strength and stiffness of the trackway; the strength and stiffness of the soil; and comparisons between cyclic loads and static loads, since observations in practice describe an accumulation of deformations over successive vehicle passes.

Once a greater understanding of the soil/trackway system has been gained this will allow the feasibility of methods for improving the performance of the current system to be assessed without the need for building prototypes.

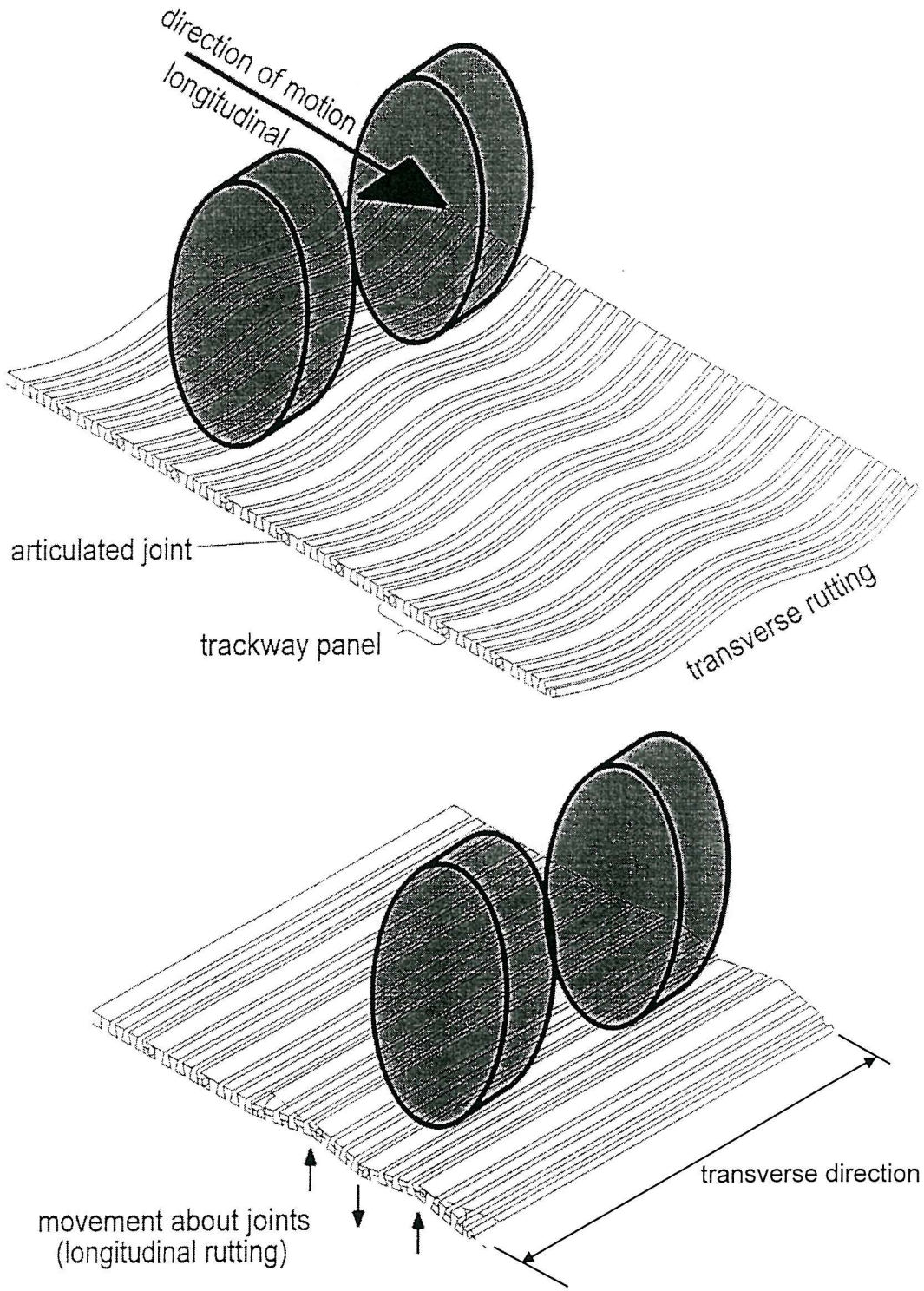

Figure 1.1: Description of trackway terms

1.3 Trackway sections

There are, at present, two main types of trackway: Class 30 and Class 60 (Figures 1.2 & 1.3), designed to support vehicles weighing up to 30 and 60 tonnes respectively. This research is primarily concerned with the Class 60 section although altering the material or geometrical properties of the trackway in the finite element models to Class 30, or any other trackway type, would be a straightforward task.

It can be seen in Figure 1.3 that each Class 60 trackway panel is 8.967″ (or approximately 228mm) wide. The standard panel length is 4.6m, thereby giving a roadway width of this dimension. Trackway panels are connected together using articulated joints. As shown in Figures 1.2 and 1.3, each panel has a male and female joint component along each of their longest sides. When connected, the joint design allows virtually resistance-free rotation but prevents pull-out of the male component under normal operating conditions. The Class 60 articulated joint allows panel rotation through about 17 degrees up and down.

DERA define failure of a trackway panel as when it becomes irretrievable and cannot be rolled back on to its spools for transport. This occurs with a permanent deflection of around 2″(51mm) measured beneath a 9′(2.7m) straight edge. Field experience of trackway failure describes a build-up of trackway deflexions over several vehicle passes rather than immediate failure of the trackway beneath one heavy vehicle.

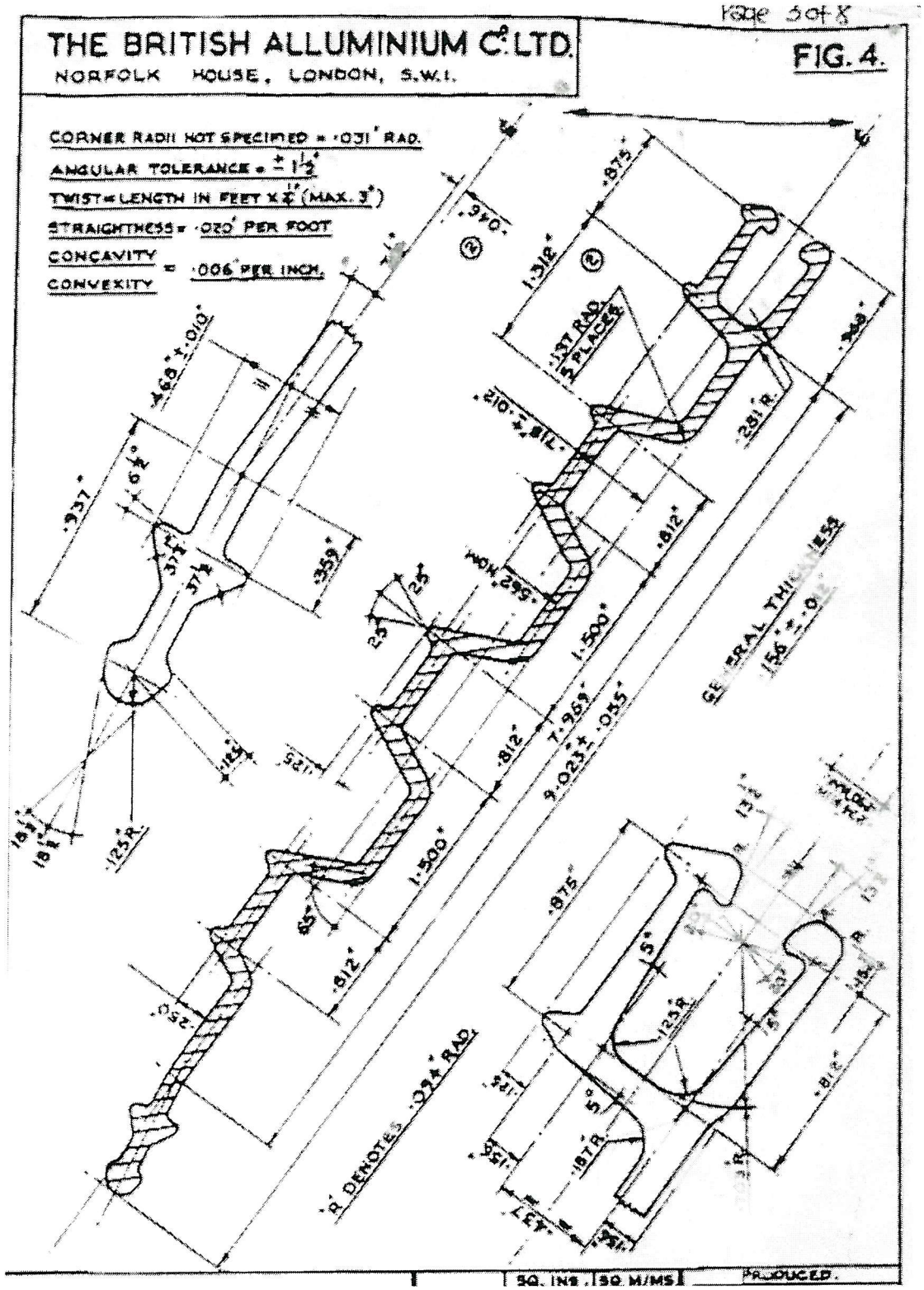

Figure 1.2 Class 30 trackway section

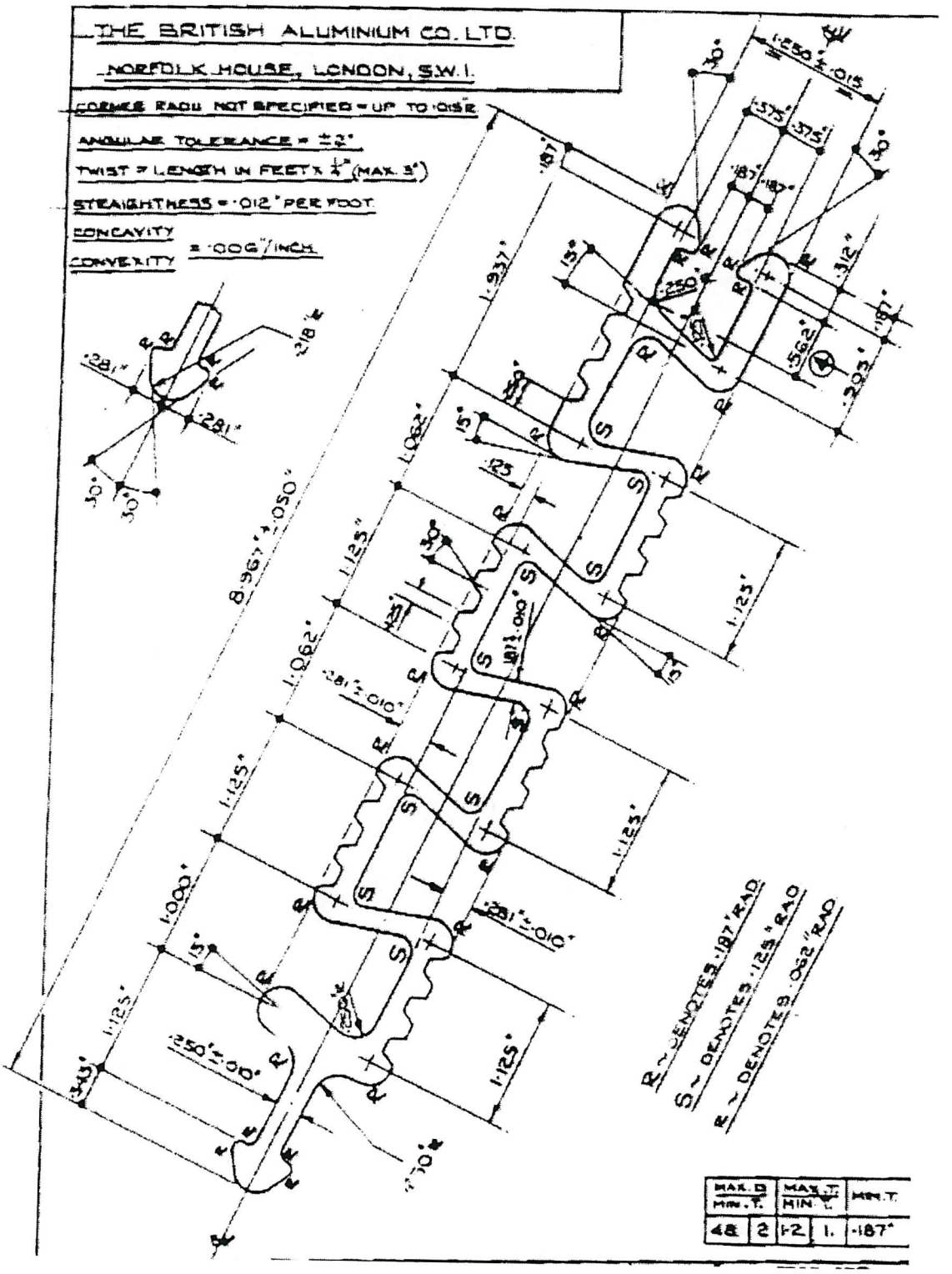

Figure 1.3: Class 60 trackway section

1.4 Military vehicles

There is a wide variety of vehicles that could feasibly use temporary roadways during normal military operations. The heaviest of these is the Challenger tank (Figure 1.4) at 62 tonnes, although its weight is distributed to the ground through twelve load-bearing wheels and two 650mm wide x 4.8m long tracks, resulting in a maximum ground pressure on hardstanding of 97.5kN/m^2. The Leyland DROPS vehicle (Figure 1.5), however, although lighter at 30 tonnes fully laden, distributes its weight through only four axles, giving a mean axle load of 7.5 tonnes (equivalent to 0.7 standard axles in highway pavement design (Croney and Croney, 1991)). The eight 458mm wide pneumatic tyres (at 2042mm spacing on each axle) have standard tyre inflation pressures of: front 519kPa, rear 727kPa, resulting in a specified mean ground pressure on hardstanding of 659kN/m^2. This ground pressure is considerably more onerous to trackway performance than the Challenger tank ground pressure, not only because of its high magnitude, but also because it is concentrated through tyres rather than tracks than can impose very high stresses on single trackway panels. Therefore, all model tests and finite element analyses in this thesis will use the load regime most detrimental to trackway performance that would be encountered in the field: the DROPS vehicle load regime.

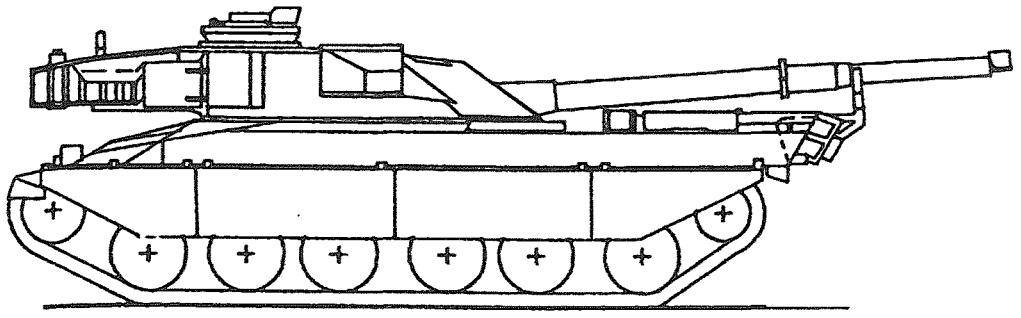

Figure 1.4: Challenger tank

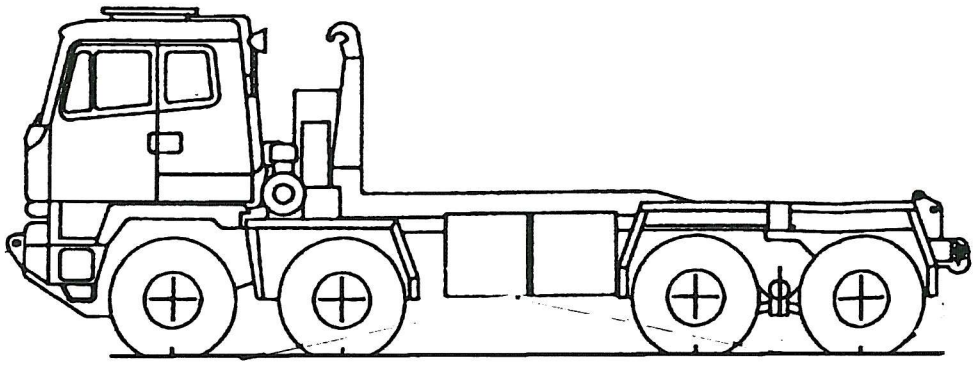

Figure 1.5: Leyland DROPS vehicle

1.5 Difficulties of Analysis

The cause of trackway failure in the field is poorly understood and involves a complicated interaction between the stiffness and failure envelopes of both the trackway and the soil. In addition, there is a wide variety of applied loads, including tyred transporters and tracked tanks weighing over 60 tonnes, which the trackway is used to support and which apply loads to it in different ways both statically and dynamically.

It is straightforward to predict the deflections and failure load of a beam whose section properties are known. Similarly, the failure load of a rigid foundation on a soil of known shear strength, which is either embedded or which has an all-round surcharge on the surrounding soil surface can also be predicted (Sokolovskii, 1965). There are also approximate methods to predict the deflection of an elastic beam lying over an elastic soil of different stiffness (Hemsley & Spence, 1987; Selvadurai, 1979). However there appears to have been little research into the modelling of a flexible surface foundation involving plastic failure of either the foundation or the soil. The observed failure of trackway in the field describes permanent deflections of both the trackway and the soil.

There has been little published research studying temporary trackway. Georgiadis (1979) analysed the behaviour of flexible landing mats: a variant of trackway used for temporary runways. With the methods of analysis available to him at the time, he concluded that:

- the major part of the load distribution was in the transverse direction along each panel and it is sufficient to model landing mats as individual beams
- the mat is as effective in distributing load to the ground when the load is over a joint as when it is in the centre of a panel.

With the lack of available data on the performance and the mechanisms of failure of such systems, physical model testing and finite element analysis represent the most feasible methods of investigating this complex soil/structure interaction problem.

Further complications which need to be addressed include the inherently large deformations of both trackway and soil involved in their combined failure mode and which are difficult to re-create in finite element analyses; the trackway applies a surface load to the underlying soil, with no surrounding surcharge, giving rise to very low (or zero) calculated values of bearing capacity; the very different material properties between aluminium alloy and soft soil cause very different responses to the applied loads which create analytical difficulties when the two materials are in direct contact; and the trackway response to vehicle loads has a 3-dimensional deformation pattern. It can rut transversely (Figure 1.1) beneath the tyres or tracks of vehicles, but there is also rotation about the articulated joints of trackway panels, or longitudinal rutting, (Figure 1.1) in response to vehicle passes. This movement can be rapid and cyclic as wheels or tank tracks pass over the trackway. In addition, there is the problem of rutting increasing over several passes of vehicles: failure deformations do not necessarily occur after the passage of one vehicle but often accumulate to unacceptable levels over an as yet unknown number of passes.

In addition, trackway is invariably laid directly on to the soil surface with no removal of topsoil, due both to its temporary nature and the inherent haste of military operations.

Soil surfaces are normally vegetated and composed of a firm crust of significantly higher shear strength than the underlying saturated soil. Even in wet areas the surface layer of soil can be partially saturated and this region of soil will behave in a different, more complex way to saturated soil.

Chapter 2 of this thesis shows the results of some investigative work into the bending properties of Class 60 trackway and the nature of a soft clay that, if encountered in the field, would compromise vehicle mobility and provide a challenging surface for Class 60 trackway.

Chapter 3 details the development of both the plane strain and rolling vehicle centrifuge models, together with appraisals of the loading apparatuses and modelling procedure. In Chapter 4 the results of the plane strain centrifuge tests involving static and cyclic loads imposed on a flexible aluminium plate overlying a soft clay are presented. The results of the rolling vehicle tests over jointed and unjointed trackway are also presented. The results from all the centrifuge tests are compared and discussed in Chapter 5. The effects of loading pattern and trackway type on soil/trackway performance are also discussed.

In Chapter 6 the results of a series of CRISP finite element analyses, in which both the centrifuge tests and some trackway modifications were modelled, are presented. The derivation and suitability of the input parameters is also discussed. The results of the finite element analyses are discussed in Chapter 7 with particular reference to trackway deflexions and soil/trackway contact stresses. The results are compared with the centrifuge test data presented in chapter 4.

Chapter 8 presents conclusions and suggests areas of further possible research.

Chapter 2

Preliminary Testing

2.0 Introduction

The results of physical tests carried out on trackway and soft clay samples, to provide material parameters for the physical and numerical modelling, are presented.

2.1 Trackway testing

2.1.1 Calculation of section properties

DERA provided the dimensioned cross-sections of the Class 60 trackway, shown in Figure 1.3, together with the material properties of the particular aluminium alloy used in fabrication shown in Table 2.1. The value of yield stress was obtained via a conventional tensile test carried out to British Standard 18 (1987) at the University on a sample of the trackway aluminium.

Young's modulus	69 kN/mm^2
Poisson's ratio	0.3
Density	2700 kg/m^3
Tensile yield stress	270 N/mm^2

Table 2.1 Trackway aluminium alloy material properties

In order to calculate the section properties (area (A), second moment of area (I_{xx}) and plastic section modulus (S_{xx})) of Class 60 trackway, its cross-section was simplified into a series of rectangles of similar area and moments were taken about the base of the section to calculate the position of the centroid. Using this, I_{xx} and S_{xx} were calculated (see Tables 2.2 and 2.3).

CLASS 60 Element	Horizontal width B (mm)	Vertical height D (mm)	Area B*D C (mm^2)	Height of el.centroid y_c (mm)	Moment of area Cy_c (mm^3)	Vert. dist. $Y_c - y_c$ y (mm)	Parallel axis correct'n Cy^2 ($E3mm^4$)	Ixx_c ($E3\ mm^4$)	I_{xx} Ixx_c+Cy^2 ($E3\ mm^4$)
1.1	38.1	5.6	213.36	2.8	597.4	11.54	28.412	0.5576	28.9693
1.2	38.1	5.6	213.36	26.4	5632.7	12.06	31.034	0.5576	31.5913
1.3	38.1	5.6	213.36	2.8	597.4	11.54	28.412	0.5576	28.9693
1.4	38.1	5.6	213.36	26.4	5632.7	12.06	31.034	0.5576	31.5913
1.5	38.1	5.6	213.36	2.8	597.4	11.54	28.412	0.5576	28.9693
2.1	5.3	18.0	95.40	14.6	1392.8	0.26	0.006	2.5758	2.5823
2.2	5.3	18.0	95.40	14.6	1392.8	0.26	0.006	2.5758	2.5823
2.3	5.3	18.0	95.40	14.6	1392.8	0.26	0.006	2.5758	2.5823
2.4	5.3	18.0	95.40	14.6	1392.8	0.26	0.006	2.5758	2.5823
2.5	5.3	18.0	95.40	14.6	1392.8	0.26	0.006	2.5758	2.5823
3	58.7	5.8	340.46	26.4	8988.1	12.06	49.521	0.9544	50.4751
4	6.9	18.0	124.20	14.6	1813.3	0.26	0.008	3.3534	3.3618
5	32.5	6.0	195.00	2.8	546.0	11.54	25.967	0.5850	26.5518
6.1	7.9	3.2	25.28	25.2	637.1	10.86	2.982	0.0216	3.0033
6.2	7.9	3.2	25.28	7.5	189.6	6.84	1.183	0.0216	1.2042
7	8.7	25.5	221.85	14.6	3239.0	0.26	0.015	12.0215	12.0365
8	21.4	6.9	147.66	14.6	2155.8	0.26	0.010	0.5858	0.5959
9	8.7	13.1	113.97	14.6	1664.0	0.26	0.008	1.6299	1.6376

Vertical height of section centroid, Y_c =14.34 **Total I_{xx} 261.87 E3 mm^4**

$Y_c = \Sigma (Cy_c)/\Sigma (C)$. Second moment of area of element about its centroid, $Ixx_c = BD^3/12$. Using parallel axis theorem, second moment of area of section about its centroid, $I_{xx} = \Sigma (Ixx_c + Cy^2)$

I_{zz}, for bending in longitudinal direction across thinnest part of section, = 14.87 E3 mm^4 per m panel length

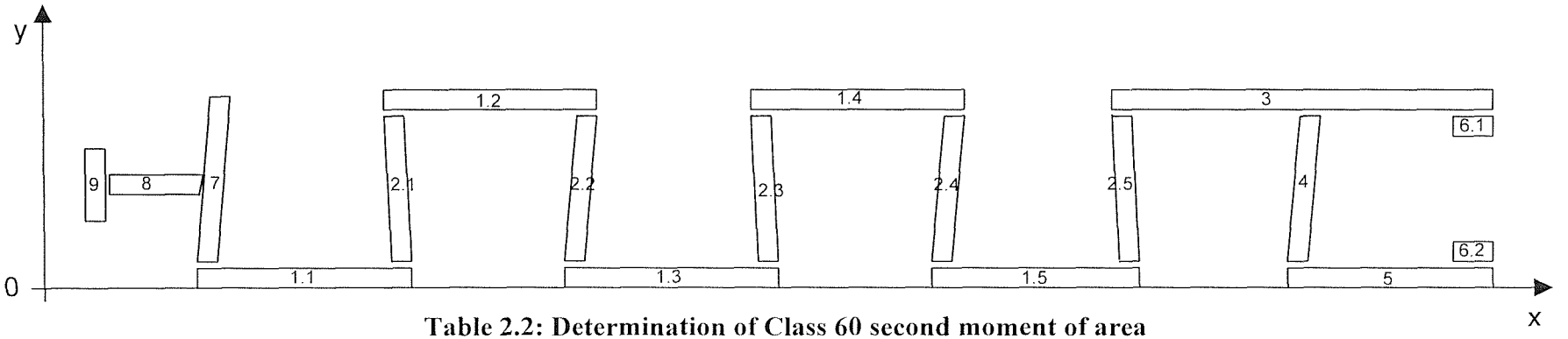

Table 2.2: Determination of Class 60 second moment of area

CLASS 60 Element	Horizontal width B (mm)	Vertical height D (mm)	Area B*D A (mm^2)	Height of centroid y_c (mm)	First mom. of area Ay_c (mm^3)
1.2	38.1	5.60	213.36	12.06	2573.12
1.4	38.1	5.60	213.36	12.06	2573.12
2.1	5.3	9.25	49.03	4.63	226.99
2.2	5.3	9.25	49.03	4.63	226.99
2.3	5.3	9.25	49.03	4.63	226.99
2.4	5.3	9.25	49.03	4.63	226.99
2.5	5.3	9.25	49.03	4.63	226.99
3	58.7	5.80	340.46	12.06	4105.95
4	6.9	9.25	63.83	4.63	295.51
6.1	7.9	3.20	25.28	10.87	274.79
7	8.7	16.82	146.33	8.41	1230.67
8	21.4	3.72	79.61	1.86	148.07
9	8.7	6.80	59.16	3.40	201.14

Plastic section modulus, $S_{xx}=2\Sigma ay_c$ **S_{xx} = 25.07E3 mm^3**

Refer to Table 2.2 for element definition and determination of section centroid.

S_{zz} for bending in the longitudinal direction across thinnest part of section, = 3920 mm^3 per m panel length.

Table 2.3 Determination of Class 60 plastic section modulus

2.1.2 Trackway bending tests

In order to validate the section properties calculated from the simplified trackway cross-section, bending tests were carried out on sections of Class 60 trackway, in both the longitudinal and transverse directions. The longitudinal bending test was carried out in the manner described in Figure 2.1 and the central load, P increased until deflexion increased at constant load. Selected load-deflexion values from this test are compared in Table 2.4 with values calculated from the material properties in Table 2.1 and the simplified cross-section I_{zz} and S_{zz} values (Tables 2.2 & 2.3), to help verify these values.

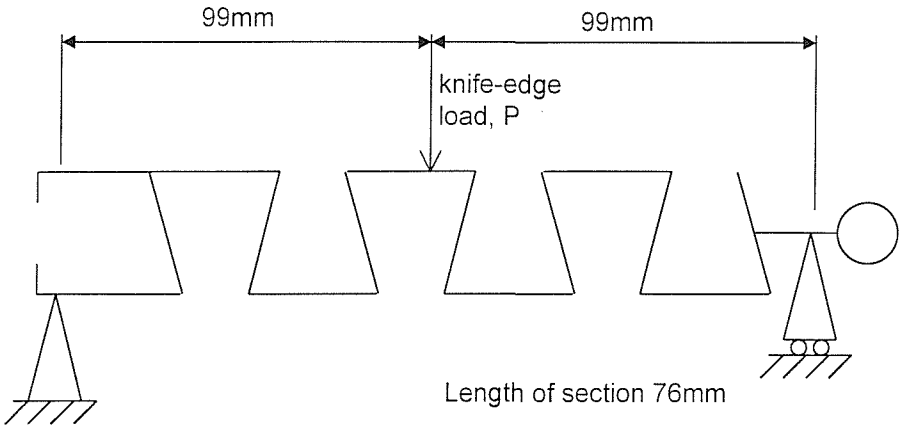

Figure 2.1: Longitudinal trackway bending test

3 point longitu. bending	P = 500N deflexion (mm)	Elastic limit		plastic hinge
		P (N)	deflexion (mm)	P (N)
Measured values	2.9	910	5.1	2248
Calculated values	2.6	1086	5.7	1629

Deflexions predicted using formula max.$\Delta=WL^3/48EI$, elastic limit using Engineer's bending formula $M/I=\sigma/y$, plastic hinge moment using formula $Mp=S_{zz}\sigma_y$. Elastic limit determined as limit of proportionality on load-deflexion graph.

Table 2.4 Class 60 longitudinal bending test results and calculated values

The calculated loads and deflexions are close to the test values for the elastic state, but significantly under-estimate the load at which a plastic hinge develops. This is most likely due to the S_{zz} value being derived from the thinnest part of the section between the ridges in Class 60 trackway (Figure 1.3), as yield occurs there is likely to be a redistribution of stress to thicker areas of the section.

The transverse bending test was carried out on one panel with two simple roller supports, 1.8m apart, and a central knife-edge load (Figure 2.2). The load, P, was increased until the trackway began to yield at constant load. A load-deflexion graph for the test is shown in Figure 2.3 in addition to values calculated from the material properties in Table 2.1 and the section properties from Tables 2.2 and 2.3, where the

length of the plastic portion of the graph was assumed to be similar to that of the measured case. Selected load-deflexion values are also compared in Table 2.5.

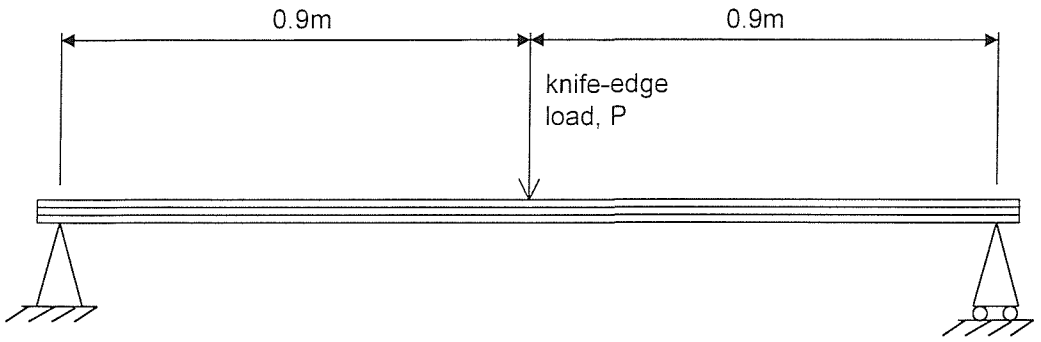

Figure 2.2: Transverse trackway bending test

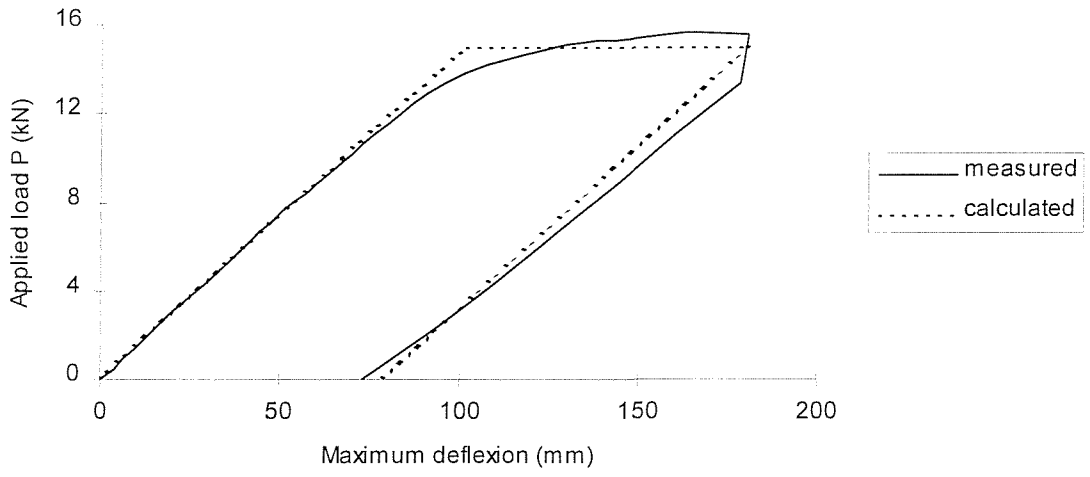

Figure 2.3: Transverse trackway bending test load-deflexion graph

3 point transverse bending	P = 5 kN deflexion (mm)	Elastic limit		plastic hinge P (kN)
		P (kN)	deflexion (mm)	
Measured values	33	10.67	72	15.61
Calculated values	33.6	10.03	67.4	15.04

Deflexions predicted using formula max.$\Delta=WL^3/48EI$, elastic limit using Engineer's bending formula $M/I=\sigma/y$, plastic hinge moment using formula $Mp=S_z\sigma_y$. Elastic limit determined as limit of proportionality on load-deflexion graph.

Table 2.5 Class 60 transverse bending test results and calculated values

As can be seen in Table 2.5 and in Figure 2.3, the test results and calculated values are very similar for both the elastic and plastic states. This fully verifies the material and section properties used in the beam equations to predict these values.

Comparing the longitudinal and transverse bending stiffness values of Class 60 trackway a single panel is 3.8 times stiffer in transverse bending than longitudinal bending. If the virtually zero rotational stiffness of the articulated joints were incorporated into the overall trackway stiffness in the longitudinal direction, the difference between longitudinal and transverse stiffness becomes even greater. Although failure of trackway usually occurs by excessive rutting in the stiffer transverse direction it is possible that bending of the trackway in the more flexible longitudinal direction and, more particularly about the articulated joints, is significant during the onset of trackway failure.

A summary of the transverse trackway bending stiffness values used throughout this thesis is given in Appendix A.

2.2 Soil sampling

Trackway is often used where there are difficult ground conditions on the approaches to temporary bridges. A problem soil that is likely to be encountered is a soft silty-clay alluvium, found on the flood plains of rivers and which typically would form temporary bridge approaches. Alluvia are variable, recent deposits of river sediment which, in the

silty-clay case, are very soft in nature. It was decided to adopt the performance characteristic of this type of soil in all the model tests and analyses, given its occurrence in typical fields of operation and challenging engineering properties in terms of trackway performance.

To analyse the true nature of this material and to obtain certain soil parameters, samples of alluvia were collected from the flood plain of the river Arun in West Sussex. The precise location was in the river's lower course near Amberley, upstream of the chalk of the South Downs. This ensured that the river had drained entirely from the sands and clays of the Lower Cretaceous so that the flood plain deposits would comprise clays and silts with no deposits of gravel or calcium carbonate (tufa). The site is shown in Figure 2.4. Samples were taken from the area of flood plain between the levée in the foreground and the river bank, where trackway would be laid if a temporary bridge were placed over this river. The site had grass vegetation and an approximate 0.4m depth of partially saturated topsoil overlying a dark grey clayey alluvium with small pockets of sand and organic material. Eight U38 tube samples were obtained in all at depths of 0.6, 0.8 and 1.0m. Laboratory soil tests were carried out and the parameters obtained are summarised below in Table 2.6.

Particle size distribution (PSD) was also determined and a typical PSD curve is shown in Figure 2.5. The curve shows that the sample is composed almost entirely of silt and clay particle size with a predominance of the clay particle size (65% by weight).

Depth of sample (m)	0.6	0.8	1.0
$w^{(1)}$ (%)	91.4	102.7	110.4
$\rho_{bulk}{}^{(2)}$ (mg/mm^3)	n/a	1.44	1.43
$c_u{}^{(3)}$ (kPa)	n/a	17.5	6.5
$k_v{}^{(4)}$ (m/s)	4.9×10^{-10}	7.0×10^{-10}	n/a
organic content$^{(5)}$ (%)	9.2	10.1	5.9

1 - moisture content in accordance with BS 1377:Part2:1990, 2 - bulk density in accordance with BS 1377:Part 2:1990 specimen direct from sample tube, 3 - undrained shear strength by unconsolidated undrained triaxial test, 4 – vertical permeability by falling head permeameter test, 5 - mass loss on ignition in accordance with BS 1377:Part 3:1990 100% passing 2mm. n/a – not available.

Table 2.6 Arun valley alluvium soil properties

All the samples possessed a high water content which increased with depth, as shown in Table 2.6, suggesting the likelihood of partially saturated conditions near the surface. As the water table seasonally rises and falls, surface layers of the alluvium normally become lightly over-consolidated (Schumm et al, 1987) and this is reflected in the both the higher values of undrained shear strength and lower water content values at 0.8m depth than 1.0m depth.

It was attempted to replicate this typical field material in the centrifuge model tests described in Chapter 3 using kaolin. Kaolin is a well-defined silty-clay (Al-Tabbaa, 1987) and has been used in several other centrifuge model investigations (Richards, 1995; Sun, 1990; Powrie, 1986). Some typical parameters for the kaolin clay used in the centrifuge tests are shown in Appendix B.

Figure 2.4: Arun valley soil sampling site

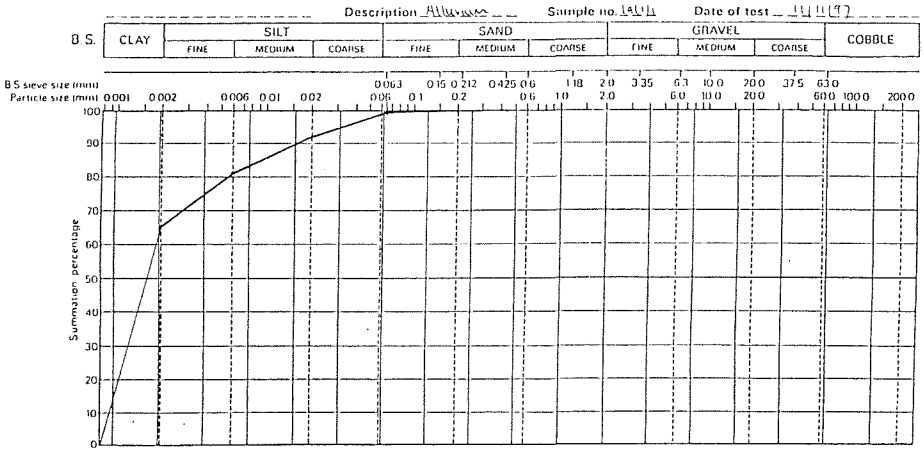

Figure 2.5: Arun valley alluvium PSD curve

Chapter 3

Centrifuge Modelling Procedure

3.0 Introduction

A series of centrifuge model tests was performed on the London Geotechnical Centrifuge. The aim of these tests was to develop an appropriate experimental technique, and then to investigate the nature of trackway failure on soft soil. In this chapter, the general principles of centrifuge modelling are summarised and the main features of the tests are discussed in detail. The performance of the apparatus is appraised, and the suitability of the data generated is assessed.

3.1 Centrifuge modelling

Successful centrifuge modelling depends on correctly scaling the essential behaviour of the prototype (Schofield, 1980). The model is a reduced scale version of the prototype, it is tested by replicating an event comparable to what occurs in the prototype and the results then extrapolated to the prototype situation. The scale of the model is reduced by a factor of N and its self weight is increased by the same factor due to the effect of a radial acceleration of N gravities in the centrifuge. This will allow the vertical stresses in the prototype to be correctly modelled. In addition, the time scale for consolidation is reduced by a factor N^2 due to the drainage path lengths in the model being reduced by a factor of N. Provided the area of interest is remote from all model boundaries, there is no reason why a carefully constructed model should not accurately simulate the behaviour of the prototype. There are, however, several factors which can contribute to errors in the modelling process:

1. The centrifugal acceleration field $r\omega^2$ varies with the radius and therefore cannot be uniform over the whole height of the model. Since the trackway itself and the soil immediately beneath it formed the primary area of interest, the radius to the soil surface was used to determine the required rotational speed of the centrifuge. This caused parts of the apparatus radially inside (i.e. above) soil level to be under stressed, and the soil outside (below) the surface to be over-stressed. The rotational speed of the centrifuge was necessarily adjusted appropriately between Test Levels 1 and 2 (Section 3.6).
2. In contrast to some centrifuge machines, the model package is mounted so that the model width dimension on plan (200mm) is subjected to a variation in direction of the radial acceleration field due to curvature. However, the use of a flat soil surface gives a variation in load "verticality" across the width of the model of only 0.23%.
3. A further potential source of error in the centrifugal acceleration field arises from model movements within the plane of rotation. Movements within this plane will generate Coriolis accelerations and distort the normal centrifugal acceleration. This would be particularly significant when vehicle movements occur in the model. To keep the ratio of Coriolis accelerations to centrifugal accelerations to less than 10%,

it is recommended that vehicle speeds are kept outside the range $0.05V < v < 2V$, where V is the speed of the whole centrifuge model and v is the speed of the vehicle, for the worst case when vehicle movements are along the radial axis of the centrifuge (Taylor, 1995).

4. A conflict exists between the time scaling factors for dynamic events (1/N) and consolidation ($1/N^2$). Where dynamic modelling and consolidation occur as separate events, each scaling factor can be applied independently. However, with longer periods of dynamic modelling, significant seepage flow could occur concurrently, leading to a conflict between time scaling factors. The two scaling factors can be harmonised by reducing the model soil's permeability: either by reducing the particle size or by increasing the viscosity of the pore fluid (Steedman and Zeng, 1995). When modelling a clay, as in this research, reducing the particle size is not feasible. A significant drawback with using a viscous pore fluid is the considerable lengthening of the re-consolidation time (Section 3.5). Provided careful consideration was given to these conflicting scaling factors, it was not considered detrimental to the validity of the tests to use them.

From the relationships for self-weight stress (1:1), length (1:N) and gravitational acceleration (1:1/N), the scaling relationships for all related quantities for quasi-static and dynamic tests can be derived. These are set out in Table 3.1.

3.2 The London Geotechnical Centrifuge Centre

The London Geotechnical Centrifuge Centre is housed at City University. The centrifuge is a purpose built Acutronic 661 machine with a swinging platform which carries the model strongbox. In flight the surface of the platform will be approximately vertical, rotating about a vertical axis in a circle with a radius of 1.8m. The centrifuge is rated as a 40g-tonne machine, being capable of supporting a maximum payload of 400kg at 100g. A counterweight system is used to balance the model on the swinging arm. There are electrical slip rings for data acquisition (64 channels), DC and AC power to

motors, valves, cameras and lighting on the arm. In addition, a 5-port rotary union allows hydraulic and pneumatic connections to the model. The principal design considerations and the specification of the Acutronic 661 machine are given by Schofield and Taylor (1988).

Quantity	Prototype	Model
Length	1	1/N
Mass	1	$1/N^3$
Stress	1	1
Force	1	$1/N^2$
Strain	1	1
Young's Modulus E	1	1
Second moment of area I	1	$1/N^4$
Velocity	1	1
Acceleration	1	N
Time		
In dynamic problems	1	1/N
In consolidation	1	$1/N^2$
Frequency	1	N

Table 3.1: Scaling factors for centrifuge tests

3.3 Model geometry

The overall geometry of the centrifuge model, Figure 3.1, was based on 4.6m wide prototype Class 60 trackway. Using a centrifuge scale of N = 38, a model trackway width of 120mm was required. The distance between the strongbox side-walls and the trackway was 215mm, at least $3^1/_2$ times the trackway half-width. This allowed the trackway to mobilise the largest area of soil should it fail in a rigid manner. Typically, when a bearing capacity type failure occurs, the passive zones under a rigid strip

foundation extend outwards to a maximum distance of approximately $2^1/_2$ times the foundation half-width for a soil with an internal friction angle of 26° (Sokolovskii, 1959). Had the model trackway failed in a rigid manner, the $3^1/_2$ times trackway half-width distance to each of the side-walls would have been sufficient to eliminate end-effects within the passive zones.

The trackway loading pattern replicated that imposed by a military DROPS vehicle. Since this is the heaviest of the tyred vehicles currently used in operations involving temporary roadways, it represented the load most detrimental to trackway performance. At model scale (1:38), each tyre is 12mm wide and the total track width across both tyres is 66mm. In tests 1 and 2 a plane strain load was imposed with two 15mm wide "tyre" loads being provided by extending loading strips across the full width of the strongbox. In tests 3 and 4, the rolling vehicle tests, a pair of rubber tyred wheels, 41mm diameter, were joined together at the correct spacing by a fixed axle, and were driven repeatedly over the model trackway from one end to the other. All the loading apparatus is described in more detail in section 3.7.

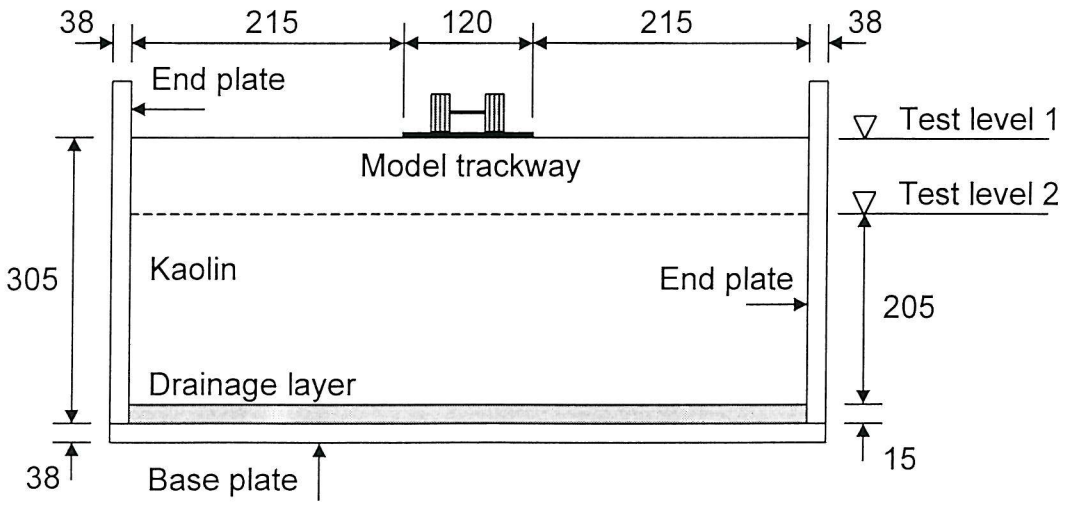

Figure 3.1: Centrifuge model geometry, dimensions in mm at model scale

For tests 1 and 2, the plane strain tests, and test 3, one of the rolling vehicle tests, the trackway was unjointed and was modelled as a simple aluminium plate, extending across the full 200mm width of the strongbox. A 0.6mm depth replicated the section properties, and hence transverse bending strength and stiffness, of Class 60 trackway at the model scale. The data obtained from tests 1 and 2 was used to calibrate two-dimensional plane strain finite element models of soil/trackway behaviour. The material and section properties of the model trackway are discussed in detail in section 3.7.1.

For test 4, the other rolling vehicle test, the trackway was divided into individual panels of Class 60 width (joint to joint: 216mm prototype, 5.7mm model) joined in series to form a model trackway road across the full width of the strongbox (35 panels in all). The panels were held together by two 50mm wide continuous strips of 30μm aluminium foil adhesive tape. Again, 0.6mm thick aluminium sheets were used and each panel itself was 5.5mm wide. A 0.2mm gap between each panel ensured free rotation about each joint and maintained the 5.7mm joint to joint dimension. The model trackway is described in greater detail in Section 3.7.1.

Preliminary finite element analyses and developmental centrifuge tests showed that, because of its shallow nature, the model trackway's depth of influence (i.e. the depth to which significant deviatoric stresses were measured in the soil) was in the region of only 100mm at model scale. With a strongbox depth of 376mm two tests could comfortably be carried out using one sample of soil. The first test could be carried out at Test Level 1, with an approximate soil depth of 305mm (11.6m prototype). Prior to the second test, 100mm of soil was excavated to expose a new surface and Test Level 2 for the model trackway (Figure 3.1). Provided the mean normal effective stress, p′, in the first test at a depth of 100mm or more never exceeded the p'_c value during sample preparation, the properties of the second surface would be the same as those for the first. Moreover, each soil layer was prepared from the same mix with the same stress history. This is covered in detail in Section 3.6.

3.4 Modelling technique

A plane strain strongbox, manufactured from 38mm Dural plate, was filled with a de-aired kaolin slurry and placed on a 200kN capacity constant load consolidation machine (see section 3.6). The loading platen (550mm long x 200mm wide, corresponding to the plan dimensions of the strongbox) was lowered onto the top of the slurry. To the underside of the platen was attached Vyon porous plastic which, together with the grooves machined on the underside of the platen, allowed drainage to occur at the top of the sample. Similarly, machined drainage grooves and drainage holes at each end of the strongbox baseplate, together with another Vyon plastic sheet overlying a 15mm layer of 18/25 Leighton Buzzard sand, allowed drainage at the base of the sample. A load cell located between the cylinder ram and the loading platen measured the load on the platen. As the kaolin consolidated, the platen moved under the applied constant load. The movement of the platen was monitored using a dial gauge indicator, with the next increment of load being applied when downward movement of the platen, due to the previous load, had effectively ceased. A detailed description of the sample preparation is given in section 3.6.

During the sample consolidation stage stiffened Dural strongbox side plates were used to keep side deflexions to a minimum and to ensure that loading was one-dimensional.

In the consolidation machine, the sample was gradually consolidated to a vertical effective stress of 106kPa. Once the clay sample had reached equilibrium at a vertical effective stress of 106kPa, the loading platen was withdrawn and the strongbox removed from the press.

The stiffened front plate was removed and replaced with a Perspex viewing window. Whenever strongbox plates were bolted together, care was taken to ensure that the rubber sealing cord, located within a groove machined around the outer edges of the base- and side-plates, was positioned correctly between the mating faces of the box. This ensured that the box was watertight.

Pore water pressure transducers (PPTs) were positioned within the clay model at various depths beneath and around the trackway and were used to measure the pore water pressure response of the clay during key stages of the test. The positioning and performance of the PPTs are discussed in section 3.7.4.

The next stage involved the removal of excess clay down to the required level, providing a clean, flat surface on which to place the model trackway. This was accomplished by dragging a metal scraper, set to an appropriate excavation depth, successively across the clay until an overall soil depth of 302mm was achieved. The instrumented model trackway was then placed centrally onto the newly exposed surface, taking care not to indent the soft clay in any way and to ensure the trackway was placed squarely into the strongbox (so that plane strain conditions prevailed). During the model-making procedure, the exposed surfaces of the model were covered by plastic film to prevent desiccation of the clay sample. Seven strain gauges were attached to each model trackway to measure the distribution of load within the trackway and hence the deflexion of the plate. The strain gauge leads needed to be routed and fixed along the trackway and out of the strongbox so that they caused minimal interference to the trackway, the soil and the loading apparatus. Section 3.7.1 contains a more detailed discussion of the positioning and performance of the strain gauges.

A rigid top plate, supporting either a pneumatic cylinder and loading beams for plane strain modelling, or an axle drive train and electric motor, was bolted across the top of the strongbox, over the model trackway. These loading devices are discussed in detail in section 3.7. In the tests involving the pneumatic cylinder, the top plate also supported two linear variable differential transformers (LVDTs), used to measure displacements of the model trackway. The pneumatic cylinder shaft was connected to the loading beams via a miniature tension/compression load cell which directly measured the load imposed by the cylinder onto the trackway.

In the pneumatic cylinder tests, a second top plate located above the soil to one side of the trackway was then bolted into place and four LVDTs, used to measure soil displacements, were clamped into position. Prior to the test, the LVDTs were adjusted so that the linear portion of the LVDT stroke could be fully utilised during the test. The positioning and performance of the LVDTs are discussed in detail in section 3.7.5.

The centrifuge model was then placed onto the centrifuge platform and all the transducers plugged into the junction boxes. Water was supplied to the model by a simple drip feed to the clay surface at one end of the box. A surface drain at the other end of the box ensured the model did not flood. In addition, to supply water to the base at an appropriate hydrostatic pressure, a second centrifuge drip feed was placed in a standpipe that had an internal overflow set to the equivalent height of, or just below, the soil surface (~2mm tolerance). This overflow was positioned to take account of the effects of the curved free water surface during the test and, being set at about the same potential as the soil surface, ensured the clay remained saturated (to within 0 to 2mm of the surface) throughout the test.

During the initial stage of the test, in which the clay sample comes into equilibrium under its enhanced self-weight (re-consolidation phase), the clay has two-way drainage which allows hydrostatic equilibrium to be achieved comparatively rapidly. It was important to ensure that all loading devices and/or model vehicles were supported clear of the soil during the re-consolidation phase to prevent uneven compression of the soil surface under their enhanced self-weight. In tests involving the pneumatic cylinder to provide surface loadings, a negative cylinder pressure was provided to support the attached loading platen; in tests involving the rolling axle, temporary support was provided by a small, solenoid valve controlled, pneumatic cylinder.

On completion of the re-consolidation phase, as evidenced by the pore pressure transducer responses (Section 3.5), the main part of the test was started. This involved decreasing the datalogging recording interval to its minimum value (approximately 0.6s) immediately before subjecting the model trackway to its strip, or vehicle, loading.

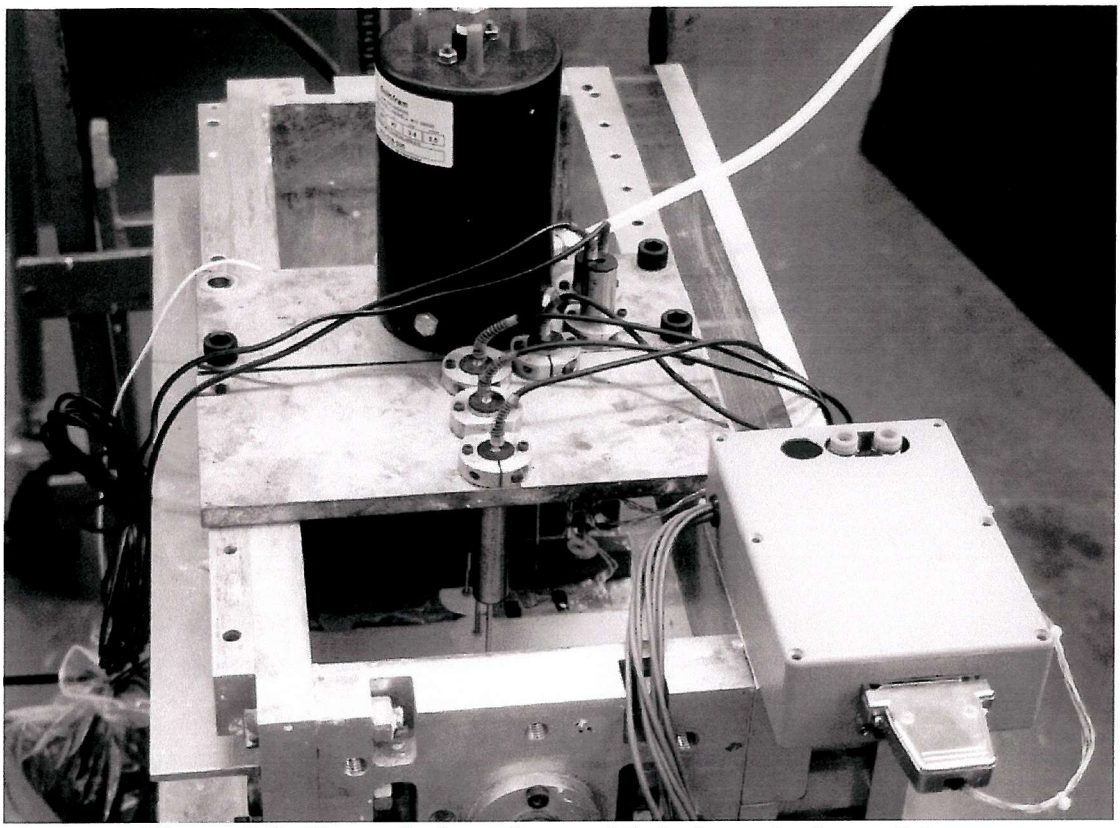

Figure 3.2: General view of assembled plane strain model

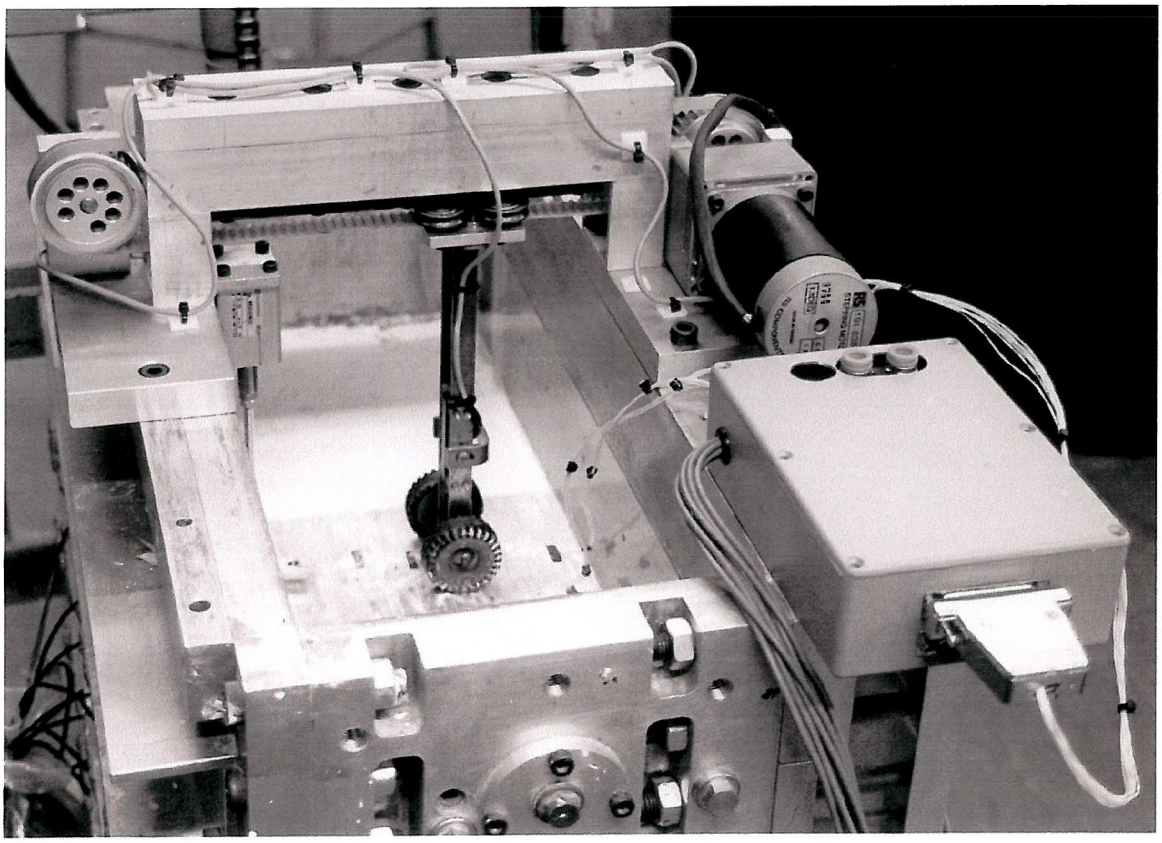

Figure 3.3: General view of assembled rolling vehicle model

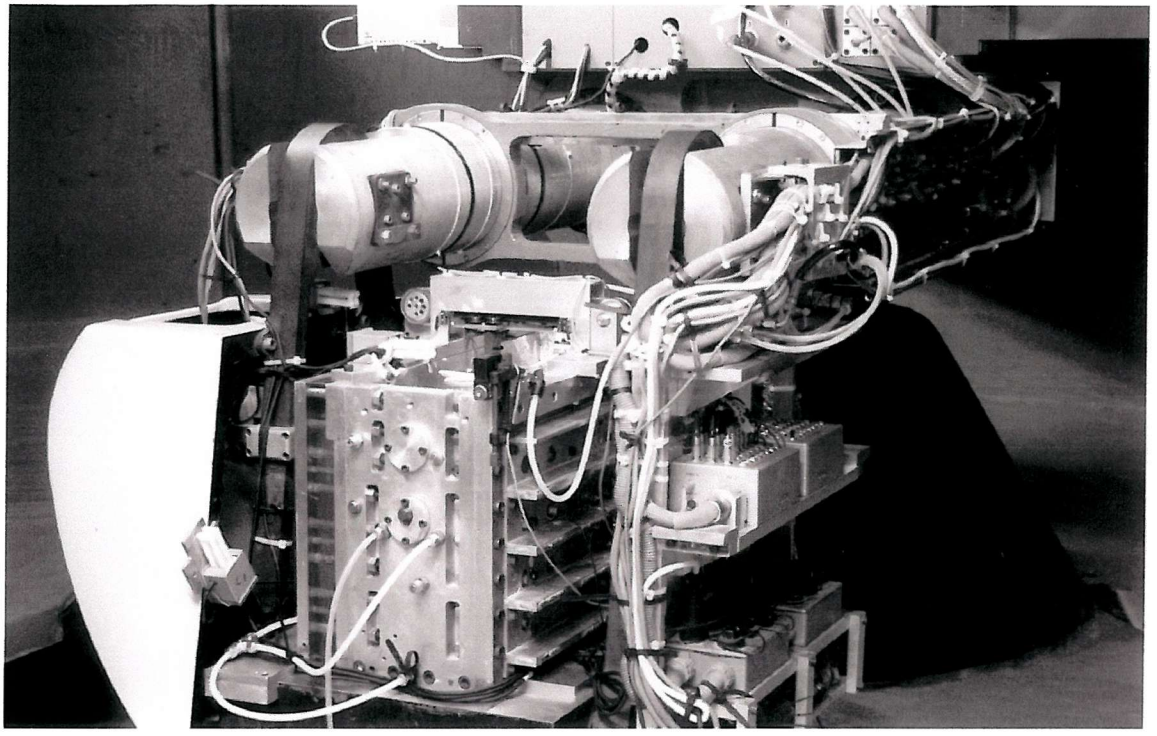

Figure 3.4: Strongbox positioned on centrifuge platform ready to start test

Tests 1 and 2 were the plane strain tests. Test 1 imposed a double strip load replicating vehicle loadings on the trackway in a simple static fashion. The load magnitude was increased in steps until failure of the soil/trackway system occurred. Test 2 imposed the same loading pattern, again increasing its magnitude in steps to failure, but this time with a continuous 1 Hz cycle introduced instead of a simple static load. Since the applied load is of a plane strain nature, each load peak represents a 'whole vehicle load'. At the prototype scale, the cyclic load pattern represents the passage of a heavy vehicle every 38 seconds. Each increase in load amplitude represents a heavier series of vehicles. In effect, the applied vehicle weight increases until failure of the soil/trackway system occurs. The purpose of the load cycling tests was to determine, to what extent, cyclic 'whole vehicle loads' are detrimental to soil/trackway performance compared with a single, static vehicle load.

Tests 3 and 4 involved the rolling vehicle. At the end of the re-consolidation phase the vehicle support was released, allowing the vehicle to impose its enhanced self-weight

(equivalent to 4900kg at prototype scale) onto the trackway for the first time. This prototype scale load is similar to that exerted by a typical DROPS vehicle axle (Section 1.4). Immediately after releasing the vehicle, it was driven backwards and forwards along the trackway with a length of travel on each leg of 130mm. Each complete cycle (see Figure 3.5) took 2.7 seconds, a vehicle speed of 0.1m/s. With a centrifugal acceleration of 38g at the soil surface, the linear speed of the strongbox at any one time is 23.3m/s. As the vehicle moved along the soil surface, changes to its radius of centrifugal rotation were less than 3mm, hence Coriolis accelerations were negligible. Although the prototype vehicle speed of 0.2mph is significantly lower than normal vehicle speeds (~5-10mph), modelling constraints prevented faster vehicle speeds being used, it does represent a vehicle pass, each way, every 50 seconds. In addition, since the velocity scale factor in the centrifuge model is 1:1, the risk of damaging the delicate model trackway or causing it to "ruck up" at elevated speeds (a particular problem in the field), or indeed, the problem of obtaining a sufficient quantity of data, at a model speed of 10m/s, say, did not make such speeds realistic. Centrifuge modelling generally involves a series of compromises that need to be carefully considered to arrive at a reasonably accurate, yet practical, model.

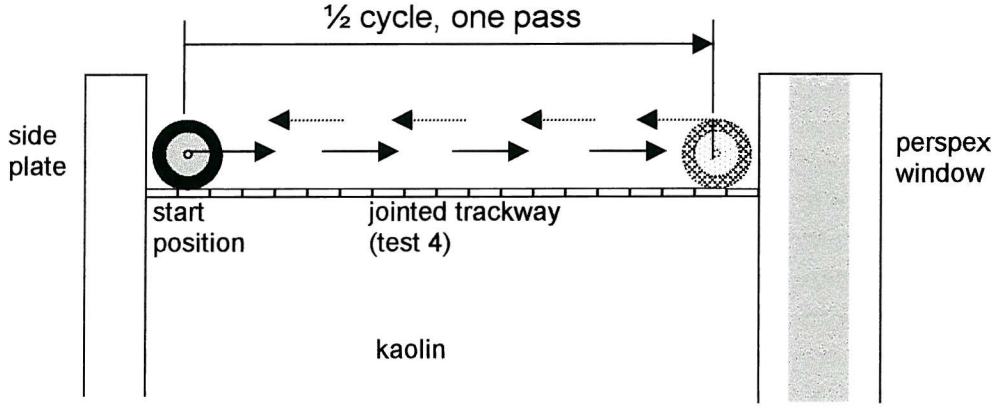

Figure 3.5: Rolling vehicle terminology

The rolling vehicle was driven over the unjointed aluminium plate in test 3 and over jointed trackway in test 4. Rather than subjecting the soil to 'whole vehicle load' cycles

as in test 2, axle load cycles were imposed on the soil and, indeed, in test 4 the vehicle loads were transferred to the soil through the cyclic rotation of the trackway panels themselves. By comparing the data from the jointed and unjointed roadway, the effect of the trackway joints on soil/trackway performance could be assessed. In both tests vehicle passes continued until trackway deflexions had either stabilised at a constant value or reached a point where the vehicle's mobility was seriously impaired through trackway distortion.

3.5 Re-consolidation

During the first stage of the centrifuge test, the clay sample is allowed to come into equilibrium (re-consolidate) under its enhanced self-weight. Re-consolidation is deemed to be complete when excess pore pressures in the clay have fully dissipated and hydrostatic equilibrium has been restored to the sample. Figure 3.6 shows the pore pressures recorded by PPTs against root time for test 3. It can be seen that the time taken for excess pore pressures to dissipate was approximately 9 hours at prototype scale, after which pore pressures reached their approximate hydrostatic value, as shown in Figure 3.7. This was the shortest time required to achieve equilibrium for any of the tests discussed in this dissertation, although it never exceeded 11 hours.

The self-weight of the model trackway was the only imposed load on the soil surface during the re-consolidation phase. Both the jointed and unjointed model trackways each weighed 40grammes at 1g, and imposed a stress of approximately 0.6kPa on the soil surface at 38g (prototype Class 60 trackway applies a surcharge of 0.4kPa). This slight increase in stress beneath the trackway is likely, therefore, to cause a negligible degree of settlement over and above that caused by the soil's self-weight.

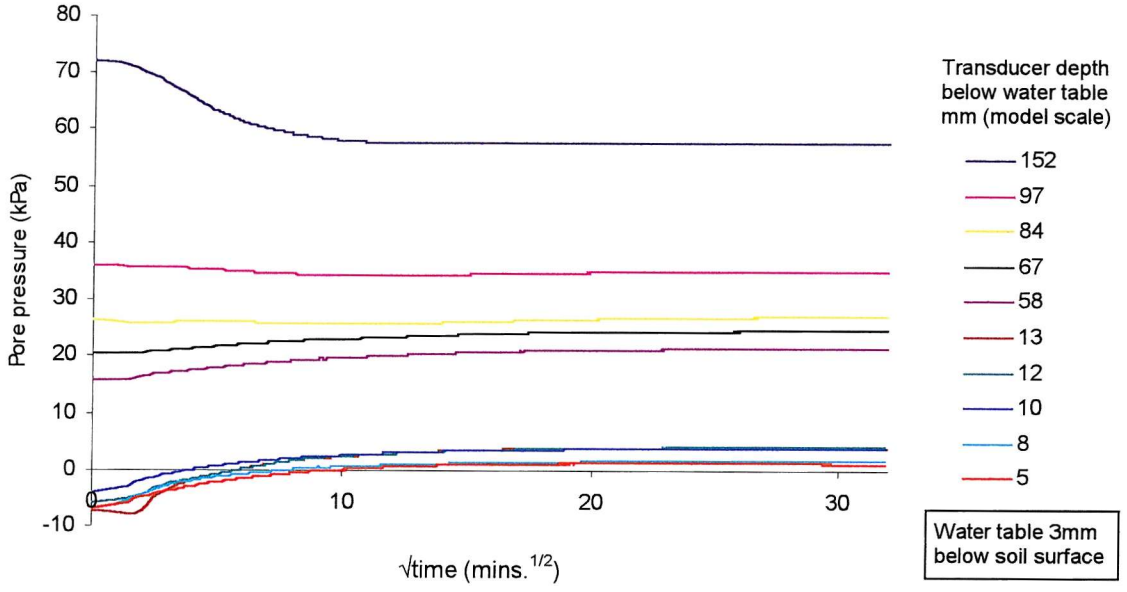

Figure 3.6: Pore pressures during re-consolidation

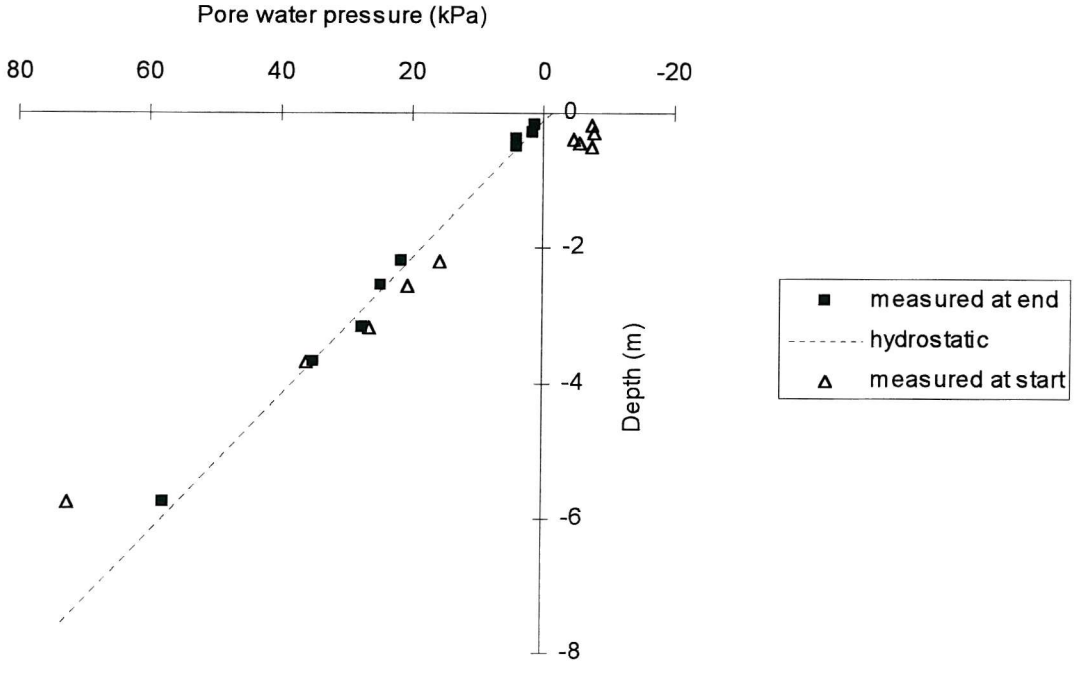

Figure 3.7: Pore water pressure profiles during re-consolidation

3.6 Stress history & sample preparation

The clay used in all tests was speswhite kaolin, which was selected because it has a relatively high permeability, typically 4×10^{-9}m/s, and its basic properties are well researched (Al-Tabbaa, 1987). Moreover, speswhite kaolin has been widely used in previous centrifuge model tests on clay soils (Powrie, 1986; Sun, 1990; Richards, 1995). Each sample was prepared by mixing kaolin powder with de-aired water under a vacuum to a slurry with a moisture content of 95%, which is well in excess of the liquid limit (60%). The slurry was then poured into the extended strongbox and compressed one-dimensionally to a vertical effective stress of 106kPa over a period of approximately 7 days. On stripping out the sample from the consolidation press, after approximately 4 days at 106kPa, the clay was normally-consolidated and the average effective stress p′ was approximately 80kPa (Jaky, 1944; Eqn. 3.1)

$$\sigma'_h = \sigma'_v(1 - \sin\phi') \qquad 3.1$$

This stress history was adopted to produce a soft clay of a similar strength and stiffness to that sampled at the Arun valley (Section 2.2) and which represents a typical operational application for temporary trackway. The model clay was such that, if soil was encountered of equivalent stiffness in the field, it would certainly require the use of trackway for vehicles to traverse it unhindered.

In terms of changes in stress, the time the model spends in the centrifuge can be divided into two stages. The first stage is known as the re-consolidation phase and was described earlier in Section 3.5. The second stage is when the changes in stress due to the events which constitute the test take place, i.e. trackway loading. During the first stage the in-situ lateral earth pressure coefficient, K_0 and stress profiles in the clay change significantly from those immediately after preparation.

Once equilibrium is reached at a vertical stress of 106kPa in the consolidation press, the clay is normally consolidated and the vertical effective stress is uniform. In the

centrifuge, rather than being applied by a press, the vertical stresses in the soil are due to its enhanced self-weight and therefore increases with depth from a value of zero at the surface. Figure 3.8 compares the different stress profiles before and after re-consolidation. The soil in the centrifuge becomes over-consolidated throughout and at the surface, where the vertical stress is zero, the OCR is infinitesimal. Even at the deepest level in the clay, the OCR is about 1.3. The centrifuge soil is not, therefore, normally or lightly over-consolidated as is the case with Arun valley alluvium. However, with the use of a consolidation press in sample preparation an OCR significantly greater than 1 near the surface is difficult to avoid since the press applies a uniform stress throughout the sample. Mayne and Kulhawy (1982) proposed empirical methods for predicting K_0 for over-consolidated clays, and which has seen widespread use by other researchers (Powrie, 1986; Li, 1990; Richards, 1995), based on laboratory data from over 170 different soils. Calculating effective stresses using

$$\sigma'_h = \sigma'_v(1 - \sin\phi')\mathrm{OCR}^{\sin\phi'} \qquad 3.2$$

from Mayne & Kulhawy (1982), a specific volume profile for the model clay using

$$v = N_p - \lambda \ln p'_o + \kappa \ln(p'_o/p') \qquad 3.3$$

and kaolin parameters from Al-Tabbaa (1987) and comparing this with corresponding values on the critical state line, it is possible to determine whether the model clay lies on the wet or dry side of the critical state line. Figure 3.9 illustrates the results of this analysis for test levels 1 and 2 and shows that for shearing within approximately 110mm (4.2m prototype) of the surface, the model clay will tend to dilate (soften), rather than compress (harden) like the Arun valley alluvium. Under short-term loads in partially drained conditions, undrained shearing will predominate and, as was the aim with the model soil, its undrained strength is very similar to that of the Arun valley alluvium, both having an undrained strength, c_u, of approximately 18kPa. Both clays are also very soft and under drained conditions, particularly near the surface, both would experience large volume changes. The centrifuge model effective stress profiles shown in Figure 3.8

are applicable to both test levels and, since the maximum mean effective stress of 80kPa in the consolidation press is not exceeded during the tests, both samples are positioned on the same unload/reload lines in v-ln p′ space and have the same values of p′ and v. At the end of each test, clay samples were taken from undisturbed regions of the model to ensure moisture contents remained consistent across all the tests.

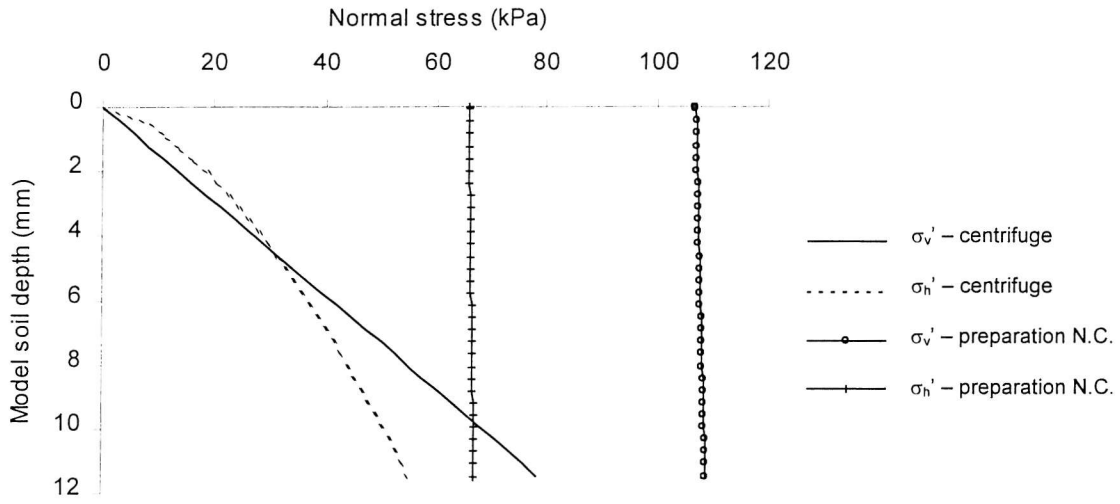

Figure 3.8: In-situ effective stress profiles of clay model

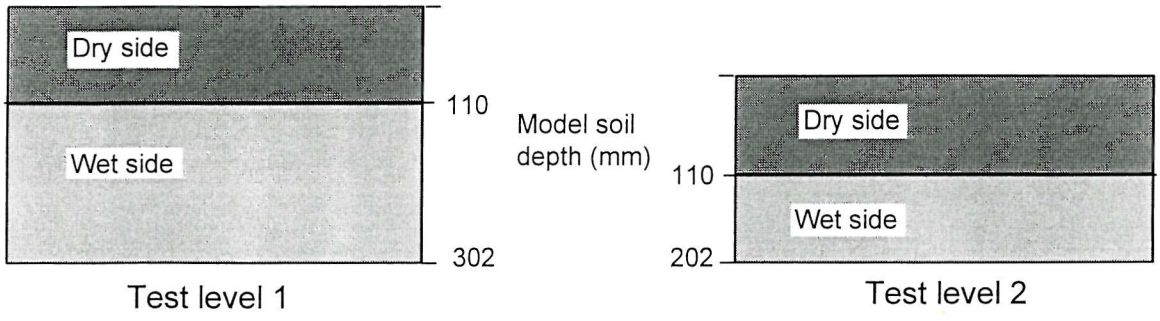

Figure 3.9: Model clay states in the centrifuge

3.7 Description of main apparatus

3.7.1 Model trackway

New model trackways were used in each test since, invariably, the trackway suffered permanent deflexions at the end of each test. All the trackway models nominally modelled the transverse bending stiffness of prototype Class 60 trackway. Since it was possible to investigate variations in trackway stiffness using the numerical model, it was not necessary to re-create a wholly accurate scale representation of Class 60 trackway in the centrifuge model.

The intricate, corrugated nature of trackway sections makes them extremely difficult to re-create at $1/38^{th}$ scale. Therefore, trackway was modelled in the centrifuge using uniform 0.6mm thick aluminium alloy plates, with a Young's Modulus of $69kN/mm^2$ and a yield stress of $80N/mm^2$. The plate, shown in Figure 3.10 (with strain gauges – see section 3.7.2), was 120mm wide, the scaled width of Class 60 trackway, and 199mm long to extend across the full width of the strongbox while still maintaining a clearance from the front and back plates at each end. The first limitation in using a uniform plate to represent the trackway is its isotropic section properties in the transverse and longitudinal directions (Figure 1.1). Prototype trackway, because of its corrugated section, is 17 times stiffer in bending in the transverse direction than the longitudinal direction. However, experience in the field suggests that the longitudinal stiffness of an individual panel is of little consequence given both the zero rotational stiffness of the joints and the fact that trackway never fails through bending of an individual panel in the longitudinal direction. It is considered that trackway deforms primarily in the transverse direction in the field, thus it is important that the trackway possesses a similar scaled stiffness in this direction in the model.

A second drawback of using a uniform plate lies in attempting to match closely its bending stiffness as well as its yielding characteristics with those of a corrugated section. Accurately scaling bending stiffness in the model trackway invariably resulted

in a grossly inaccurate plastic moment capacity, and vice versa. Therefore, a compromise was reached.

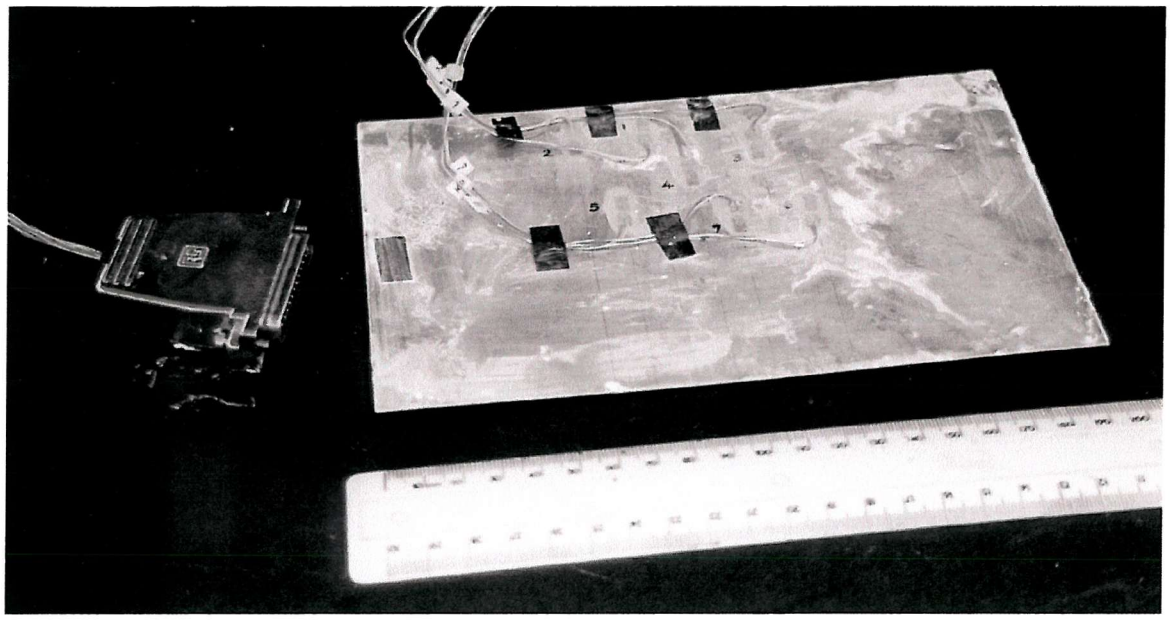

Figure 3.10: Unjointed plane strain model trackway

The prediction of deflections for thin plates is not straightforward. Where large deflections compared to plate thickness predominate, the assumption of zero strain along a neutral axis does not hold. Supplementary stresses are generated in the middle plane giving a non-linear load-deflection response. Very thin plates with low resistance to bending behave more as membranes, except for narrow edge zones where bending may occur because of the loads or boundary conditions imposed on the plate (Timoshenko, 1959). Given these difficulties in the mathematical prediction of thin plate deflections, a comparison between prototype and model trackway properties is better made between the results of laboratory calibration tests.

The class 60 trackway 3-point transverse bending test described in section 2.6 produced bending stiffness EI = 79.4kNm^2/m and plastic moment capacity M_p = 30.5kNm/m in the transverse direction. In order to obtain equivalent values for the model trackway a

bending test was carried out to failure, as illustrated in Figure 3.11. The loading pattern was similar to the plane strain centrifuge tests, with two long loads at 65mm spacing, except that knife-edge loads were used for a more straightforward load application. A graph of the total load imposed along both knife-edges against the maximum deflexion along the centre-line of the model trackway is shown Figure 3.12. As predicted by Timoshenko (1959), the deflexion response is non-linear and significantly greater than predicted by elastic beam deflexion equations using an EI section value. The aim was to use a model trackway with similar scaled transverse bending properties to prototype Class 60 trackway. Given the centrifuge scaling factors for E, I and moment of 1, $1/N^4$ and $1/N^3$ respectively, the target values for EI and M_p were 38.0kNmm^2 per 1/N m length and 14.6Nmm per 1/N m length respectively. Analysis of the model trackway bending test yields values for EI of 23.5kNmm^2 per 1/N m length and M_p of 191Nmm per 1/N m length. The model section, therefore, is somewhat of a compromise, having a slightly lower EI value and a much higher M_p value than the prototype.

In addition to the uniform aluminium plate, which formed the unjointed model trackway, a jointed replica of the Class 60 trackway was constructed, as shown in Figure 3.13. It used the same 0.6mm thick aluminium alloy plate in its construction as the unjointed plate and thus had the same section properties per unit length. However, the aluminium alloy plate was divided into 5.5mm lengths forming individual trackway panels, 120mm wide at model scale, the same as the unjointed aluminium alloy plate. A total of 35 panels was joined in series to form a model Class 60 trackway temporary road across the 200mm width of the centrifuge strongbox. The joints between the panels were formed using two continuous 50mm wide strips of 30μm aluminium foil adhesive tape carefully fixed along the underside of the trackway. A regular 0.2mm spacing between each panel allowed free rotation through about 15° upwards and 45° downwards, and also gave an overall panel spacing of 5.7mm, accurately modelling the 216mm spacing of Class 60 trackway panels. Figure 3.13 shows the model trackway after test 4 and, although a couple of panels have partly separated from the aluminium tape, the bond between each panel proved to be very effective with no joints failing during their use in the centrifuge model.

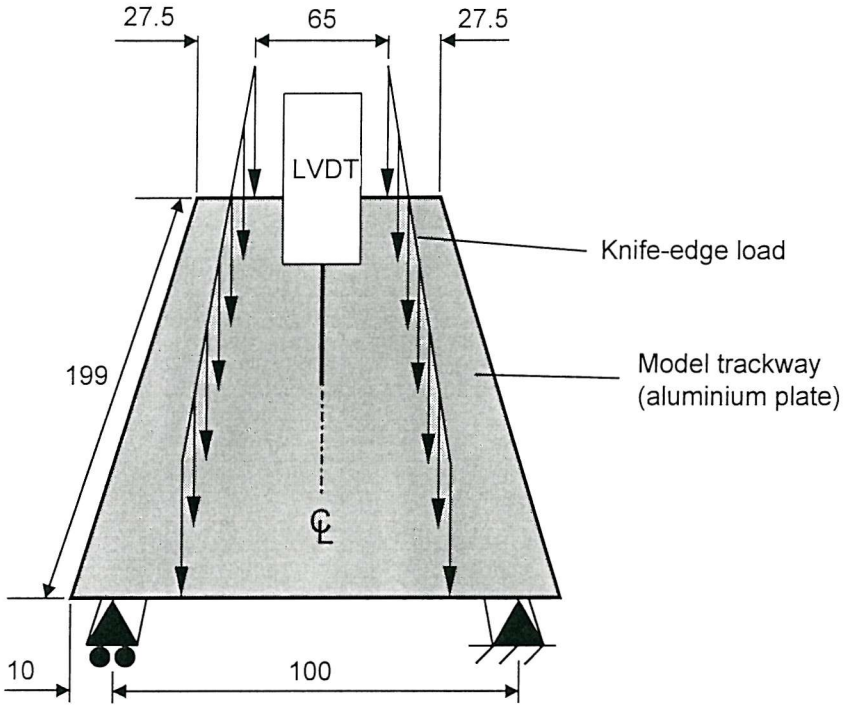

Figure 3.11: Model trackway bending calibration test

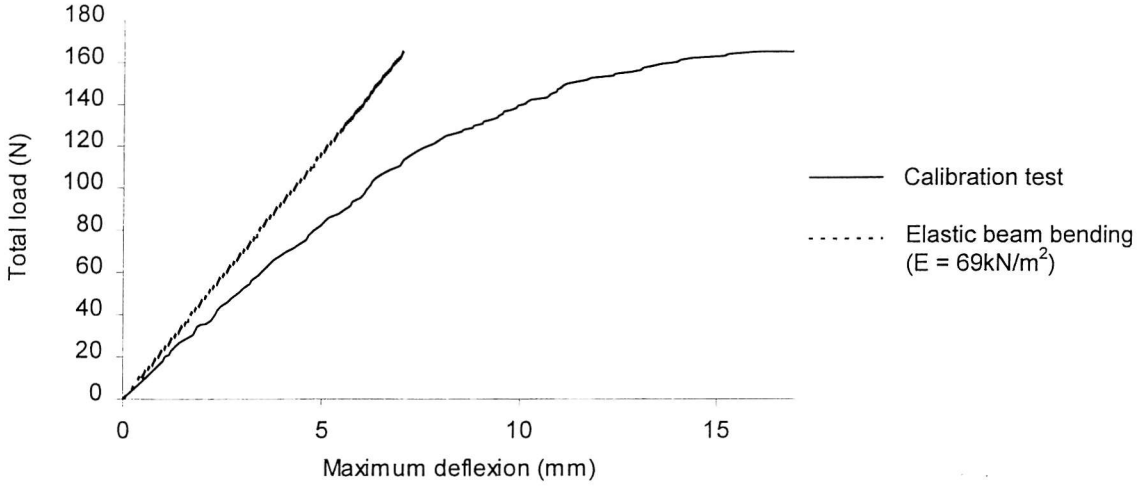

Figure 3.12: Unjointed model trackway load-deflexion response

As well as providing a more accurate representation of Class 60 trackway, the jointed model trackway allowed a direct assessment of the effect of trackway joints on the overall soil/trackway performance. In comparing jointed and unjointed model trackway behaviour on identical soils, subjected to identical vehicle loads, while the longitudinal trackway stiffness varies enormously, it is essential that the transverse stiffnesses are the same. Consequently, a laboratory bending test was carried out on the jointed model trackway, in an identical manner to that illustrated previously in Figure 3.11, to determine whether the trackway panel spacing or the addition of aluminium foil tape had seriously altered the trackway's transverse bending stiffness properties. The load-displacement response of both the jointed and unjointed model trackways are compared in Figure 3.14. The graph clearly shows the jointed model trackway to be slightly less stiff and slightly less strong than the unjointed trackway. Indeed, analysis of the jointed trackway results gives an EI value of 23.0kNmm^2 per 1/N m length (2.0% lower than the unjointed model trackway) and an M_p value of 180Nmm per 1/N m length (5.8% lower than the unjointed model trackway). On balance, however, the transverse bending performance of the jointed and unjointed model trackways is sufficiently similar to allow the effect of the joints to be compared in isolation.

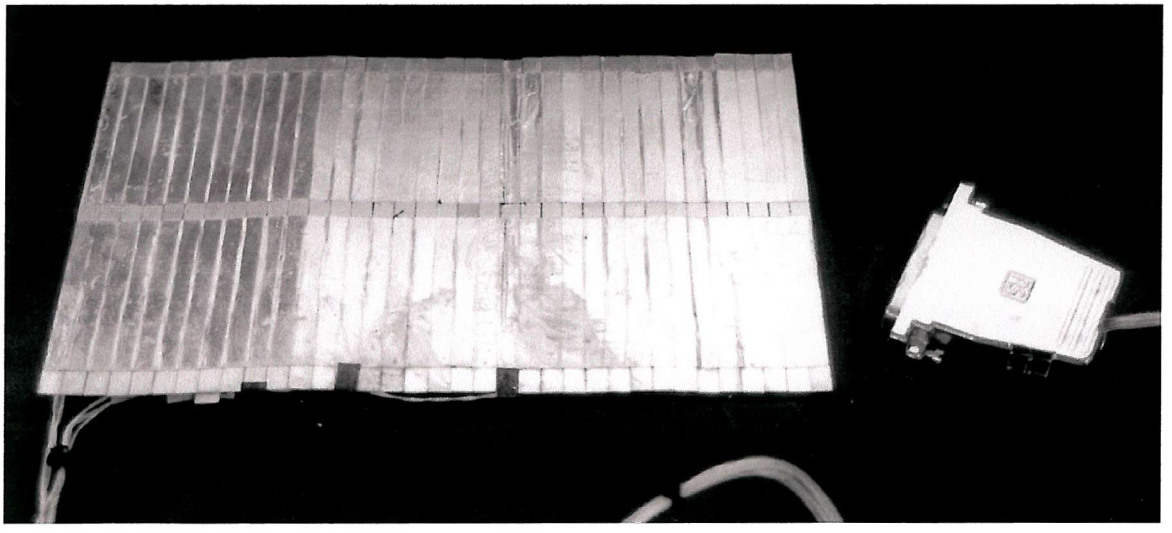

Figure 3.13: Jointed model trackway

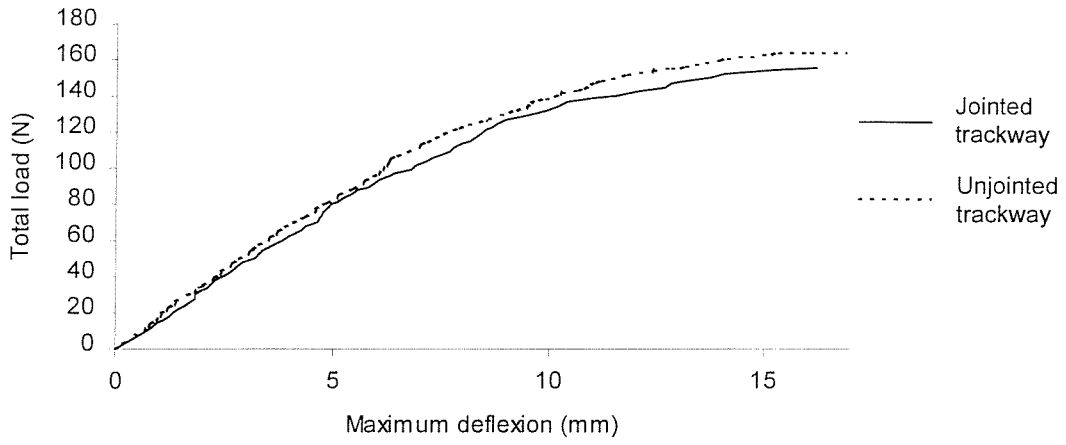

Figure 3.14: Jointed model trackway load-deflexion response

3.7.2 Strain gauges

All the model trackways used in the tests were fitted with an array of seven single strain gauges, whose arrangement is shown in Figure 3.15, and measured the strain on the upper surface in the transverse direction. The data from each array would allow trackway deformation profiles to be generated throughout all four tests.

Each gauge was bonded to the aluminium alloy with cyanoacrylate adhesive and the connecting pads and gauges were sealed against water penetration and apparatus damage with a Neoprene rubber coating. This rubber coating proved to be very effective with no gauges becoming damaged in any of the tests, even in the loaded areas. The single core leads from all the gauges were fed via a 25-way 'D' plug to a mating socket on a control box. The control box, which was mounted to the top of the strongbox, housed the bridge completion resistors for each strain gauge on a circuit board. The resulting bridge output voltage was connected directly to the centrifuge junction box, which, in addition to feeding the output signals via amplifier boards to the datalogging PC mounted on the centrifuge axis, provides the bridge excitation voltage of 10V. Data from the datalogging

PC is fed to the control room PC via an RS232 link through the slip ring to allow the user to continuously monitor the model data.

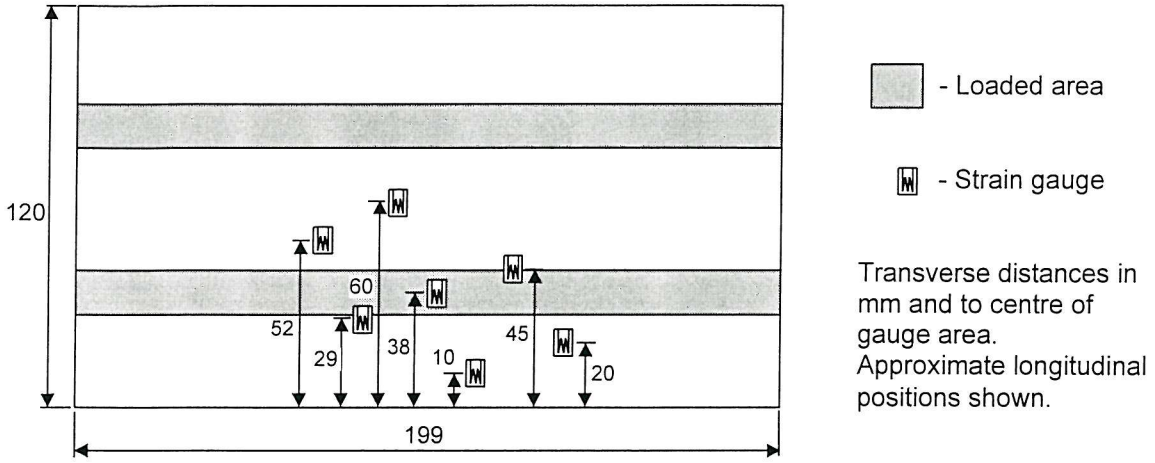

Figure 3.15: Strain gauge arrangement for all model trackways

3.7.3 Plane strain loading apparatus

Two rigid steel beams were used to apply a normal vertical load to the model trackway. Each beam was 15mm wide, simulating approximately a DROPS vehicle tyre width (Section 1.4), and 199mm long, the full width of the strongbox with 0.5mm clearance at each end. With a depth of 20mm, each beam was sufficiently rigid to ensure an even deflexion of the soil and trackway across the width of the strongbox, and that plane strain conditions prevailed. The centre spacing between each beam of 50mm, again modelled the wheel spacing on a DROPS vehicle axle and each beam was held parallel at this spacing by a rigid cross-piece bolted to each beam.

Rather than loading the trackway with a rigid steel contact zone, a softer tyre/trackway interface was simulated by fixing a 1.5mm thick layer of Neoprene rubber to the base of each beam. However, there was some concern that the high friction characteristics of a rubber/aluminium interface could have caused the model trackway to be "pinched" in

one position under loading, preventing trackway deflexion between the beams and causing the aluminium plate to behave rather like a tensile membrane. To prevent this, both the rubber and aluminium surfaces were smeared with water resistant silicone grease before each test.

The total load imposed on the model trackway by the two beams was measured using a 500lb tension/compression miniature load cell manufactured by RDP. The load cell was connected to the rigid cross-piece with the shaft of the cylinder via a thread converter between the load cell and the ¾" diameter cylinder shaft. The arrangement of the two beams, the cross-piece and the load cell is shown in Figure 3.16. During the re-consolidation phase, the two beams were supported clear of the model trackway, by locking the cylinder, so that they imparted no load on the model. The tension in the load cell during this stage was effectively the enhanced self-weight of the two beams and the cross-piece. This tension was added to the load cell output during loading to obtain the true value of applied load.

The load cell was powered by a constant 5V DC supply. The signals were fed to the datalogging PC mounted on the centrifuge axis and the data in turn was fed to the control room via an RS232 link through the slip ring. The load cell was calibrated before and after each test in compression using a load hanger. The calibration factor remained consistent over a large range of loads and throughout the testing programme.

The source of the applied load was a Bellofram rolling diaphragm pneumatic cylinder – chosen because of its low friction characteristics compared with a conventional piston seal cylinder. Pressure to the double-acting cylinder was controlled with a Buzmatic (proportional) E/P converter housed inside the control box. However, the low pressures in the cylinder during operation necessitated the use of a high pressure pilot operated solenoid valve to switch between an up and down cylinder action. The cylinder required a rigid mounting both because of its significant self-weight and to ensure it maintained its position and vertical orientation throughout the test. Hence, the cylinder was bolted onto a 12mm thick steel plate which bridged the width of the strongbox and was in turn

bolted to the window and back plates. This plate also supported the displacement transducers, which further necessitated the need for a rigid mounting plate which would deflect to a negligible degree during the test.

The full arrangement of the plane strain loading apparatus is shown in Figure 3.17.

In test 2 a 1Hz cyclic load was applied by the cylinder to the trackway. A signal generator in the control room was used to apply a sinusoidal d.c. voltage to the E/P converter via the sliprings, once an initial load had been established by lowering the beams onto the trackway.

The method of load control in tests 1 and 2 was rather crude, in that it did not use the load cell output to complete the control loop but rather was controlled manually from the control room. This was not detrimental to the quality of the tests since the main aim was to bring about, and monitor, failure of the soil/trackway system. Controlling the applied load output to precise target values was not necessary. In test 2 the method of load control did not allow for switching the pressure between extending and retracting during cycling. Due to the enhanced self-weight of the loading apparatus during flight, this prevented applied loads reducing to zero on each cycle. As such the load cycling did not entirely represent the passage of vehicles, although, at higher applied loads, the amplitude of cycling was considerably in excess of that caused by a passing DROPS vehicle. It was felt that the achievement of such an amplitude of cycling was sufficient to assess the trackway's resistance to "whole vehicle load" cycling, regardless of the mean applied stress. Cycling to zero load could have been achieved by using a servo-cylinder, but at too great a cost for a single test.

3.7.4 Rolling vehicle

The most onerous load applied to in-service trackway is likely to be imposed by the DROPS vehicle, due to its large mass being imparted to the ground through only four

pairs of tyred wheels (see Section 1.4). The model rolling vehicle, therefore, replicated a pair of wheels on a single axle of the DROPS vehicle. A single axle was used to allow a greater length of travel across the width of the model and because it required a simpler method of propulsion than that of an entire model vehicle. Also, since each rolling axle load may be more significant in trackway deformation than each 'whole vehicle load', it was more straightforward to isolate axle loads from vehicle loads and to count rolling axle passes with a single axle rather than a whole vehicle. In order to replicate accurately the dimensions of a DROPS vehicle axle at the model scale, two 44mm diameter rubber "robotic" wheels were fixed, at 50mm spacing, to a 4mm diameter steel spindle. To avoid the difficulty of applying a vertical load to an axle moving over uneven terrain, the axle load was applied simply using the enhanced self-weight of the axle, thereby ensuring the load was constant throughout the test, no matter how much the model trackway deformed. Consequently, lead weights needed to be inserted into the rubber wheels to increase their weight to $1/38^3$ the mean axle weight of an unladen DROPS vehicle. It would have been possible to use the mean fully-laden axle load of 7.5 tonnes (see Section 1.4) but it was considered to be too onerous and may have caused failure of the soil/trackway system after only two or three passes, giving little opportunity to record data. Therefore, a partially laden mean axle load of approximately 5 tonnes (equivalent to 0.12 standard axles (Croney and Croney, 1991)) was simulated, resulting in a 90 gram axle self-weight at model scale and total of 80 passes in Test 4 before failure occurred. Extreme care was taken to ensure each wheel had the same mass, so that the axle imposed a symmetrical load, and that each wheel was balanced so that it rotated evenly. Only a slight imbalance in either wheel would have imposed a significantly uneven load under their enhanced self-weight in the centrifuge. The spindle was sufficiently stiff not to deflect significantly under its own weight or deform when driving each of the heavy wheels, thereby ensuring the axle load was always applied vertically to the model trackway.

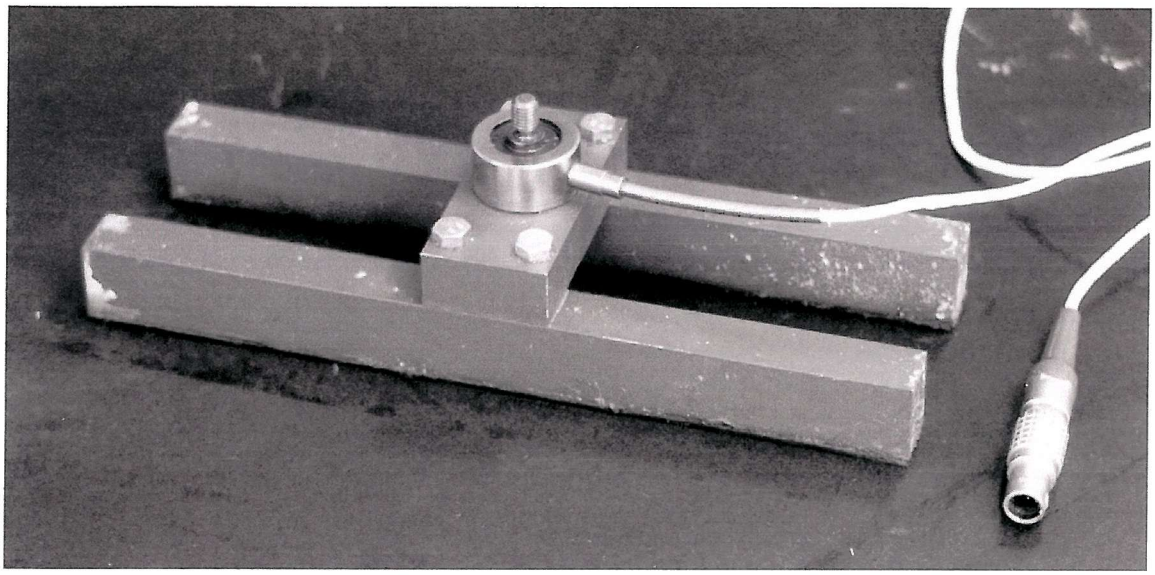

Figure 3.16: Plane strain loading beams and load cell

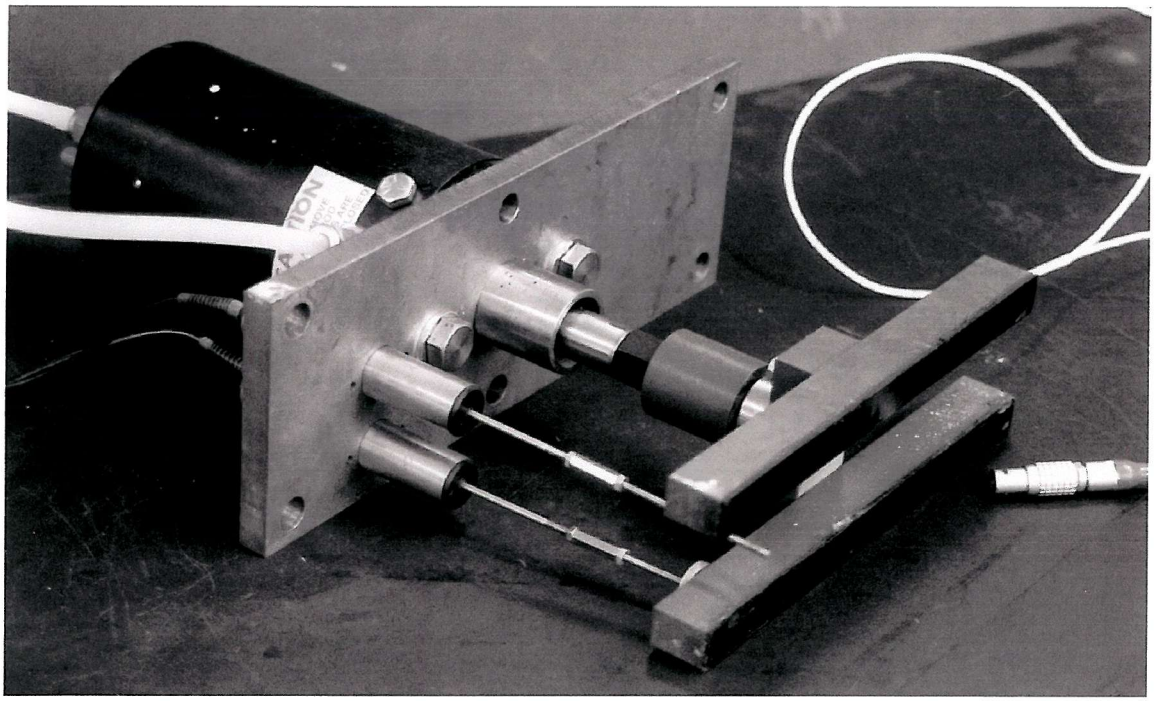

Figure 3.17: Full arrangement of the plane strain loading apparatus

The rolling vehicle was driven backwards and forwards over the model trackway by means of a pair of steel forks which slotted over the vehicle spindle and connected to the carriage plate. Having created the axle load using its self-weight, it was important that the forks, employed to accommodate vertical movement and drive the wheels, imposed no vertical loads on the rolling vehicle. This was achieved by machining slots in the forks with sufficient vertical and horizontal clearance around the spindle so that they would only apply a horizontal load to the rolling vehicle as they moved to and fro across the width of the strongbox. Two lengths of fork pairs were manufactured for the two soil depths employed in the model, each allowing a 20mm clearance above the model trackway in case it should "ruck up". A stiffening plate fixed two-thirds the way down between the forks held them parallel and ensured the rolling vehicle was driven squarely along the model trackway without either wheel skidding. The forks were suspended from a carriage plate, on which were mounted four linear slide bearings. A linear slide threaded its way between the two pairs of bearings and, while allowing the carriage plate to slide to and fro, supported the weight of the forks, the carriage plate (and the potentiometer) in the centrifuge. The slide was in turn supported by an aluminium box section spanning the width of the strongbox. The carriage plate, and ultimately the rolling vehicle, was driven to and fro by a toothed timing belt, looping through the box section and under the slide to a belt-clamp on the carriage plate. Two aluminium pulleys at each end of the box section bridge, one driven, one free, guided and supported the belt. The free pulley was supported by two ball races in a bearing block, mounted onto an aluminium plate, which in turn was fixed onto the backplate of the strongbox. The driven pulley was connected to a 4Nm 5:1 reduction gearbox driven by a hybrid stepper motor (phase current 1.8A, 6.0V), all mounted on an additional aluminium plate fixed onto the window plate of the strongbox. A stepper motor drive card, mounted near the axis of the centrifuge, provided the control voltages for the stepper motor. Step pulses were generated on the drive card (faster pulses = faster motor speeds) in response to a voltage control signal from a computer in the centrifuge control room. This was controlled with a Visual Basic program shown in Appendix A. Figure 3.3 earlier in this chapter shows the general arrangement of the rolling vehicle apparatus, together with the control box for the strain gauges in the foreground.

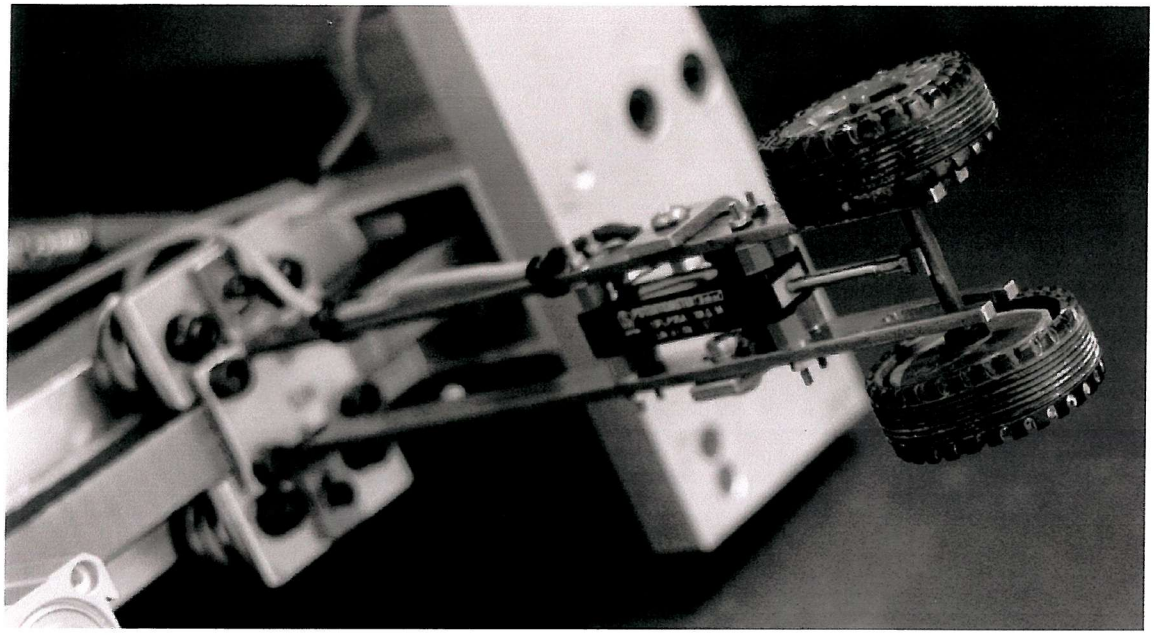

Figure 3.18: Rolling vehicle, driving forks and potentiometer

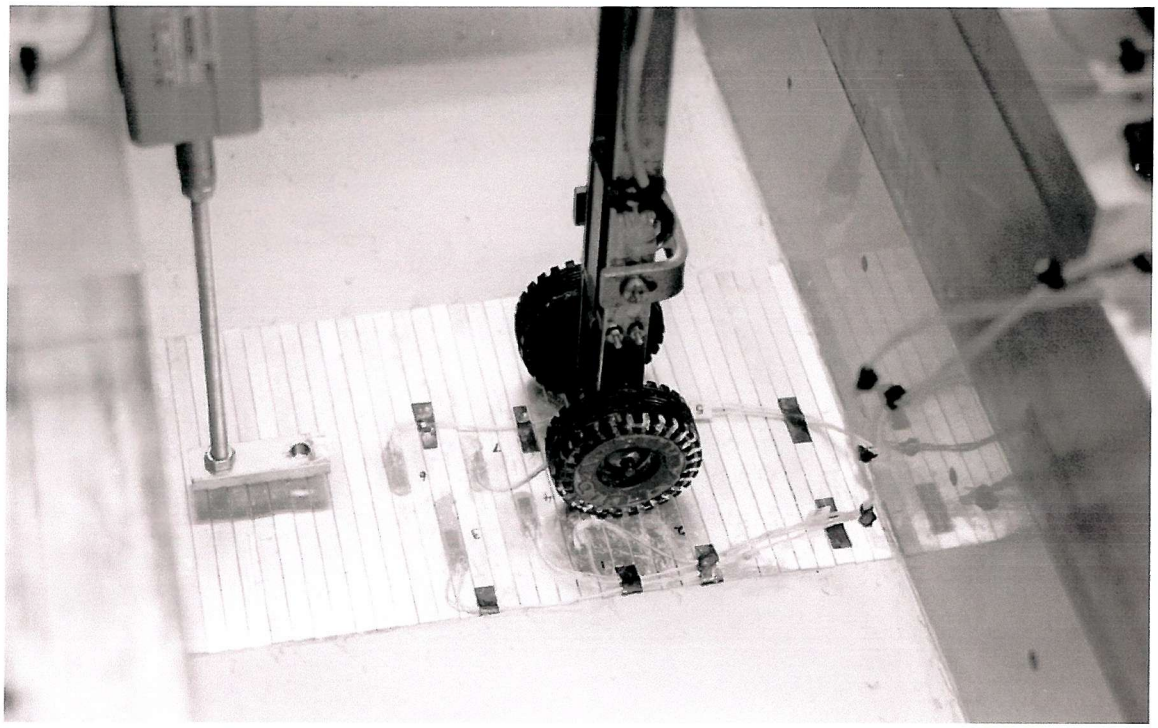

Figure 3.19: Rolling vehicle ready to be driven over jointed model trackway

To enable the rolling vehicle to reverse at each end of its travel, limit switches were mounted at each end of the bridge and were activated by the carriage plate each time it reached the edge of the strongbox. Each time a limit switch was reached, a digital latching circuit changed the motor direction signal fed to the stepper drive card, thus reversing the motor and driving the vehicle towards the other limit switch. It was necessary to "latch" the signal to prevent "switch bounce" and false direction changes.

The output of this latching circuit was fed to the control room computer, where a counter timer on an A/D card counted the number of cycles, also recorded by the Visual Basic program shown in Appendix A.

Acceleration at each direction change was virtually instantaneous, but this did not cause any problems with high motor currents, due to the modest loadings in the system.

The speed control voltage was generated on a D/A card, and experience showed a range of approximately 2.0 to 5.2 volts was suitable for the speeds required. If speed change was necessary during travelling, a ramp was generated by the program to allow a smooth progression to the higher/lower speed.

The vehicle would continue reversing with no input from the user, until the motor control voltage was reduced to zero. The vehicle driving system was very successful and no significant problems were encountered.

The deflexion of the model trackway was measured by monitoring the vertical movement of the rolling vehicle throughout the test. This was achieved by mounting a 25mm stroke potentiometer between the forks and allowing the spindle of the potentiometer to rest under its enhanced self-weight on the spindle of the rolling vehicle. Modifying the potentiometer spindle by fixing a semi-circular bracket to its end allowed it to hug the rolling vehicle spindle and not slide off, as shown in Figure 3.18.

During the re-consolidation stage it was necessary to support the rolling vehicle clear of the model trackway so that no load was imposed on it during this phase. This was done using a 20mm stroke, 20mm bore pneumatic cylinder mounted to the free pulley aluminium plate so that it was suspended vertically inside the strongbox, against the backplate, over the centreline of the model trackway. Long and short spindles, for each soil depth, had angle plates attached to their ends. At the start of each test the rolling vehicle's spindle was placed onto the plate, in its raised position, still within the slots of the forks, so that it was supported clear of the model trackway. At the end of the re-consolidation stage, the plate was lowered by means of a double-acting solenoid valve to the cylinder, so that the rolling vehicle rested on the model trackway and was ready to be driven forwards by the forks. The pneumatic cylinder, spindle and plate are visible on the left in Figure 3.19, in the lowered position. The rolling vehicle, having been driven off the plate, is also shown on the jointed model trackway, which is in turn positioned on the model clay surface.

3.7.5 Pore water pressure transducers

To measure pore pressures in the clay during the test low-range Druck PDCR81 – 100kPa and 30kPa miniature pore pressure transducers were installed at various locations within the model. Figure 3.20 shows the approximate locations of the transducers in the model section, although some variation in position did occur in each test. All four tests were subjected to a symmetric load in this plane, therefore data received from transducers offset from the centre-line would be expected to be mirrored on the opposite side of the model, thereby doubling the quantity of pore pressure data. The most significant pore pressure changes were expected to occur beneath the model trackway near the soil surface where hydrostatic pore pressures were very low, hence low-range 100kPa, and even 30kPa, transducers were installed near the soil surface to take advantage of their high resolution at low pressures.

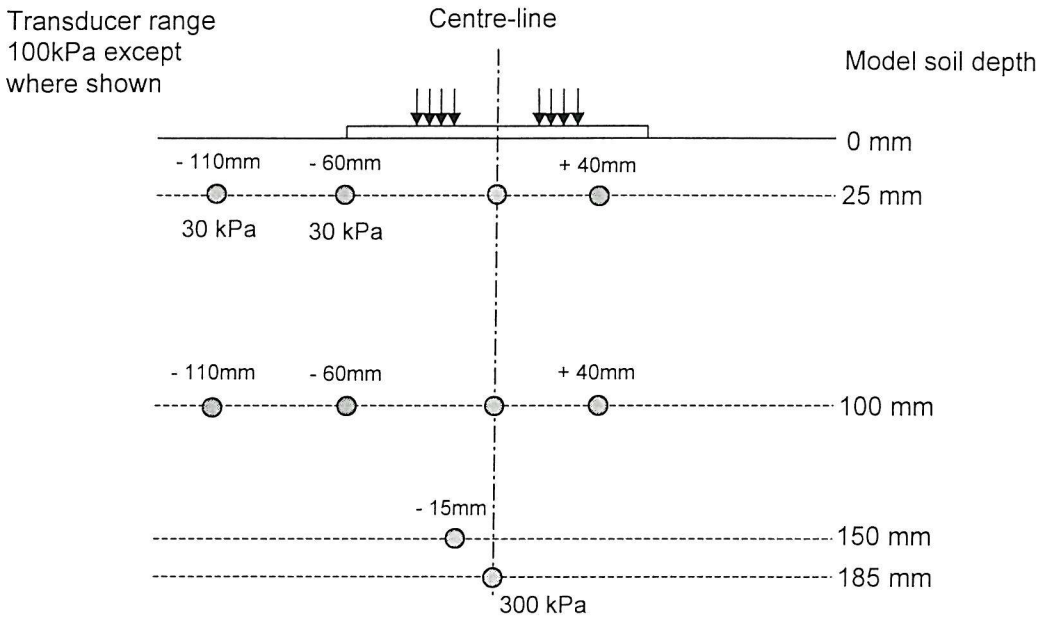

Figure 3.20: Approximate pore pressure transducer positions in all tests

The pore pressure transducers were powered by a constant 5V DC supply. The signals were fed to the datalogging PC mounted on the centrifuge axis via amplifier boards which increased signals by a factor of 100. Data from the datalogging PC were fed to the control room PC via an RS232 link through the slip ring. Holes for the transducers were augered horizontally into the clay to a depth of half the width of the sample, through holes in the backplate (i.e. the transducer was positioned on the plan centre-line of the model).

An important requirement in the use of pore pressure transducers is accurate installation prior to the start of the test. This was achieved by fixing a modified pipe fitting to the backplate which acted as a sleeve for the auger and reduced the potential for mis-alignment of the augered hole. After the transducer had been installed, the hole was back-filled with a kaolin slurry. The holes in the backplate were sealed using standard pipe fittings together with sealing rings. Each transducer had a de-aired ceramic porous stone fitted to the front in order to protect the fragile silicone diaphragm from stresses due to the soil skeleton. The stone was de-aired to ensure an instant response to changes in pore pressures during testing. The resolution of the Druck pore pressure transducers is

approximately ±0.005kN/m^2. The transducer diameter is 6mm which at prototype scale corresponds to 228mm. Each transducer will measure the average pressure over this diameter. The positioning of the transducer within the model is of over-riding importance. With the sleeve and auger arrangement, discussed earlier, it was possible to position the pore pressure transducers to within ±2mm of their required depth which represents a maximum potential error of ±0.7kPa.

After each test, as the model was being stripped down, clay was carefully removed to expose each transducer and its horizontal and vertical positions were measured. In most cases, particularly near the soil surface, the transducer had moved from its initial position, with the maximum deviation being 10mm. However, when the effects of re-consolidation and soil deflexion for each test were taken into account, as measured by LVDT's located at the soil surface and the final surface profile measured after each test, the transducers were found to be in their true positions.

The pore pressure transducers were calibrated individually using a Druck digital pressure indicator '601' (which in turn is annually calibrated against a pressure standard) before and after each test. The transducer calibration factors remained constant throughout all the tests, but sometimes calibration offsets changed, by less than 1kPa, during the course of a test. In these cases the mean value of the two offsets was used for data processing.

During the series of tests reported, a few of the pore pressure transducers were sometimes slow to respond to changes in pore pressures when compared with the response of adjacent transducers. This was attributed to either clogging of the ceramic stone with clay or the presence of air bubbles on the transducer diaphragm. To minimise the probability of either occurring, no ceramic stones were re-used in the series of tests, new stones were de-aired in boiling water prior to installation and transducers were submerged in water when the stones were installed. Indeed, Konig et al (1994) reported the findings of a collaborative study on the behaviour of the Druck PDCR81. It was stated that it was common practice to remove the stone from the transducer after each

test to be boiled. This was principally to de-air the stones, but it would also substantially remove any clay particles clogging the stone.

3.7.6 Displacement transducers

Linear variable differential transformers (LVDTs) manufactured by Schlumberger were used to monitor vertical soil and trackway deflexions in plane strain tests 1 and 2, in the positions shown in Figure 3.21. LVDTs measuring soil deflexions had lightweight plastic plates fitted to the ends of their spindles to ensure they did not embed into the soft clay under their enhanced self-weight. The kinematic envelope required by the rolling vehicle apparatus prevented the use of LVDTs in the region of the trackway in tests 3 and 4. The LVDTs were powered by a constant 10V DC supply. Signals were passed via the amplifier boards, where the gain had been set to 1, to the datalogging PC mounted on the centrifuge axis.

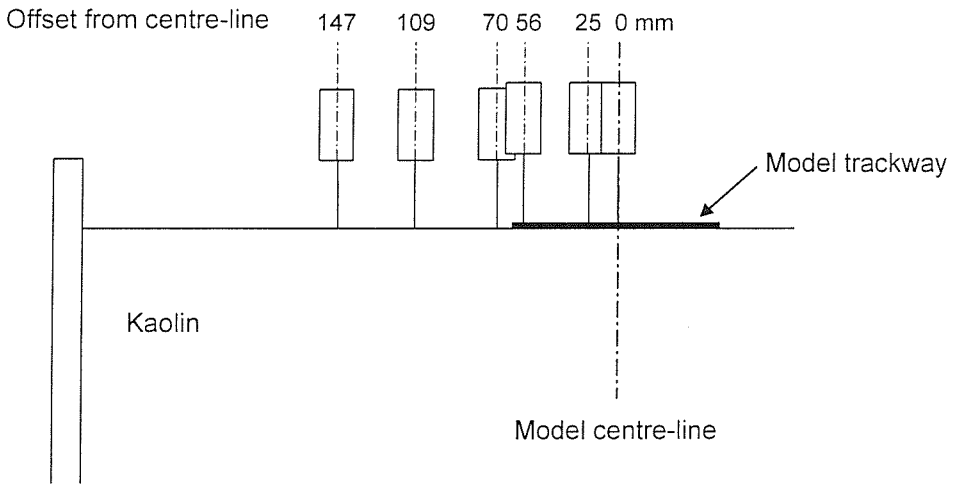

Figure 3.21: Displacement transducer positions in plane strain tests

3.7.7 In-flight video image processing

Sub-surface soil deformations were measured using an image processing system developed at City University (Chen et al, 1996). Black marker dots (3mm diameter) were inserted into the front face of the clay model in a grid pattern with a 10mm spacing, as shown in Figure 3.22. Since the tests were symmetrical about the centreline indicated, only one half of the model needed to be monitored. A video camera located within the centrifuge fairing, and pointing directly at the perspex viewing window, allowed a video image to be recorded at key points during the test. Dedicated software developed at City University scanned the image to locate all the black marker dots. The pixel co-ordinates of the video image were then converted to a co-ordinate system at model scale with allowances made for the distortion (fish eye effect) caused by the video camera lens and the perspex window.

True two-dimensional data of soil displacement can only be derived from plane strain tests. Consequently, image processing was only carried out in plane strain tests 1 and 2.

In reality, the scanning of the black marker dots proved to be only partly successful. The centrifuge fairing caused an obstruction to the perspex window, concealing a significant region near the surface of the clay on each side of the trackway (see Figure 3.22). Lighting levels were variable across any one image making the accuracy of marker dot location variable. There were a limited number of light sources to illuminate the perspex window and the top of the model for video recording (see Section 3.7.8 below), making this problem difficult to avoid. More significantly, since the clay was quite soft, some of the black marker dots became enveloped in the clay so that they were no longer clearly visible, even at the start of each test. As the tests progressed, the visible areas of the black marker dots changed shape as they were further enveloped by the clay and sometimes disappeared completely. If the marker dots appear to change shape, the position of their centroid also changes, leading to inaccuracies in the measurement of their position; if they disappear their position can no longer be determined at all.

The overall accuracy of the soil displacement data was difficult to determine given the variability of the images discussed above. It is apparent that this method would not be consistently accurate enough to be used to calculate soil strains. The measurement data are, however, sufficiently accurate to identify and compare overall patterns of soil movement.

3.7.8 In-flight video recording

A video camera mounted on top of the centrifuge strongbox in one corner, and pointing downwards onto the soil surface, model trackway and adjacent apparatus, allowed a continuous video image to be recorded throughout the test. This provided a clear record of the sequence and timing of events in each test and, particularly in the jointed trackway test 4, provided an additional valuable aid to the understanding of the processes involved in soil/trackway failure.

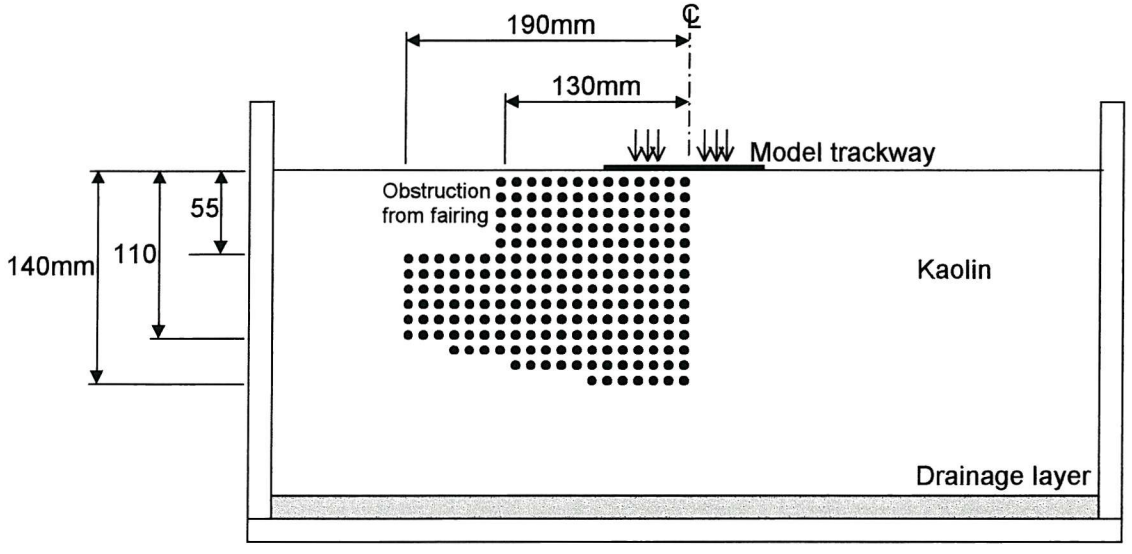

Figure 3.22: Black marker dot positions

3.8 Instrumentation calibration & discussion of errors

A six channel junction box was used for the calibration of all transducers. All transducers were calibrated before and after each test. The junction box was supplied with 15V DC and incorporates voltage regulators which ensure a constant supply of 5V or 10V DC during calibration. Various signal filters are built into the junction box together with the facility to set the gain for each channel to 1, 10 or 100. This corresponds to voltage supplies and gain settings on the centrifuge.

Before each test, one each of the pore pressure transducers, LVDTs, load cell and strain gauges were calibrated through the junction box and datalogging PC on the centrifuge arm to ensure that the calibration factors determined at Southampton were still valid using the centrifuge hardware. In all cases the calibration factors proved to be very close.

Chapter 4

Centrifuge Test Results

4.0 Introduction

The results of a series of tests carried out on model trackway are reported. In each case, the trackway was placed on the soil surface in the centre of the model, and a full height ground water level was modelled. In the first three tests an unjointed aluminium plate was used to monitor transverse deformation of the trackway only. In the fourth test, jointed aluminium panels were used to allow longitudinal, as well as transverse, trackway deformations to be determined. The first two tests simulated plane strain conditions, with a vertical applied stress (static or cyclic) imposed on the trackway. The third and fourth tests used the self-weight of a rolling vehicle to apply load to the trackway.

4.1 Test Programme

The tests reported in this dissertation are detailed in Table 4.1.

Test no.	Date	Description
1	11/9/98	Unjointed trackway, plane strain conditions, static applied load.
2	29/10/98	Unjointed trackway, plane strain conditions, cyclic applied load.
3	15/1/99	Unjointed trackway, self-weight of rolling vehicle applied load.
4	14/1/99	Jointed trackway, self-weight of rolling vehicle applied load.

Table 4.1: Details of centrifuge tests reported in this dissertation

4.2 Pore Water Pressure Response During Testing

Extreme care was taken during the installation of pore pressure transducers and this ensured that no transducers completely malfunctioned during the series of tests reported here. However, as can be seen in the hydrostatic profile of Test 3 in Figure 3.7, not all the transducers indicated the true hydrostatic pressure. A number of transducers indicate pore pressures up to 4 kPa above or below their expected values. Consolidation was considered to be complete on the basis of the pore pressures shown in Figure 3.6. Initially, the apparent errors in pore pressure readings were thought to be due to slow transducer response to actual changes in pore water pressure. However, the allowance of a further half hour at model scale produced no change in the transducer readings and, indeed, Figure 3.6 shows that all the transducers achieved well-established plateaux in their pore pressure readings. It seems likely that the erroneous transducers were at fault in some way (e.g. a blocked stone) and that the pore pressures were in fact hydrostatic.

The problem appears to rest with the absolute value of the transducer reading rather than its rate of response, since under applied load, all the transducers responded concurrently with appropriate values of excess pore pressure. Given that the excess pore pressures under applied loads were of the most interest and the method of contouring used in the interpretation of pore pressure data which resulted in some "averaging-out" of values, the slight discrepancy in hydrostatic values was not considered overly significant. As discussed in Section 3.7.5, sometimes the calibration offset changed, by less than 1kPa, during the course of a test. In these cases the average calibration offset was used.

The pore pressures presented in Figures 3.6 and 3.7 are typical of the measurements obtained in all tests towards the end of reconsolidation in that the majority of transducer readings were hydrostatic, with occasional data points slightly above or below the expected value.

As mentioned previously in Chapter 3, all pore water pressures were measured using Druck miniature pore pressure transducers (model PDCR 81). The ceramic stone used, located at the top of the transducer and required to prevent the effective stress of the soil from causing deflexion of the silicon diaphragm located within the transducer, was of the alternative specification given by Konig et al (1994). Their collaborative study on the use and accuracy of Druck PDCR 81 transducers highlighted deficiencies with the supplied ceramic stone and provided valuable information on transducer accuracy and response time.

Konig et al (1994) also highlight the difficulty, even in a series of meticulously executed tests, of obtaining consistent results, with variations in pore pressure readings of up to 20% being recorded. This, coupled with the length of time that the model was in its unloaded state during assembly, led to the need for care in the interpretation of the pore pressure transducer readings.

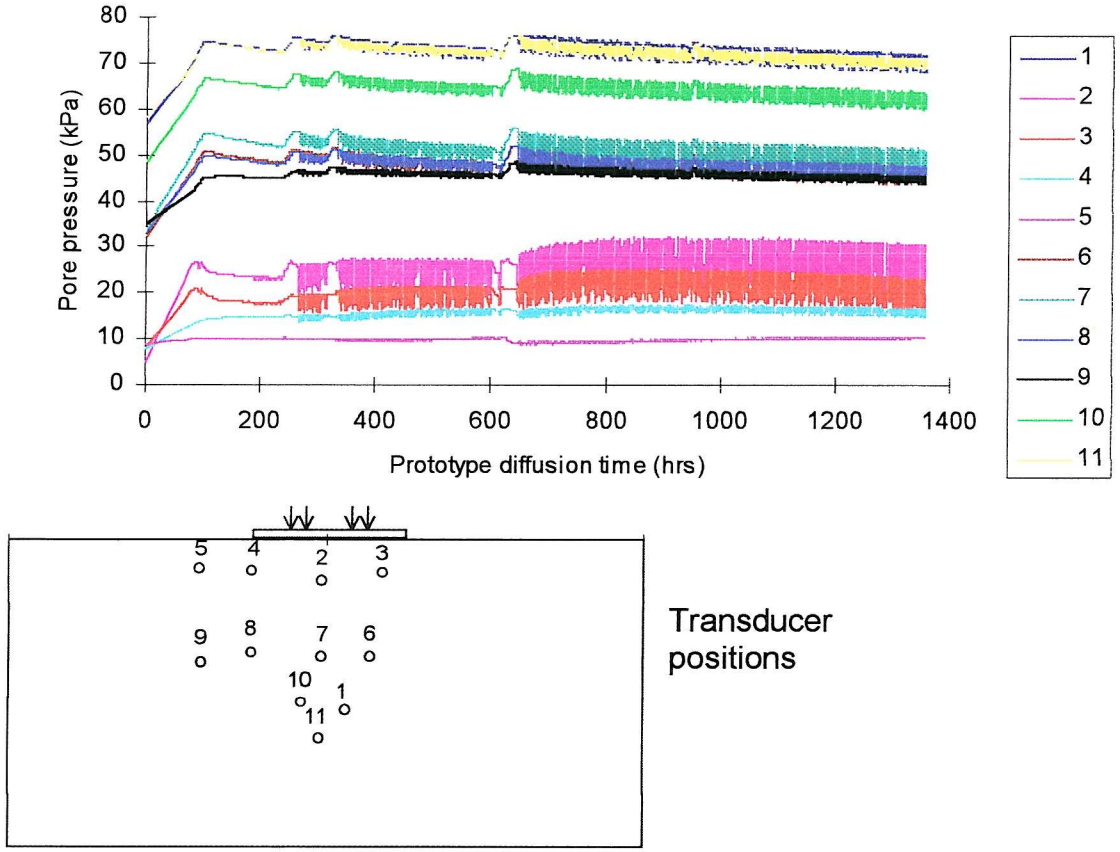

Figure 4.1: Pore pressure transducer response during Test 2

As mentioned above, despite the anomalies in the initial hydrostatic values, all the transducers responded well to the excess pore pressure generated following changes to either the hydrological regime or in response to applied loads. This is best illustrated with the transducer response to cyclic loads in Test 2 shown in Figure 4.1. The graph shows the values of total pore pressure measured by each transducer during the initial applied static load followed by three periods of sustained cyclic loading, each of increasing magnitude. The concurrent nature of the pore pressure traces and immediate response of every transducer to each cycle of applied load shows that the transducers were working well. Moreover, the amplitude of pore pressure measured by each transducer during the cyclic stages of loading, reflects its position in the model, i.e. there is a greater response nearer to the surface where loading occurred. Transducers 2 and 3 had the highest amplitude with a low total pore pressure reflecting their position near the surface of the soil, immediately below the model trackway. Transducers 4 and 5 were

also near the surface, hence their low total pore pressures, but were outside the model trackway and had very low amplitude cycles. The response to applied load of deeper transducers, such as 1, 10 and 11, also reflect their proximity to the model trackway.

Together with the continuous in-flight video of the model surface, the measured pore water pressures provided a general indication that the water supply and drainage systems were functioning satisfactorily, with re-consolidation pore pressures developing as would be expected.

4.3 Presentation of results

Since the load pattern in all the tests reported here was symmetrical in the transverse direction about the centre-line of the model, all measured data have been duplicated across the centre-line of the model to aid the presentation and interpretation of results. This allows model surface profiles and trackway strain profiles to be reflected across the full width of the model, although measurements were only taken from one side of the model in each case.

The contour plots of excess pore pressure were produced using the MathWorks MATLAB program. It interpolates the pore pressure transducer data onto the nodes of a user-defined Cartesian grid representing a transverse section through the model. Using the values of excess pore pressure on the nodes of the grid, MATLAB plots contours at user-defined intervals. The more pore pressure data MATLAB receives, the more coherent its contour plots. To this end, transducer data were also mirrored across the centre-line of the model otherwise MATLAB made no attempt to produce a symmetrical plot. The interpolation process tended to extend the value of the outer transducers to the boundaries of the grid, hence producing unrealistic plots. To prevent this the excess pore pressures along the exposed soil surface and both vertical sides of the model were fixed at zero, as would be the case. This produces very satisfactory plots of excess pore

pressure which, while only acting as a guide to actual pore pressure values, provide an effective means of comparing one test with another.

4.4 Results of centrifuge tests

The centrifuge test results are presented in numerical order. An appraisal of the results then follows.

4.4.1 Test 1 (plane strain test with static load applied to unjointed trackway)

Figure 4.2 shows the magnitude of stress applied throughout the main part of the test. This is the stress between the model trackway and the base of the two beams of the loading apparatus. The stress was increased in a series of small, short stages to 115 kPa and maintained at that level for nearly 900 hours at prototype scale in order to monitor the contribution of consolidation to trackway deflexion. This particular stress was high enough to cause significant trackway deflexion without causing failure of either the soil or the trackway. When trackway settlement had virtually ceased, the stress was increased further to 200 kPa and immediately reduced to zero. Although always significantly lower than the maximum ground pressure beneath the wheel of a DROPS vehicle (659 kPa), the stress is applied in continuous strips along the trackway to create plane strain conditions. The mean stress across the full length of a DROPS vehicle and its tyre width is only 29 kPa even when fully laden. Therefore the applied stress ultimately far exceeds that which trackway would normally be subjected to per metre run.

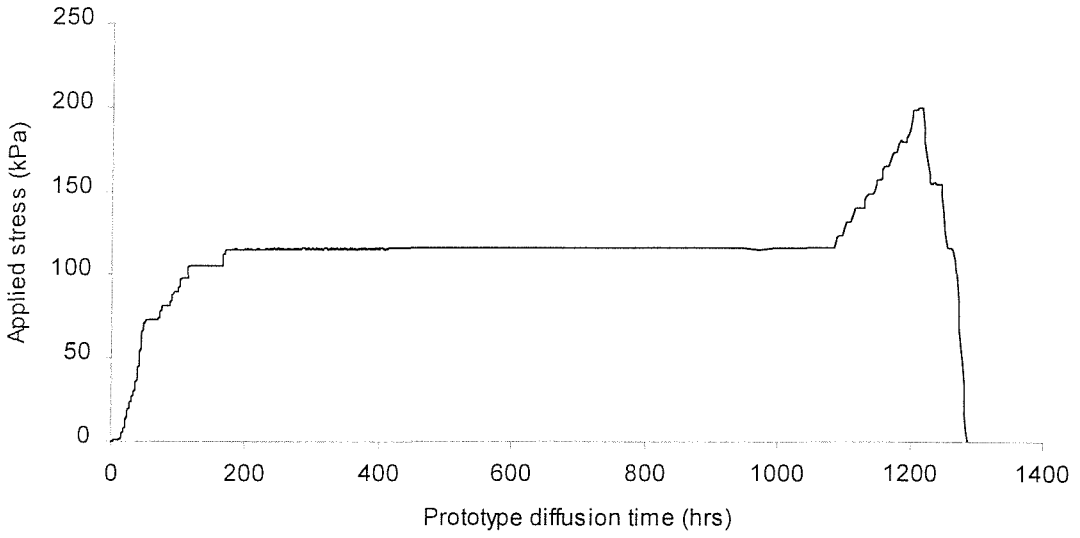

Figure 4.2: TEST1 Applied stress pattern

Figure 4.3 shows the applied stress against the maximum deflexion of the trackway at prototype scale. The maximum deflexion was always beneath the loading beams and hence was measured through the vertical displacement of the loading beams themselves. The deflexion increases approximately linearly to 92 mm at the applied stress of 115 kPa. The small plateau in the graph at 115 kPa is caused by a 20 mm consolidation settlement over a 900 hour constant stress and demonstrates the relatively small contribution of consolidation settlements to trackway deflexion, compared with soil failure. This occurred under an applied stress of approximately 180 kPa. As the soil failed, trackway deflexion increased rapidly to 800 mm and to a point where the trackway would have been untrafficable. On releasing the applied stress, both the trackway and the soil had sustained large permanent deflexions with an elastic rebound of the trackway of only 60 mm.

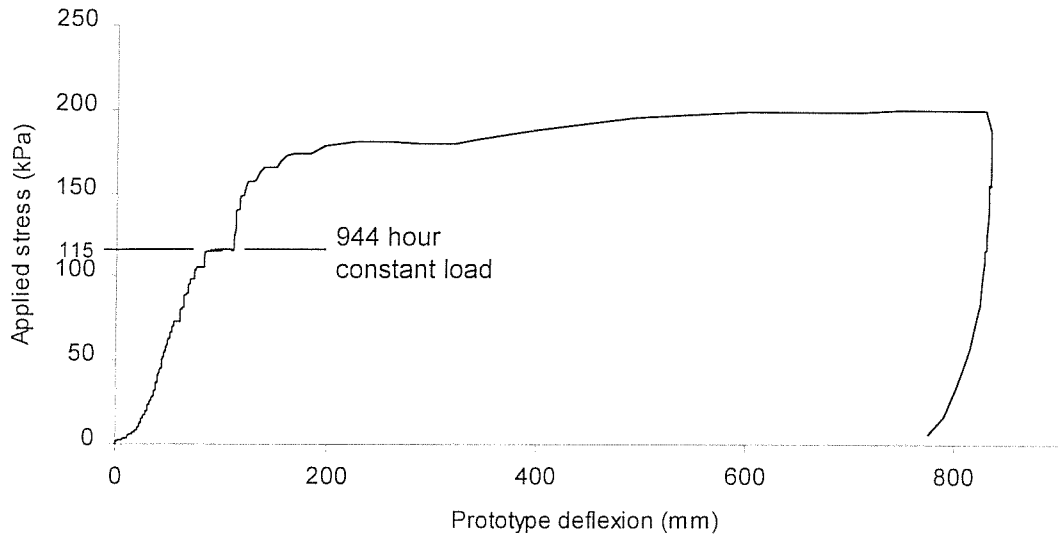

Figure 4.3: TEST1 Development of trackway deflexion with applied stress

Vector plots of soil displacement derived from the in-flight video image processing described in Section 3.7.7 are shown in Figure 4.4. Three load increments are plotted as indicated by the three colours, with the length of arrow corresponding with the scale shown. The values of displacement are likely to be somewhat underestimated due to friction between the front face of the clay and the perspex window, thereby distorting otherwise plane strain displacements. Unfortunately, due to the soft nature of the clay, many of the targets, particularly near the surface, became obscured by the clay itself. Therefore, vectors were only available below about 0.5m prototype depth and one or two other targets sometimes gave extraneous results due to the movement of their centroid through partial obscuring of the marker dot by clay. Otherwise, consistent vectors were obtained across the full matrix of targets up to an applied stress of approximately 150kPa, after which many more were lost.

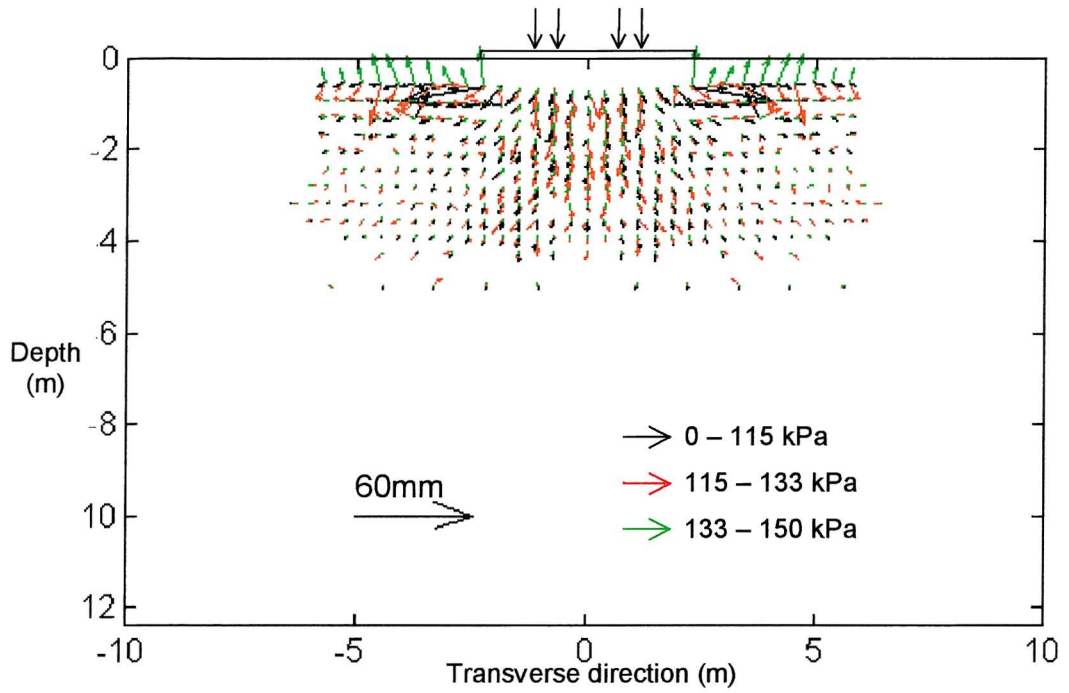

Figure 4.4: TEST1 Soil displacement vectors

As the applied stress reached 115kPa, small 5-10mm downward displacements occurred beneath the trackway as the clay compressed, with the resultant active pressures forcing the clay 10 to 20mm outwards, near the surface, to the sides of the trackway. It was unfortunate that the surface targets were obscured because these were in regions of the largest displacements. Between 115 and 133kPa, a similar displacement pattern emerged, but with each vector approximately double the magnitude of the previous load increment. The areas either side of the trackway which were moving outwards, were now being forced downwards as well by 5 to 10mm. There was still no clear evidence of shear strain occurring in the soil until the 133-150kPa stress increment. The area of soil outside the trackway experienced significant uplift of between 10 and 30mm, with rapid displacement vector rotation downwards within the edges of the trackway. The overall displacement pattern was characteristic of a bearing capacity failure.

Figure 4.5 shows the transverse profile of both the trackway and the soil surface as continuous lines for the central area of the model during the test. This area was monitored using an array of LVDTs (described in Section 3.7.6) and consists of the trackway itself, whose extent is indicated on the profile, and a 3.4 m width of soil on

each side. Measurements were recorded on one side of the model centre-line and, as discussed previously, have been projected across the model to aid visualisation. Profiles caused by four different applied stresses are shown. The first at 0 kPa shows the level starting position of the model surface, followed by 66 and 140 kPa which, according to the stress/deflexion graph in Figure 4.3, preceded trackway failure, and finally 180 kPa where the soil/trackway system did in fact fail. The two regions of maximum trackway deflexion are clearly visible beneath the two loading areas indicated by the triple arrows. The loading apparatus was rigid, so the trackway deflexion at the four corners of the loading beams can be assumed to be equal. The smaller deflexion at the centre of the trackway and the sharp bending outside the loaded area gave rise to the characteristic "W" shaped trackway deflexion profile observed in the field. It is interesting to note that the soil surface immediately outside the trackway had not risen significantly up to the 140 kPa applied stress, suggesting elastic compression and consolidation of the soil beneath the trackway. However, at the 180 kPa applied stress the soil surface had risen due to soil movement, which was also observed in the vector plots in Figure 4.4 for the 133-150kPa applied stress increment.

Profiles of strain (compression positive) measured across the upper surface of the trackway during the test are shown in Figure 4.6. The measured values on one side of the model centre-line are again mirrored to both sides and the strain at the extreme ends of the trackway are assumed to be zero. This gives a complete profile of strain across the full 4.6 m prototype width of the trackway. Four stages of applied stress are shown; firstly 115 kPa which preceded failure, 180 kPa – the point of failure, 200 kPa – the maximum applied stress, and finally the unloaded state at the end of the test. The two loaded areas are indicated by the arrows. In several ways the strain profiles correspond with the physical trackway profiles shown in Figure 4.5. Between the loaded areas the trackway deformation was slight, hence the low tensile strains in this region. The most pronounced trackway bending occurred immediately outside the loaded area and this corresponds with the large peaks in compressive strain shown beneath the outer edges of the loaded areas. The model trackway was composed of an aluminium alloy that begins to yield at a strain of about 0.002. This accounts for the low elastic strains of 0.002 or

below at the centre of the trackway returning to zero on unloading and the high 0.009 compressive strain peaks remaining permanent on unloading. If the soil failed at the applied stress of 180 kPa, sections of the trackway must have experienced strains in excess of 0.002 before this occurred and hence developed permanent deformations before failure in the soil occurred.

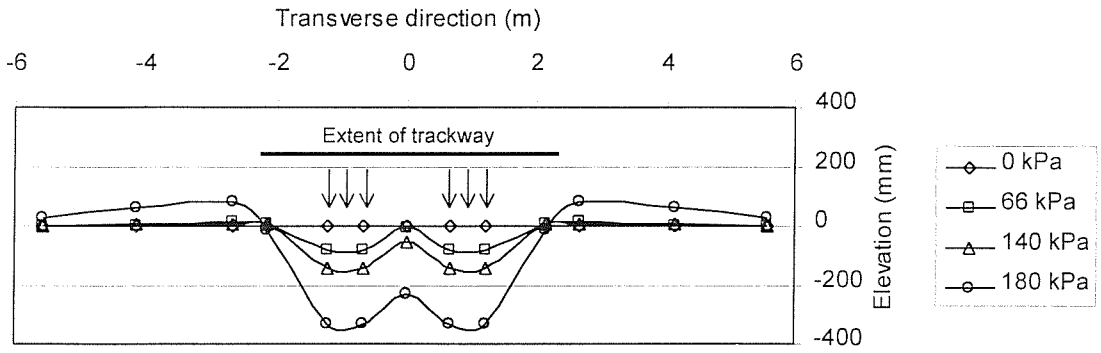

Figure 4.5: TEST1 Soil/trackway transverse deflexion profiles

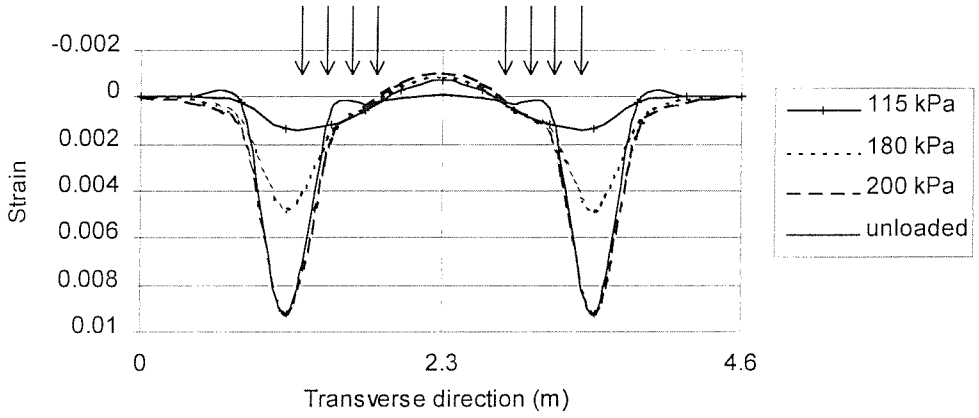

Figure 4.6: TEST1 Transverse trackway strain profiles

Figures 4.7 and 4.8 show contours of excess pore pressure at two stages in the test. The contours are plotted in a transverse section through the entire model, the boundaries of the grid representing the base and side-walls of the strongbox and the soil surface at prototype scale. The position and extent of the trackway is shown by a shallow rectangle on the top surface and the area of applied stress by a series of arrows. The pore pressure transducer positions are marked with black dots and some of the contour lines are marked with crosses and their corresponding value in kPa. The contour interval is 2.5 kPa. Figure 4.7 shows the excess pore pressure response to the applied stress of 115 kPa at the beginning of its 900 hour application. There is a steep rise in excess pore pressure from the surface to the highest value of 22.5 kPa located centrally, approximately two metres below the soil surface. Excess pore pressure reduces more gradually with depth beneath the peak and the 10 kPa contour extends almost to the base. Figure 4.8 displays the pattern of excess pore pressure after soil failure has occurred. Interestingly, the peak value is still 22.5 kPa about 2.5 m deep despite the higher applied stress although the 15 and 10 kPa contours extend over a much larger area. The regions of soil immediately beneath the edge of the trackway have developed negative excess pore pressures of up to –12.5 kPa and are characteristic of undrained shearing in an over-consolidated soil.

After spinning down and removing the model from the centrifuge platform several samples of soil were taken from the model to determine their moisture content. Moisture content values could not give an accurate indication of specific volume even if the soil was assumed saturated. This is because the soil swells after the centrifugal acceleration is removed, the water supply is removed and the drainage system disconnected, hence control of the water regime is lost. However, by comparing moisture contents of samples taken at the same time from different areas of the model it is possible to determine trends in property changes in the soil and ensure moisture content consistency in undisturbed regions of the model across all the tests.

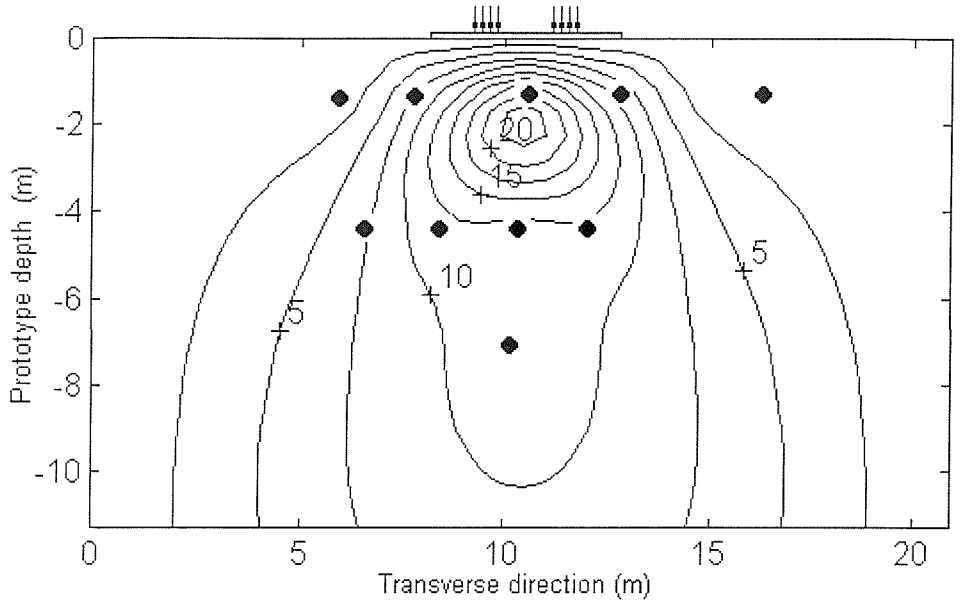

Figure 4.7: TEST1 Excess pore pressures (115 kPa applied stress)

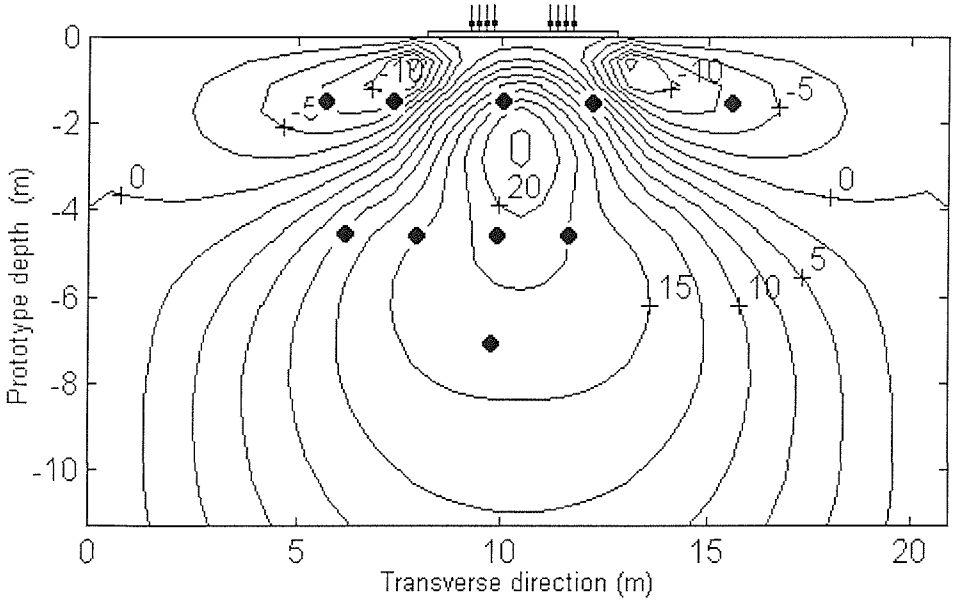

Figure 4.8: TEST1 Excess pore pressures (200 kPa applied stress)

Four soil samples were taken each from immediately beneath the failed trackway, from areas of soil uplift either side of the trackway and from the undisturbed sample outside of these areas. The mean values of moisture content for these samples are shown in Table 4.2.

Sampling region	Moisture content
Beneath failed trackway	49.3 %
Uplifted soil each side of trackway	47.9 %
Intact soil outside failure zone	48.2 %

Table 4.2: Comparison of soil moisture contents after Test 1

The values of moisture content show only minor variations in different areas of the model and, assuming all parts of the soil to be saturated, this indicates that the specific volume was relatively uniform throughout the surface region of the soil at the end of the test. The slightly higher moisture content beneath the trackway could be accounted for by the influence of the trackway itself in preventing moisture loss at the end of the test or, given that the water table was 2 or 3 mm below the surface, by the deeper sample taken from beneath the trackway which had deflected some 20 mm below the surface datum at the end of the test.

4.4.2 Test 2 (plane strain test with 1 Hz cyclic load applied to unjointed trackway)

Figure 4.9 shows the magnitude of stress applied throughout the main part of the test. It is calculated in the same way as described above for Test 1 and the values in Test 1 are included for comparison. Due to the nature of the cyclic loading apparatus stress increases could only be accomplished in static mode and, on reaching the required stress, the 1 Hz cycle introduced (38 second period in prototype). In addition, the enhanced self-weight of the loading apparatus prevented the applied stress from being reduced to any value less than 100 kPa on each cycle. However, a stress amplitude of up to 70 kPa (considerably in excess of the mean DROPS vehicle applied stress of 29 kPa) was achieved towards the end of the test.

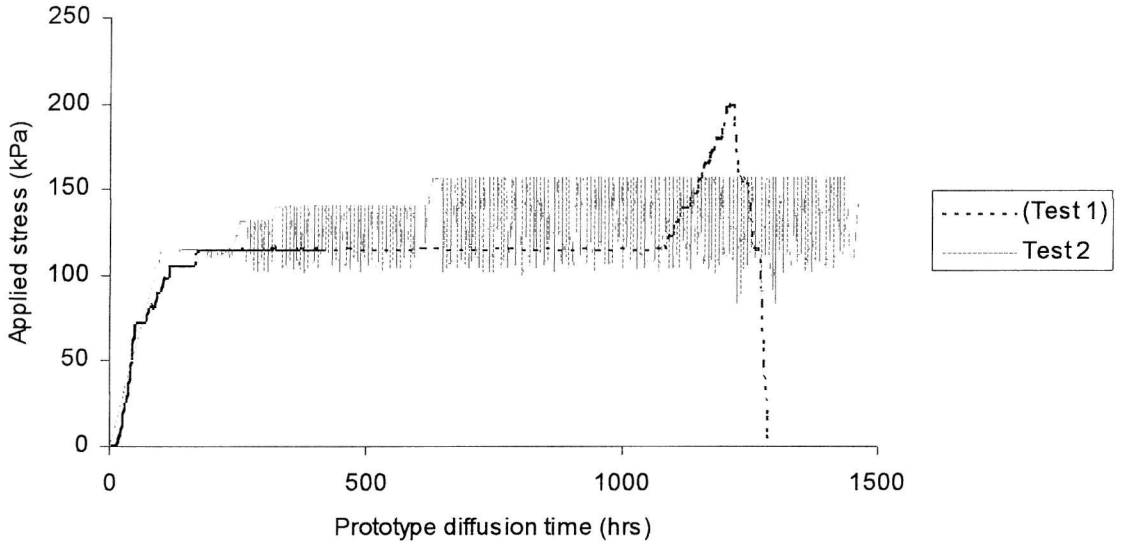

Figure 4.9: TEST2 Applied stress pattern

The applied stress was initially increased to 115 kPa, the same initial target stress in Test 1, and cycling initiated. Unfortunately, the stress amplitude was only about 4 kPa. Consequently, the static stress was increased further to 132 kPa where an amplitude of 30 kPa could be achieved. The stress was then cycled with these values for 47 prototype minutes, using the dynamic scaling factor, or for 30 prototype hours using the consolidation scaling factor. Two further increments of stress were added during the test: cycling between 140 and 105 kPa for 6.5 hours (dynamic factor) or 250 hours (consolidation factor) and between 157 and 105 kPa (decreasing to 80 kPa) for 20 hours (dynamics) or 780 hours (consolidation). The aim of stepping up the applied stress in stages was to detect a threshold stress above which sustained cycling caused a degradation of the soil through an accumulation of excess pore pressures. However, such a threshold stress was not encountered over these particular stress ranges.

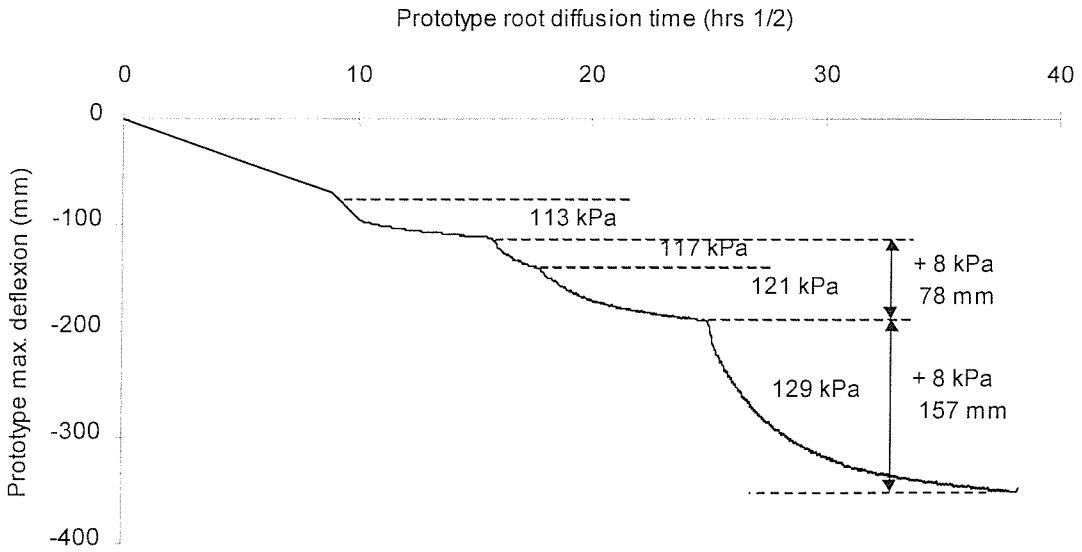

Figure 4.10: TEST2 Development of trackway deflexion with root time

Since the applied stresses were cycling within particular ranges for sustained periods of time, a load/deflexion graph would show increases in deflexion over a constant mean load, suggesting yield and hence could be misleading. A more accurate description of trackway deflexion during the test is shown in Figure 4.10 by plotting values against time or in this case, to foreshorten the curves, against root time. Characteristic curves of consolidation settlement are visible for each of the load increments, hence the use of the consolidation scaling factor for the horizontal (root time) axis.

Up to the deflexion value of 115 mm the trace corresponds with the initial increase of applied stress to 115 kPa and the small cycle of 4 kPa (mean stress 113 kPa). The beginning and end of each increment of cyclic stress is indicated by the dashed lines and the mean value of applied stress shown. Maximum deflexion is calculated in the same way as for Figure 4.3. Between the mean stresses of 113 and 122 kPa, a difference of 9 kPa, the maximum deflexion increased by approximately 78 mm. Between 122 and 131 kPa, again a difference of 9 kPa, the maximum deflexion increased by about 157 mm, which is double the deflexion caused by the previous increment. This increased deflexion must be caused by soil strains over and above those caused by elastic compression and consolidation alone, since otherwise about the same deflexion would be expected for each increment. However, due to the effects of both the cyclic stress and the difficulty of isolating soil shear strains from consolidation strains and elastic strains, it is very difficult to identify an applied stress at which the soil began to yield. The steep initial gradient of this increment suggests soil shear occurred as soon as the static stress was increased. The curve begins to flatten out to a plateau as the rate of consolidation subsides and shear strains in the soil have ceased.

Vectors of soil displacement for Test 2 (using the same scale as for Test 1 in Figure 4.4) are shown in Figure 4.11. The target visibility was better in Test 2, allowing four load increments to be plotted and greater resolution, particularly near the surface. In Figure 4.4, many of the target displacements in the surface zone were missed, and the large vectors near the edges of the trackway in Figure 4.11 demonstrate how significant these displacements were. For all four load increments, the displacement patterns were very

similar, with downwards compression of the soil beneath the centre of the trackway and a smooth rotation of vectors to about 45° upwards towards the edges of the trackway, indicative of shear strains in these regions. Downwards displacement of the clay beneath the trackway increased during the test, from 5-10mm for 0-150kPa, to 40-50mm for consolidation during the mean cyclic applied stress of 129kPa. Conversely, uplift at the trackway edges decreased during the test, with large 60mm displacements up to 115kPa, and about 20mm during the last increment, although some targets were lost. Overall, significant soil displacements were concentrated within a zone only 2m below the soil surface with evidence of shear around this zone and beneath the corners of the trackway.

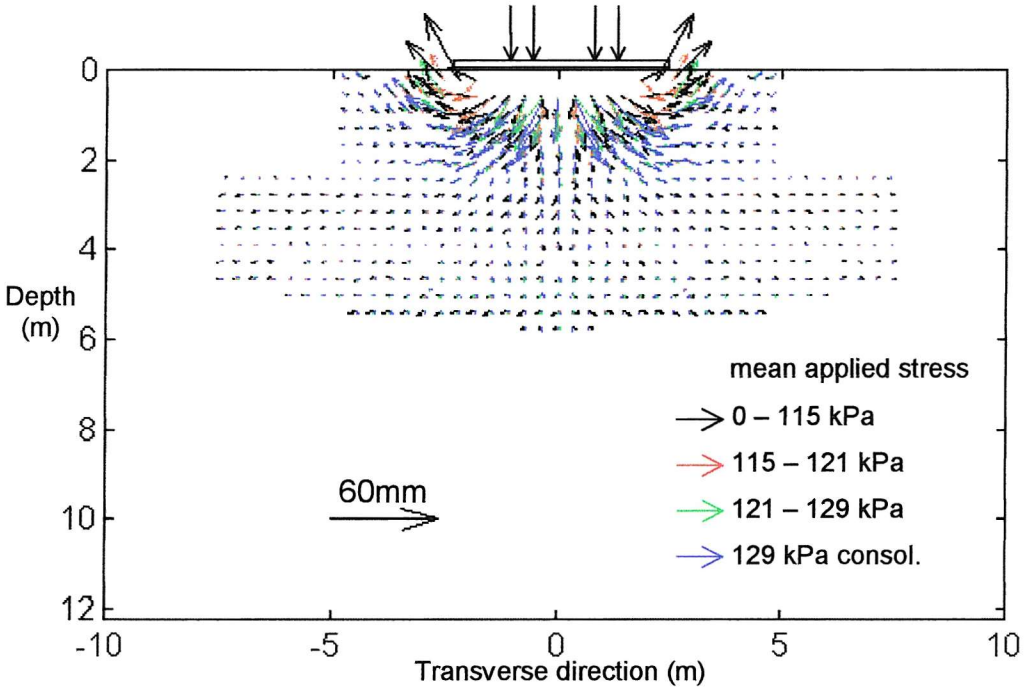

Figure 4.11: TEST2 Soil displacement vectors

Figure 4.12 shows transverse profiles of both the trackway and the soil during the test and are calculated in the same way as described above for Figure 4.5. Model profiles caused by four different mean applied stresses are shown. The first at 0 kPa shows the initial level position of the model surface, followed by 113, 122 and 131 kPa, which

correspond with the first, third and fourth increments, and the profiles presented were recorded at the end of their period of application.

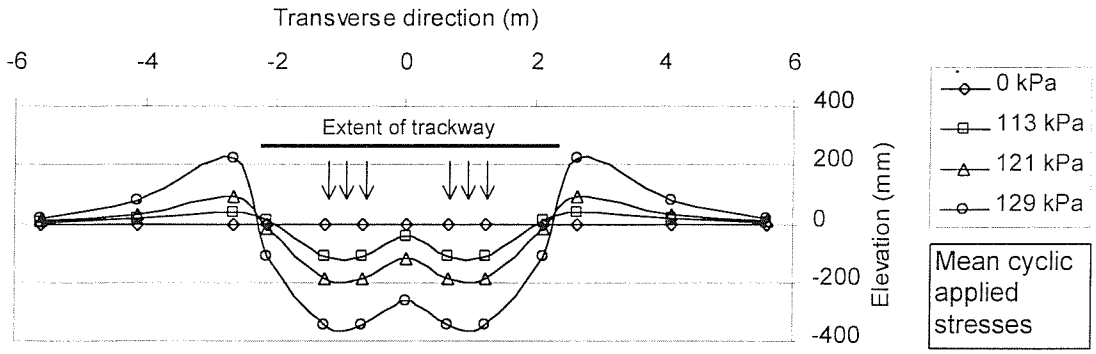

Figure 4.12: TEST2 Soil/trackway transverse deflexion profiles

The two regions of maximum trackway deflexion are visible beneath the two loading areas indicated by the triple arrows. The smaller deflexion at the centre of the trackway and the sharp bending outside the loaded area gave rise to the characteristic "W" shaped profile. Even at the relatively low mean stress of 113kPa, some soil uplift had occurred immediately outside the trackway (as observed in the vector plot in Figure 4.11) which increased slightly at 122kPa, and more significantly at 131kPa. This suggests that significant soil movement was occurring due to all of these applied stresses.

Figure 4.13 shows profiles of strain across the upper surface of the trackway during the test, presented and calculated in the same way as described above for Figure 4.6. As in Figure 4.12, the first, third and fourth increments are presented. The 115kPa and 121kPa increments show the values of strain at the ends of their application periods (refer to Figure 4.9) while the strain values for the 129kPa increment are shown at the beginning and end of its application. There are similarities between the strain profiles and the trackway deflexion profiles shown in Figure 4.12. The relative deflexion across the centre of the trackway was slight, hence there are low tensile strains in this region. The most pronounced bending occurred immediately outside the loaded area and this corresponds with the large peaks in compressive strain beneath the outer edges of the loaded area. Given that the aluminium alloy used in the manufacture of the model

trackway begins to yield at a strain of about 0.002, the region of trackway beneath the outer edges of applied stress began to yield under the first increment (115 kPa) of mean cyclic stress. These were also the only regions of trackway to show significant increases in strain with each increment. By the fourth increment, the maximum strain was 0.005 and this increased to the peak of 0.009 during the application of this cyclic stress.

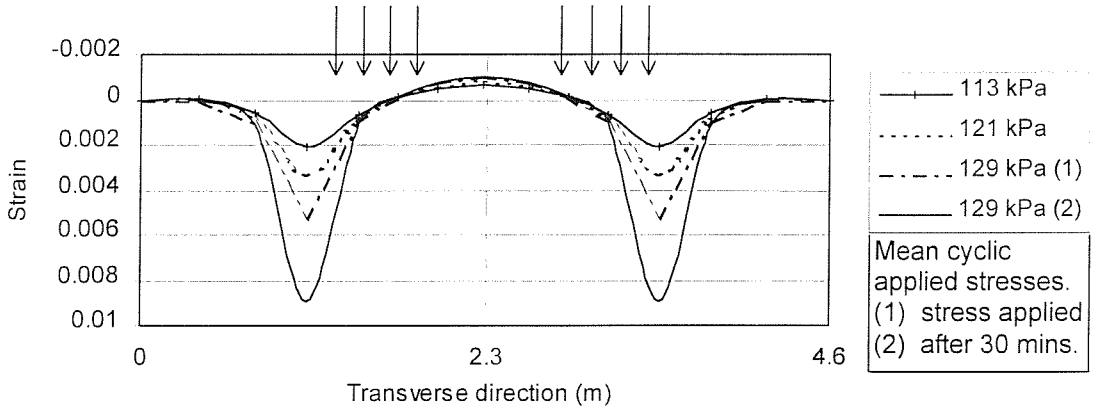

Figure 4.13: TEST2 Transverse trackway strain profiles

Figures 4.14 and 4.15 show contours of excess pore pressure at two stages in the test, plotted in the same fashion as described above for Figure 4.7. Figure 4.14 shows the excess pore pressure response at the initial application of the 129 kPa mean applied cyclic stress. There is a steep rise in excess pore pressure from the surface to the peak value of 22.5 kPa located centrally and about 2.5 m below the soil surface. Excess pore pressure reduces more gradually with depth beneath the peak and the 15 kPa contour extends to the base. Figure 4.15 shows the pattern of excess pore pressure having applied the same mean cyclic stress for 740 prototype hours (refer to Figure 4.9). Interestingly, the peak value, although at approximately the same position, has increased to 27.5 kPa, although excess pore pressure reduces more rapidly with depth beneath the peak. The 15 kPa contour extends to a depth of only 7 m compared with 11 m and the general dissipation of excess pore pressures in the lower half of the model is thought to have been caused by the base drainage layer.

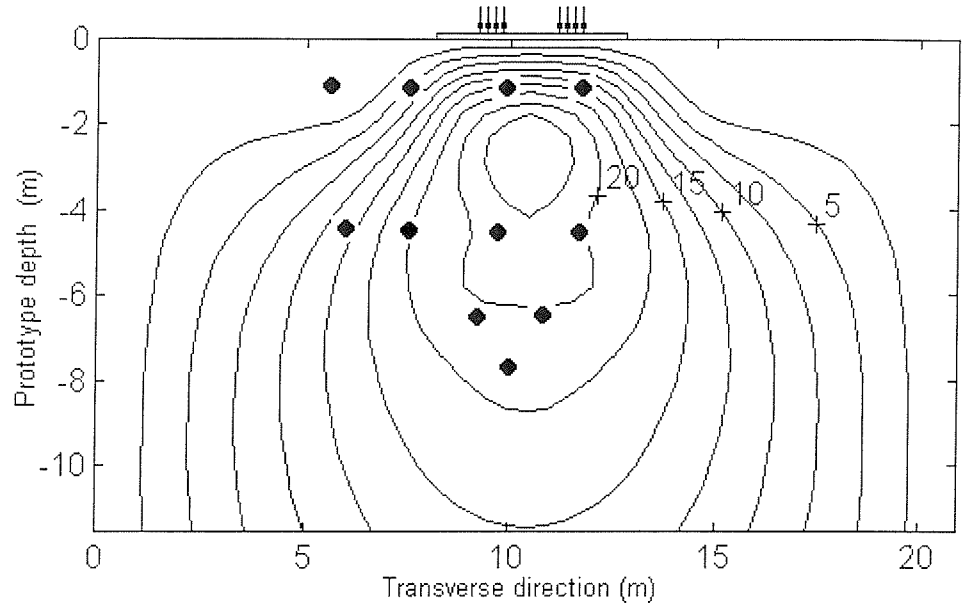

Figure 4.14: TEST2 Excess pore pressures (129 kPa mean applied stress, t = 0)

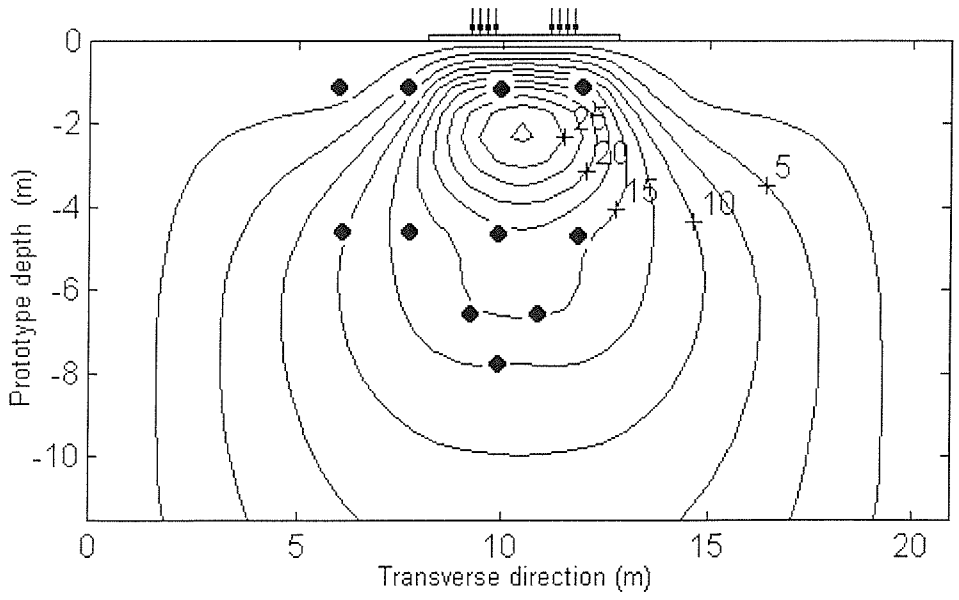

Figure 4.15: TEST2 Excess pore pressures (129 kPa mean stress, t = 740 hrs)

4.4.3 Test 3 (self-weight of rolling vehicle applied load to unjointed trackway)

Figure 4.16 shows the vertical displacement at prototype scale of the rolling vehicle through every pass of the test (a pass is a movement from one side of the model to the other, two passes constitute one cycle). Since the wheels of the rolling vehicle are in continuous contact with the trackway, the vertical displacement values give a good approximation of the maximum deflexion of the trackway. It can be seen that apart from some initial bedding-in of the trackway, which caused an immediate maximum settlement of 7 mm, there is a total deflexion of no more than 10 mm throughout the test. Through more than 2000 passes the unjointed trackway showed no signs of accumulating significant deflexions. The cyclic nature of the axle settlement trace was created as the rolling vehicle moved to and fro, causing a shallow longitudinal trough to be formed in the soil.

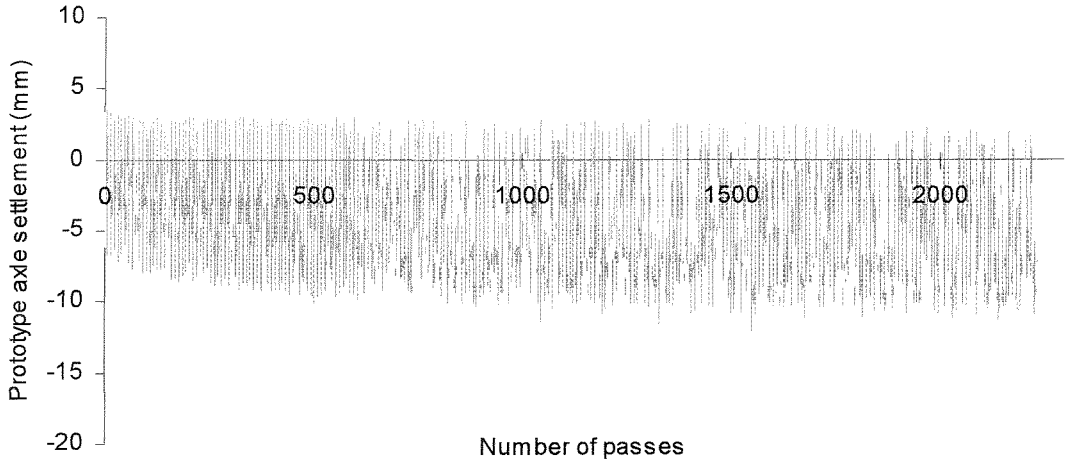

Figure 4.16: TEST3 Axle settlement of rolling vehicle

Since the use of LVDT's to measure trackway profile was not possible when operating the rolling vehicle, the transverse profile of the model could only be measured with a depth gauge after spinning down the centrifuge at the end of the test. These measurements therefore recorded the permanent deflexions in the model and are shown for Test 3 in Figure 4.17. The effects of soil uplift after the release of the centrifugal acceleration would be expected to be uniform across the whole model and not distort the shape of the transverse profile. To avoid excessive vertical exaggeration a small elevation scale has been chosen, but even with a vertical magnification of approximately three times, the profile is virtually flat. The trackway is visible as a slightly raised platform between 8.5 and 13 m on the horizontal scale. After over 2000 passes, the model vehicle caused no permanent deflexions in the soil.

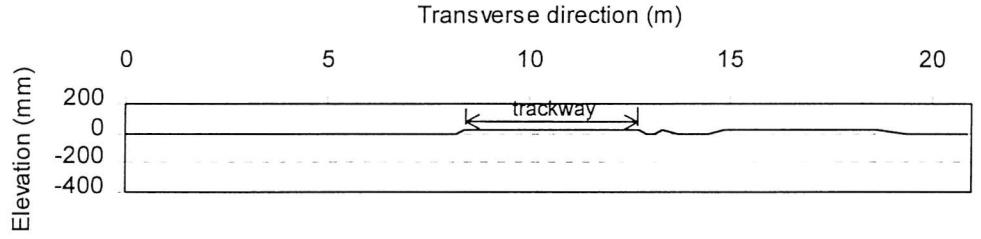

Figure 4.17: TEST3 Final permanent soil/trackway transverse profile

Figure 4.18 shows the profile of strain across the upper surface of the trackway, presented in the same way as described above for Figure 4.6. In the rolling vehicle tests, the value returned by a strain gauge depended very much on the position of the vehicle at that time, with the maximum values being recorded when the vehicle was on, or close to, a strain gauge. Since the strain gauges were fixed in various positions along the trackway, taking a "snap-shot" of readings for a transverse profile would be misleading. Therefore, the maximum absolute values of strain recorded by each strain gauge throughout the test were extracted and used to construct the profile shown in Figure 4.18. This should represent the trackway strain profile immediately beneath the rolling vehicle. The peak strain of 0.0006 occurred beneath the centre of each wheel and is below the approximate yield value of 0.002. Hence, no part of the trackway sustained permanent strains during the test. Although, since the upper surface was in compression at the centre and in tension beneath the wheels, the elastic deflexions of the trackway (which were not measurable in the final physical profile) would have formed a flattened "W" shape.

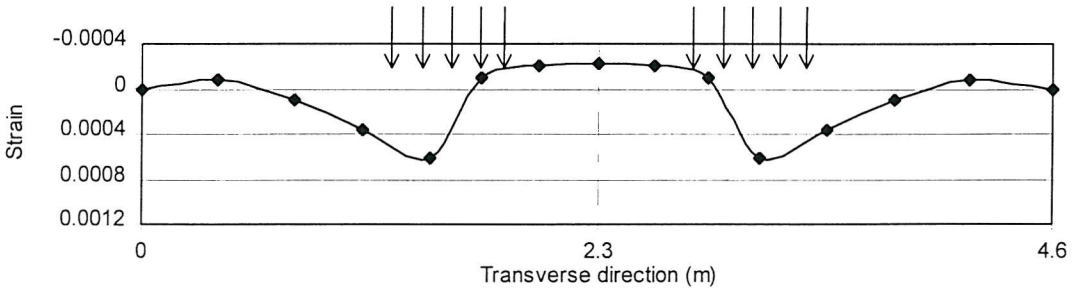

Figure 4.18: TEST3 Transverse trackway strain profiles

Figure 4.19 shows contours of maximum excess pore pressure during the test. They are presented in the same way as described above for Figure 4.7, although the section is only 7.7 m deep because this test was performed using a shallower depth of soil. For the same reasons described above, a "snap-shot" of excess pore pressure values may be misleading in a rolling vehicle test. Therefore, the contours have been calculated using the maximum absolute value of excess pore pressure returned by each transducer throughout the test and should represent a transverse section taken immediately beneath the rolling vehicle. Substantial areas of the model produced no significant excess pore pressure while a quite localised region, with a peak of 7.5 kPa, formed directly beneath the trackway. The peak is about 1 m below the surface and is kidney-shaped, demonstrating the stress contribution from each wheel of the vehicle.

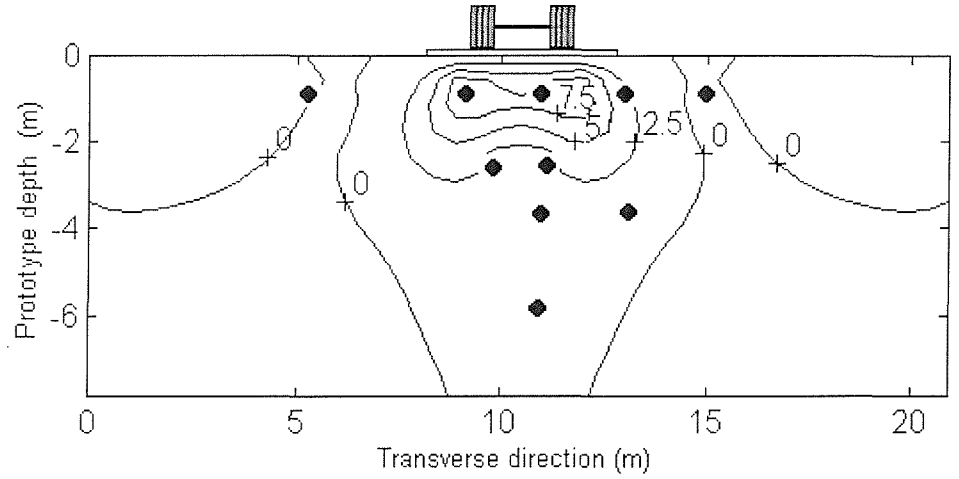

Figure 4.19: TEST3 Maximum excess pore pressures

At the end of the test samples of soil were taken from the model to determine their moisture content. Four soil samples were taken each from the clay immediately beneath the trackway and from areas of intact soil from the surrounding surface and at least 10mm beneath the trackway. The mean values of moisture content for these samples are shown in Table 4.3.

Sampling region	Moisture content
Soil surface immediately beneath trackway	48.8 %
Intact soil below and around trackway	49.5 %

Table 4.3: Comparison of soil moisture contents after Test 3

The values show that the motion of the model vehicle caused no significant changes to the properties of the clay beneath. Immediately beneath the trackway the clay was slightly drier, perhaps due to slight consolidation due to the weight of the model vehicle.

4.4.4 Test 4 (self-weight of rolling vehicle applied load to jointed trackway)

Figure 4.20 shows the vertical displacement of the rolling vehicle throughout the test which, as explained above for Figure 4.16, gives a good approximation of trackway deflexion. Trackway deflexion occurs immediately on the first pass and increases at a high rate to a maximum value of 96 mm after 80 passes. The to and fro motion of the rolling vehicle tended to create a longitudinal trough in the underlying soil. This can be seen in Figure 4.21 which shows the trackway at the end of Test 4. In addition to clay slurry being driven out towards the sides of the trackway and up between the joints, some was also pushed towards each end of the trackway. This accounts for the cyclic nature of the axle settlement trace in Figure 4.20, as the rolling vehicle moved in and out of the trough its axle settlement, after 80 passes, reduced from 96mm in the trough to only 17 mm at each end.

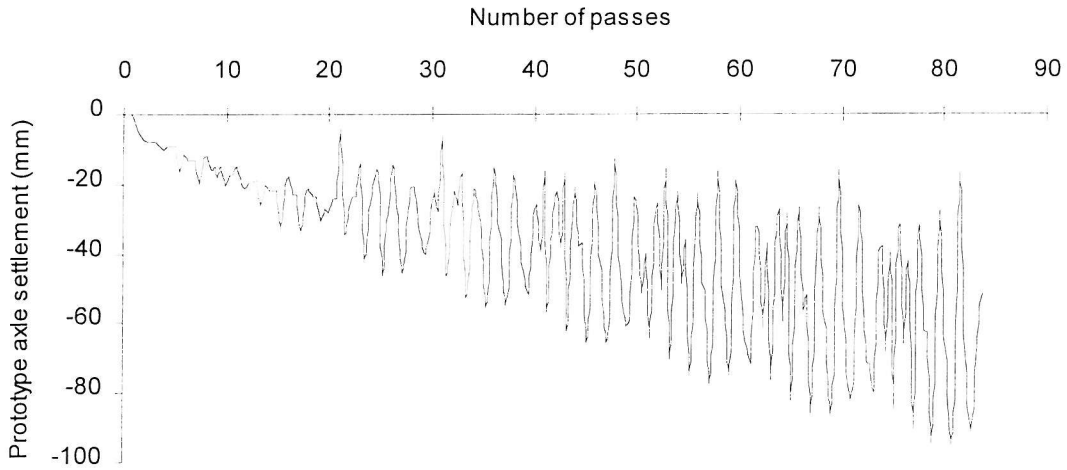

Figure 4.20: TEST4 Axle settlement of rolling vehicle

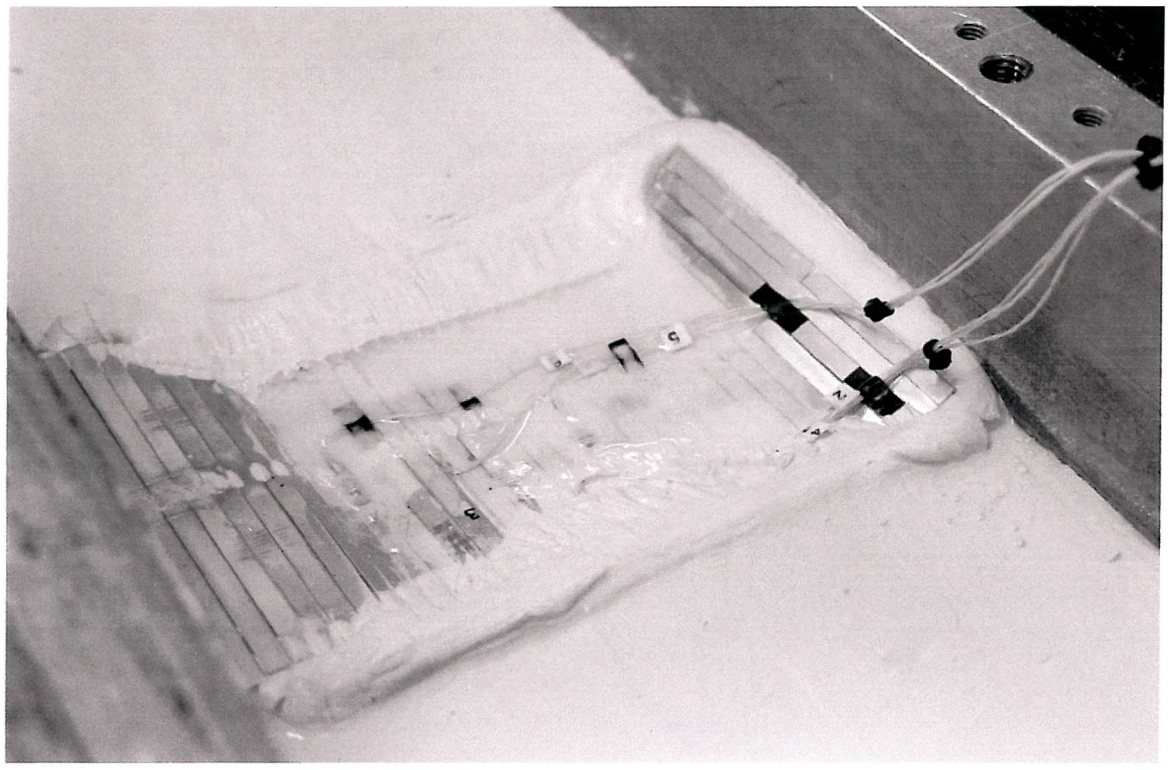

Figure 4.21: TEST4 Centrifuge model at end of test

The permanent transverse profile at the end of the test is shown in Figure 4.22. It was measured in the same way as described above for Figure 4.17. The final trackway position is marked with a grey line and, although the soil/trackway system had failed, it did not deform transversely into the characteristic "W" shape. The trackway tended to deform more in the longitudinal direction. As the soil degraded beneath, the trackway became unstable and tilted to one side in the transverse direction, with soil slurry tending to be driven towards the high side. The maximum soil deflexion on the low side was 245 mm and, as shown in Figure 4.22, the trackway ends became buried in the soft slurry. Above the high side of the trackway the soil profile had risen by 130 mm. However, this was not a deep-seated failure causing uplift of soil outside the trackway but merely a deposit of degraded soil, or slurry, from immediately beneath the trackway which occupied a considerably larger volume than its original state. Figure 4.21 shows that not only was slurry deposited along the edges of the trackway, but large volumes of slurry were driven by the motion of the rolling vehicle to each end of the roadway as well.

Once the deposits of slurry had been removed from the surface of the model, there was no measurable uplift of the intact soil at all.

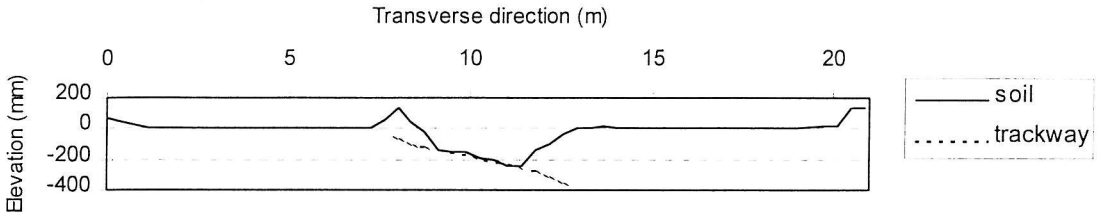

Figure 4.22: TEST4 Final permanent soil/trackway transverse profile

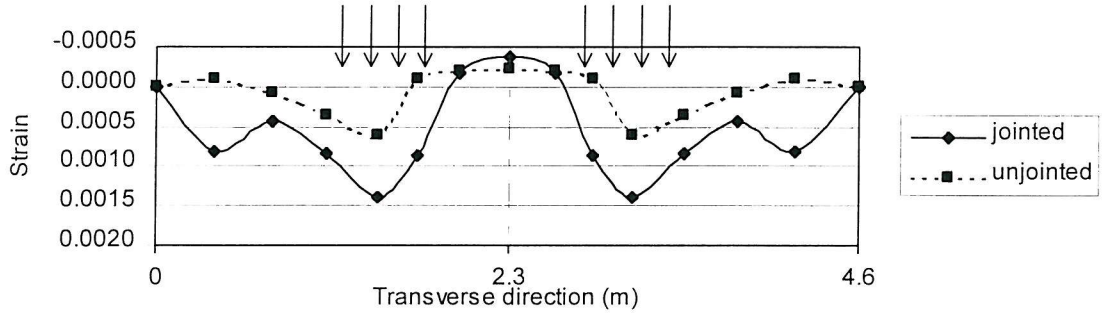

Figure 4.23: TEST4 Transverse trackway strain profiles

A profile of maximum strain in the trackway was calculated for this test in the same way described above for Test 3. It is shown in Figure 4.23 together with the Test 3 results. As would be expected, the peak strain was beneath the wheels of the rolling vehicle (whose positions are indicated by the vertical arrows). The strain values in the vicinity of the vehicle wheels were two to three times the unjointed values, showing that there were significantly more transverse deformations in the jointed trackway. The shape of the strain profile suggests that the trackway deformed into the characteristic "W" shape in the transverse direction, but since most of the strains were within the elastic region (< 0.002), this was not measurable in the permanent transverse profile at the end of the test.

Figure 4.24 shows contours of maximum excess pore pressure recorded during the test. They have been calculated and presented in the same way as described above for Figure 4.19. Most areas of the model registered no significant excess pore pressures. Only a small, localised region, at a depth of about 2 m beneath the trackway, produced a peak excess pore pressure of 2 kPa. The 2 kPa contour is kidney-shaped, reflecting the contribution of each wheel of the rolling vehicle to the formation of excess pore pressure.

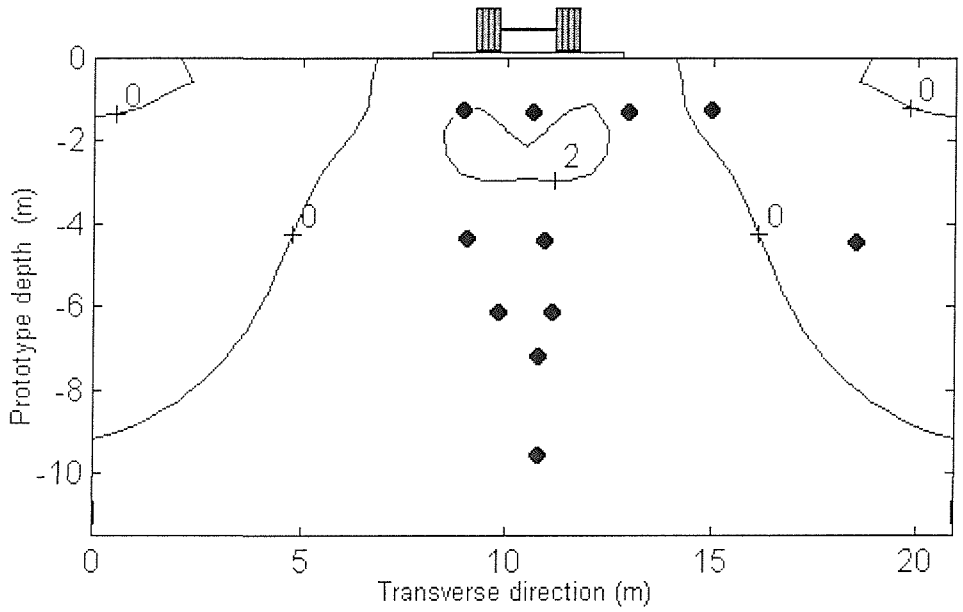

Figure 4.24: TEST4 Maximum excess pore pressures

The in-flight video recording of the model surface gave a visual record of the events throughout the test. Four stills from this recording at different stages of Test 4 are shown in Figure 4.25. Unfortunately, due to the poor lighting in the model and the quality of the video images, the stills have a low resolution. However, it is possible to detect an accumulation of slurry and trackway deflexion during the test. After two passes of the rolling vehicle (Figure 4.25A) slurry was already visible in the joints of the trackway. After 6 passes, slurry had been deposited along the edges of the trackway and a visible wave in the trackway, either side of the vehicle wheels, followed the wheels as they moved backwards and forwards. After 20 passes significant longitudinal deflexion of the trackway was visible and at 29 passes (Figure 4.25B) slurry had seeped through the

joints and can be seen deposited across the whole trackway. At 46 passes (Figure 4.25C) thick deposits of clay slurry can be seen along the edges and across the top of the trackway and also beneath the trackway at each end of the vehicle's maximum point of travel. These deposits grew until at the 82nd pass (Figure 4.25D) the test was terminated since the vehicle was now moving through a significant depth of clay slurry and its mobility was being compromised by the depth and steepness of the longitudinal trough. Since a DROPS vehicle has four axles, the soil/trackway system failed after an equivalent of 20 DROPS vehicle passes.

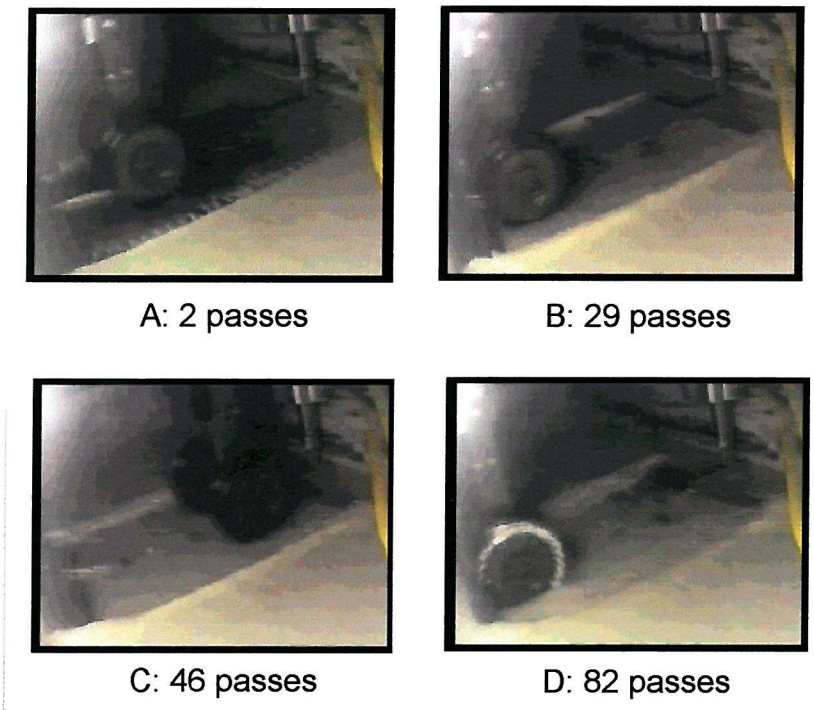

Figure 4.25: TEST 4 In-flight video stills

After spinning down and removing the model from the centrifuge platform several samples of soil were taken from the model to determine their moisture content. Four soil samples were taken each from the clay slurry deposited on the trackway, from scrapings of slurry on the soil surface immediately beneath the trackway, and from areas of intact soil 3-4 mm below the trackway and from the surrounding surface. The mean values of moisture content for these samples are shown in Table 4.4.

Sampling region	Moisture content
Trackway surface deposits	56.1 %
Soil surface immediately beneath trackway	55.8 %
Intact soil below and around trackway	49.1 %

Table 4.4: Comparison of soil moisture contents after Test 4

The values show that the clay slurry and a thin layer of soil immediately beneath the trackway had a moisture content some 7 percent higher than the surrounding intact soil. If all the soil was saturated, this could be interpreted as a 14% increase in the volume of slurry over the surrounding intact soil.

Chapter 5

Discussion of Centrifuge Test Results

5.0 Introduction

By comparing the results from the centrifuge tests, the influences of loading pattern and trackway type on soil/trackway performance are discussed and conclusions drawn.

5.1 Trackway deflexion

The maximum trackway deflexions under the static and cyclic stresses of Tests 1 and 2 are compared in Figure 5.1. The first 34 √hours of the static deflexion trace represents the elastic compression and consolidation of the underlying soil due to the constant applied stress of 115kPa. In an attempt to determine a definitive static "failure stress" for this particular soil/trackway configuration, the applied stress was increased rapidly to failure. Soil/trackway failure caused a large 650mm deflexion over and above that caused by the initial 115kPa stress application. The large rebound of deflexion from 860mm down to 280mm was caused both by the elastic recovery of the soil and, more particularly, by the elastic recovery of the trackway. In fact, the trackway straightened its transverse profile to such an extent that it lifted the central region of its base just clear of the deformed soil surface.

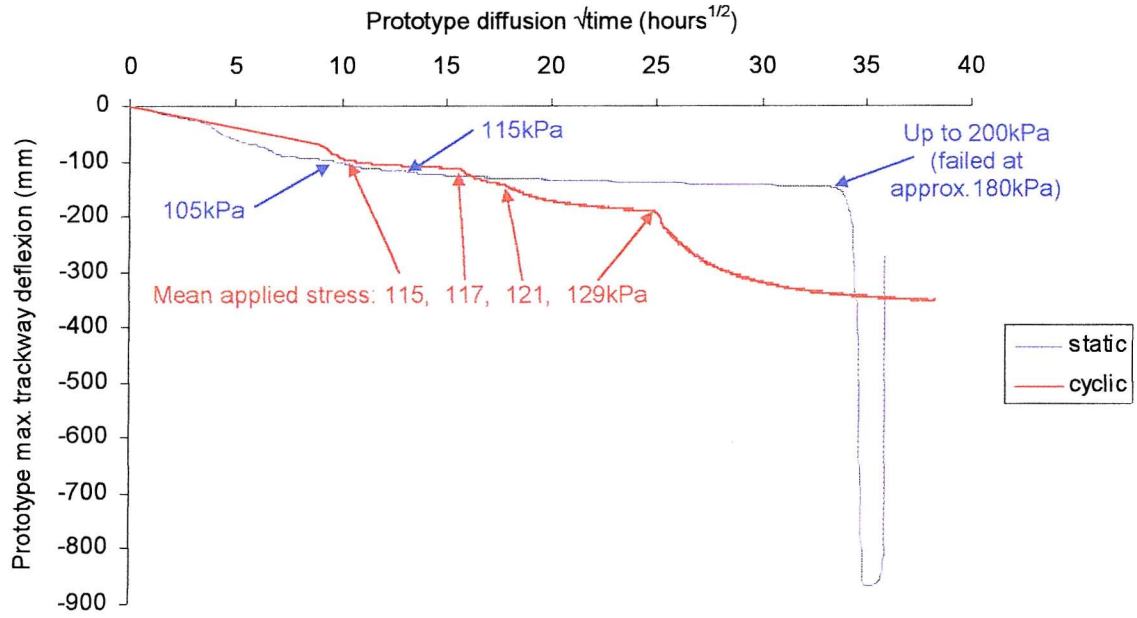

Figure 5.1 Comparison of trackway deflexions under static and cyclic loads

A small part of the load-deflexion trace at the onset of failure in Test 1 is shown in Figure 5.2. The small increments of stress up to 156, 165, 173 and 181kPa are clearly visible. The soil/trackway system begins to yield at the applied stress of 181kPa, or approximately 180kPa. If this value is assumed to be the soil/trackway failure stress, it would be interesting to compare it with a value predicted by a rigid strip bearing capacity equation. The rapid nature of the failure of the soil/trackway system indicated by the near vertical portion of the static applied stress graph beyond 34 $\sqrt{}$hours in Figure 5.1 and the shear zones with significant negative excess pore pressure in Figure 4.8 suggest that it was caused by undrained shearing of the soil. The undrained shear strength (c_u) near the surface of the kaolin used in the tests reported here was approximately 22kPa (Appendix B). This was the target c_u value during sample preparation and is verified by the discussion of pore pressure data in Section 5.3. The predicted bearing capacity of this soil beneath a rigid strip footing is $5.14c_u$ = 113.1kPa. If this calculated failure stress was distributed evenly across the full width of the trackway (refer to Figure 5.3) this corresponds to an applied stress under the loaded area of 452kPa. If, as is more likely considering the steep slopes of the trackway either side of the loading beams after failure, the calculated failure stress was distributed evenly between the loading beams (see Figure 5.3) this corresponds with an applied stress of 209kPa. Clearly, the flexibility of the trackway plays a detrimental role in the bearing capacity of the soil/trackway system compared with that predicted for a rigid strip footing. The measured failure stress of 180kPa is significantly lower than the calculated value of 209kPa, particularly since the calculated value represents the absolute minimum, with the applied stress only being distributed between the loading beams.

The overall nature of the static failure of the trackway in Test 1 is inconsistent with field experience. In the field, trackway deflexions build up with successive vehicle passes to such a degree that the passage of traffic becomes compromised. There is never a rapid increase in trackway deflexion due to bearing capacity failure beneath a single vehicle. Clearly the prediction of soil/trackway strength using bearing capacity factors or a simple static plane strain numerical model would be inadequate.

An attempt to recreate the field experience of a successive build up of trackway deflexions was made in Test 2. Instead of a static stress, the applied stress was cycled at 1Hz, each cycle representing the passage of a whole vehicle. The significance of the cycling can be determined by comparing the trackway deflexion response to a static stress with its equivalent mean cyclic stress. If the stress cycles played a detrimental role in soil/trackway degradation, larger deflexions would be expected beneath the cyclic stresses.

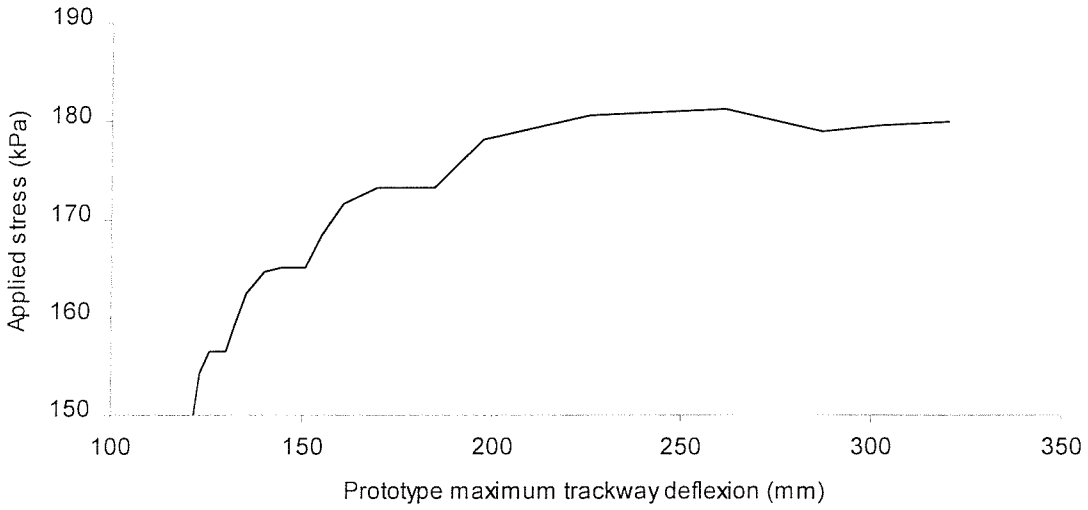

Figure 5.2: TEST1 Load-deflexion trace at onset of failure

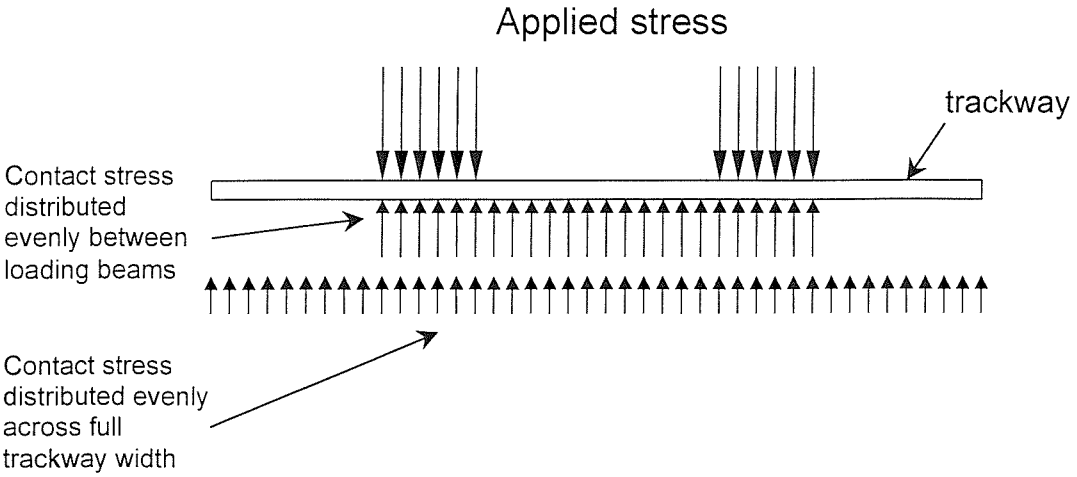

Figure 5.3: Idealised stress distributions between trackway and soil surface

Comparing the static and cyclic deflexion traces in Figure 5.1, the cyclic applied stress appears neither to be particularly detrimental to soil/trackway performance nor is a threshold stress amplitude reached where soil strains become unstable and increase their rate of accumulation. In the initial stages of both tests the static applied stress was 115kPa and the mean cyclic applied stress was 113kPa up to 15 √hours where it was increased to 117kPa. The deflexions in the static and cyclic tests were very similar, within 10% of each other throughout these increments. Indeed, at 113kPa the cyclic deflexion is slightly smaller compared with the 115kPa static stress, and when increased to 117kPa, crosses the static trace and remains slightly higher than the static stress to the end of the increment. Further increases in mean cyclic stress to 121 and 129kPa produce significant but still small deflexions compared with the very large deflexion at failure in the static test. The increments of 121 and 129kPa mean cyclic stress show characteristic consolidation curves. Rather than deflexions continuing to accumulate or accelerate, they approached stable plateaux. As described in Section 4.4.2, the increase in deflexion due to the 129kPa mean stress increment was large compared with the others, suggesting some yielding of the soil and the generation of shear strains (as shown in the vector plot in Figure 4.11), although, again, deflexions stabilised. This is similar behaviour to that observed by Ansal and Erken (1989) in their study of the undrained behaviour of kaolin under cyclic shear stresses. Their results indicated that there is a threshold cyclic shear stress amplitude, typically about 50% the undrained static shear strength, below which shear strains will not increase significantly and will remain stable no matter how many cycles are applied. At shear stress amplitudes above this threshold, shear strains accumulate and become unstable as their rate of increase accelerates towards failure. The Test 2 behaviour is consistent with an applied cyclic stress amplitude close to, but still below, the threshold stress described by Ansal and Erken (1989). Their results showed that stress ratios approaching the threshold could cause initially significant shear strains which still stabilised no matter how many cycles of stress were subsequently applied. Bearing in mind that during the final increment of cyclic stress, the stress amplitude was more than double the mean DROPS vehicle applied stress (refer to Section 4.4.2), it is clear that "whole vehicle loads" would not cause failure of this particular soil/trackway system, certainly not without the aid of long-term consolidation.

The nature of trackway loading in the field is so transient, that its failure is unlikely to be caused by consolidation of the underlying soil. However, both the static and cyclic tests show that, at the vehicle loads occurring in the field, deep-seated undrained shearing of the underlying soil is also unlikely.

Having established that deep-seated failure of the soil due to "whole vehicle loads" was unlikely, Tests 3 and 4 studied the effects of axle loads on trackway. When analysing vehicle wheels or tracks, the contact stress between them and the trackway panels becomes significant, as does the interaction between each panel, particularly at the joints, and the soil surface. Although axle loads are smaller than whole vehicle loads, they can impose higher stresses in key areas of the soil/trackway system. Instead of searching for a conventional bearing capacity of the soil/trackway system due to "averaged out" applied vehicle stresses, Tests 3 and 4 assessed the effects of small scale interactions between the vehicle wheels, the trackway and the soil surface.

Figure 5.4 highlights the difference between the axle settlements of Tests 3 and 4, labelled as unjointed and jointed respectively. A log scale was chosen to extend the more significant early portions of each trace. Consequently, the graphs begin after the first pass and the frequency of passes appears to reduce during the test.

The unjointed trackway proved to be a very effective support for the rolling axle, its maximum deflexion reaching only 9mm after 2200 passes. The unjointed trackway possessed only the transverse bending stiffness of class 60 trackway, albeit in both the transverse and longitudinal directions because of its isotropic section. However, it distributed the very high contact stresses from the wheels, in the region of 500kPa, so effectively that no permanent deflexion in the trackway could be measured, even on the soft clay used in the tests. A cycling applied stress with an amplitude of 500kPa is very significant and after 2200 cycles at about 0.7Hz there were still no signs of degradation of the underlying soil. The cyclic nature of the applied axle loads could not cause failure of the trackway alone and does not explain the field experience of an accumulation of trackway deflexions.

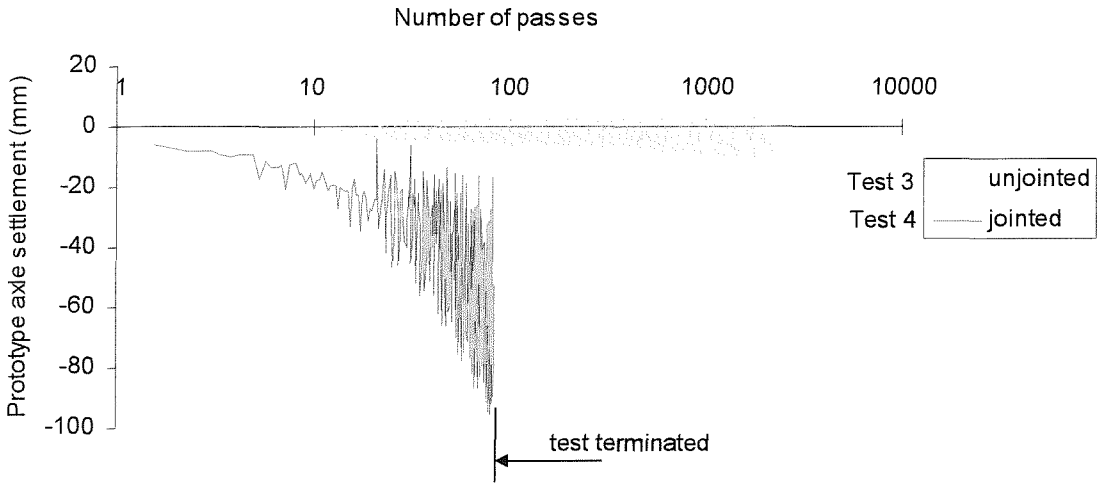

Figure 5.4: Comparison of axle settlements over unjointed and jointed trackway

The deflexions under the unjointed trackway clearly contrast with those beneath the jointed trackway. After only 80 axle passes (equivalent to 20 DROPS vehicle passes) the maximum trackway deflexion had increased rapidly to 95mm and the axle's mobility had become seriously impaired. The pattern of trackway deflexion matched closely with that experienced in the field. It accumulated over successive axle passes and, although no permanent deflexion of the trackway could be measured at the end of the test, the strain profile in Figure 4.23 suggests the elastic deformation of the trackway formed the characteristic "W" shaped profile. Field experience shows that permanent transverse deflexions do occur and it is these which prevent trackway from being retrieved and re-used. Permanent transverse deflexions were not achieved in the model due to the unavoidable nature of the rolling vehicle's movement. The model vehicle had a short length of travel on each pass (approximately 5.7m at prototype scale) and it was continually reversing. Once a slurry had been generated through the action of the joints, it was then driven to each end of the vehicle's travel causing the trackway to deflect into a longitudinal trough (Figure 4.21). In the field, temporary roadways are generally longer and trafficking tends to be uni-directional, making the formation of a longitudinal trough less realistic: transverse troughs normally form, causing permanent transverse

rutting of the roadway. The most significant finding in Test 4 was that soil degradation and failure was brought about beneath the jointed trackway. The behaviour of the resulting slurry, which determines the final deflected shape of the trackway (as discussed below), was more difficult to control. To reproduce the transverse rutting observed in the field, a longer length of roadway would be required to prevent most of the slurry from being driven to each end and allow permanent transverse ruts to form.

The cyclic nature of the applied axle stress is clearly significant because of the accumulation of trackway settlement over the 80 passes. It is important to determine whether the degradation of the underlying soil and the resultant accumulation of trackway settlement was caused by a threshold cyclic shear stress being exceeded (Ansal and Erken, 1989) or by the simple failure of the underlying soil at the surface after the first pass. Ansal and Erken showed that when the threshold cyclic shear stress amplitude is exceeded shear strains initially increase at a low rate. The process of soil degradation due to cyclic loading begins to tell and the accumulation of shear strains accelerates until failure occurs. The accumulation of axle settlement was plotted on an arithmetic scale in Figure 4.20 and shows that, rather than accelerate, the fastest rate of settlement growth occurred in the first 15 passes and slowly declined during the rest of the test. This does not match the pattern of failure described by Ansal and Erken, but rather suggests that soil failure occurred immediately at the start of the test. Indeed, in the video still after 2 passes shown in Figure 4.25, degraded clay in the form of a slurry is clearly visible between the joints and along the near edge of the trackway which was not visible before the rolling vehicle began to move. It is important to note that the supply of water to the surface of the model (small volumes to replenish losses due to evaporation) could be controlled very precisely by means of a micrometer gauged valve. The water supply rates in both Tests 3 and 4 were kept the same to ensure they did not influence the formation of a slurry. This was borne out by the similar values of moisture content measured for the undisturbed regions of clay at the end of both tests. The use of two different test levels was not significant since both clays possessed the same stress state and the speed of the centrifuge was set to create precisely 38g radial acceleration at each test level.

The evidence suggests that a thin layer of surface soil beneath the trackway failed on the first vehicle pass. The negligible longitudinal bending stiffness of the trackway's articulated joints caused it to distribute the applied stress to the soil very inefficiently and is the most significant factor in its poor performance on soft soils. The shallow nature of the soil failure suggests micro-mechanisms were forming in the clay, rather than conventional deep-seated bearing capacity failures, as illustrated in Figure 5.5, due to contact stresses being concentrated beneath the joints. It is difficult to estimate the distribution of contact stress beneath the joint. The worst case would involve a 0.2mm (model scale) wide line load across the gap width and along the length of the joint, which would result in a mean contact stress from the rolling vehicle of 1386kPa. Assuming an undrained bearing capacity factor of $(2 + \pi)$, and $c_u = 22$kPa (Appendix B), the bearing capacity would be 113kPa. Therefore the worst case applied load is considerably in excess of this. The rolling vehicle load would distribute a mean contact stress of 113kPa along a 2.45mm (93mm at prototype scale) wide load strip along the length of a trackway panel. It is feasible that when the rolling vehicle was on a joint, its weight was distributed through a strip equal to or narrower than 2.45mm, thus causing immediate shallow-seated bearing capacity failure in the clay. As failure occurred under each joint in rapid succession, the individual micro-mechanisms would have rapidly merged to form one continuous surface shear zone.

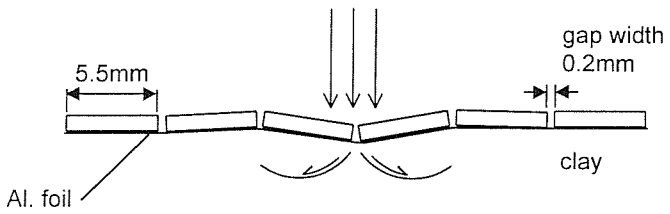

Figure 5.5: Possible mode of soil/trackway failure in Test 4

The accumulation of trackway deflexions was caused by the by-product of shearing, degraded slurry, being pumped away from the surface shear zone by the rocking action of trackway panels as the model vehicle passed over. Intact soil was exposed, which in

turn was degraded and either pumped through the joints or driven by the bow wave in front of the vehicle to each end of the roadway, eventually creating a large void in the underlying soil. The trackway deflected into this void since it did not possess the strength and stiffness to bridge it. Thus trackway strength only becomes significant in the later stages of soil/trackway failure, after the degradation of the underlying soil and during the build-up of permanent transverse deflexions. Trackway strength does not seem to be relevant in terms of initial failure of the clay and development of the slurry.

The contrasting performance of the jointed and unjointed trackway raises questions about some of the Georgiadis (1979) conclusions. Even though the major part of the load distribution is in the transverse direction, since this is stiffer, the poor distribution in the longitudinal direction cannot be ignored since this transmits high contact stresses to the soil through the joints. The tests indicate that it is not sufficient to model jointed trackway as individual, unconnected beams, since their performance would be equivalent to the unjointed trackway and would therefore miss the detrimental effect of the joint.

Given that the amount and shape of trackway deflexion depends largely on the deformed shape of the underlying soil, it is interesting to compare the build up of soil movements and trackway deflexions in parallel during the tests. The maximum trackway deflexion occurs directly beneath the loaded areas and in these regions of the highest applied stress, the underside of the trackway is always in direct contact with the soil. Therefore, the maximum vertical trackway deflexion provides a direct reflection of the maximum soil settlement. The maximum value of strain measured in the trackway is dependent on the degree of transverse bending at the location of the strain gauge. In Tests 1 and 2 the maximum value was always immediately outside the loaded areas and reflected the amount of transverse bending of the trackway at this location. Additionally, the strain value indicated whether the aluminium had reached its yield point (~0.002 strains); if yielding had extended through the full depth of the section, a plastic hinge would have developed, compromising the trackway's strength.

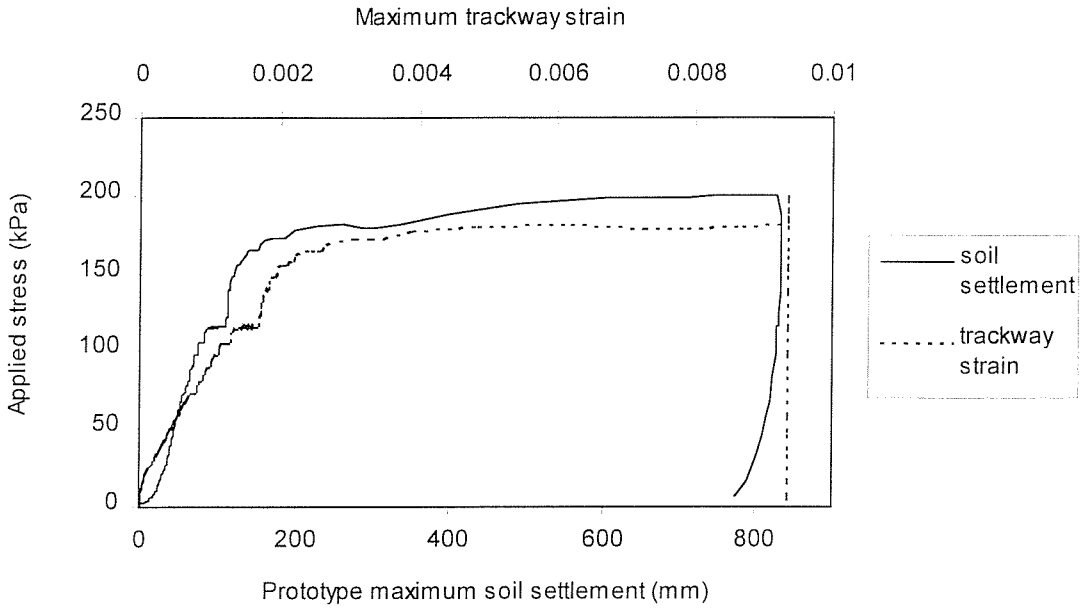

Figure 5.6: TEST1 Comparison of trackway strain and soil settlement

The maximum soil settlement and trackway strain during Tests 1 and 2 are compared in Figures 5.6 and 5.7 respectively. For Test 1 the settlement and strain are plotted against the applied stress to compare the reaction of the trackway and soil to load. The initially high rate of soil settlement was due to some bedding-in of the trackway but once this had ceased the growth of settlement and strain were very similar, with every step of applied stress being matched between the traces. After failure, the strain trace could not match the settlement trace because the strain gauge exceeded its recording range, but the two traces turn to the horizontal at the same value of applied stress. The aluminium in the trackway began to yield at a strain of about 0.002, but there was no evidence of a resultant compromise in trackway performance in either the value of strain or soil settlement. The trackway deformation continues to react continuously to the soil settlement.

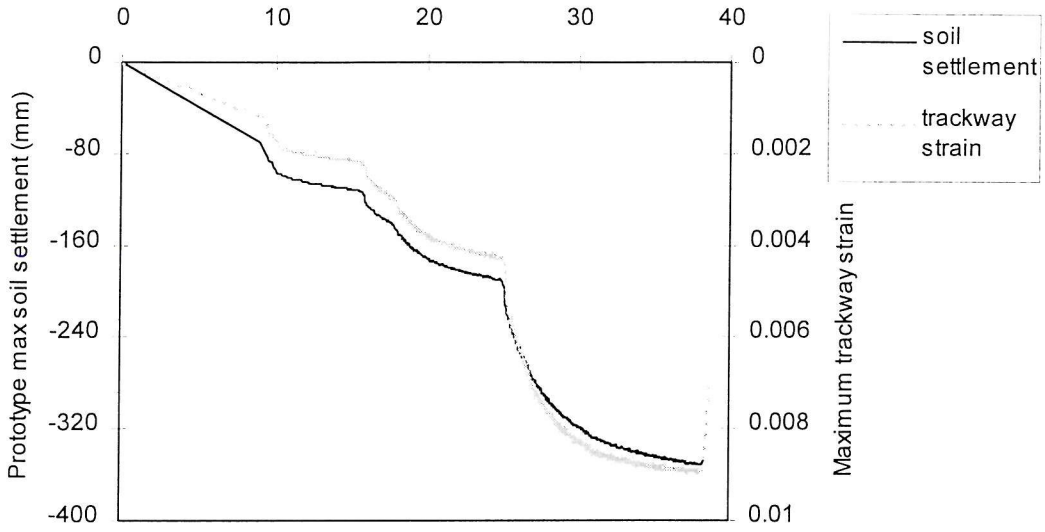

Figure 5.7: TEST2 Comparison of trackway strain and soil settlement

In Figure 5.7 the trackway strain and soil settlement during Test 2 are plotted against √time to compare their build up during the test in real time. Again, the traces are very similar, the growth of trackway strain corresponding with the characteristic consolidation profiles of the soil settlement. There is also no obvious change in the maximum displacement of the trackway following trackway yield. The trackway strain initially increases at a slower rate compared with the soil settlement but after 16 √hours it became steeper so that it crosses the soil settlement line by 27 √hours. This did not occur in Test 1, but can be accounted for by the greater soil uplift on each side of the trackway in Test 2 compared with Test 1, as noted in Section 4.4.2.

Figures 5.6 and 5.7 show that trackway deformation is intrinsically linked to the deformation of the underlying soil. Whether the soil consolidates, shears or compresses elastically, loaded trackway will react and deform according to the shape of the underlying ground surface. There is no evidence to suggest that transverse yielding of the trackway compromises its stiffness or transmits greater stress to the underlying soil. The increasing concentration of applied stress to the soil as the trackway deforms is likely to be a continuous process, as illustrated in Figure 5.8.

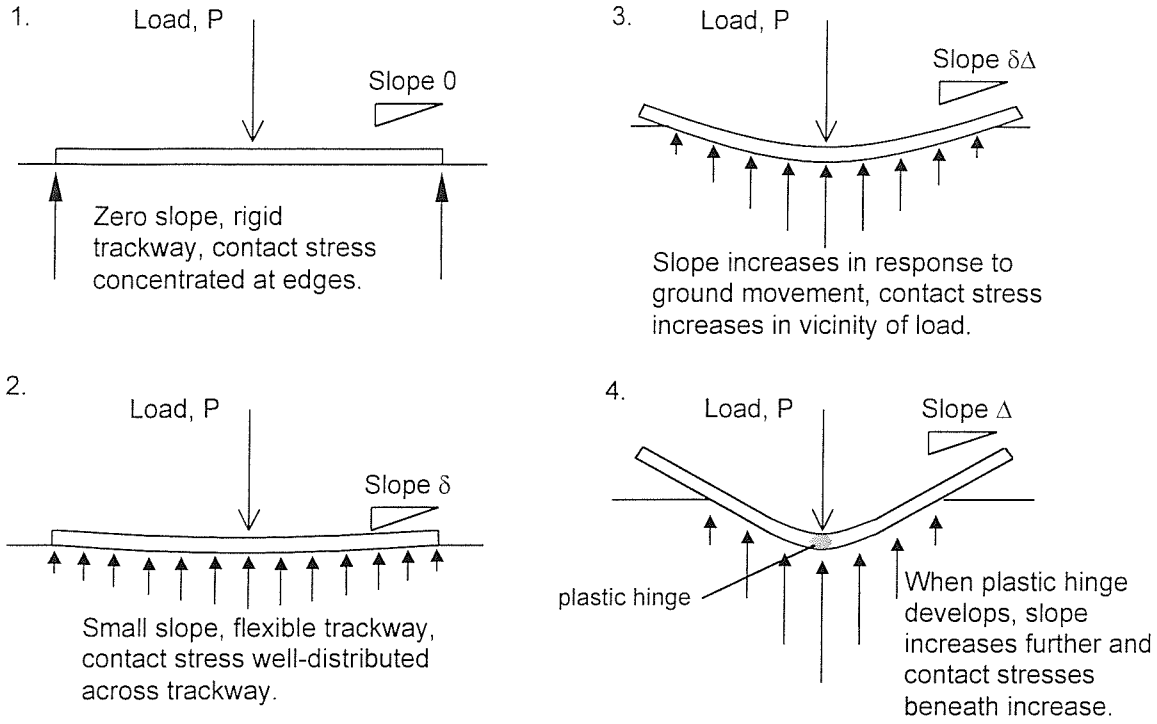

Figure 5.8: Effect of trackway slope on contact stress

Hemsley and Spence (1987) obtained exact solutions for the transverse flexure of a strip foundation in frictionless contact with an elastic half-plane. Numerical results in terms of slope and contact pressure are available for strip foundations of a given relative stiffness. They show that contact pressure between the strip foundation and the underlying homogeneous half-plane is directly related to the slope of the foundation as it flexes/deforms. Indeed, in their computations, the contact pressure is obtained directly from the foundation's slope. These findings can be applied directly to trackway in bending: the more it flexes, the less efficient it becomes at distributing the applied stresses to the soil (Figure 5.8). Yielding of trackway is therefore less significant, the concentration of applied stress, as suggested above, is a continuous process as the trackway bends, regardless of whether it yields.

The importance of the deflected slope of the trackway becomes more significant in the longitudinal direction and could explain the difference in performance between the unjointed and jointed trackways in Tests 3 and 4. The longitudinal slope of the unjointed

trackway beneath the rolling vehicle was small, therefore the contact pressure beneath the trackway was small. When the jointed trackway was loaded, the longitudinal slope, particularly when the rolling vehicle was positioned on a joint, would have been steep and the contact pressure beneath the joint would have been high, and possibly sufficiently high to cause failure of the soil. This would explain both the poor performance of the jointed trackway and the immediate appearance of slurry between the joints of the trackway.

The deflected slope of the trackway is determined by its flexural stiffness, leading to a direct relationship between trackway flexural stiffness and soil contact pressure. Hemsley and Spence (1987) presented the profiles of contact pressure for different relative foundation stiffnesses shown in Figure 5.9. These profiles are based on the plane strain flexure of a strip foundation subjected to a symmetrical pair of line loads positioned at 0.4 times the foundation half-width from the centreline, similar to the value of 0.42 in the centrifuge tests reported here. Figure 5.9 shows half-profiles from the foundation centreline at $\xi = 0$ to one edge at $\xi = 1.0$, with contact stress measured as a fraction of mean foundation contact stress, for various values of relative foundation stiffness, K_r.

$$K_r = \frac{E_1\left(1-\nu_2^2\right)}{E_2\left(1-\nu_1^2\right)}\left(\frac{h}{a}\right)^3$$

where h = thickness of foundation, a = half-width of foundation and subscripts 1 and 2 refer to the foundation and half-plane respectively.

The plane strain conditions, the use of a line load and the frictionless interface will tend to overestimate peak contact stresses compared with those generated in the centrifuge tests. However, despite this it usefully demonstrates the significance of trackway bending stiffness to its contact stress. In the case of class 60 trackway transverse stiffness, or the model trackway used in the centrifuge, if they were used on the centrifuge soil, their relative stiffness value, K_r, would be 0.002. This would produce an

elastic contact stress profile similar to the $K_r = 0.001$ case and shows the considerable concentration of stress beneath such a flexible foundation, reaching some 6 to 7 times the mean contact stress that would be expected beneath a rigid foundation. However, this occurs at the transverse trackway stiffness. In the longitudinal direction, the relative stiffness, K_r, of the trackway would be lower, particularly if the near zero stiffness of the articulated joints was taken into account. However, both are well outside the range of values presented by Hemsley and Spence.

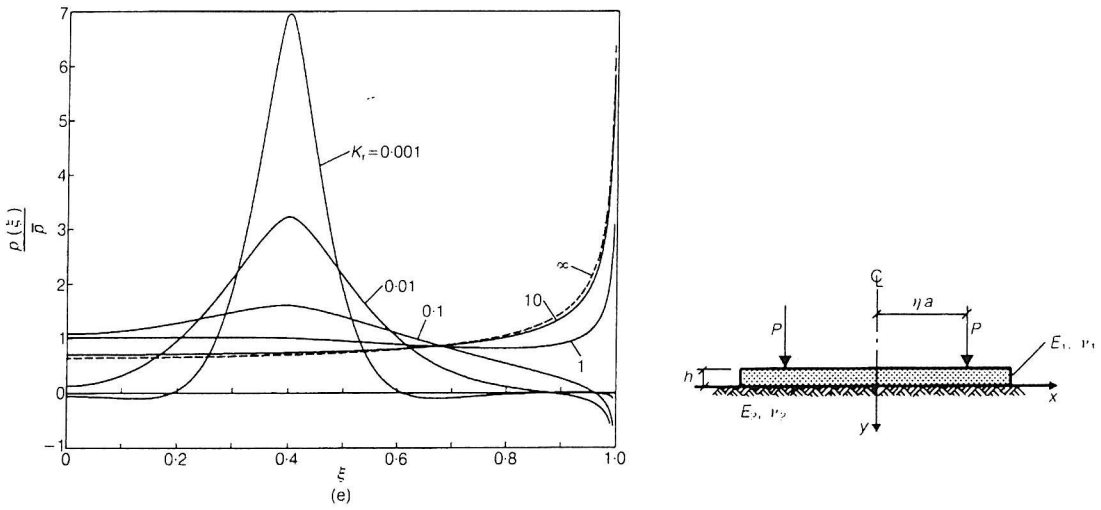

(Hemsley and Spence, 1987)

Figure 5.9: Contact pressures for foundations of different stiffnesses

Selvadurai (1979) presented an approximate method of analysis of loaded plates resting with frictionless contact on an elastic half-space. This allows point loads to be applied, rather than line loads, and, because of its relative simplicity, the stress response for different relative plate stiffnesses is straightforward to calculate. Again, since point loads are applied and the interface is frictionless, contact stresses may be overestimated compared with the centrifuge tests reported here, but the calculations do demonstrate the significance of trackway stiffness. The contact stress returned by two values of relative trackway stiffness are shown in Figure 5.10. Both are half-profiles from the trackway centreline at x = 0 to one edge at x = 2.3m, and are based on an equivalent point load

equal in magnitude to the prototype load from the DROPS vehicle wheel in centrifuge Tests 3 and 4. The relative stiffnesses used in the calculations were based on using the centrifuge model soil. The EI value of 78kNm^2/m is the transverse bending stiffness per metre width of class 60 trackway, the EI value of 1.03kNm^2/m is the longitudinal bending stiffness per metre width of a class 60 trackway panel.

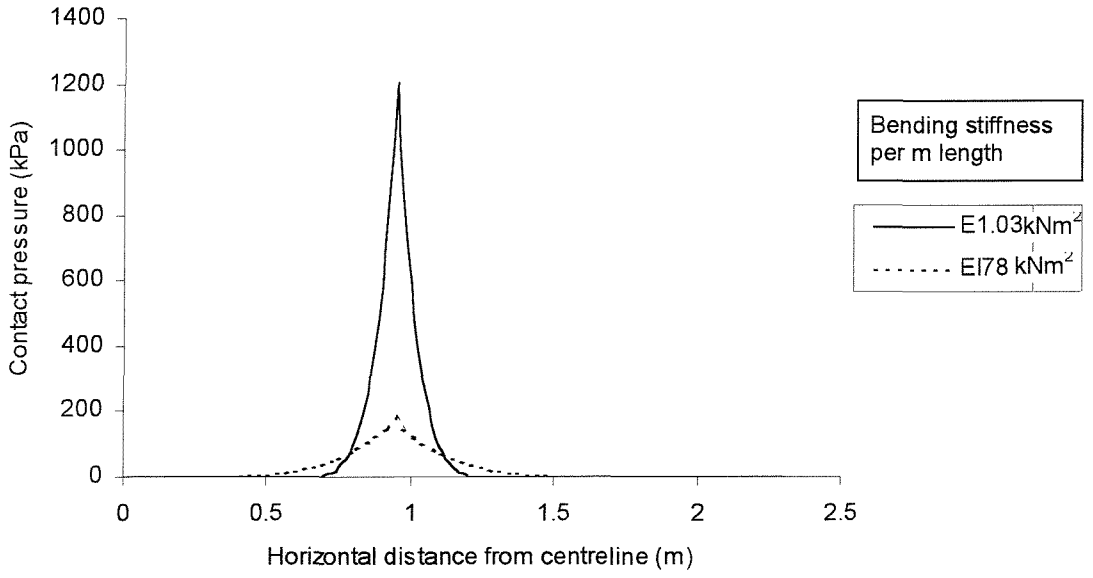

Figure 5.10: Elastic contact stress caused by two trackway stiffnesses

The 78kNm^2 profile compares well with the K_r = 0.001 profile in Figure 5.9, reaching a peak of 178kPa, equivalent to 7.4 times the mean contact stress based on a 1m^2 plate, compared with 7.0 in Figure 5.9. In Test 1, the plane strain applied failure stress was 180kPa. Bearing in mind the expected over-estimation of contact stresses using this method, the maximum stress of 178kPa beneath trackway of isotropic transverse stiffness should be below this failure stress and may account for the good performance of the unjointed trackway in Test 3.

The 1.03kNm^2 bending stiffness profile reaches a considerably larger peak of 1200kPa, well in excess of the failure stress of the underlying soil. The calculation method must break down somewhat at this very low value of relative stiffness because the areas under

each profile should be the same since the same total load was applied in each case. However, it serves to demonstrate the much higher stress concentrations caused by the lower longitudinal trackway stiffness. The lower bending stiffness contact stress profile ($EI = 1.03kNm^2$) assumes there are rigid joints between the trackway panels. It is difficult to estimate an equivalent longitudinal stiffness of jointed trackway but given that it would be lower than $1.03kNm^2$, and hence could transmit a contact stress in excess of 1200kPa beneath a point load of only 29kN, would account for the poor performance of the jointed trackway in Test 4. The immediate appearance of clay between the joints is unsurprising given this estimate of the contact stress.

It is clear from Tests 3 and 4 that the rocking action of the trackway joints plays a detrimental role in soil/trackway failure. In Test 4, the prototype scale joint spacing was 0.23m and the trackway performed poorly. In Test 3, the joint spacing was infinity and the trackway performed well. Between these two extremes a trend may exist relating increasing joint spacing with improving trackway performance. Further research would be required to obtain an equivalent stiffness value incorporating the trackway bending stiffness and the joint spacing.

The effectiveness of trackway depends primarily on an equivalent flexural stiffness in both the transverse and longitudinal directions. The effects of the differing longitudinal trackway stiffnesses in Tests 3 and 4 can also be illustrated by the comparison between the permanent transverse profiles shown in Figure 5.11. There were no permanent deflexions of the unjointed trackway measurable at the model scale at all. The jointed trackway had assumed a new permanent profile by the end of the test, with a maximum deflexion beneath the slurry of 340mm. As described above, the jointed trackway deformed into a longitudinal trough, with no permanent deflexion in the transverse direction. It is interesting to note that soil failure, which led to failure of the whole soil/trackway system, was brought about without material failure of the trackway. The poor distribution of applied stress by the jointed trackway caused failure of the underlying soil. The subsequent deflexion of the trackway was in direct response to the

deformation of the soil. The deflexion of trackway and its possible yielding, seem to be the effect rather than the cause of soil/trackway failure.

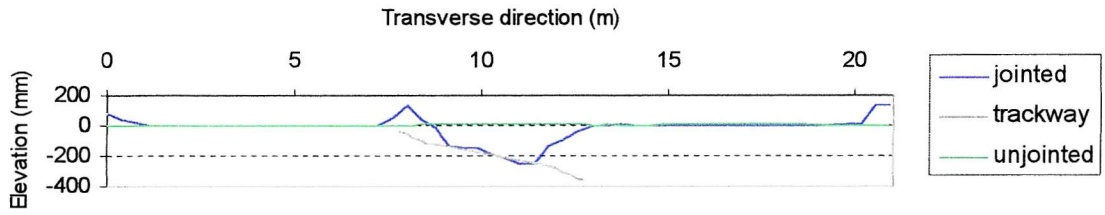

Figure 5.11: Comparison of final transverse profiles after Tests 3 and 4

5.2 Moisture contents

After Test 4, several samples of soil were taken from the model for moisture content tests, as described in Section 4.4.4. The results showed that the deposited clay slurry and a 3-4mm deep layer of soil beneath the trackway were considerably wetter than the surrounding intact soil. Assuming all the soil was saturated, the clay slurry was formed after a 14% increase in its in-situ volume. This increase in moisture content and the subsequent volume increase were characteristic of an overconsolidated clay in shear.

The formation of the thin surface layer of softened clay was a result of the shallow shear failure mechanisms described earlier in this chapter and illustrated in Figure 5.5. The motion of the vehicle would have caused shear planes to form in rapid succession beneath each joint and the softening zones associated with each would have quickly merged together to form a continuous layer of clay slurry. The dilation and softening of the clay occurred very rapidly because the slip zones were small and their dilations demanded only small volumes of water from the surrounding clay.

This softening associated with overconsolidated clays in shear was described by Schofield and Wroth (1968). From an investigation of a retaining wall failure, they presented the water content profile shown in Figure 5.12. The slip zone is only 5mm wide and the approximate 8% rise in moisture content in this zone is consistent with the

measured rise in the 3-4mm surface layer beneath the trackway in Test 4. Schofield and Wroth describe the by-product of the dilation in the slip zone as a "lubricating clay paste". The formation of a lubricating paste between the trackway and the intact soil would further deteriorate the trackway's effectiveness by reducing friction at the soil/trackway interface. This would also facilitate the driving of the clay paste, or slurry, to the ends of the trackway panels by the action of passing vehicles.

The measured moisture content values in Test 4 contrast well with those taken after Test1. Soil samples were taken from immediately beneath the trackway, either side of the trackway and from intact, undisturbed soil as described in Section 4.4.1. There were no significant differences between the moisture content values, the maximum range being only 1.4%. Large deflexions were imposed on the soil/trackway system and the soil certainly failed in shear. However, the slip zones described by Schofield and Wroth (1968) would have been deep-seated, as in a conventional bearing capacity failure, and their moist layers not detected by the moisture content samples taken at the surface.

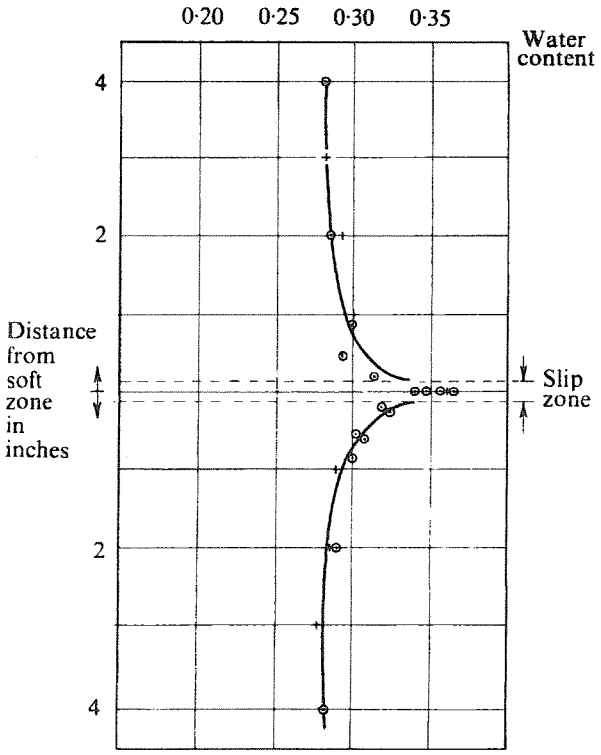

(Schofield and Wroth, 1968)

Figure 5.12: Observations of water content across a slip zone

In addition, the consistent values of moisture content of the undisturbed clay at the end of all the tests (Tables 4.2, 4.3 and 4.4) is demonstrable of a consistent method of sample preparation, producing a clay of similar void ratio each time.

5.3 Pore water pressures

The maximum contour value of excess pore pressure in Test 1, at the 115kPa applied stress, shown in Figure 4.7, was 22.5kPa. This was still the case when the applied stress was further increased to failure. The pattern of excess pore pressures at failure is characteristic of a deep-seated bearing capacity failure and confirms the findings of the trackway deflexion and moisture content results discussed above.

In cyclic Test 2, the same contour peak of 22.5kPa at a depth of 2.6m, but at a mean applied stress of 131kPa, was shown in Figure 4.14. After cycling for 740 prototype diffusion hours, this peak had increased to 27.5kPa. However, this value was calculated through the interpolation process in MATLAB, the maximum pore pressure transducer reading was still 22.5kPa, but a steeper gradient of excess pore pressure beneath the peak, due to excess pore pressure dissipation at the base, was interpreted by MATLAB as a rise in the peak. The possible over-estimation of the peak contour by MATLAB and the dissipation of pore pressures near the base, suggests that overall the excess pore pressures were dissipating rather than accumulating over this long stress cycling period. Below the Ansal and Erken (1989) threshold stress, described in Section 5.1, excess pore pressures do not develop. This provides further evidence to the deflexion data that the threshold cyclic shear stress was not reached in Test 2.

Wood (1982) conducted a comprehensive literature review of undrained cyclic laboratory tests carried out on clays. For each over-consolidation ratio there appeared to exist a threshold amplitude of cyclic loading below which failure would not occur. For a normally-consolidated clay above this threshold there was a steady upwards migration of pore water pressure to failure; for clays with an OCR of 4, there was a steady, but slower, accumulation of negative excess pore pressure until failure occurred through

softening. Neither of these phenomena were observed in Test 2, since excess pore pressures tended to dissipate from positive values rather than accumulate. It seems unlikely that the deep-seated whole vehicle stress cycling in Test 2 would lead to the migration of pore water pressure and failure described by Wood.

Tests 1 and 2 both exhibited large values of excess pore pressure due to the plane strain nature of the tests. Tests 3 and 4 achieved lower values because of the smaller, more localised applied stresses involved. In Test 3, using the unjointed trackway, the maximum excess pore pressure value was 7.5kPa and this occurred nearer the surface, at about 1.0m depth, because of the more localised nature of the vehicle load. As would be expected, since no accumulation of pore pressures was observed under the higher stresses in Test 2, no further development of pore pressure occurred over the 2200 passes of the model vehicle in Test 3.

In Test 4, the peak registered excess pore pressure was only 2kPa. The first row of pore pressure transducers, at a model depth of about 30mm, were not close enough to the soil surface to register the high excess pore pressures that must have occurred there. If a similar excess pore pressure zone to that recorded in Test 3 was concentrated in the top 1.5m layer of soil in Test 4, the magnitude of excess pore pressure must have been considerably higher. In concluding that the highest transient stresses in the soil were experienced near the surface, this confirms the interpretation of the moisture content data above. The jointed trackway was very ineffective at distributing applied stresses to the soil and caused them to be concentrated at the soil surface.

5.4 Conclusion

Analysis of the centrifuge model test data showed that soil/trackway failure could not be explained by the deep-seated effects of whole vehicle loads. The interaction between trackway and the soil surface was more significant, with a rolling vehicle on jointed trackway causing rapid degradation of the underlying soil.

Elastic methods of foundation analysis showed that the bending stiffness of trackway was one of the main determinants of its contact stress with the underlying soil. A method of incorporating joint spacing and stiffness into an equivalent value of trackway stiffness might allow contact stresses beneath jointed trackway to be calculated. In addition, trackway flexure depended primarily on the deformation of the underlying soil.

Moisture content data showed that jointed trackway interacts directly with small-scale slip zones in the soil. These slip zones formed on the first pass of the rolling vehicle because of the poor distribution of applied stress through the trackway joints. The softening of the clay within these slip zones caused a lubricating slurry to form which accentuated the movement of the joints. The degraded slurry was driven out by the action of the rolling vehicle to expose intact soil which was in turn degraded, eventually forming voids beneath the trackway, causing the trackway to deform further.

Chapter 6

Finite Element Analysis Procedure

6.0 Introduction

The results of a series of CRISP finite element analyses, in which it was attempted to model the trackway centrifuge tests, are presented. The suitability of the input parameters used is discussed with reference to the centrifuge test results.

6.1 Finite element model

The principle of the finite element method is to approximate a structure or material to be analysed by dividing it into a number of elements joined by nodes. Polynomials are then used to describe the variation of a variable such as stress or strain within each element.

The most common approach, the displacement method, involves expressing the displacement inside each element as a polynomial function of the displacement at the nodal points and the position of the element. The condition of compatibility is then used to obtain the strains inside the element from the nodal displacements (Zienkiewicz, 1967). In order to determine the stresses inside the elements in terms of the nodal displacements, the stress-strain relationship for the material (D-matrix) is used. Then, in order to determine the equivalent nodal forces which are in equilibrium with this state of internal stress, the principle of virtual work is applied. The nodal forces should balance the loads due to self-weight and boundary stresses. Full details of this method can be found in Britto and Gunn (1987).

With care it should be possible to discretize any irregular geometry into a continuum of small regular elements such as triangles and quadrilaterals. Having done this, it will then be possible to solve most boundary value problems, even though a closed-form analytical solution may not be available. A further advantage of finite element methods is the comparative ease with which non-homogeneous and anisotropic materials such as soil can be modelled.

6.2 Finite element program SAGE CRISP

CRISP (CRItical State Programs) is a suite of finite element programs developed principally for soil mechanics. SAGE CRISP was launched in 1995, using a new Microsoft Windows based mesh generator and graphical post-processor interface (for two-dimensional problems), but essentially retaining the same program capabilities as

the CRISP 94 DOS version. It has been written and developed by numerous research workers since 1976, most notably by Britto and Gunn (Britto and Gunn, 1987) since 1977. As the program name suggests, its most significant feature is the incorporation of the critical state concepts of soil mechanics into a finite element program.

Since the program has been written as a research tool, with the structure of the program such that amendments to the program can be easily implemented, many variations of the program exist. In its basic form the program can perform drained, undrained or time-dependent static problems of two-dimensional plane strain or axi-symmetric and three-dimensional problems. The soil models that are available include anisotropic elasticity, non-homogeneous elasticity (properties vary with depth), elastic-perfectly plastic models incorporating various yield criteria and critical state based models.

For strains which vary linearly within an element, 6 noded triangles and 8 noded quadrilaterals are used (with additional pore pressure nodes available). To model soil/structure interaction effects, an interface element is available, together with discrete bar and beam elements. For three-dimensional analyses only a 20 noded linear strain brick element can be used.

CRISP uses an incremental or tangent stiffness approach to model the non-linear stress-strain response that characterises soil. For this reason the change in the loading of the soil due to some event such as a vehicle load, is divided into a number of smaller increments and the program applies each of these incremental loads in turn. In order to limit the output (particularly voluminous when using the double precision version of CRISP) and the computational time taken for each analysis, a balance has to be made between the numbers of elements and loading increments. In each increment the stiffness properties appropriate to the current stress level are used in the computation.

Since CRISP uses a small-strain/small displacement approach, it is not suitable for large deformation analysis, although this is partially provided by the co-ordinate update

option. This adds to the co-ordinates the displacements undergone by the nodes during the increment and uses these new co-ordinates during the next analysis increment.

A major advantage of using CRISP is its ability to model consolidation during an analysis by introducing the pore water pressure as an extra unknown. For this, consolidation elements (which have additional nodes to deal with this extra degree of freedom) must be used. For a consolidation analysis, time increments are specified, which allow loading sequences to be modelled in real time.

CRISP is unsuitable for stress cycling or dynamic problems in its present form, nor is it capable of analysing partially saturated soil conditions.

6.3 Selection of CRISP soil model

It was considered desirable to model class 60 trackway use at prototype scale, i.e. in a block of clay 12m deep and 21m long, with the trackway placed centrally on the clay surface. The soil was modelled using a behavioural regime proposed by Schofield (1980) which incorporates the Cam-clay yield surface on the wet side of critical state and the Hvorslev surface and a no-tension cut-off on the dry side. Heavily over-consolidated clays will generally fail by the formation of ruptures associated with dilation and softening. Hvorslev (1937) found that within a certain range of effective normal stress, the shear stress on these rupture planes increased approximately linearly with the effective normal stress. Since Cam-clay and modified Cam-clay over-predict the yield stress for soils in this over-consolidated region, it was suggested by Schofield and Wroth (1968) that the Hvorslev surface defined a region of failure in the soil that cut across the Cam-clay state boundary surface.

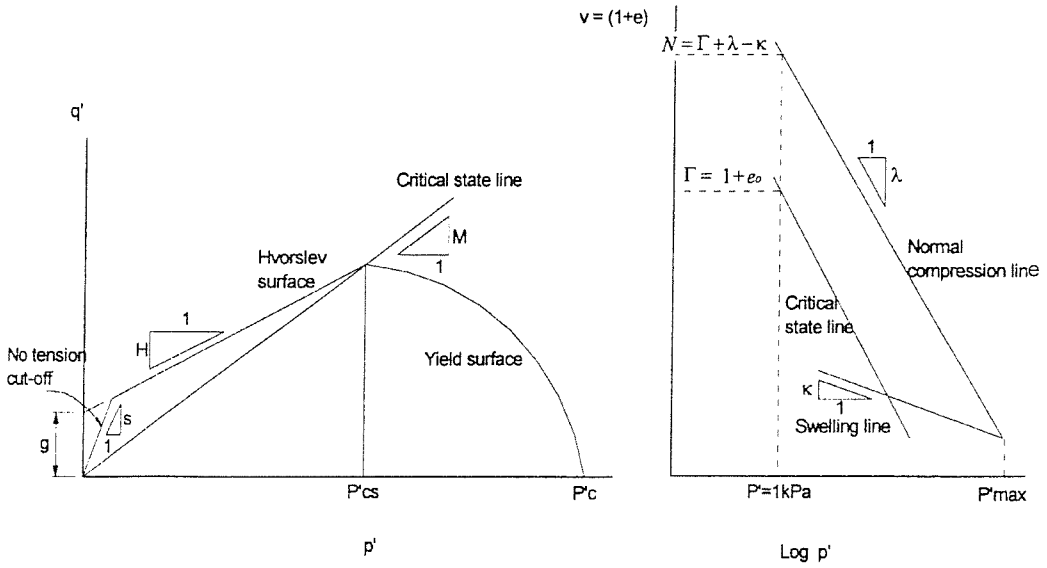

Figure 6.1: Schofield soil model

The Schofield model is an elasto-plastic soil model which requires three parameters to describe the state of the soil. These are the effective mean normal stress, p′, the deviatoric stress, q and the specific volume, υ. Many real soils may be modelled provided that appropriate parameters are chosen. With reference to Figure 6.1, equations for the various lines in υ-ln p′ space are:

Isotropic normal consolidation line:

$$v = N - \lambda \ln p' \qquad 6.1$$

where $N = \Gamma + \lambda - \kappa$.

Critical state line:

$$v = \Gamma - \lambda \ln p' \qquad 6.2$$

Isotropic swelling line:

$$v = v_\kappa - \kappa \ln p' \qquad 6.3$$

The yield surface for the Schofield model is the same as that for Cam-clay provided that $p'/ p'_{cs} > 1$. This corresponds to an OCR on p′ of up to 2.3. If the normality condition applies, the yield surface for the Cam-clay model can be found by applying the flow rule and the normality condition of plasticity theory (i.e. plastic strain increment vector is normal to the plastic potential) and the equation is:

$$q = M\, p' \ln(p'_c / p') \qquad 6.4$$

If $p' < p'_{cs}$ then rupture will occur which is governed by the Hvorslev failure criterion. In the finite element formulation, however, the Hvorslev stress state is treated as a yield surface.

The Schofield model models the soil isotropically and makes no attempt to model the recent stress history of the clay sample. Soil anisotropy has a significant effect on its small strain stiffness and considerable work has been undertaken to investigate the relationship between small strain stiffness and the recent stress history of soils. These effects can be modelled using the three surface model (Stallebrass, 1990), the non-linear ground model (Jardine et al, 1991) and the brick model (Simpson, 1992). However, the soft clay in the centrifuge model tests was subjected to large yield strains in the vicinity of the loaded trackway and the non-linearity of the small elastic strains was not considered to be significant.

Al-Tabbaa (1987) and others have showed that the yield locus for one-dimensionally consolidated Speswhite kaolin is not symmetrical about the p′ axis but has an inclined axis of symmetry in q- p′ space, indicating stress-induced anisotropy. Richards (1995) described the Sharma method of modelling a soil in an anisotropic stress state using the Schofield model. However, it is not straightforward, and involves changes to the CRISP program including defining the horizontal and vertical permeabilities as functions of the current void ratio based on relationships suggested by Al-Tabbaa (1987).

It was decided, therefore, to model the centrifuge tests using the Schofield model in the standard version of CRISP. Emphasis was placed on producing a straightforward analysis using a standard soil model, and one set of soil parameters to model all stages of the test, particularly bearing in mind the likely use of the models by other parties.

6.4 Slip elements

Slip elements are used to allow slip to occur between materials having a large difference in their stiffnesses, for example, aluminium trackway overlying soft clay, whose deformed responses to any applied load would differ significantly. It would be possible to use ordinary linear strain quadrilateral elements with appropriate values of stiffness, but the interface element allows the use of slender elements without the need to refine the mesh. CRISP provides the Goodman interface element, using the basic finite element code by Ghaboussi et al (1973), which limits the shear stress along it to a user-specified interface shear strength. The Mohr-Coulomb yield criterion is used to check whether the shear stress exceeds the maximum shear strength. If so, the shear modulus reverts to a user-specified residual value for the calculation of element stiffness. Checks are also performed on whether the element has gone into tension. If so, both the normal and shear stiffnesses are multiplied by a factor of 1/10 000 so that the element simulates separation.

The nodal co-ordinates for the two-dimensional slip element are the same for the two rows of nodes along the length dimension of the element. The element thickness is specified by the user and is used in the calculation of stiffness.

Hitherto, the stresses at the interface have been calculated as total stresses only. Since the slip element had no pore pressure nodes it could only be used between non-consolidating elements. This would have been very restrictive in these analyses, particularly in view of the large degree of consolidation occurring in the plane strain centrifuge tests, and thus the need for a two-dimensional 'effective stress' slip element was identified.

Consequently, a two-dimensional 'effective stress' element was developed by the CRISP Consortium. It is the same as the traditional 'total stress' element, except that it allows for the presence of two pore pressure nodes on one side. Only two were necessary since it was unlikely a slip element would be required between two consolidating materials.

The excess pore pressure variables for these nodes belong to the neighbouring consolidation element and a search is performed to identify the adjacent consolidation element properties. The normal and shear stresses are calculated in the normal way without pore pressure. The effective normal stress is used in the Mohr-Coulomb yield criterion to check whether the shear stress has exceeded the shear strength. Pore pressure is then added to the normal stress if the slip element is in compression so that the correct normal forces are calculated. The element geometry is shown in Figure 6.2.

Previously, the Goodman slip element was only available in CRISP in two-dimensions, which was detrimental to the validity of soil/trackway analyses which lacked slip elements when in three dimensions. Therefore, a three-dimensional slip element was also developed by the CRISP Consortium for this research. It is similar to the 20-noded 'brick' element except that the nodal co-ordinates are the same in the upper and lower faces of the element. The element is planar in the x-z plane and the thickness, or height, is user-specified as for the two-dimensional element. The calculation of normal and shear stresses, shear strains and the use of the Mohr-Coulomb yield criterion are all carried out in the same way as for the traditional two-dimensional 'total stress' element described above. The element geometry is shown in Figure 6.3.

Full details of the slip element development and calibration examples are given in Rahim (1998).

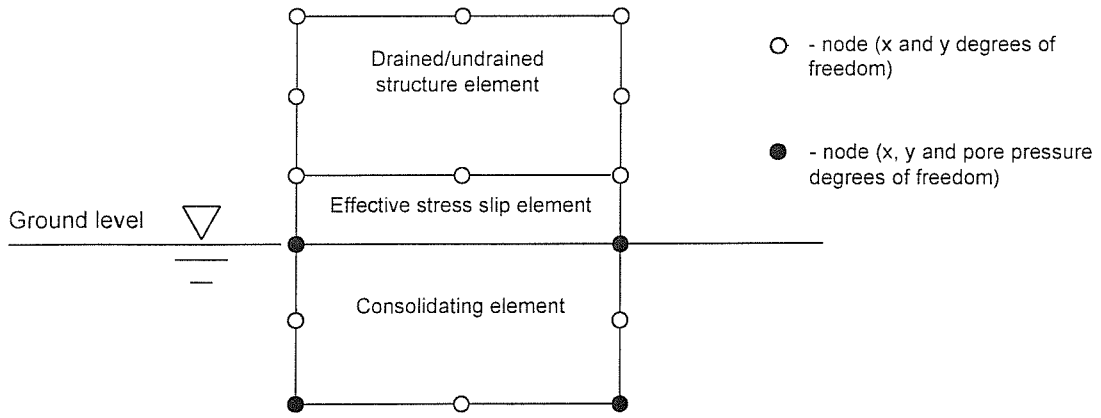

Figure 6.2 Two-dimensional 'effective stress' slip element geometry

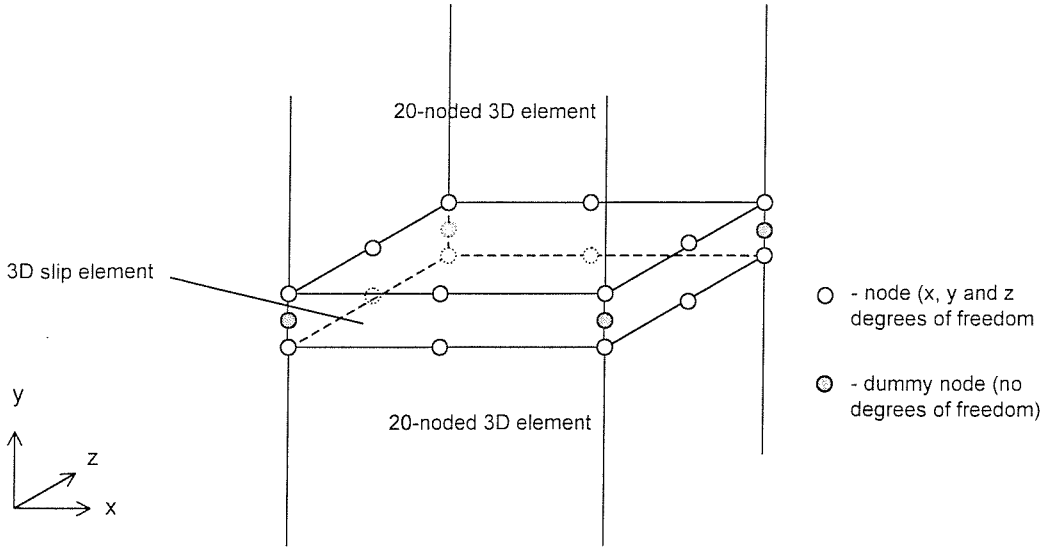

Figure 6.3: Three-dimensional slip element geometry

An evaluation of the new slip elements is made in the interpretation of the finite element analyses later in this chapter.

6.5 Large strain formulation

Conventional finite element formulations assume that the deformation is small and that changes in mesh geometry do not affect the stiffness or resulting displacements and stresses. The failure of trackway on soft clay involves significant changes in mesh geometry whose effects on soil stiffness and displacements cannot be ignored.

It is possible in CRISP to analyse large displacements by requesting the nodal co-ordinates to be updated after each increment of the analysis, by adding to the co-ordinates the displacement undergone by the nodes during the increment. The stiffness matrix of the continuum is then calculated with respect to these new co-ordinates during the next analysis increment. Using this process, at the end of the analysis, equilibrium will be satisfied in the final, deformed model. Although this approach is more appropriate for the large deformations involved in soil/trackway failure, it does not

constitute a rigorous treatment since it does not account for changes in stresses due to rotation of the initial stress field.

Since accounting for stress field rotation would be relatively straightforward, a new simple algorithm was developed by the CRISP Consortium for this research, in which stresses are updated in each iteration by accounting for rigid body rotation.

Rate terms of stresses and strains were used and are equivalent to incremental stresses for a static analysis.

Decomposition of stresses:

The rate of Cauchy stress $\{\dot{\sigma}\}$ can be considered to be the sum of two parts as follows:

$$\{\dot{\sigma}\} = \{\overset{\nabla}{\sigma}\} + \{\dot{\sigma}_g\}$$

where $\{\overset{\nabla}{\sigma}\}$ is the Jaumann rate of Cauchy stress or the stress due purely to stretching or shearing.

$\{\dot{\sigma}_g\}$ is the rate of change of stress due to the rotation of the initial stress field, as would occur with a rigid body motion.

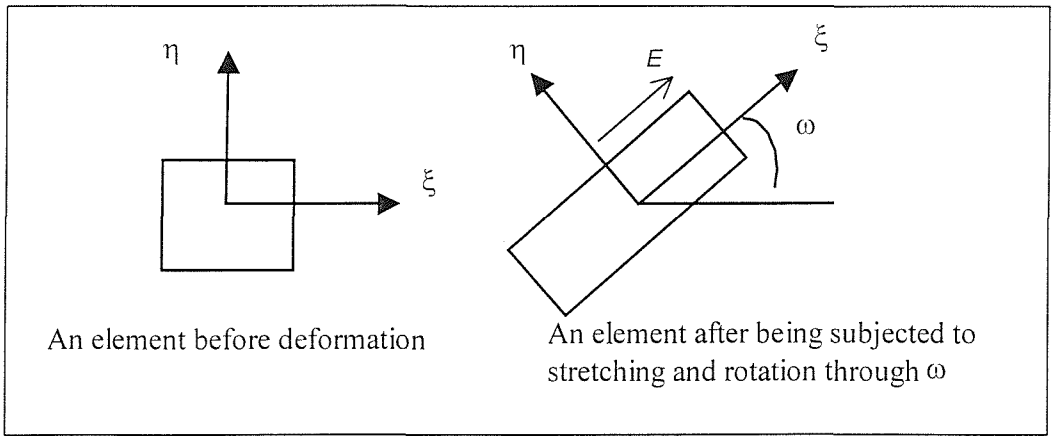

Figure 6.4: Rotation of stress field

The Jaumann rate of Cauchy stress is defined as:

$$\overset{\nabla}{\{\sigma\}} = [D]\{\dot{\varepsilon}\}$$

where [D] represents the constitutive relationship and $\{\dot{\varepsilon}\}$ consists of the rate of strain.

The rate of change of stress due to rotation, $\{\sigma_g\}$, for plane strain case is given as follows:

$$\{\sigma_g\} = \begin{Bmatrix} -2\tau_{xy}W_{xy} \\ 2\tau_{xy}W_{xy} \\ -W_{xy}(\sigma_y - \sigma_x) \end{Bmatrix}$$

Where $\sigma_x, \sigma_y, \tau_{xy}$ are the total stresses at the start of increment, and W_{xy} is rate of spin or rotation which is the product of the derivatives of the shape functions multiplied by the incremental displacements as follows:

$$W_{xy} = \left\{ \frac{\partial N_i}{\partial x} \quad \frac{\partial Ni}{\partial y} \quad i = 1, nnode \right\} \begin{Bmatrix} u_i \\ v_i \\ i = 1, nnode \end{Bmatrix}$$

In conventional small deformation, it is assumed that the terms in $\{\sigma_g\}$ are very small in comparison to the terms in $\overset{\nabla}{\{\sigma\}}$ and hence can be ignored.

Solution method:

1-After displacements are calculated in CRISP, the incremental stresses $\overset{\nabla}{\{\sigma\}}$ are calculated using the usual constitutive relationship.

2-The spin tensor is then evaluated, and the stresses due to rotation $\{\sigma_g\}$ are calculated.

3-The Jaumann rate of stress $\overset{\nabla}{\{\sigma\}}$ is then added to the stress due to rotation $\{\sigma_g\}$ to obtain $\{\dot{\sigma}\}$. These final incremental stresses are then added to the initial incremental stress value and the material is checked for yield. If the new total stresses exceed the yield

limit, stresses are brought back to the yield surface after accounting for plastic deformation.

4- The nodal co-ordinates are updated by adding the displacements to the current co-ordinates.

5- Force residuals are calculated and convergence is checked.

6- Solution is repeated as above for the next increment, or iteration if convergence needs to be satisfied.

Full details of this method and calibration examples are given in Rahim (1998a).

At present, this method is only available in two-dimensional analyses, which was not a significant drawback in this research since large soil displacements only occurred in the plane strain analyses.

The large strain formulation is evaluated in the interpretation of the finite element analyses later in this chapter.

6.6 Two-dimensional plane strain analysis

6.6.1 Selection of elements and number of load increments

The mesh used in the analyses, shown in Figure 6.5, comprised 888 linear strain triangular elements. The trackway was modelled using 76 linear strain quadrilateral elements which, since aluminium trackway is impermeable, did not require pore water pressure nodes. Two-noded slip elements were placed between the trackway elements and the underlying soil elements. The mesh was constructed to have smaller elements concentrated beneath the trackway, particularly beneath loaded areas, where the most significant changes in stress and strain in the soil due to applied loads were expected to occur.

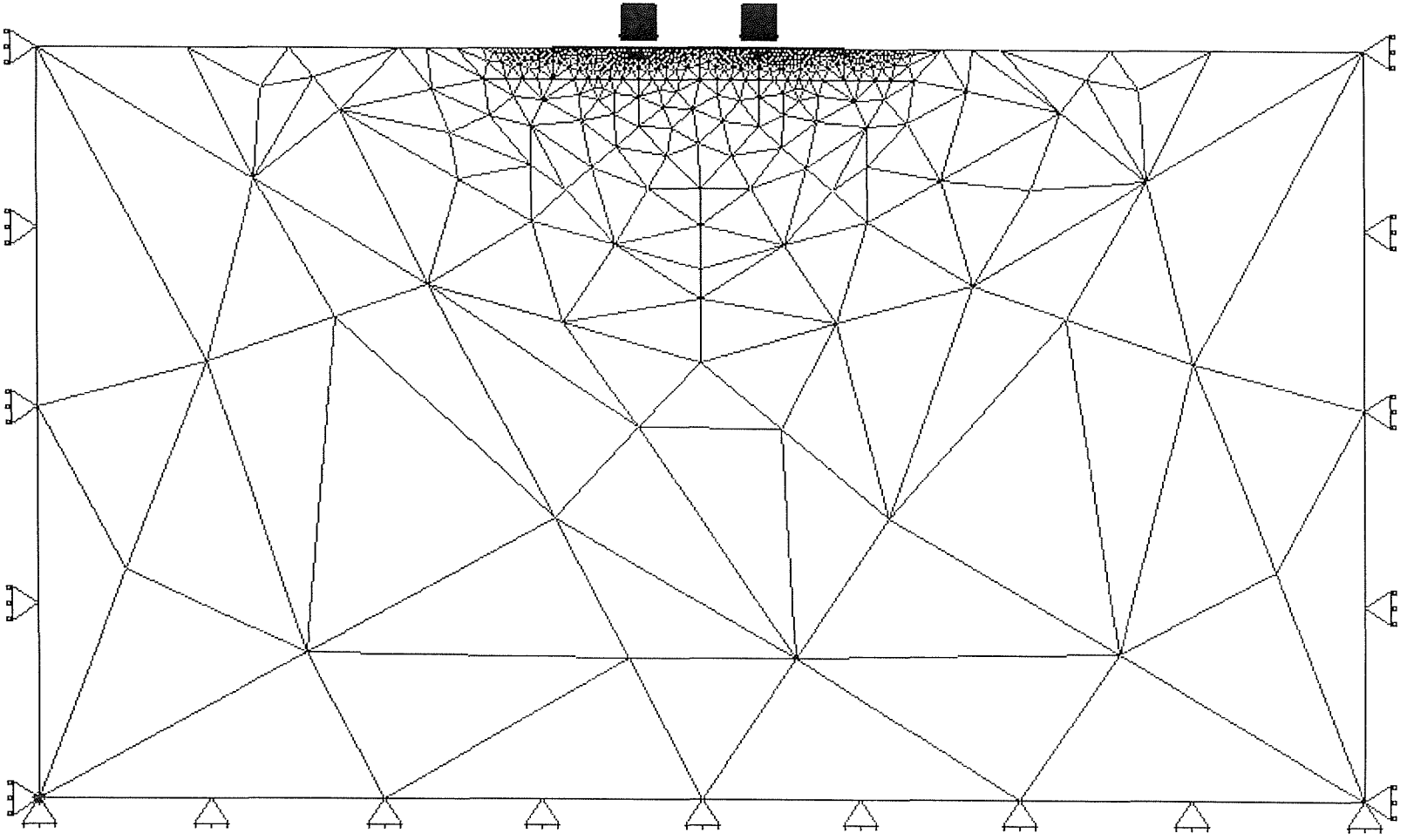

Figure 6.5: Two-dimensional finite element mesh, applied loads & boundary conditions

In all analyses, two load strips, each representing a DROPS vehicle tyre width and spacing, were applied on to the trackway. In a similar fashion to centrifuge model *Test 1*, the applied stress was initially increased to 115kPa over a period of 140 hours. This was achieved over a single increment block of 60 equal load and time increments. The applied stress remained constant for 944 hours over a second increment block of 20 equal time increments. During the third increment block of 200 equal load and time increments, the applied stress was further increased over a period of 133 hours to 150kPa. At an applied stress of 150kPa, soil strains began to increase more significantly and a higher stress could not be applied without significant equilibrium errors and numerical instability. Unfortunately, the entire *Test 1* procedure could not be replicated in the finite element analysis for this reason. Considerable time was taken to optimise the number of increments in each block by increasing their number until there were no further significant differences in the results. Since the only real effect of increasing the number of increments over those described above was to increase the size of the output files, it was decided to perform all analyses using this increment configuration.

6.6.2 Idealised geometry

The centrifuge model tests carried out in this research were all symmetrical about the centre line and it would have been feasible to construct a finite element mesh representing one half of a cross-section through the centrifuge model. However, to improve the visualisation of model behaviour and to aid comparisons with the centrifuge model data, both halves of the model at prototype scale were analysed.

The idealised geometry, shown in Figure 6.6, approximates the centrifuge model as a 21m wide x 12m deep sample of soil, with the lower horizontal boundary to the mesh being set at the bottom of the strongbox. The dimensions and position of the trackway match the prototype scale centrifuge values exactly and hence replicate the true behaviour of class 60 trackway in the same way as described in Section 3.7.1. The nodes along the base of the mesh were modelled as fully pinned. The boundaries at the sides of

the mesh were modelled as being restrained in the horizontal direction only. The analyses commenced with only the soil in place, the trackway and slip elements being placed in a subsequent increment block.

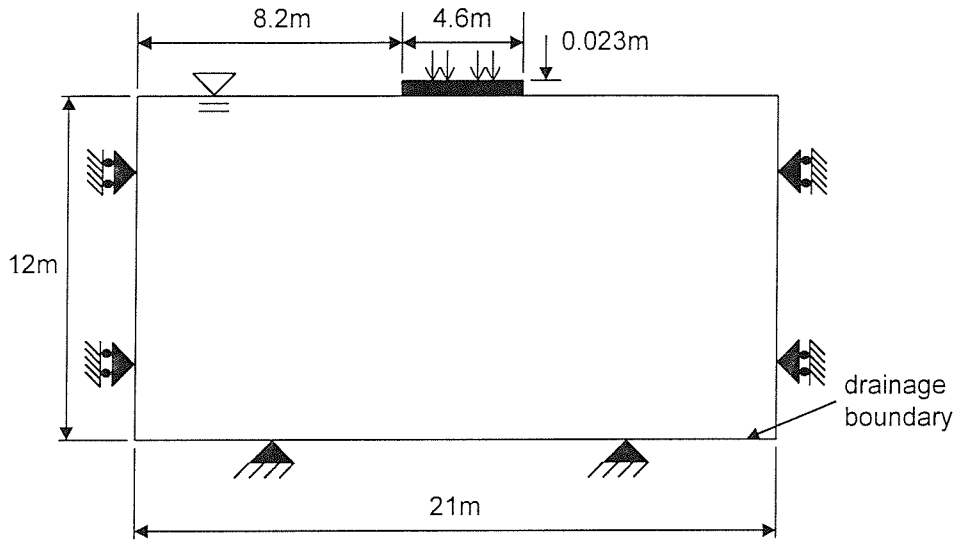

Figure 6.6: Idealised geometry of two-dimensional FEA model

6.6.3 Selection of input parameters

A lot of work has been carried out determining soil parameters for Speswhite kaolin. The input parameters for the Schofield model used by Richards (1995) and Li (1990) were adopted for the finite element analyses in this project. Since the analysis is of a plane strain nature, adjustments needed to be made to parameters derived from conventional triaxial tests. In cylindrical triaxial tests the intermediate principal stress, σ_2, equals the minor principal stress, σ_3. However, in plane strain conditions, $\sigma_2 > \sigma_3$, causing strength criteria to differ from those derived from cylindrical triaxial tests. Since the Mohr-Coulomb yield criterion, defined as:

$$\sigma'_1 - \sigma'_3 = \sin\phi'.(\sigma'_1 + \sigma'_3)$$

is not influenced by the value of σ_2, it is valid for both triaxial tests and plane strain conditions. Specifying a critical state cone that touches the Mohr-Coulomb surface ensures its yield locus is valid in plane strain conditions. Consequently, the values of M, H and S were reduced from their triaxial values to 0.65, 0.59 and 2 respectively so that the critical state cone touched the Mohr-Coulomb surface corresponding to plane failure conditions (Bolton et al, 1989). However, when 0.59 was used as the slope of the Hvorslev line, the soil appeared to exhibit an overly-stiff and strong response compared with the centrifuge tests and the analysis was susceptible to large equilibrium errors. Near the surface, where mean effective stresses are very low, soil is very weak and the occurrence of high stress ratios caused by a Hvorslev line with a slope of only 0.59 gave the soil an unrealistically strong surface layer. It is possible that the use of the large strain formulation in the analysis accounted for the stiffer load-deflexion response of the soil near failure, and substituting a standard small-strain formulation caused an overly-flexible response and greater analysis instability. It was felt that a larger value of H of 0.64 would stabilise the analysis and keep stress ratios low near the soil surface; in addition, it errs on the conservative side. The horizontal and vertical permeability values were the mean of those obtained directly from permeability tests carried out on samples of the centrifuge model clay after the tests. The slightly higher value of vertical permeability ($1.0\text{x}10^{-9}$ m/s) compared with the value used by Richards ($0.66\text{x}10^{-9}$ m/s) reflects the higher maximum consolidation stress used in the preparation of his clay samples. As does the lesser degree of anisotropy in permeability values. The bulk unit weight of soil, measured using soil samples taken from the centrifuge model tests, was taken as 16.66kN/m^3. Details of the soil parameters are given in Table 6.1.

Slope of one-dimensional compression line in υ-lnp' space	$\lambda = 0.25$
Slope of unload/reload line in υ-lnp' space	$\kappa = 0.05$
Specific volume (and void ratio) on critical state line at p'=1kPa in υ-lnp' space	$\Gamma = 3.48$ ($e_0 = 2.48$)
Slope of critical state line in q-p' space	$M = 0.65$
Poisson's ratio	$\nu' = 0.33$
Unit weight of water	$\gamma_w = 9.81$ kN/m^3
Bulk unit weight of soil	$\gamma_{bulk} = 16.66$ kN/m^3
Permeability in vertical direction	$k_v = 1.0\text{x}10^{-9}$ m/s
Permeability in horizontal direction	$k_h = 1.5\text{x}10^{-9}$ m/s
Slope of Hvorslev surface in q-p' space	$H = 0.64$
Slope of no-tension cut-off in q-p' space (for plane strain conditions)	$S = 2$
Permeability in vertical direction for tensile fracture region	$k_y = 1.0\text{x}10^{-7}$ m/s
Permeability in horizontal direction for tensile fracture region	$k_x = 1.0\text{x}10^{-7}$ m/s

Table 6.1: Soil parameters used in finite element analyses

A significant degree of yielding occurs in the trackway material during failure. CRISP provides an elastic-perfectly plastic model which, as the name implies, generates a wholly elastic response until a yield surface is encountered. After which the material experiences only plastic yielding with no hardening or softening of the yield surface. Several different yield criteria are provided, with Von Mises, a yield criterion for ductile materials, being the most suitable for the aluminium alloy trackway material. Since yielding of ductile materials is due to shear stresses causing slippage between layers in the material, the Von Mises yield criterion is appropriately based on shear stress. It states that yield will occur when the root mean square maximum shear stress in a general state of stress equals the root mean square maximum shear stress at yield in a simple tension test (root mean square values are used to take into account shear stresses on planes at right angles to that of the absolute maximum). Since the maximum shear stress

in uniaxial tension is simply half the value of normal yield stress, the failure criterion can be defined using only the tensile yield stress of the material. In CRISP, the yield criterion is specified in τ-σ' space, therefore it is defined as a 'cohesion intercept', C at $\sigma'=0$, which is equivalent to half the tensile yield stress.

Young's modulus	$E = 37.6 \times 10^6$ kN/m^2
Poisson's ratio	$\nu = 0.3$
Cohesion (half tensile yield stress)	$C = 34.2 \times 10^3$ kN/m^2
Bulk unit weight	$\gamma_{bulk} = 26.7$ kN/m^3

Table 6.2 Trackway material parameters used in finite element analyses

The trackway material parameters used in these analyses were derived from a finite element calibration analysis simulating the model trackway calibration test described in Section 3.7.1. This analysis was a good approximation of the model trackway behaviour and its material parameters, detailed in Table 6.2, were used in all the analyses described in this chapter.

The slip element material parameters were more difficult to define because they could not be derived directly from measured quantities. It was found from successive parameter analyses that a normal stiffness, k_n, comparable with the trackway Young's modulus was required to form a stable boundary between soil and trackway and to eliminate horizontal equilibrium errors. The shear stiffness, element thickness values and frictional strength of the soil/trackway interface were chosen after many trial analyses to give the interface good stiffness and stability while still allowing slippage to occur under significant applied stresses. It was important not to create an interface that was too flexible, leading to excessive movement of the trackway and an unrealistic representation of a relatively well bonded interface in the prototype. The parameters detailed in Table 6.3 were used in all the analyses described in this chapter. They were found to produce very similar soil/trackway behaviour to that observed in the centrifuge tests. However, the model's behaviour was not very sensitive to the slip element material

parameter values chosen compared with the soil and trackway parameters, and minor changes to the values in Table 6.3 had no significant effect on the analysis.

Cohesion	$C = 0$ kN/m^2
Angle of friction	$\phi = 15°$
Normal stiffness	$k_n = 3.0 \times 10^7$ kN/m^2
Shear stiffness	$k_s = 5.0 \times 10^3$ kN/m^2
Residual shear stiffness	$k_{s\,res} = 1.0 \times 10^3$ kN/m^2
Thickness of slip element	$t = 0.01$m

Table 6.3: Slip element parameters used in finite element analyses

6.6.4 In-situ stress state

In common with the centrifuge model tests, the stress history of the kaolin sample was assumed to comprise one-dimensional compression to a maximum vertical effective stress of 106kPa followed by unloading to equilibrium effective stresses at the end of the re-consolidation phase in the centrifuge. The initial "in-situ" lateral effective stresses, corresponding to the end of re-consolidation in the centrifuge, were computed using Equation 3.2 (Mayne and Kulhawy, 1982) up to the passive limit $K_p = 2.25$ for $\phi'_{crit} = 22.6°$. The water table was set at ground level. Assuming a uniform bulk unit weight of 16.66kN/m^3, the profiles of vertical and horizontal normal effective stress shown in Figure 6.7 were obtained. Since in-situ stresses are specified in CRISP using horizontal layers, there is some approximation from the true calculated values of horizontal stress which are also shown in Figure 3.8 for comparison.

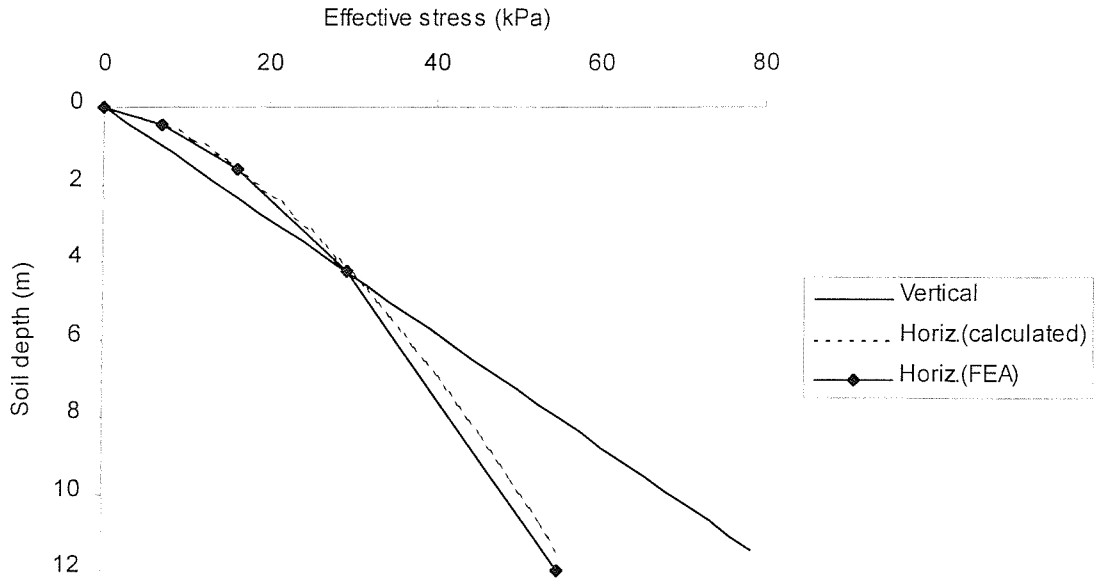

Figure 6.7: In-situ soil stresses

6.6.5 Sequence of analysis

The sequence of each analysis was as follows:

i. Trackway and slip elements added effectively simultaneously.

ii. Applied vehicle stress increased at a constant rate to 115kPa over a period of 139 hours and held at that value for 944 hours.

iii. Applied vehicle stress further increased to 150kPa over a period of 133 hours.

6.6.6 Analysis of *Test 1*

Figure 6.8 shows the increase in maximum vertical deflexion of the trackway during the test, which always occurred beneath the applied stress. The deflexion initially increased linearly with time to about 0.11m, reflecting the linear stress increments up to 115kPa. For the last stress increment to 115kPa, the rate of deflexion increase falls as the underlying soil stiffens under consolidation, to a value of 0.12m. Over the 944 hour period of constant applied stress, the trackway deflexion, caused by consolidation of the

clay, increased at a very slow rate. Overall, under a constant stress, trackway deflexion only increased to 0.13m. As the applied stress was increased further to 150kPa, the trackway deflexion increased sharply and at a growing rate. The steepness of the graph approaching 1200 hours compared with the initial 139 hours was particularly significant given that the rate of applied stress increase at the end of the test was less than a third of the rate during the initial increase to 115kPa. This suggests that the soil/trackway system had reached failure. However, the applied stress could not be increased further without causing large equilibrium errors and numerical instability in the analysis, due to the material failure itself.

The vertical deflexion of the entire trackway and some of the surrounding soil surface at several stages of the test is shown in Figure 6.9. The lines on the graph follow the paths of the top surface of the mesh during the test with the trackway located between 8.2 and 12.6m on the horizontal axis. The uplift of the trackway ends is clearly visible in the 150kPa applied stress case, as is the characteristic 'W' shaped profile of the trackway as it deforms. The growth of trackway deflexions corresponds with the graph shown in Figure 6.8 with a rapid increase initially to about 77kPa applied stress, which slowed to 115kPa, and a small increase during the 944 hour constant stress period. As the applied stress was increased to 132kPa the trackway deflexion increased rapidly again, and up to 150kPa increased at an even higher rate. It is interesting to observe the uplift of the soil surrounding the trackway during the test. Even up to the applied stress of 132.5kPa, the soil uplift was slight: the displaced volume of soil was much lower than that beneath the trackway, suggesting that most of the trackway deflexions were due to volume change of the soil, i.e. consolidation. Only after 150kPa was applied, did the soil uplift increase at an amount corresponding with the displaced soil beneath the trackway. This, together with the latter steepening of the graph in Figure 6.8, confirm that the soil suffered bearing capacity failure approaching the 150kPa applied stress level.

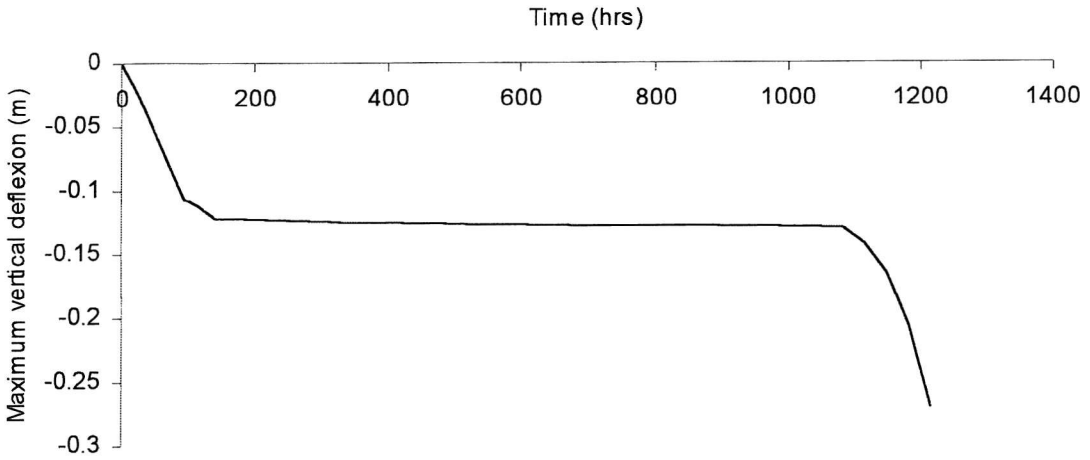

Figure 6.8: *Test 1*, development of maximum trackway deflexion

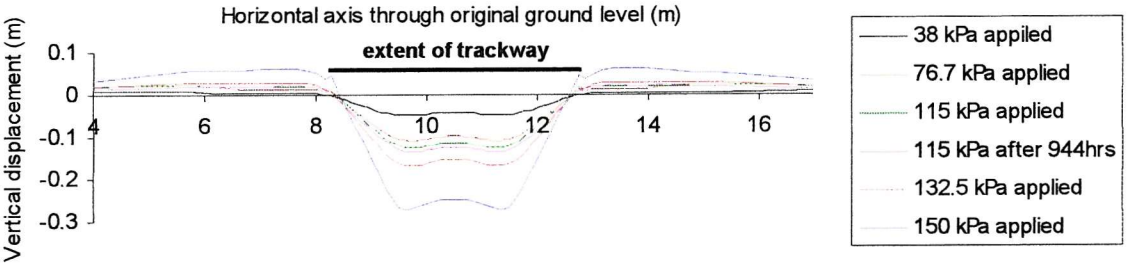

Figure 6.9: *Test 1*, transverse soil/trackway deflexion profiles

Figure 6.10 shows the development of horizontal strain on the upper surface of the trackway during the analysis. There was little development of strain between '115kPa applied' and '115kPa after 944 hours', with both showing smooth profiles of strain with compression (to about 0.002) beneath the two strips of applied stress and tension (to about 0.001) in between, reflecting the development of the 'W' shape observed in Figure 6.9. After the application of 132.5kPa, the strain immediately beneath the applied stress increased to 0.004, and after 150kPa was applied, increased more significantly to 0.011, although confined to the same restricted area immediately beneath the applied stresses. The strain in other parts of the trackway did not increase significantly in comparison. The concentration of strain in these areas suggests plastic hinges developed at the 132.5kPa applied stress and that during soil/trackway failure, a significant part of

trackway deformation occurred in these regions. Given the analysis values for Young's modulus of 37.6 kN/mm^2 and yield stress of 68.4 N/mm^2, yield in the trackway would be expected at a strain of around 0.0018 and corresponds with the apparent plastic hinge development in regions of strain exceeding 0.002. It is interesting to note that the trackway deflexions shown in Figures 6.8 and 6.9 did not accelerate to a large extent when the plastic hinge developed in the trackway and the trackway material essentially failed. A further increase in applied stress to 150kPa was required before failure of the soil/trackway system as a whole.

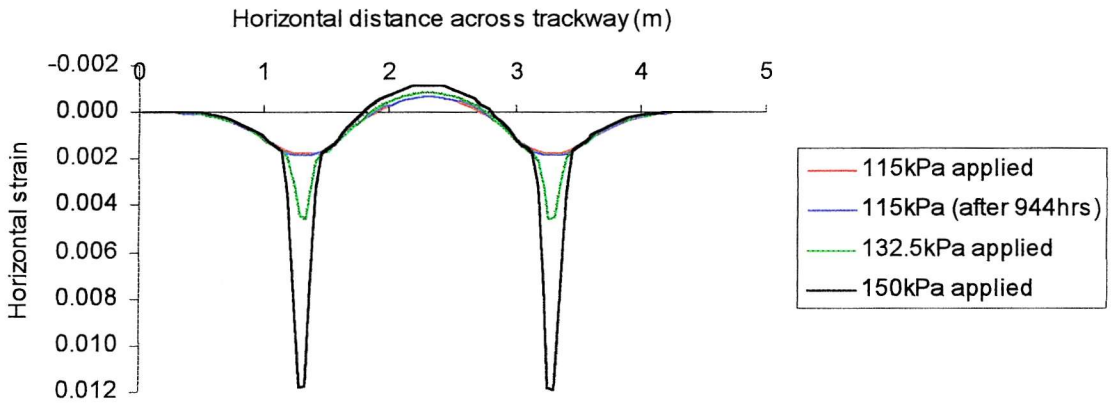

Figure 6.10: *Test 1*, transverse trackway strain profile

Figures 6.11 and 6.12 show the excess pore pressure in the model at two key stages in the test: at 115kPa and 150kPa applied stresses respectively. At 115kPa, the greatest excess pore pressures occur about 0.5m centrally beneath the trackway, reaching 33kPa. A bulb of pressure extends downwards 2 to 3m beneath the trackway, with a smaller peak of 15 to 20kPa. At each side of the trackway, there were regions of slight negative excess pore pressure extending 3m outwards and about 1m below the soil surface. At the 150kPa applied stress, the large peak in excess pore water pressure immediately beneath the trackway had dissipated somewhat, leaving a maximum value of 22kPa at about 1.5m beneath the trackway. However, the contours of 10, 15 and 20kPa extend over much larger areas in Figure 6.12, as do the areas of suction. Negative excess pore pressures begin about 0.8m under the ends of the trackway and extend 5m away on each side at a depth of 1 or 2 metres. The peak values of negative excess pore pressure of – 8kPa occur just outside the trackway ends at about 1m depth and are characteristic of the shear zones occurring in a bearing capacity failure in an over-consolidated clay.

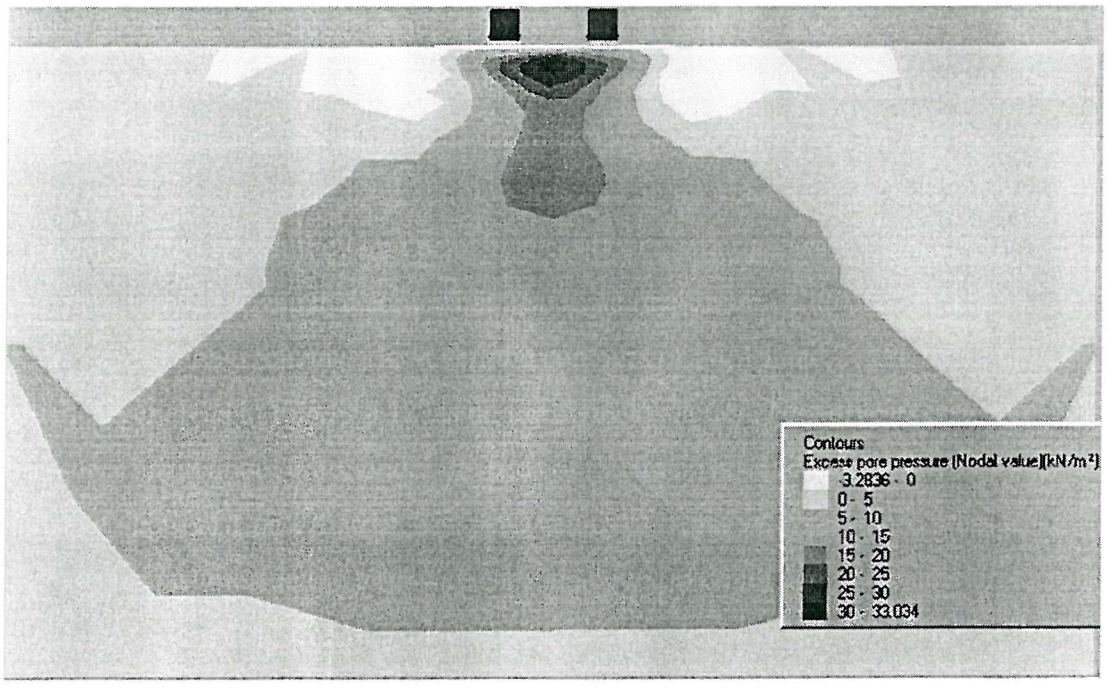

Figure 6.11: *Test 1*, excess pore pressures (115kPa applied stress)

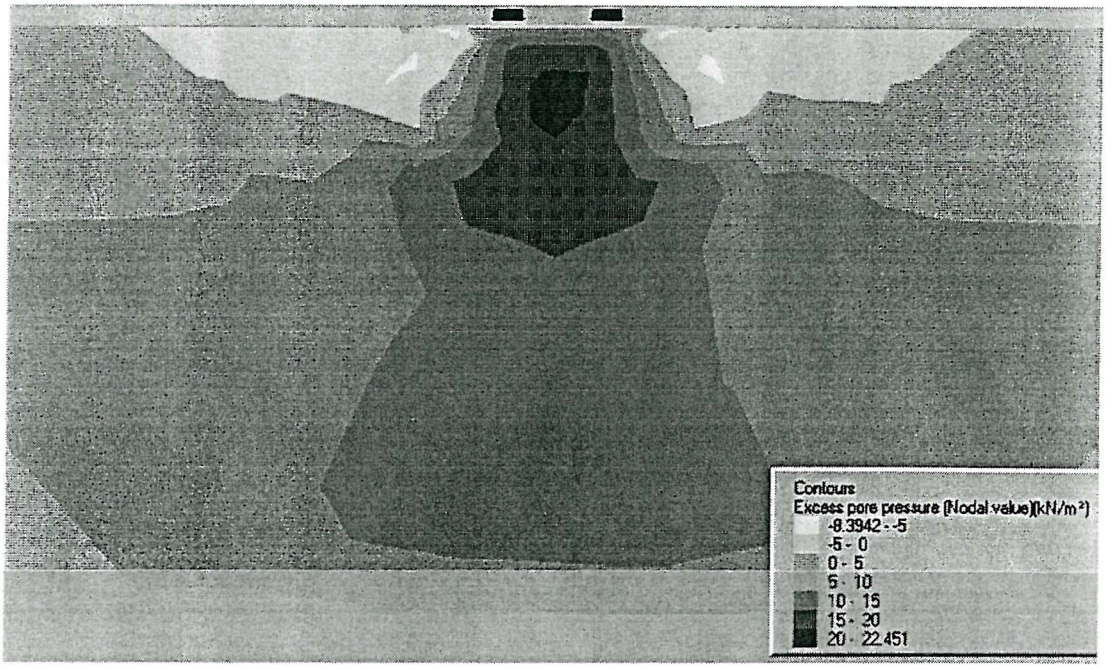

Figure 6.12: *Test1*, excess pore pressures (150kPa applied stress)

Although soil/trackway contact stresses could not be measured in the centrifuge tests it is useful to calculate them in the finite element analyses given their importance in the discussions of trackway behaviour in Chapter 5. The contact stress across the soil/trackway interface in this analysis at an applied stress of 115kPa is shown in Figure 6.13. Clearly, the output of stress was rather unstable as would be expected at the boundary of two materials with very different constitutive properties. Using the contact stress output of the slip element, or the vertical stresses in the trackway base or the underlying soil surface gave even more erratic stress profiles. The most satisfactory output, in terms of visual interpretation, was achieved by recording the total mean normal stress in the soil immediately beneath the trackway, which was used in Figure 6.13. Therefore, the values of contact stress indicated on the graph can only be used as a guide, but nevertheless would provide a useful comparison of contact stress between different trackway configurations used in this analysis. The profile of contact stress in Figure 6.13 shows there was an average stress across most of the interface of about 10kPa, reducing steadily to zero over the last 0.5m at each end. This is a characteristic stress distribution beneath a relatively flexible foundation.

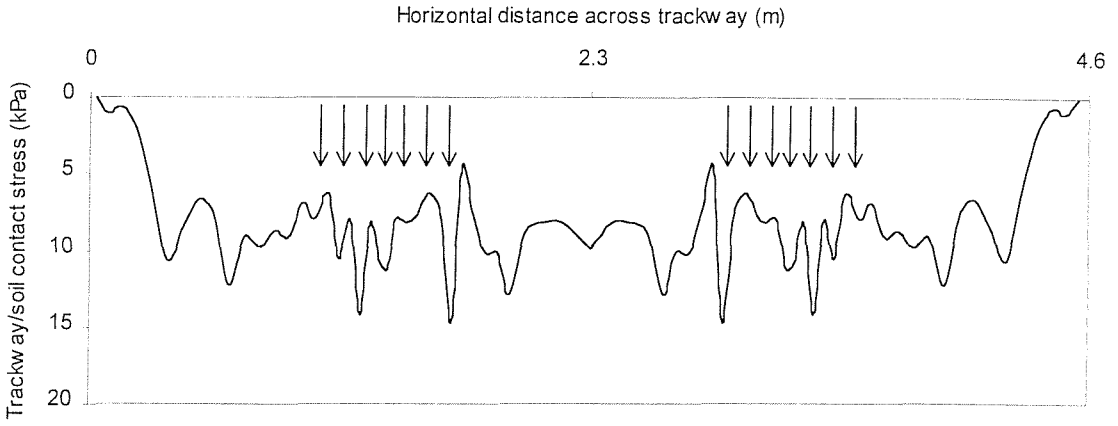

Figure 6.13: *Test 1*, p′ in soil immediately beneath trackway (115kPa applied stress)

Figures 6.14 and 6.15 show a number of stress paths in q-p′ and υ-lnp′ space respectively, at various depths in the soil directly beneath one of the applied stresses. In Figure 6.14, the Cam-clay yield locus on the wet side of the critical state line, and the Hvorslev line on the dry side have been plotted, together with four stress paths at increasing depth beneath a loaded region of the trackway. The stress path nearest the surface, at 6cm depth, reaches the Hvorslev line and ruptures almost immediately. Had the Hvorslev line been set at a shallower gradient, larger stress ratios (q/p′) would have been generated, leading to an over-prediction of the surface strength of the clay. The stress paths at 0.5 and 2.1m depths initially increase in q with no change in p′ under undrained conditions until reaching, and following, the Hvorslev line. The interpretation of the stress paths was further complicated by the partly drained conditions, with continuous consolidation of the clay hindering its softening along the Hvorslev line. The soil at 4.5m depth was sufficiently deep to experience little consolidation, and its stress path rose vertically to stay just within the Cam-clay yield locus.

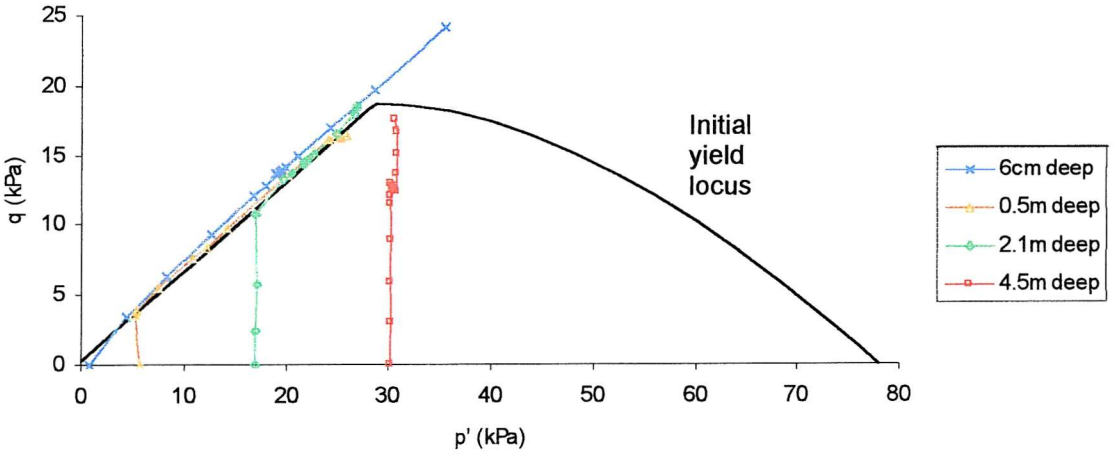

Figure 6.14: *Test 1*, stress paths in q-p′ space

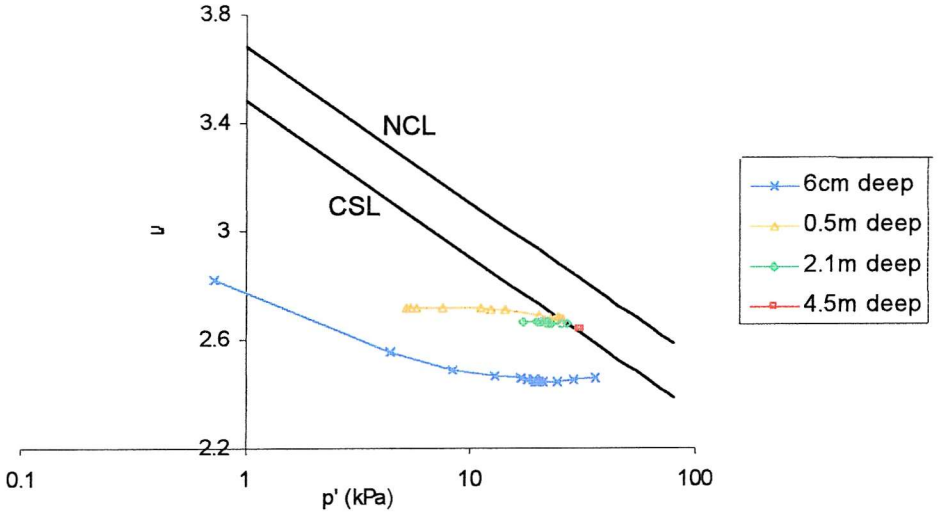

Figure 6.15: *Test 1*, stress paths in υ-lnp′ space

In Figure 6.15 the 6cm deep stress path, although on the Hvorslev rupture line in q-p′ space, shows a large degree of consolidation in the initial stages of the test, with υ falling from 2.8 to 2.45 during the initial application of 115kPa. The stress path remains stationary during the 944 hour constant stress period and when the applied stress was further increased to 150kPa there was an increase in p′ and υ, showing a tendency to dilate and indicating shear failure near the soil surface. The stress path for the soil at 0.5m depth, perhaps because it was further from the surface drainage boundary, showed more characteristic undrained yielding of an over-consolidated clay, with an increase in p′ and constant υ. When the path reaches the critical state line, it stops and shear failure occurs. The stress path at 2.1m depth behaved in a very similar way, although beginning at a higher value of p′. The stress path for the soil at 4.5m depth was sufficiently deep to experience no yield or consolidation.

The overall response of the model in q-p′ space is better illustrated by the stress state plots shown in Figures 6.16, 6.17 and 6.18. Figure 6.16 shows the stress state caused by an applied stress of 115kPa, clearly there was a large area of the soil rupturing on the Hvorslev line beneath the trackway to a depth of 3m and spreading along the surface of the soil 8m from the trackway ends in the passive zone. The orange zone beneath this was in an elastic state but on the dry side of the critical state line because the clay at this depth was still heavily over-consolidated. Below 4m depth the clay was elastic on the wet side of the critical state, corresponding with the dry/wet boundary at model scale shown in Figure 3.9, (110mm depth in the model corresponding with 4.2m depth at prototype scale). A region of clay across the base and rising in the centre was hardening on the wet side of the critical state: this was caused by the applied stresses reacting with the base of the mesh and because the clay at this depth was only lightly over-consolidated and prone to hardening when subjected to only light additional normal stresses. Figure 6.17 shows the stress state at the end of the analysis under an applied stress of 150kPa. Below 4m depth there was little change from the 115kPa case. However, beneath the trackway, to a depth of 4m, the clay showed the effects of consolidation with a large zone hardening below, and sometimes above, the critical state line. This hardening zone extends from immediately beneath the loaded regions of the

trackway, where in the 115kPa case the clay was rupturing on the Hvorslev line. The top 1 to 2m of clay either side of the trackway remained on the Hvorslev line as did, more significantly, the region of clay beneath and around the trackway ends where the negative excess pore pressures shown in Figure 6.12 and shear failure occurred, causing a bearing capacity failure at around 150kPa.

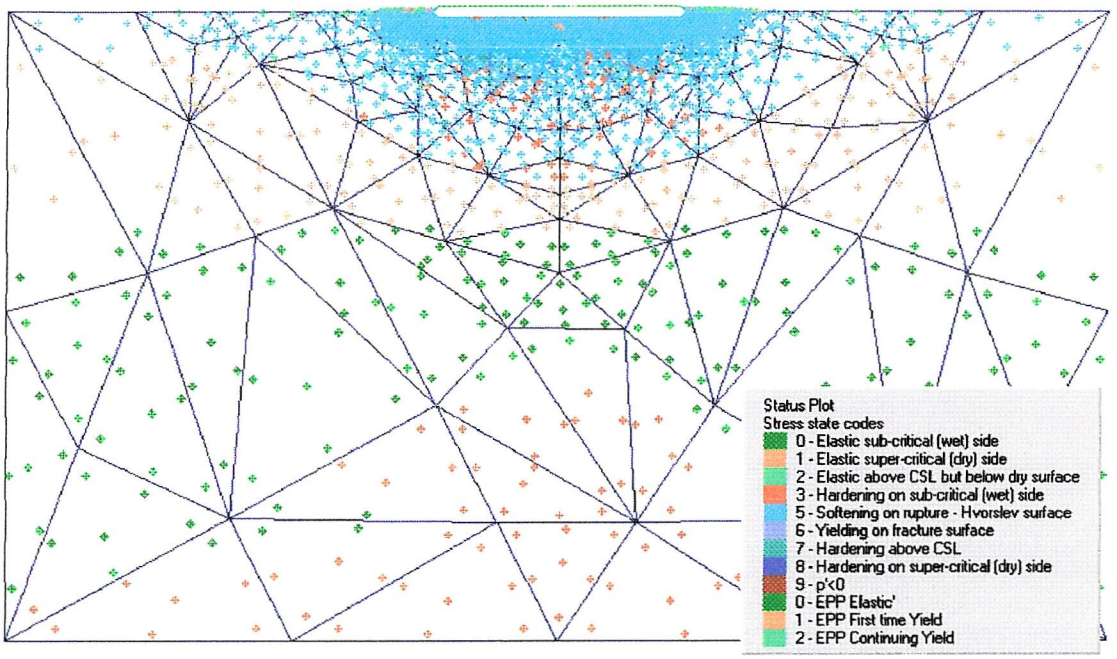

Figure 6.16: *Test 1*, plane strain stress states (115kPa applied stress)

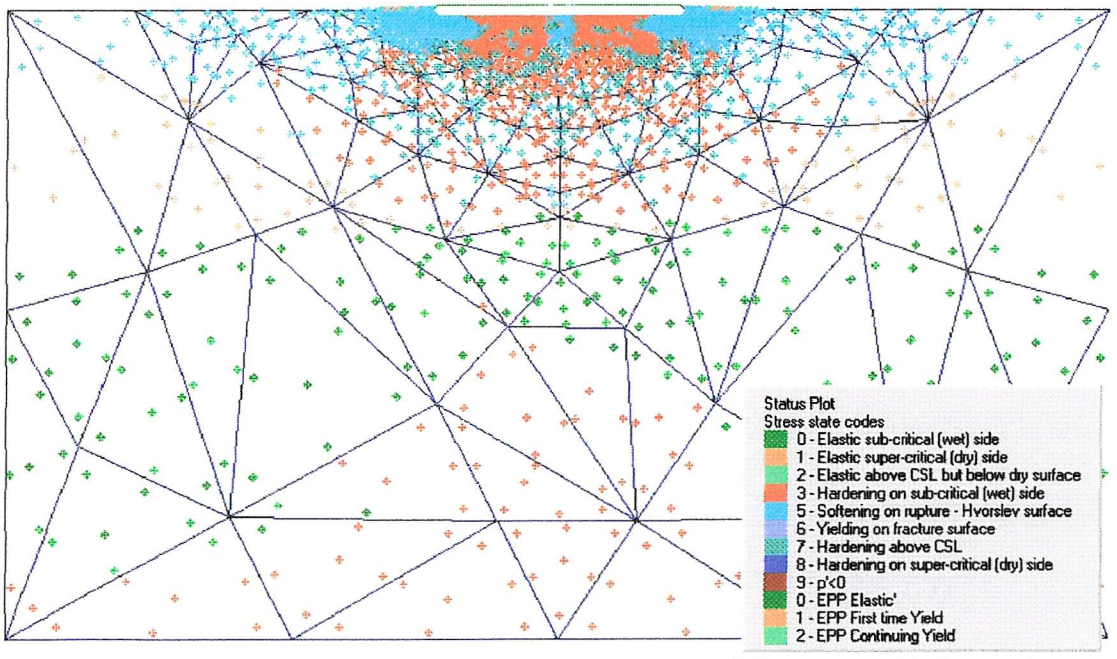

Figure 6.17: *Test 1*, plane strain stress states (150kPa applied stress)

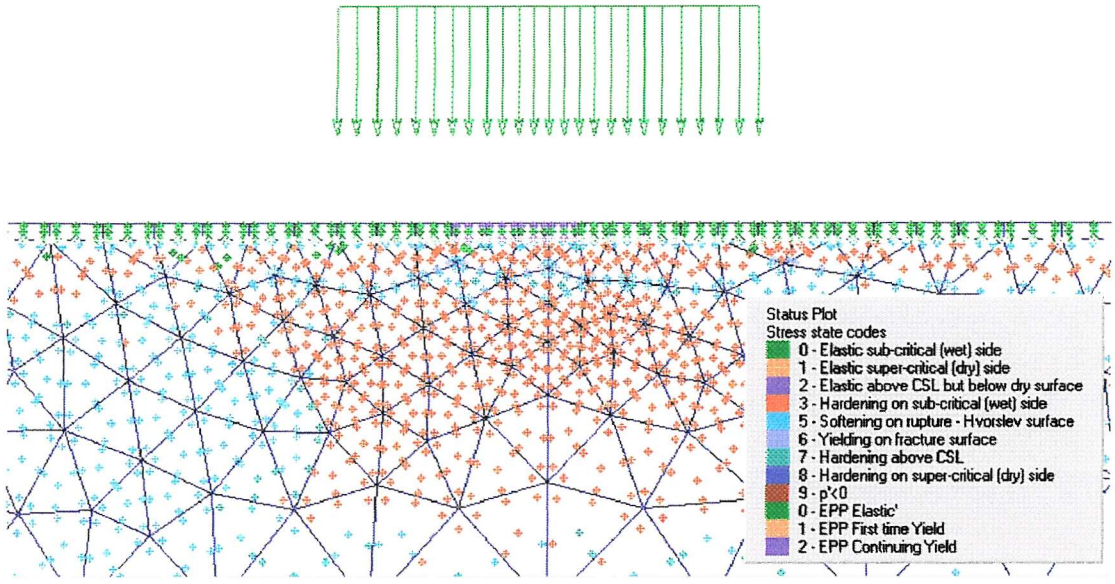

Figure 6.18: *Test 1*, plane strain trackway stress state (123.75kPa applied stress)

The strain profiles shown in Figure 6.10 suggested a possible yielding of the trackway material at an applied stress of 132.5kPa and the stress state plot in Figure 6.18 confirms this. In addition to the stress state of the soil, a straightforward elastic or plastic state is returned for the elastic-perfectly plastic material model used for the trackway. Figure 6.18 shows a small part of the mesh in the vicinity of a loaded area of trackway. A 0.2m length of trackway beneath the applied stress experienced yield along its upper and lower surfaces at an applied stress of 123.75kPa, which had not occurred under the 115kPa applied stress and corresponds with the shape of the strain profile in Figure 6.10. Again, it is interesting to note that yielding of the trackway at 123.75kPa did not lead to immediate failure of the soil/trackway system, rather it occurred closer to the 150kPa applied stress.

6.6.7 *Test 1* with non-yielding trackway material properties

A further analysis was carried out to assess the effect of the yielding properties of trackway and the development of plastic hinges on trackway performance. This was achieved by making one change to the *Test 1* analysis above: removing the Von Mises

yield criterion from the trackway material model so that the trackway only deformed in an elastic manner. By comparing the results of this analysis, denoted *Test 1(elastic trackway)*, with *Test 1* above, the compromising effect of trackway yield on its performance could be measured.

Figure 6.19 compares the increase in maximum trackway deflexion with time during the two analyses. As would be expected, up to 1080 hours, before any trackway yield occurred in *Test 1*, the two lines are colinear. After 1080 hours, when the applied stress was increased further and the trackway began to yield in *Test 1*, the maximum deflexion increased at a faster rate than in *Test 1 (elastic trackway)*. At the end of the analysis, the maximum deflexion was significantly higher, 0.27m compared with 0.21m in the elastic case. This confirmed that the yielding of trackway and the development of a plastic hinge was detrimental to its performance. Nevertheless, the slope of the graph at the end of the elastic analysis was steep compared with the initial slope up to 100 hours, given that the final stress increment was only 35kPa compared with the initial increment of 115kPa.

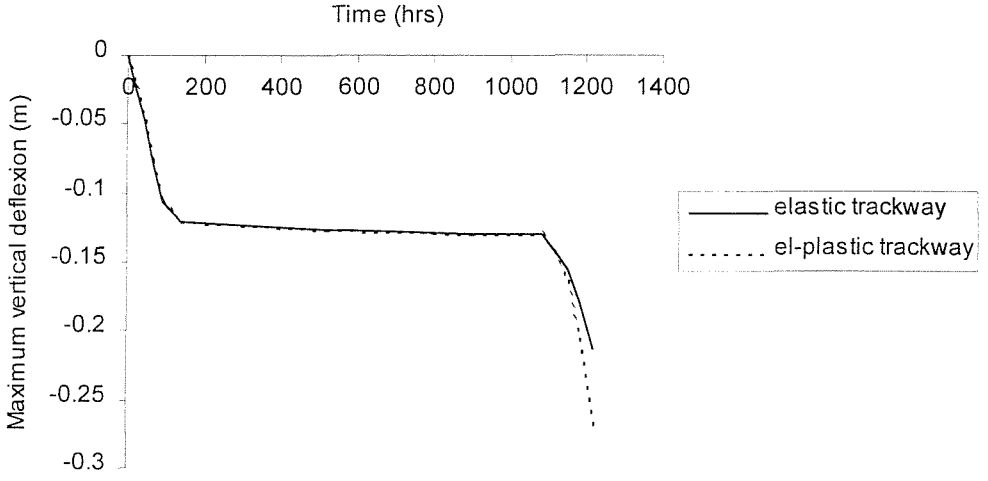

Figure 6.19: *Test 1 (elastic trackway)*, development of maximum trackway deflexion

Figure 6.20 shows horizontal profiles of the mesh at key stages of the analysis and should be compared with the similar graph for *Test 1* in Figure 6.9. Again, up to the applied stress of 115kPa, the *Test 1* and *Test 1 (elastic trackway)* profiles are identical. As the applied stress increased, in a similar way to *Test 1*, trackway deformation increased at a faster rate. Although trackway deflexions at the end of *Test 1 (elastic trackway)* were lower than for *Test 1*, it is interesting to note the heave either side of the trackway at 150kPa, similar to the heave that occurred in *Test 1*, suggesting that the clay also failed in *Test 1 (elastic trackway)*.

To confirm that the trackway in analysis *Test 1 (elastic trackway)* did not yield, strain profiles during the analysis are shown in Figure 6.21. The values of strain around the areas of applied stress did increase as the soil failed, but because no plastic hinge developed, there was more re-distribution of stress along the trackway and strain increased over wider areas of the trackway and was not concentrated as large peaks in small areas at plastic hinges as shown in Figure 6.10 for *Test 1*.

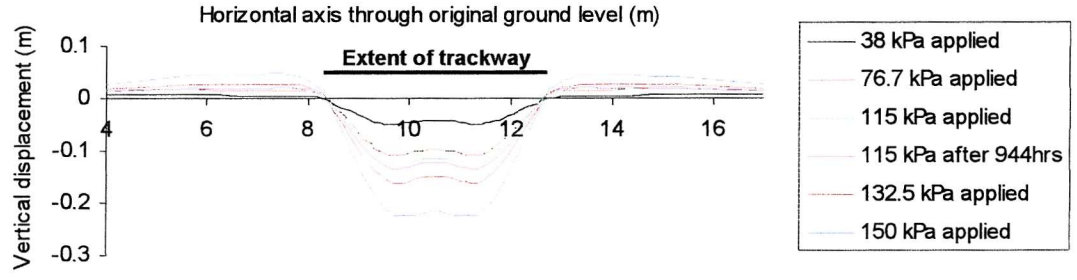

Figure 6.20: *Test 1 (elastic trackway)*, transverse soil/trackway deflexion profiles

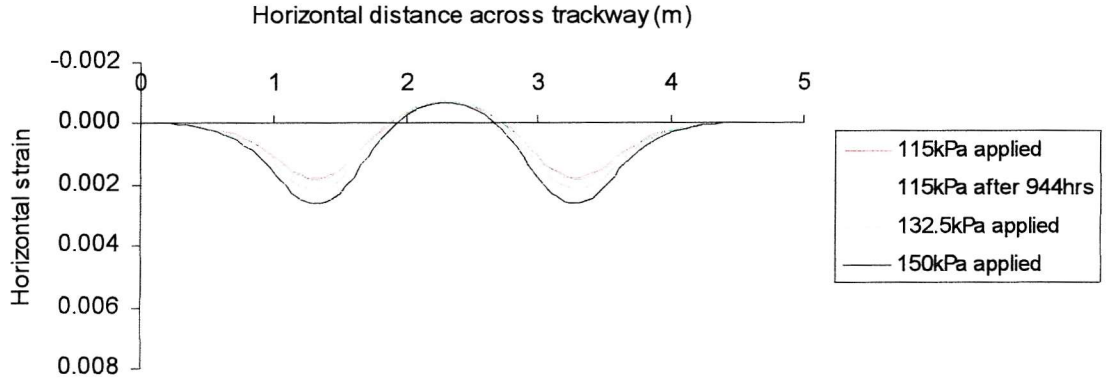

Figure 6.21: *Test 1 (elastic trackway)*, transverse trackway strain profiles

6.6.8 Trackway bending stiffness analysis

To assess the effect of transverse trackway elastic bending stiffness on its performance, a series of analyses was performed with trackway bending stiffness as the only variable. In all other respects the analyses were identical to *Test 1 (elastic trackway)*, since the elastic model was used for the trackway to eliminate the effects of trackway yield. In this series of analyses, the name of *Test 1 (elastic trackway)* was changed to *EI38* to reflect the transverse bending stiffness (EI) of 38 kNm^2 per trackway panel used in this analysis. It was the EI value in CRISP that most closely replicated the bending behaviour of the centrifuge model class 60 trackway. Other analyses in this series had similar names to reflect their value of trackway bending stiffness.

One of the most significant effects of bending stiffness in this project, discussed in Chapter 5, is on contact stress between trackway and soil. Contact stresses, for several different trackway stiffnesses used in these analyses, under an applied stress of 115kPa, are shown in Figure 6.22. Analysis *EI38* is included again to serve as a comparison and is identical to the profile shown in Figure 6.13. For the same reasons as described for Figure 6.13, the profiles were very erratic, which does not allow straightforward comparisons. However, the weakest trackway, *EI13*, can be seen to produce the largest peaks of contact stress in the vicinity of the applied stresses, but reduces the most steeply to zero at the trackway edges, and, indeed, reaches zero 0.3m within the trackway. The stiffest trackway, *EI10 000*, gave a contact stress typical of a rigid foundation. It reached high peaks at the extreme ends of the trackway but showed the most consistent, and generally lowest stress distribution across the trackway and seemed unaffected by the position of the applied stress. The contact stresses at other trackway stiffnesses showed approximate trends between these extreme values of trackway stiffness. In the vicinity of the applied stresses, the *EI13* contact stresses were markedly higher than the others, which tended to cluster around similar values, even though they spanned a wide range of trackway stiffnesses. This suggests that the effect of trackway stiffness on contact stress is very much more significant at lower values, particularly those below Class 60 transverse stiffness. Notably, there was a rapid change in the

trackway from apparently flexible behaviour to rigid behaviour. At trackway stiffnesses up to 50kNm^2, contact stresses return to zero at the trackway edges, above 200kNm^2, contact stresses reach high peaks at the trackway edges, signifying rigid behaviour. *EI100* seemed to mark the transition value between these two characteristics, since its contact stress was approximately 10kPa across the entire width of trackway.

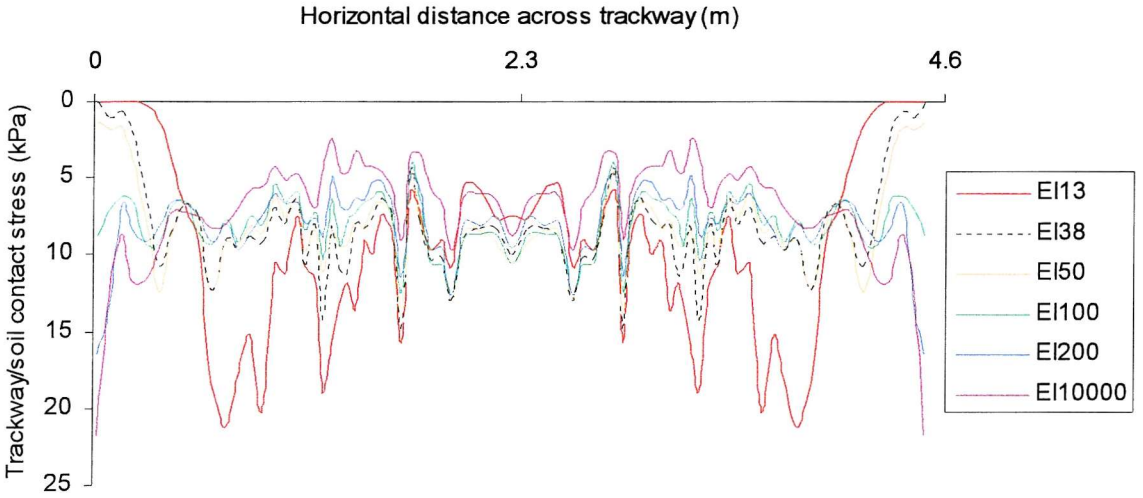

Figure 6.22: Soil/trackway contact stress for different trackway stiffnesses

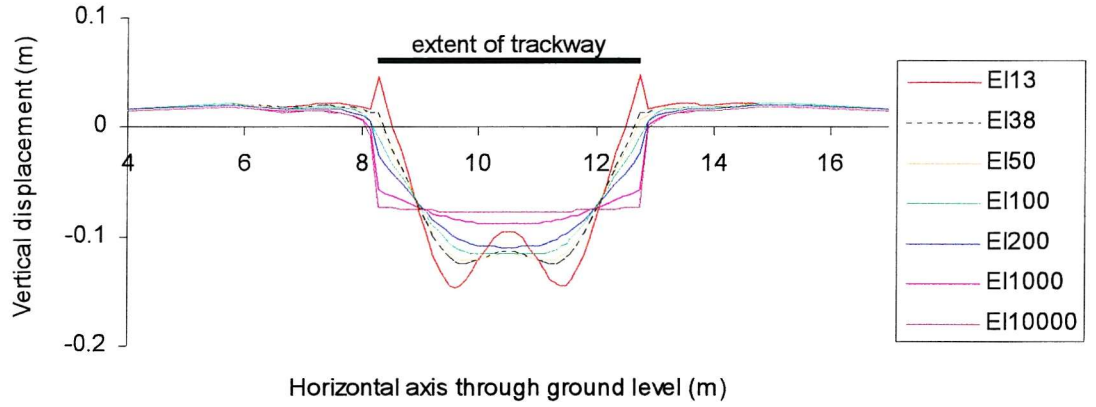

Figure 6.23: Transverse soil/trackway profiles for different trackway stiffnesses

The transfer of trackway behaviour from flexible to rigid was also apparent in the transverse analysis profiles, at the applied stress of 115kPa, shown in Figure 6.23. It also suggests that analysis *EI100* marked the transition to flexible behaviour since *EI200* was the last analysis to indent the soil at the extreme edges of the trackway. While analysis profiles for *EI38* and *EI200* clustered around similar values, *EI13* again marked a significant change to more flexible behaviour, producing a pronounced 'W' shape with large displacements beneath each applied stress and significant uplift of the trackway ends.

To assess the effect of bending stiffness on trackway performance, the maximum deflexions at an applied stress of 115kPa are compared in Figure 6.24 for all the analyses in this series. The circled value is for *EI38* and signifies the relative performance of existing class 60 trackway in transverse bending. As indicated by the two preceding graphs, trackway stiffness becomes most significant at lower values. The curve, plotted with a logarithmic scale for EI, is at its steepest when EI is low. An EI value of 13kNm^2 was the lowest permissible in these analyses before significant equilibrium errors occurred, even at the applied stress of 115kPa. Had lower EI values been achievable, the curve would have steepened to a point where the trackway contributed no stiffness to the soil/trackway system. As the EI value increases, the curve becomes flatter and, although rigid behaviour was observed in the preceding graphs from an EI value of around 200kNm^2, trackway performance still improved up to a value of 10 000kNm^2. Above this value trackway stiffness contributed very little more to its performance, it was truly rigid and its deflexion depended wholly on the soil's stiffness.

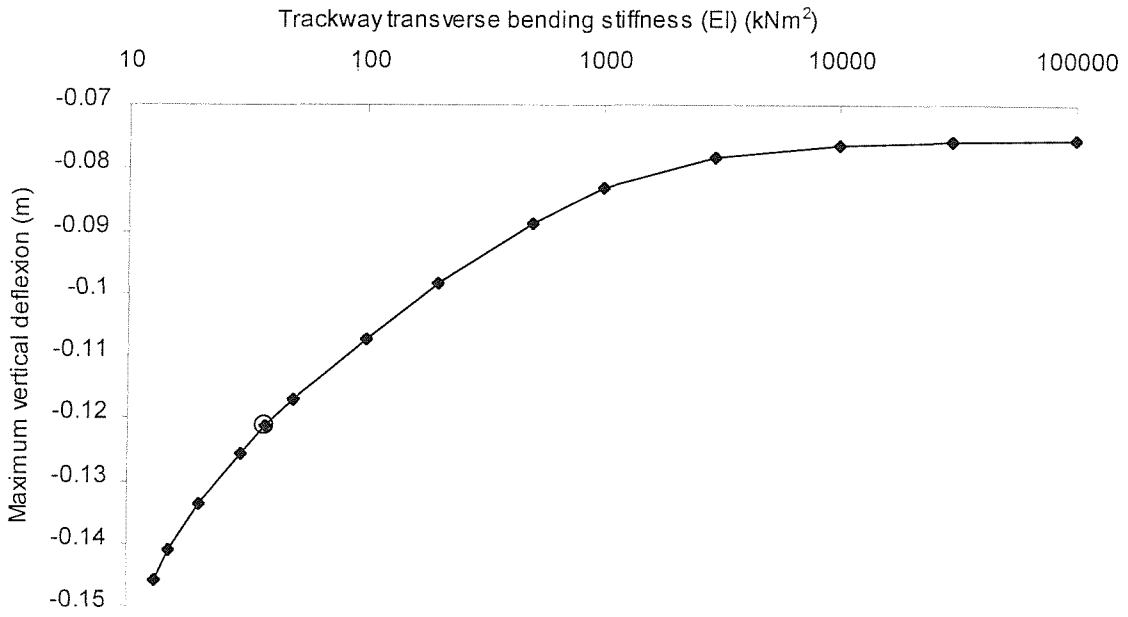

Figure 6.24: Effect of bending stiffness on trackway performance

6.6.9 Slip element assessment

The success of the new 'effective stress' slip element is borne out by the satisfactory outputs of pore water pressure during the *Test1* analysis presented in Figures 6.11 and 6.12. The positive effects of the use of slip elements are best viewed in the transverse deflexion profile of analysis *EI13* in Figure 6.23. The pronounced "W" shape demonstrates the ability of the trackway to deform unhindered despite its high stiffness compared with the soil and the inherent slippage that must have occurred between such different materials. Whilst allowing slippage, the slip elements still provided sufficient normal stiffness in compression to transmit applied stresses unhindered to the soil beneath and produce the soil/trackway profile shown.

In addition, significant uplift of the trackway ends in analysis *EI13* is visible in Figure 6.23. The uplift was very localised and since none of the surrounding soil was pulled upwards by the trackway ends demonstrates that, when under tension, the slip element

normal stiffness reduced to its very low factored value and simulated soil/trackway separation.

This is a significant development in the use of slip elements in soil mechanics programs since it now allows their use in long-term soil/structure interaction problems and where outputs of pore pressure in the vicinity of the structure are required. This has hitherto not been possible.

6.6.10 Large strain formulation assessment

The success, and accuracy, of the large strain formulation is demonstrated by the close agreement between the plane strain finite element analyses and centrifuge tests 1 and 2 discussed in Chapter 7. When using the standard small-strain formulation, maximum soil and trackway deflexions were 5-10% higher than both the large strain formulation and the centrifuge tests for large deformations. This is shown in the comparison of maximum trackway deflexions during the analysis using the large strain and small strain formulations in Figure 6.25. In addition, perhaps due to its prediction of higher stresses, the small strain formulation analysis could not complete and suffered excessive numerical instability during the period of constant load consolidation. Consequently, none of the two-dimensional analyses could have been completed without the large strain formulation.

When using the "update co-ordinates" option, soil/trackway deflexions and stresses were identical to the new large strain formulation. As a result, it is difficult to assess its performance in these analyses. A more detailed assessment would be required to determine whether it possesses any advantages over the "update co-ordinates" option.

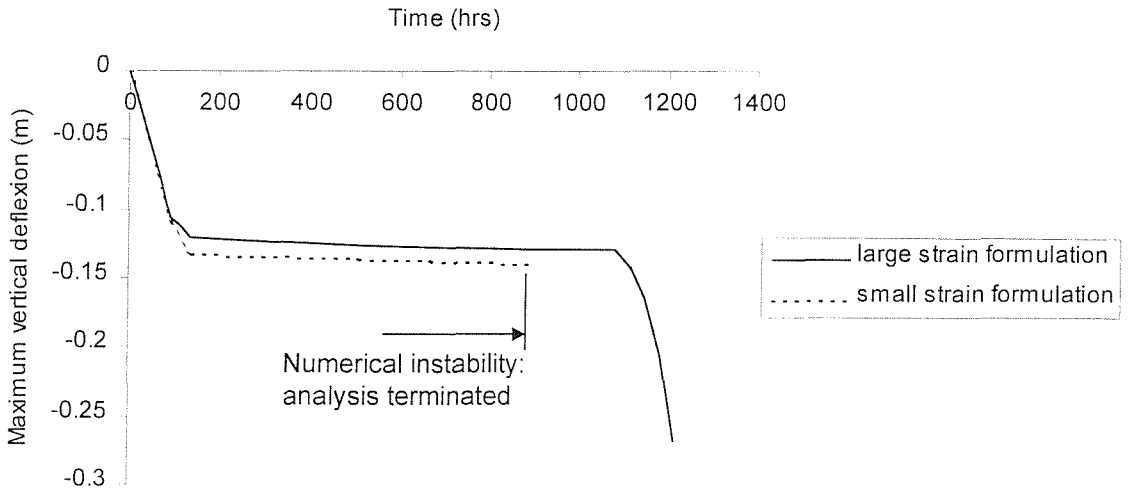

Figure 6.25: Comparison of large strain and small strain formulations

6.7 Three-dimensional analysis

6.7.1 Selection of elements and number of load increments

The mesh used in the three-dimensional analyses, shown in Figure 6.26, comprised 1344 linear strain brick elements and 128 three-dimensional slip elements. Since the aim of these analyses was to study contact stresses and deflexions due to the static application of an axle load, rather than the process of soil degradation and softening, consolidation was not simulated and no pore pressure nodes were required. This also helped to reduce the considerable computation time required for each analysis. It was difficult to concentrate smaller elements around the loaded areas without considerably increasing the total number of elements because only brick elements are available to construct three-dimensional meshes in CRISP. However, the need to use smaller elements to reduce element topography effects is less significant in three-dimensions than in two. Each trackway panel was composed of 16 brick elements (2 across its width, 8 along each length and 1 deep), this allowed tyre loads to be placed on one element face adjacent to a trackway joint, hence allowing the panel to rotate about the joint. The articulated joints between each trackway panel, shown in detail in Figure 6.26(a), were

modelled by connecting elements across the joint through a pair of nodes along adjacent element sides on the base of the trackway. On the top surface of the trackway adjacent nodes across a joint were separated by 10mm, thus causing negligible changes to each panel section geometry. Effectively, the joints had relative translational fixity (i.e. could not separate or overlap) with zero rotational stiffness. Although prototype trackway joints have a nominal rotational stiffness due to friction, it is still very low compared with the bending stiffness of the panels themselves and it was felt that this method of modelling was sufficient to analyse the detrimental effects of the joints on trackway performance. The main drawback was the unrestricted rotation of the joints, whereas prototype joints have a limit to their rotation of about 17°. However, during all the analyses, joint rotation was checked and never exceeded 17°.

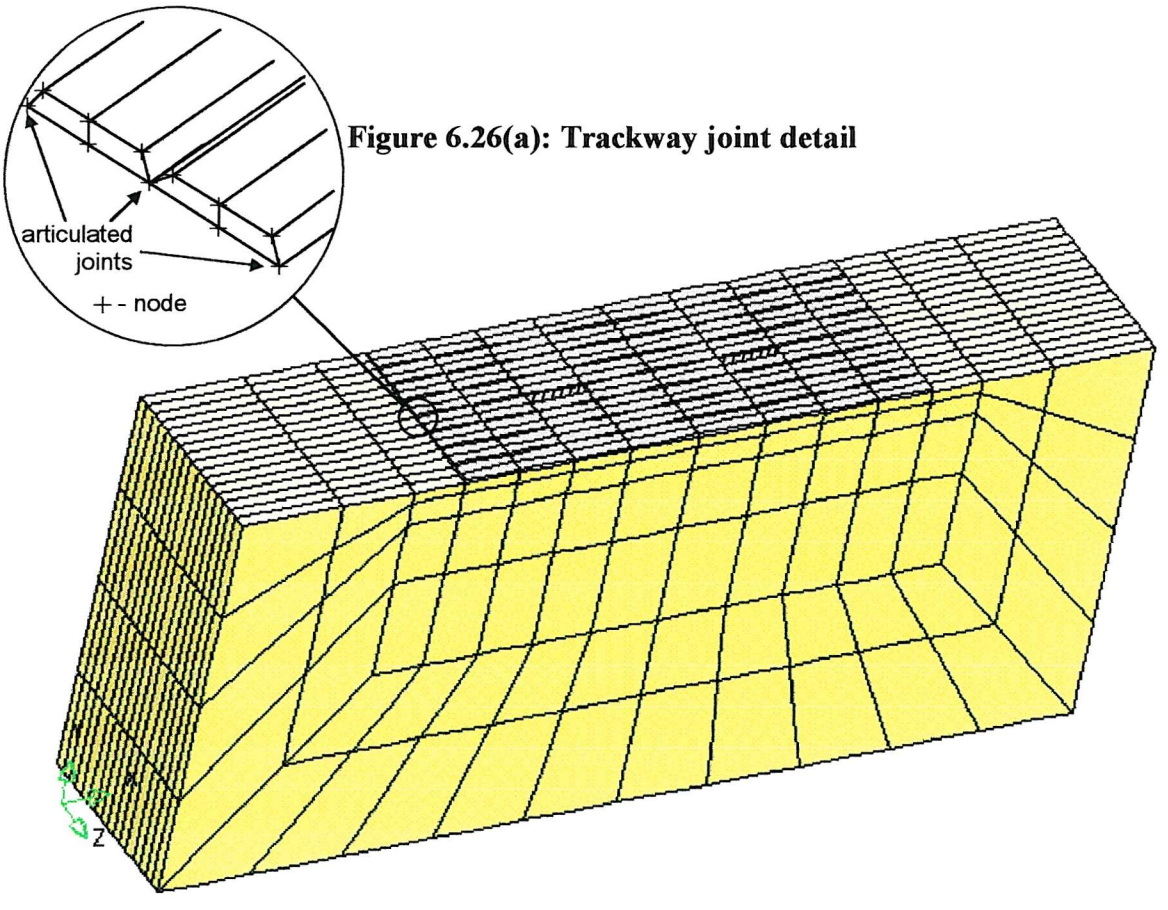

Figure 6.26(a): Trackway joint detail

Figure 6.26: Three-dimensional finite element mesh

Slip elements were located between the trackway and soil elements. This allowed slippage between the two materials and, more importantly, allowed some separation between trackway and soil along the joints to allow trackway panels to rotate up and away from the soil as well as down.

Due to the complexity of calculations involved in three-dimensional analyses, a single loading increment for these analyses took in the region of four hours to compute. It therefore became necessary to use the smallest possible number of load increments to ensure analysis run times were kept within practical limits. Fortunately, a three-dimensional analysis is less susceptible to equilibrium errors than a two-dimensional analysis and the overall applied loads were low. In each analysis, a single increment block was used to apply a pair of DROPS vehicle tyre loads on to the trackway. This increment block was divided into four equal increments, which was sufficient number to eliminate any significant equilibrium errors during the analysis. Output was generated for the final increment only to maintain output files at manageable sizes.

6.7.2 Idealised geometry

The data from centrifuge tests 3 and 4 showed that the zone of influence of a DROPS vehicle axle on the soil/trackway system was small, with no significant excess pore pressure values being measured at depths greater than 4m (prototype scale) or greater than 1m either side of the trackway. Therefore it was unnecessary to model the entire geometry of the centrifuge model and to enable smaller elements to be used, only a part of the centrifuge model was modelled in the analysis. The mesh geometry, shown in Figure 6.27 was 4m deep in the y direction with eight trackway panels placed on the surface across the entire width of the mesh, giving a z-dimension to the mesh of 1.84m. Provided all loads were applied to one of the two middle trackway panels, no soil stresses interacted with the z-faces of the mesh. To allow the effects of applied stresses to encroach beyond the ends of the trackway panels, the soil mesh was extended in the x-direction 2.2m from each panel end, giving a total length of 9m.

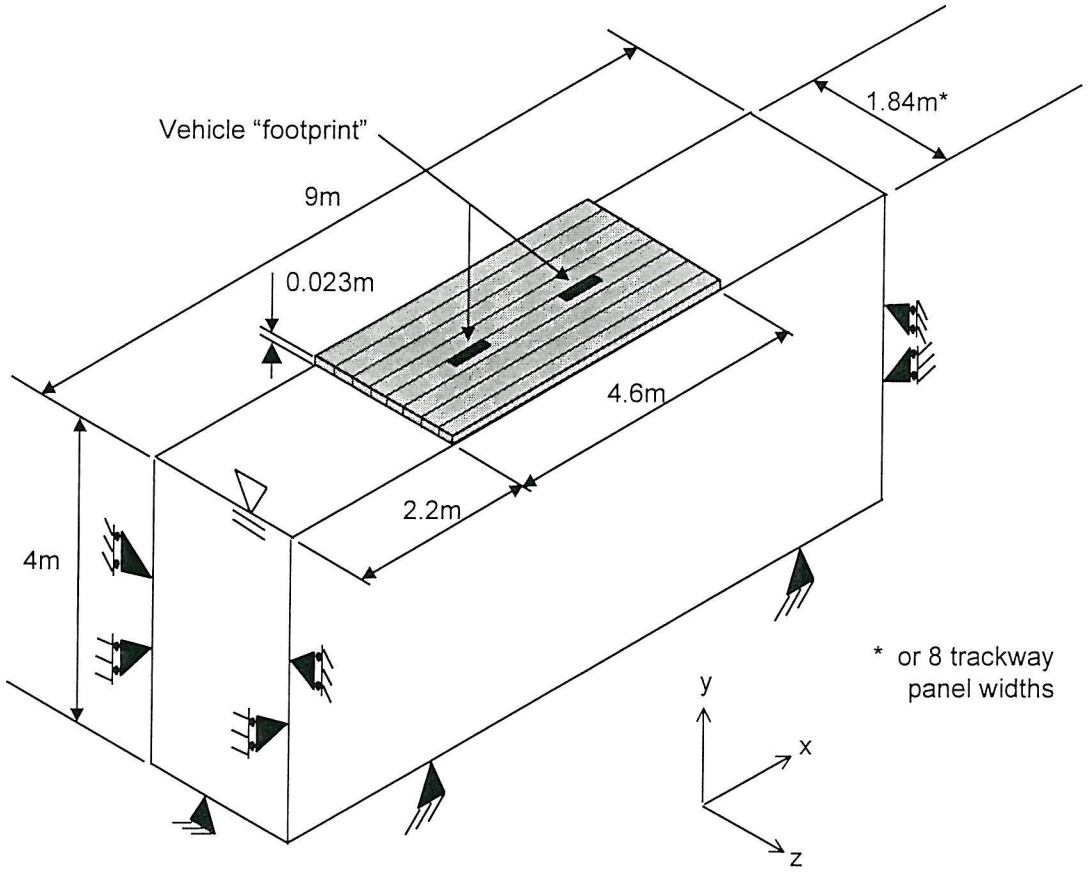

Figure 6.27: Idealised geometry of three-dimensional FEA model

6.7.3 Selection of input parameters

The input parameters for the Schofield model were transferred from the two-dimensional analysis and are shown in Table 6.3. M and H reverted to their normal values of 0.88 and 0.86 respectively, removing the adjustment for plane strain conditions. Since only the immediate response of the soil and trackway to a single axle load was of interest, the clay was assumed to be undrained and permeability values were not required.

It was found that combining an elastic-perfectly plastic model for the trackway with the Schofield model, as in the two-dimensional analysis, resulted in excessively long computation times for each analysis. Since most trackway deformations would be

concentrated around the flexible joints and because applied stresses were low, an elastic model was used for the trackway, whose parameters were transferred from the two-dimensional analysis described in Section 6.5.3.

The slip element parameters were also transferred directly from the two-dimensional analysis, as described in Section 6.5.3.

6.7.4 In-situ stress state

The in-situ soil stresses, as shown in Figure 6.28, were calculated in the same way as described in Section 6.5.4. Since the three-dimensional mesh was only 4m deep, in-situ stresses needed only to be calculated to this depth.

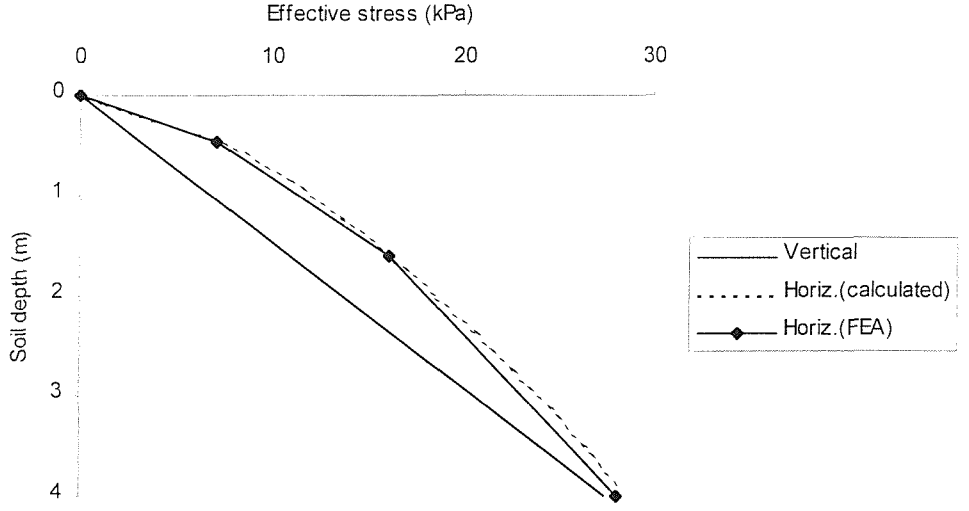

Figure 6.28: In-situ soil stresses

6.7.5 Sequence of analysis

The sequence of each analysis was as follows:

i) Trackway and slip elements added effectively instantaneously.

ii) 48kN total axle load applied to the trackway effectively instantaneously, equivalent to an applied stress of 183kPa over axle "footprint".

6.7.6 Analysis of *Test 4*

Figure 6.29 shows the deformed shape of the mesh at the end of the analysis. The soil elements are coloured red and the trackway elements orange: the trackway joints can be seen as double lines from left to right, every two elements. The loaded areas of trackway, or the DROPS axle "footprint" are shaded and their effect in causing the immediately adjacent trackway panels to rotate, and the nearest joint to embed into the soil can clearly be seen. The deformation in both the soil and the trackway were very localised, with no visible displacement beyond one or two panels immediately adjacent to the applied stress. The mesh displacement data were also used to produce the two graphs shown in Figures 6.30 and 6.31, which actually quantify the displacements. Both graphs contain surface profiles of the mesh along the top surface of the trackway at the end of the analysis. Figure 6.30 shows the profile in the longitudinal direction, across all the trackway joints and through one of the loaded areas (between z = 0.92 and 1.035m). The effect of the joints was particularly marked, with the maximum vertical deflexions of 0.13m clearly located at the joint adjacent to the applied stress. At one panel width away from the applied stress in either direction, the vertical deflexion reduced considerably and remained less than 0.03m. The profile in Figure 6.31 was taken in the transverse direction along the trackway joint adjacent to the applied stress and the soil surface on either side. The load was applied between x = 3.265 and 3.835m and x = 5.165 and 5.735m. The maximum vertical deflexion of 0.13m at x = 3.835 and 5.165m corresponds exactly with the maximum value in Figure 6.30 and the intersection of the two profiles. The main difference between the two profiles was the shape, with

significant deflexions of above 0.08m along almost the entire length of the joint. In contrast with the longitudinal profile with deflexions concentrated over a short distance. The soil heave either side of the trackway in Figure 6.31 was only 0.01m and showed that no failure of the soil occurred in the transverse direction.

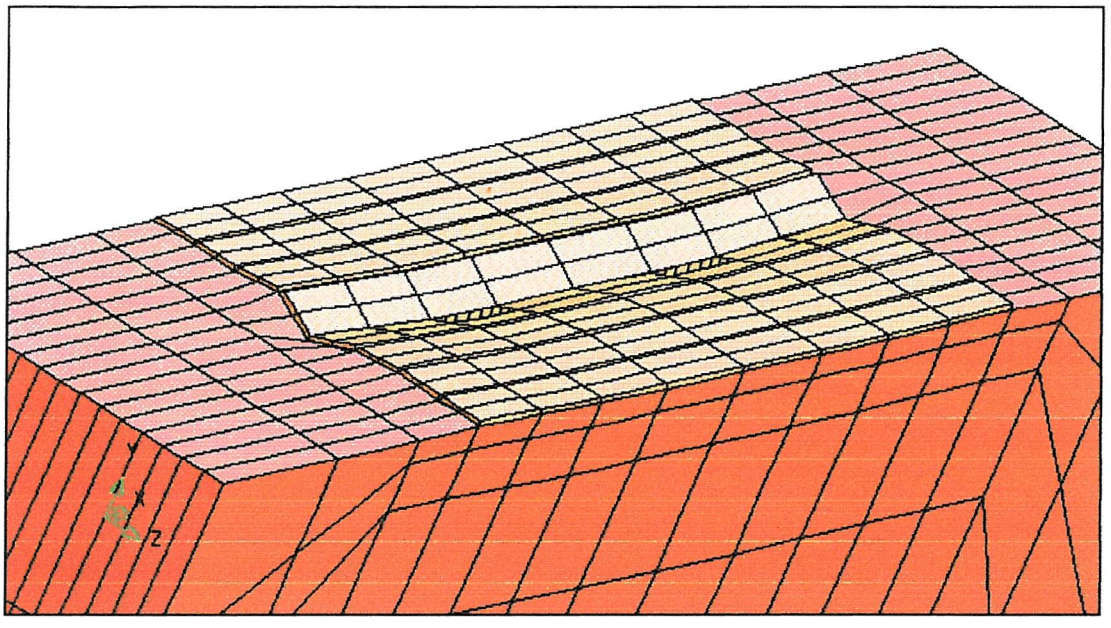

Figure 6.29: *Test 4*, deformed mesh (actual deformed scale)

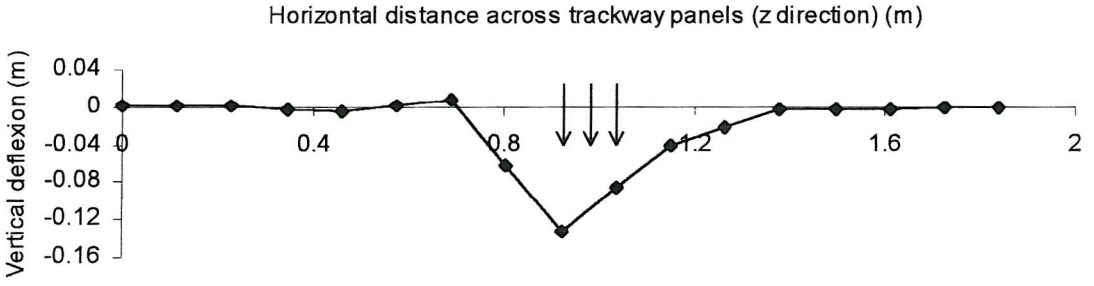

Figure 6.30: *Test 4*, longitudinal trackway deflexion profile

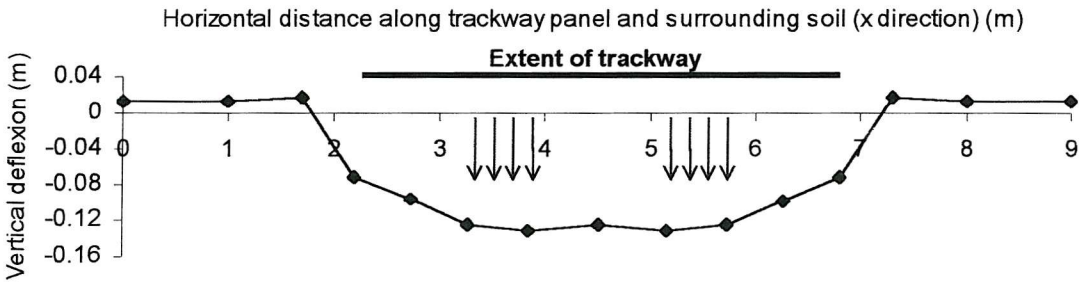

Figure 6.31: *Test 4*, transverse soil/trackway deflexion profile

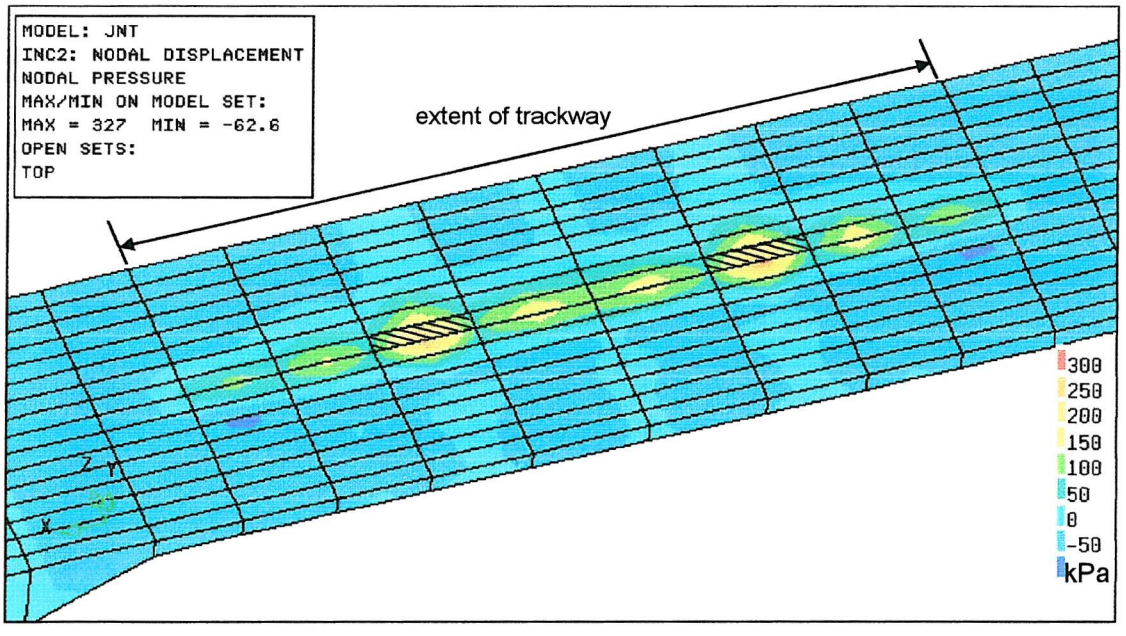

Figure 6.32: *Test 4*, soil/trackway contact stress

Figure 6.32 shows a contour plot of soil/trackway contact stress, plotted onto the soil surface. The trackway and slip elements have been removed to aid interpretation but their extent is marked and the areas immediately below the applied stresses are shaded. The contact stress values were derived directly from the total stress at the soil surface in the same way as described for Figure 6.13. Again, there was significant variability of values across elements, perhaps due to the coarseness of the mesh, particularly at a material boundary. Nevertheless, it is possible to see that contact stresses were very concentrated along the trackway joint adjacent to the applied loads, with values consistently in the range 100 to 200kPa along the full length of each panel. In contrast, there was no significant distribution of contact stress to adjacent panels in the longitudinal direction.

A contour plot of pore water pressure beneath the loaded trackway at the end of the analysis is shown in Figure 6.33. It is plotted on a section through the mesh, across the eight trackway panels which are visible at the top, and through one of the applied stresses. It shows that excess pore pressures were highly concentrated around the joint adjacent to the applied stress. A very high value of 327kPa was returned at the node immediately below the joint, but the pore pressure dropped very rapidly to less than 100kPa at only 0.2m depth and one panel width away from the joint; falling to less than 50kPa at a depth of 0.7m.

Figure 6.34 shows a contour plot of deviatoric stress, q, at the end of the analysis on a cut away section of the model. The trackway and slip elements have been removed and the mesh cut away so that the area of soil immediately beneath the applied stress, shown shaded, is on the corner of the mesh. This makes it possible to visualise the distribution of q in all directions away from the loaded areas. It can be seen that the peak stress of 20-24kPa was located at about 0.25m depth below the two loaded areas. Significant values of q of above 16kPa occurred at depths of between 0.1 and 0.35m along the length of the trackway panels but only 0.2m (trackway panel width) away from the joint. The region of high q values effectively formed a sausage shape the length and width of a trackway panel, at a depth of only 0.25m.

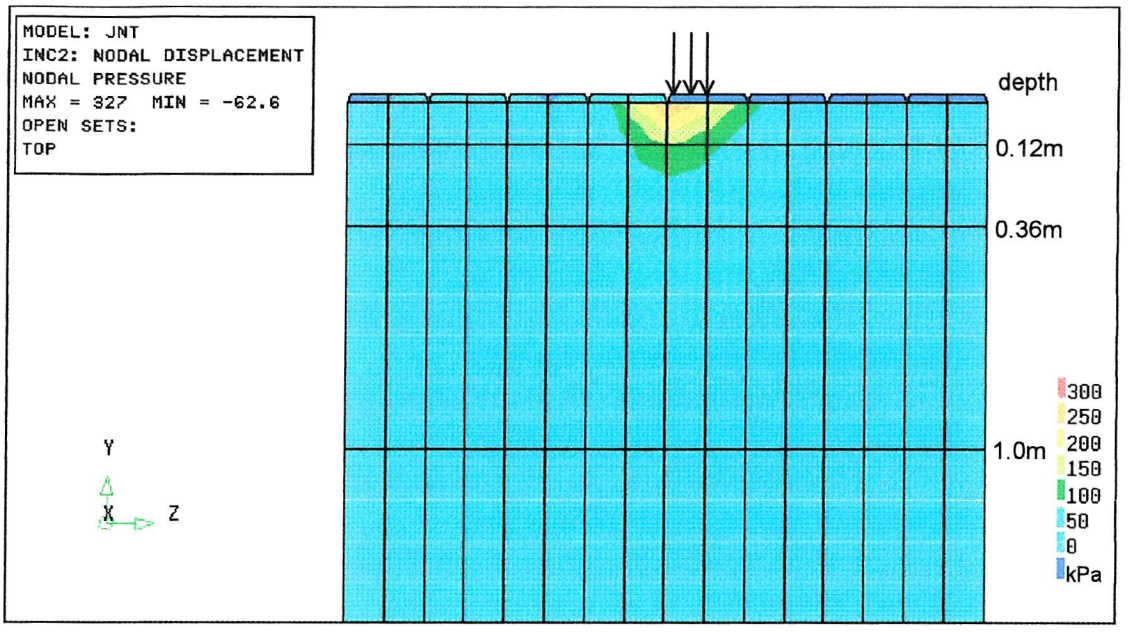

Figure 6.33: *Test 4*, total pore pressure on longitudinal section

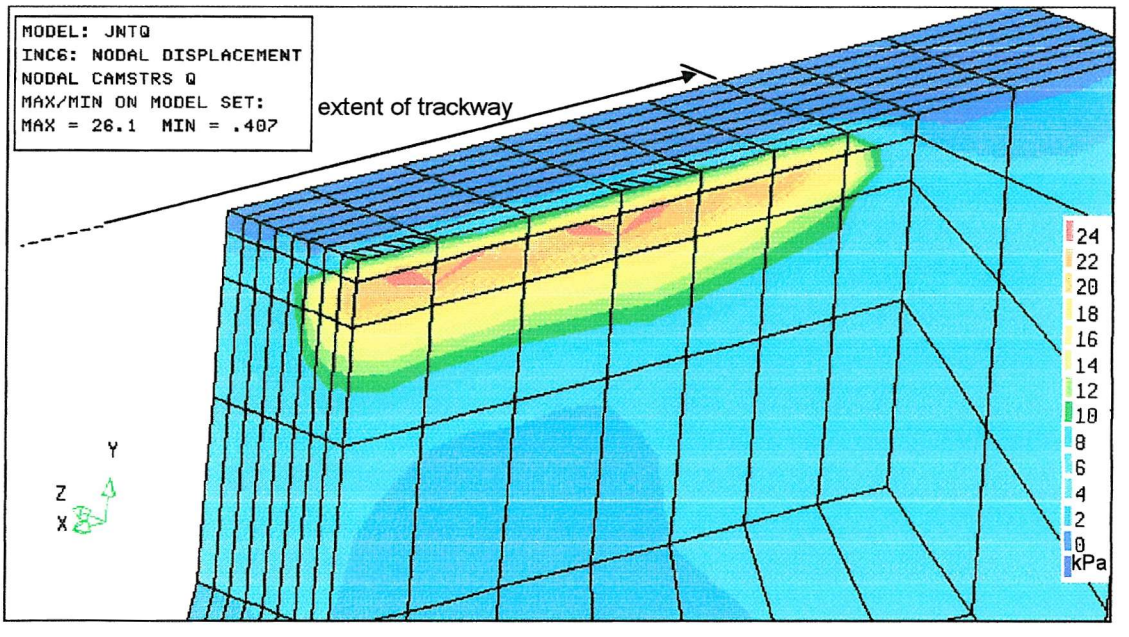

Figure 6.34: *Test 4*, deviatoric soil stresses

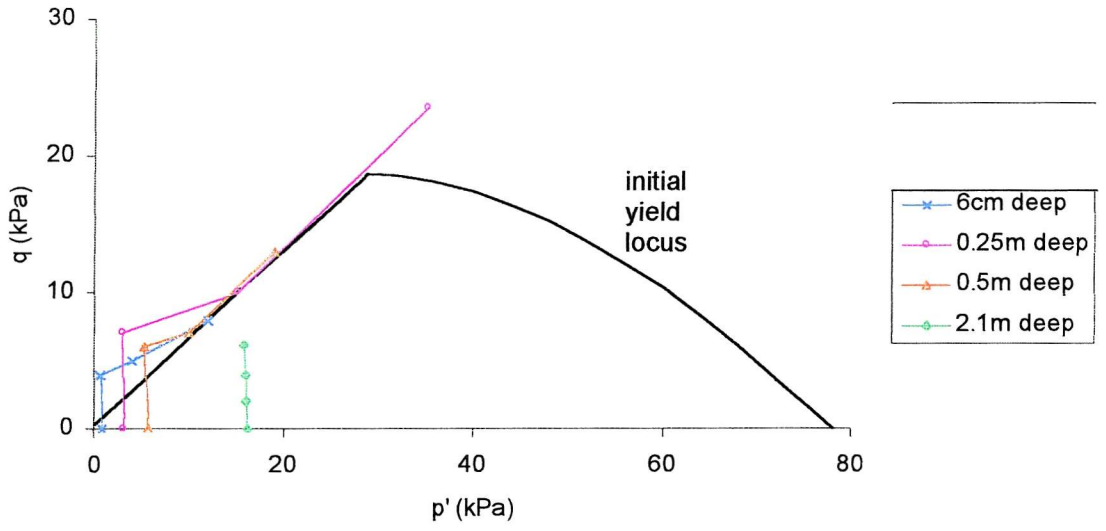

Figure 6.35: *Test 4*, stress paths in q-p′ space

This region of high q values is also evident in the stress paths in q-p′ space shown in Figure 6.35. They were recorded at various soil depths immediately beneath a loaded region of the trackway. There was a clear peak q value of 23kPa at 0.25m depth, corresponding with the contour plot in Figure 6.34. Other stress paths at 6cm and 0.5m depth also reached high q values showing that at least a 0.5m deep zone of soil immediately beneath the loaded area of trackway ruptured on the Hvorslev line. However, q values beneath this zone dropped very sharply with depth: at 2.1m depth the stress path remained well within the yield locus, in contrast with the equivalent stress path for analysis *Test 1* in Figure 6.14 which ruptured on the Hvorslev line. The effect of the jointed trackway was to concentrate very high deviatoric stresses in a shallow zone of soil beneath.

Stress paths in v-lnp′ space are not shown because an undrained soil model was used in the three-dimensional analyses.

The horizontal strain along the centre line and upper surface of the loaded trackway panel is shown in Figure 6.36. The profile resembled the characteristic 'W' shape with compression beneath the applied stresses and tension in between. The absolute

maximum strain of 0.0009, occurring beneath the applied stresses, was well below the approximate yield strain of 0.0018 showing that all trackway deformations would have been elastic with or without the Von Mises yield criterion.

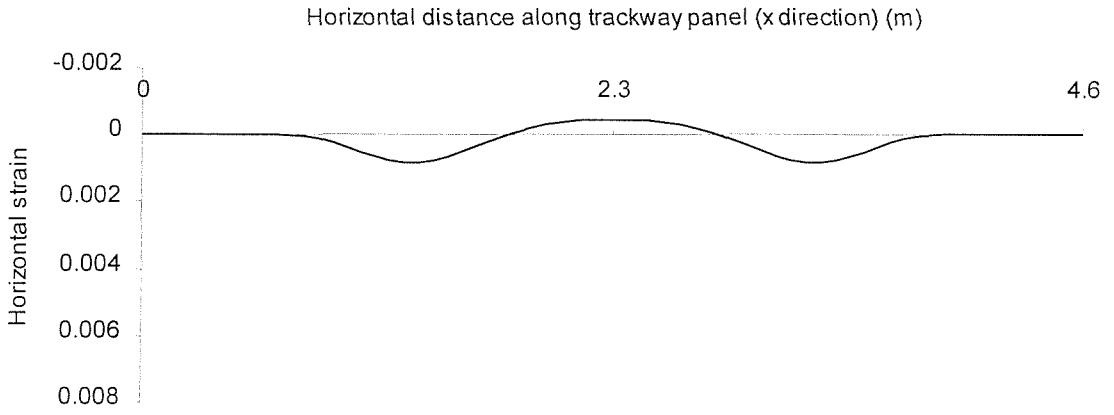

Figure 6.36: *Test 4*, transverse trackway strain profile

6.7.7 Analysis of *Test 3*

Centrifuge *Test 3* was identical to *Test 4* in all respects except that the trackway was unjointed. In a similar fashion, the only modification to this analysis was to remove the joints by changing the trackway elements to form a uniform mesh with full nodal connectivity along all the element edges.

The change is immediately evident in Figure 6.37 which shows the deformed mesh at the end of the analysis. The double-lines in the trackway mesh have disappeared and the trackway has become a uniform plate. The applied loads were located in the same areas, (shown shaded) but caused no significant visible deformation in the mesh. Profiles across the trackway surface, similar to those plotted in Figures 6.30 and 6.31, are shown in Figures 6.38 and 6.39. The jointed trackway profiles from the previous analysis have been plotted as a comparison. Clearly, the absence of joints has a significant effect on the longitudinal profile in Figure 6.38, with deflexions remaining consistently low, at

about 0.01 to 0.03m across all the trackway. In the transverse direction in Figure 6.39, overall deflexions were considerably reduced compared with the jointed trackway, all staying below 0.03m in contrast with consistent values of above 0.08m in the previous analysis. Interestingly, the amount of uplift in the soil on either side of the trackway was very similar in both analyses, showing that the large deflexions of the jointed trackway tended to drive the soil in the longitudinal direction as the panels rotated.

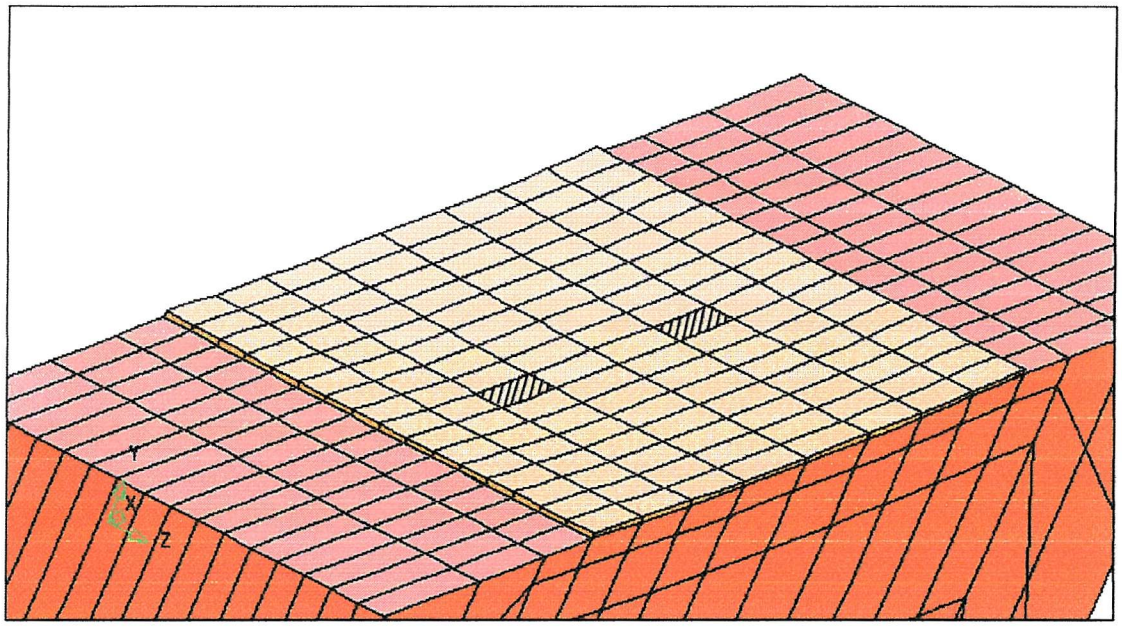

Figure 6.37: *Test 3*, deformed mesh (actual deformed scale)

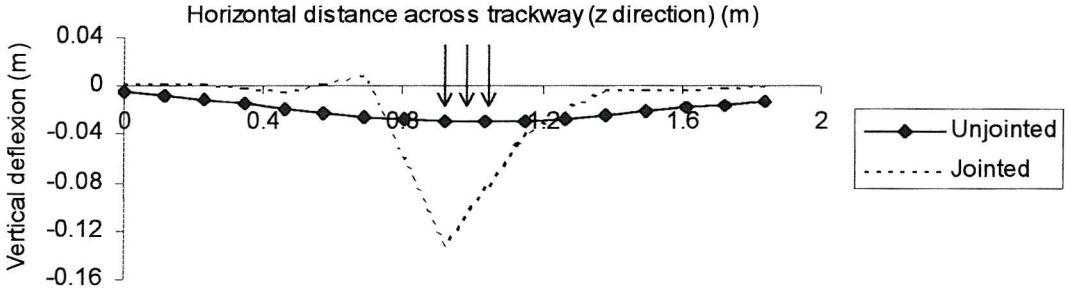

Figure 6.38: *Test 3*, longitudinal trackway deflexion profile

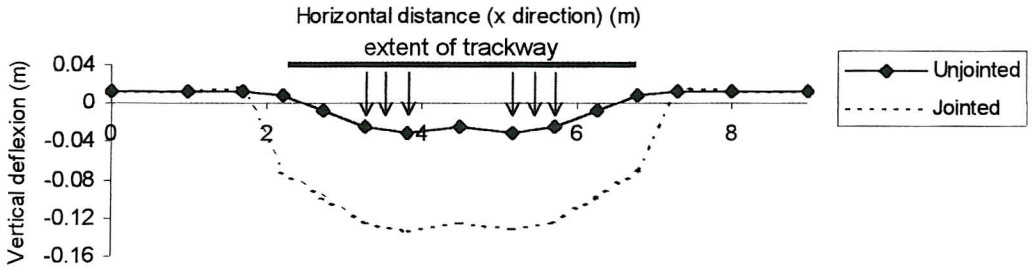

Figure 6.39: *Test 3*, transverse soil/trackway deflexion profile

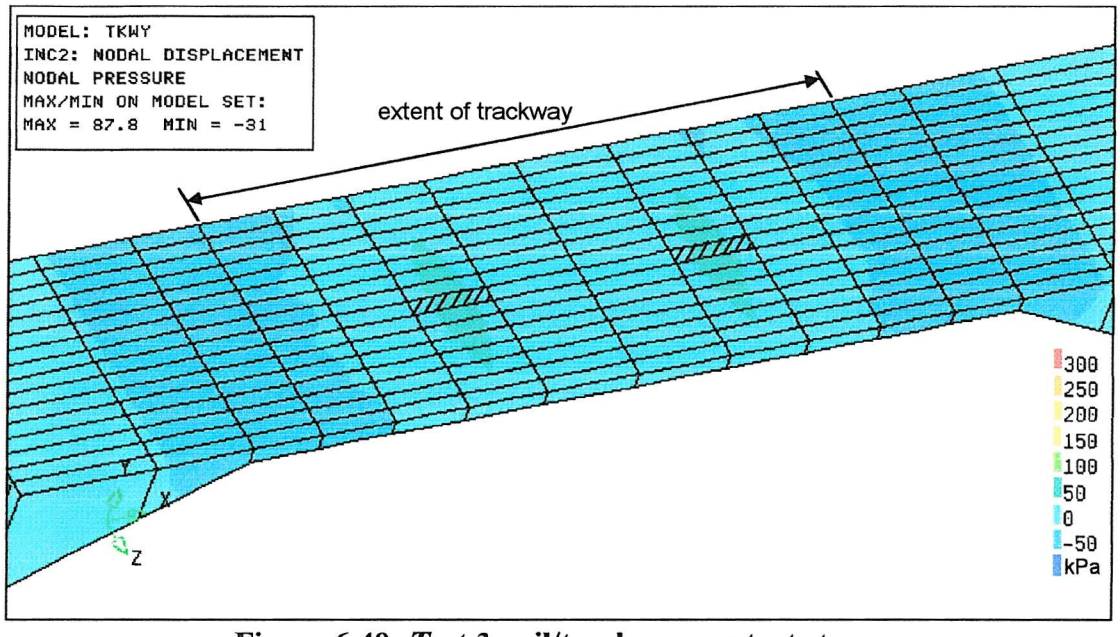

Figure 6.40: *Test 3*, soil/trackway contact stress

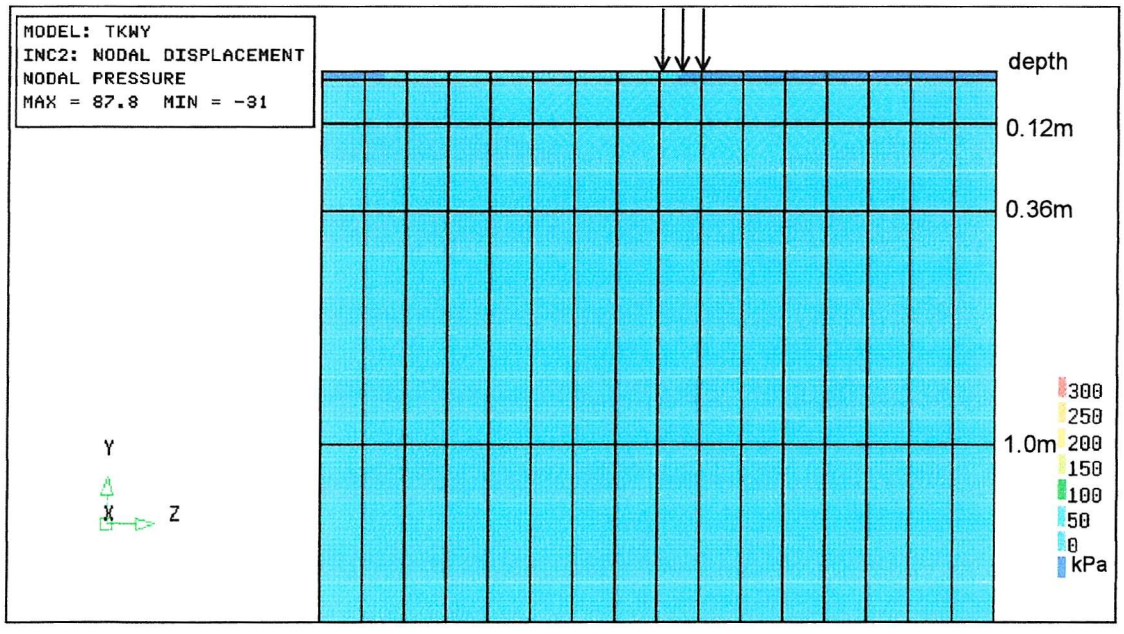

Figure 6.41: *Test 3*, total pore pressure on longitudinal section

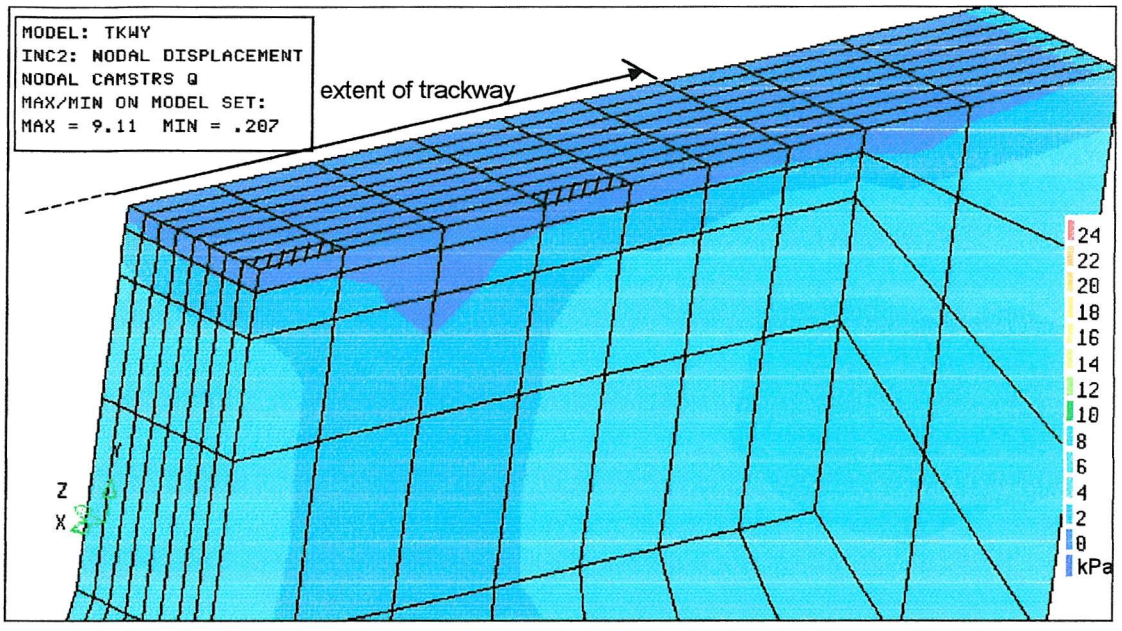

Figure 6.42: *Test 3*, deviatoric stresses

As a comparison with the *Test 4* analysis, identical contour plots to those shown in Figures 6.32, 6.33 and 6.34 are presented for this analysis in Figures 6.40, 6.41 and 6.42 for contact stress, pore pressure and deviatoric stress respectively. Since the same contour intervals have been used in these plots as in the previous analyses, no significant zones of contact stress or deviatoric stress can be seen, thus demonstrating the far superior stress distribution properties of the unjointed trackway over the jointed. Only in Figure 6.41 is the effect of the applied stress visible where pore pressures in excess of 50kPa occurred immediately beneath the trackway to a depth of 2.5m and spreading across five trackway panel widths. This is significantly wider than the two panel widths for *Test 4* and shows that the unjointed trackway was distributing the applied stresses far more effectively in the longitudinal direction.

The strain along the trackway in the transverse direction at the end of the analysis is plotted in Figure 6.43, together with the profile for *Test 4*. The two profiles were not as different as might be expected given the large differences in their deflexions, the strain in this analysis was only 10-20% lower than for the jointed trackway. It shows that the large trackway deflexions of the jointed trackway were primarily caused by the rotation

of the trackway panels and the embedment of trackway joints into the soil, rather than transverse bending of the trackway panels.

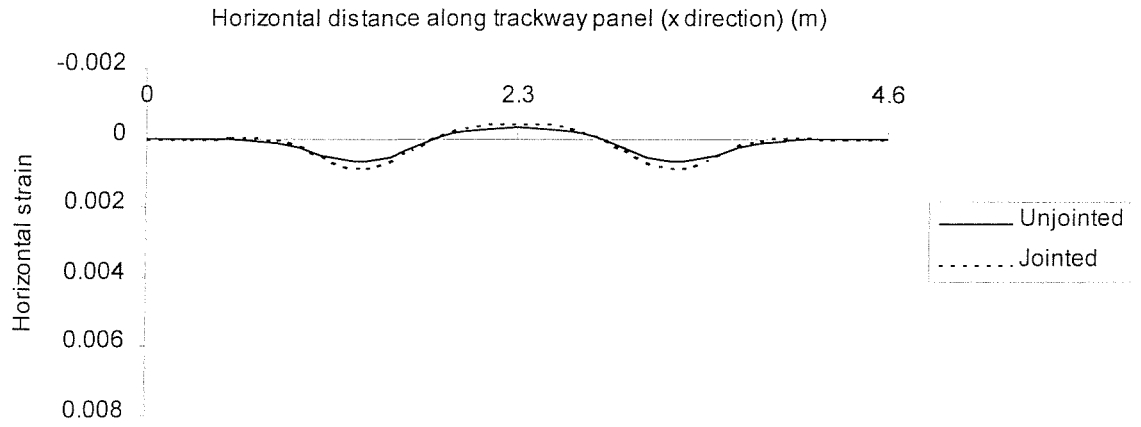

Figure 6.43: *Test 3*, transverse trackway strain profile

6.7.8 Slip element assessment

To assess the effect of excluding slip elements from the analysis, the *Test 4* analysis with jointed trackway was repeated after removing the slip elements from the mesh. This meant that the trackway elements were connected directly to the soil surface and no relative slippage or separation could occur between them. This analysis was denoted *noslip*.

Comparing the *noslip* analysis with the *Test 4* analysis results, no significant difference between the displacement profiles of the trackway were detected, showing the slip element had little effect on deflexions. However, when comparing measured stresses in the soil/trackway system there were considerable differences in the computed output. Figure 6.44 shows the measured contact stress between soil and trackway, calculated in the same way as described for Figure 6.32 above. The trackway has been cut away to expose the soil surface and the areas beneath the applied stresses are shaded. In these areas, rather than experiencing the high compressive stresses visible in Figure 6.32, only

small compressive stresses of less than 75kPa occurred, compared with a peak of 327kPa with slip elements in place.

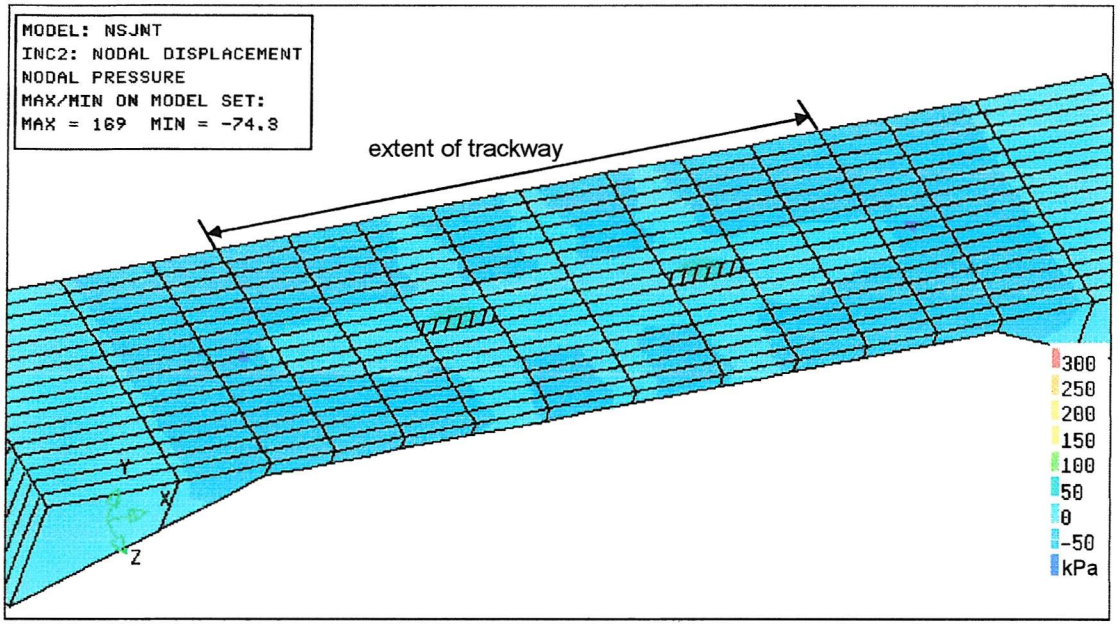

Figure 6.44: *Noslip*, soil/trackway contact stresses

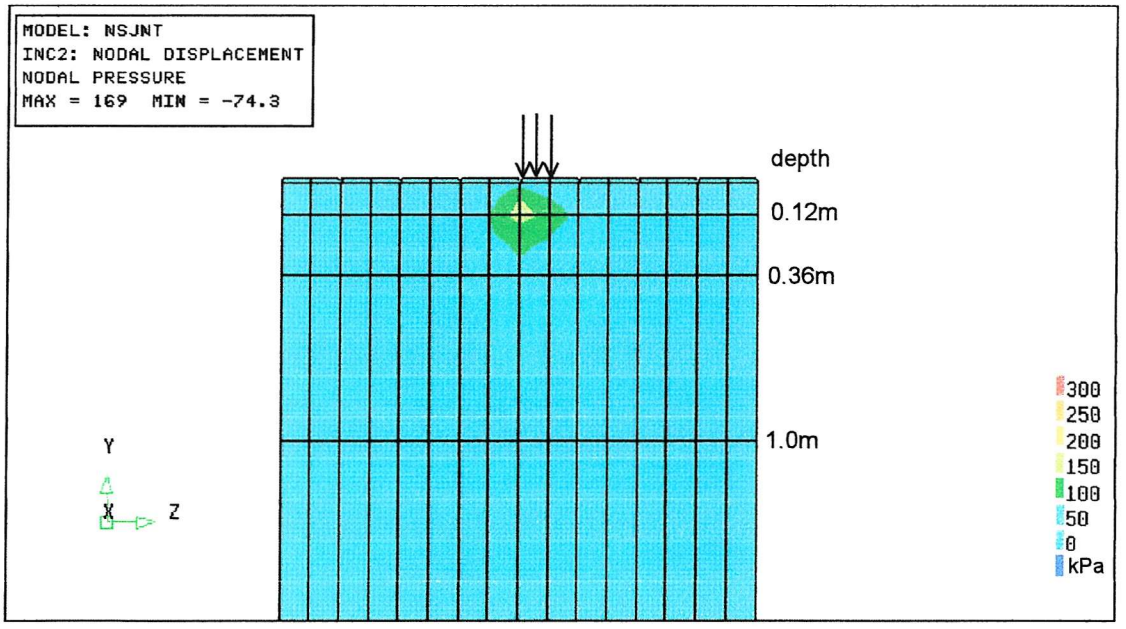

Figure 6.45: *Noslip*, total pore pressure on longitudinal section

The pore pressure beneath the trackway on the same section of soil in Figure 6.33 is shown for *noslip* in Figure 6.45. While the maximum pressure of 169kPa was high, it was about half the value obtained with slip elements. Nor did the peak pore pressure occur immediately adjacent to the joint, but at a depth of 0.1m. It is apparent that the applied stress was not being concentrated through the joint as much in the absence of slip elements, perhaps because uplift of the adjacent joints and soil/trackway slippage were not permitted, reducing the rotation of the panels under the applied stress. Clearly, the use of slip elements was required for these analyses to allow accurate interpretation of soil stresses.

6.7.9 Trackway modification

With the ultimate goal of improving trackway performance, some modifications were made to the trackway in these analyses to assess their feasibility for further investigation. The first modification was to restrain the ends of the trackway panels against rotation. This could be accomplished in the field with existing class 60 trackway by fixing clamps along the ends of the trackway panels, after it has been rolled out, or by any other means, to prevent joint rotation. This analysis was denoted *restrain* and the modification to the trackway is best illustrated in the deformed mesh shown in Figure 6.46. When the trackway was loaded, in an identical way to the preceding analyses, the panels rotated and the loaded joint embedded into the soil. However, the trackway ends remained horizontal because the elements had full nodal connectivity at the ends, hence removing the articulated joint or simulating a rigidly fixed joint at the end. The difference is most marked when compared with the deformed mesh for *Test 4* in Figure 6.29. Not only was panel rotation severely restricted at the ends, but also along the full length of the loaded panel, rotations were reduced. Therefore fixing the joints at the ends of the panels helped to restrain the joints along the panels by utilising the torsional stiffness of the panels. The torsional stiffness is not used in conventional trackway but allows the more effective transverse panel section to contribute much needed stiffness in the longitudinal direction.

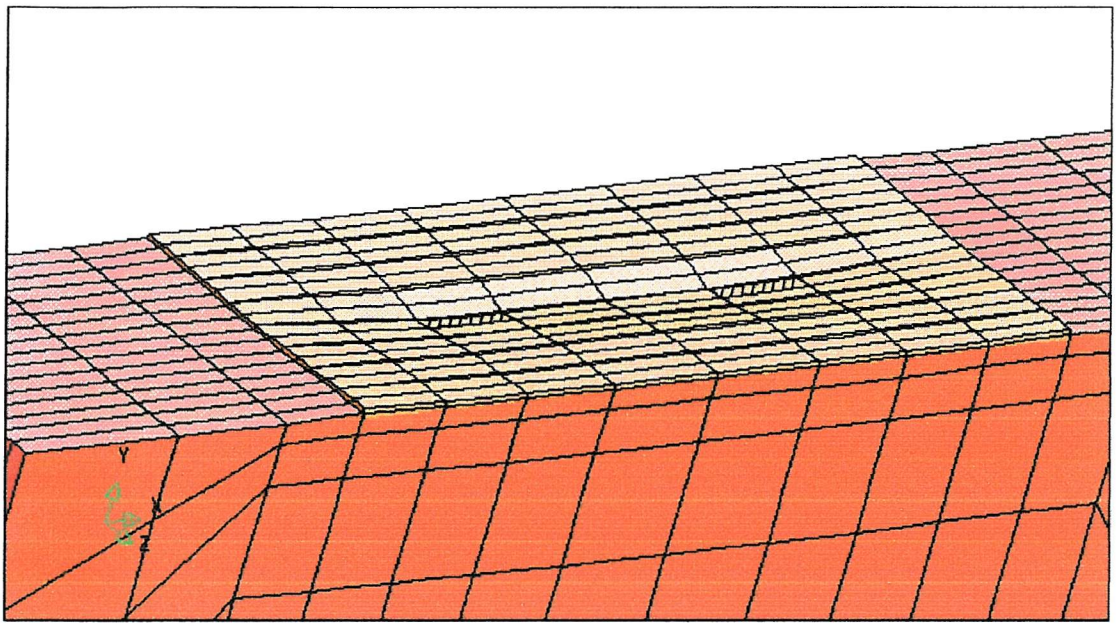

Figure 6.46: *Restrain*, deformed mesh (actual deformed scale)

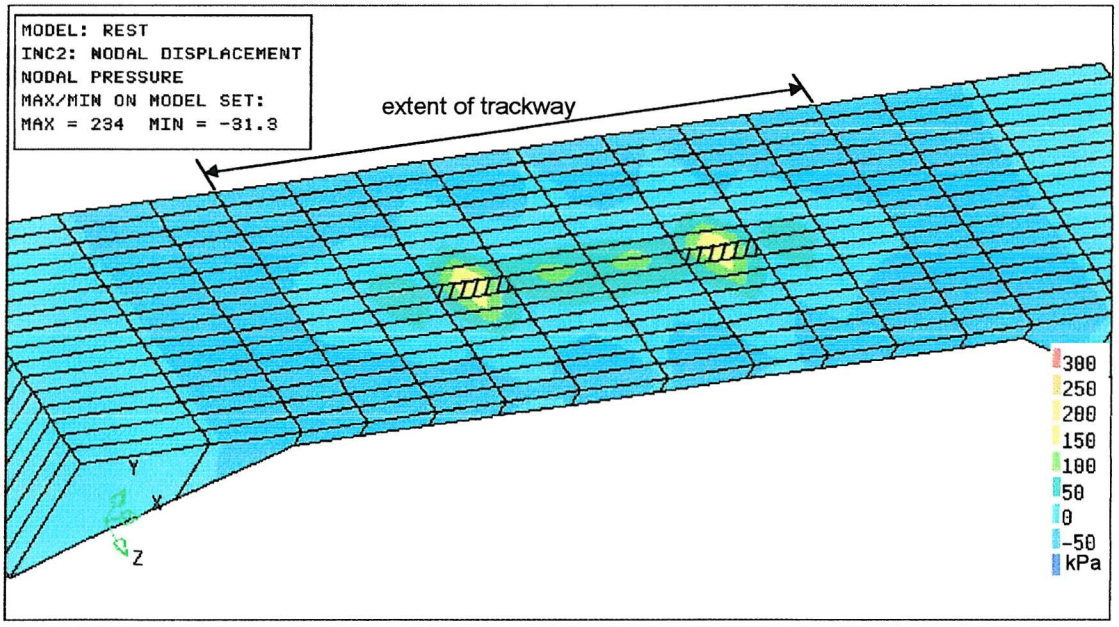

Figure 6.47: *Restrain*, soil/trackway contact stress

The contact stress distribution between the restrained trackway and the soil, calculated in the same way as described above, is shown in Figure 6.47. They were consistently reduced by 50-100kPa along the full length of the loaded panels, when compared with the contact stresses for *Test 4* in Figure 6.32, with a peak stress of about 200kPa rather than 300kPa. It is also of note that restrained trackway seemed more effective at distributing stress in the longitudinal direction, with the contours being more elongated across adjacent panels than before.

The trackway displacement profiles will be compared for all the modified trackway configurations at the end of this chapter.

A second proposed modification was to increase the panel widths of the trackway to reduce the number of joints (the weakest point) per unit length of roadway. Two modified finite element meshes were set up: one with panels $1^1/_2$ times as wide as existing class 60 trackway, denoted *wide1.5*; the other with panels twice as wide, denoted *wide2*. These modifications were made by simply changing the positions of the articulated joints to form trackway panels three elements wide and four elements wide for *wide1.5* and *wide2* respectively. The *restrain* modification was removed for these analyses. The modified meshes also allowed an assessment of the different effects of loading the joints and loading the centre of the panels. Since each panel was now at least three elements wide, the vehicle load could be applied either adjacent to a joint or in the centre of the panel.

Figure 6.48 shows the deformed mesh at the end of analysis *wide1.5* with a central load whose area of application is shown shaded. The double lines on the mesh showed that the joints now occurred every three rows of elements. The trackway deflexions were smaller and had a different shape to the *Test 4* analysis. Since the panel was loaded centrally, it remained horizontal, the joints did not embed into the soil and the deflexion profile was much flatter. In contrast, Figure 6.49 shows the same deformed mesh when the panel was loaded adjacent to a joint. Here, the deflected shape looks considerably more similar to *Test 4*. The loading of a joint had a very detrimental effect on trackway

performance. This is in contrast to the Georgiadis (1979) study of landing mats which stated that the mat was as effective in distributing load to the ground when the load was over a joint as when it was in the centre of a panel.

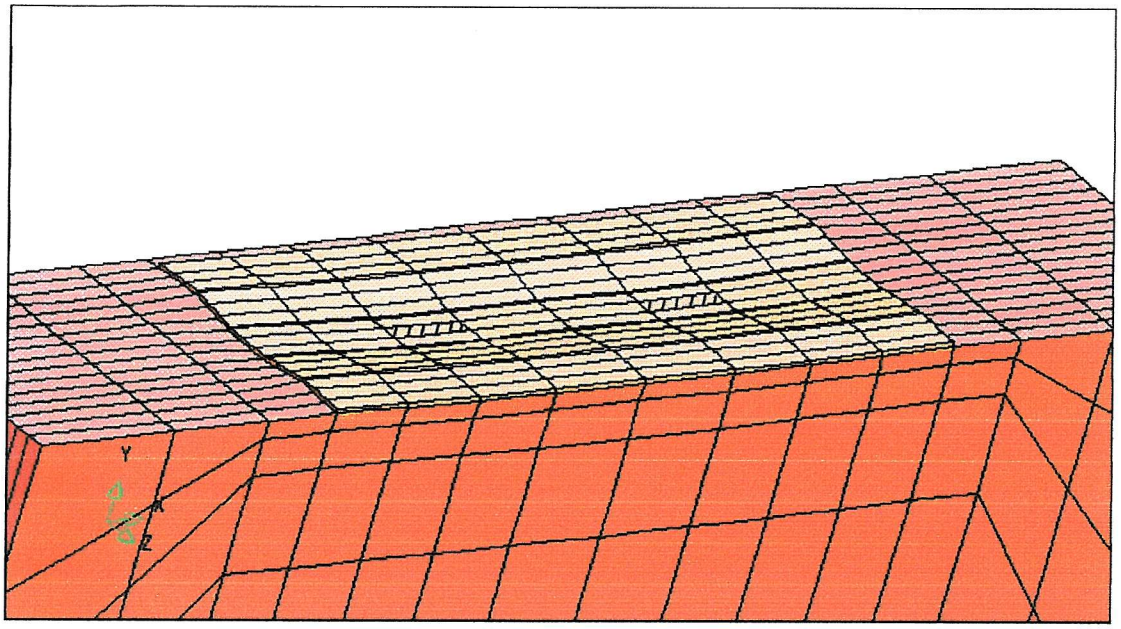

Figure 6.48: *Wide1.5*, central load deformed mesh (actual deformed scale)

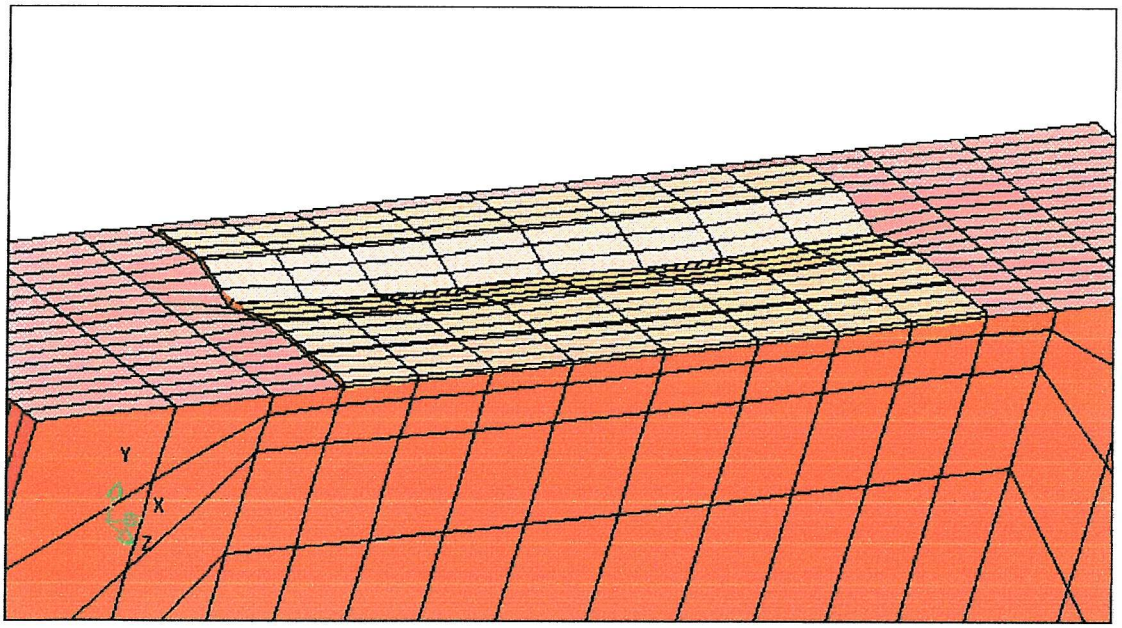

Figure 6.49: *Wide1.5*, joint load deformed mesh (actual deformed scale)

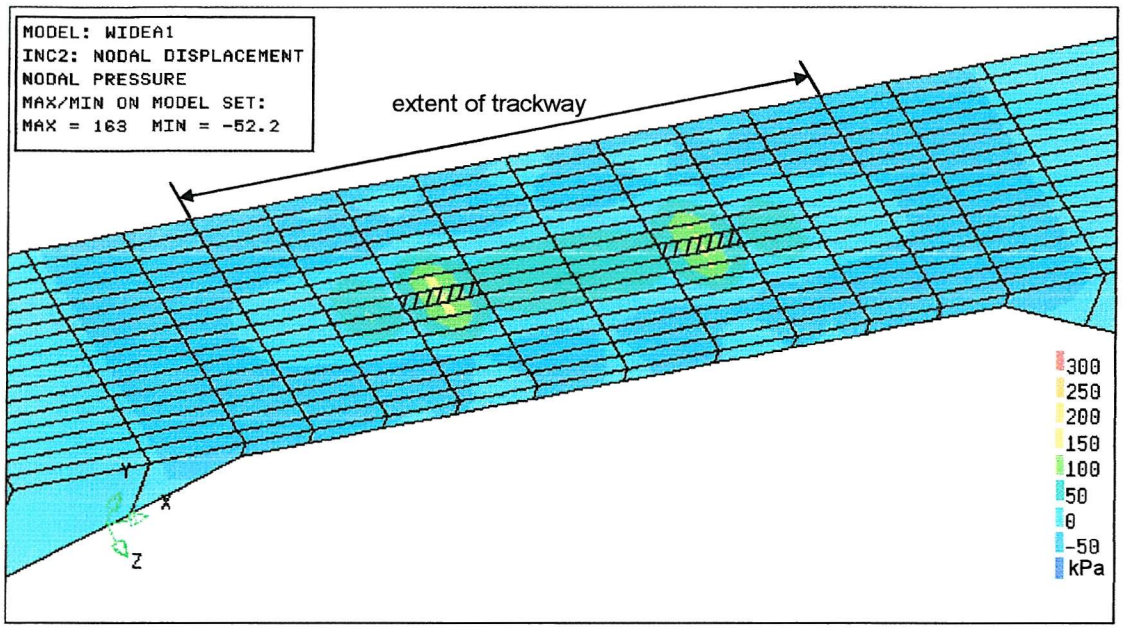

Figure 6.50: *Wide1.5*, central load soil/trackway contact stress

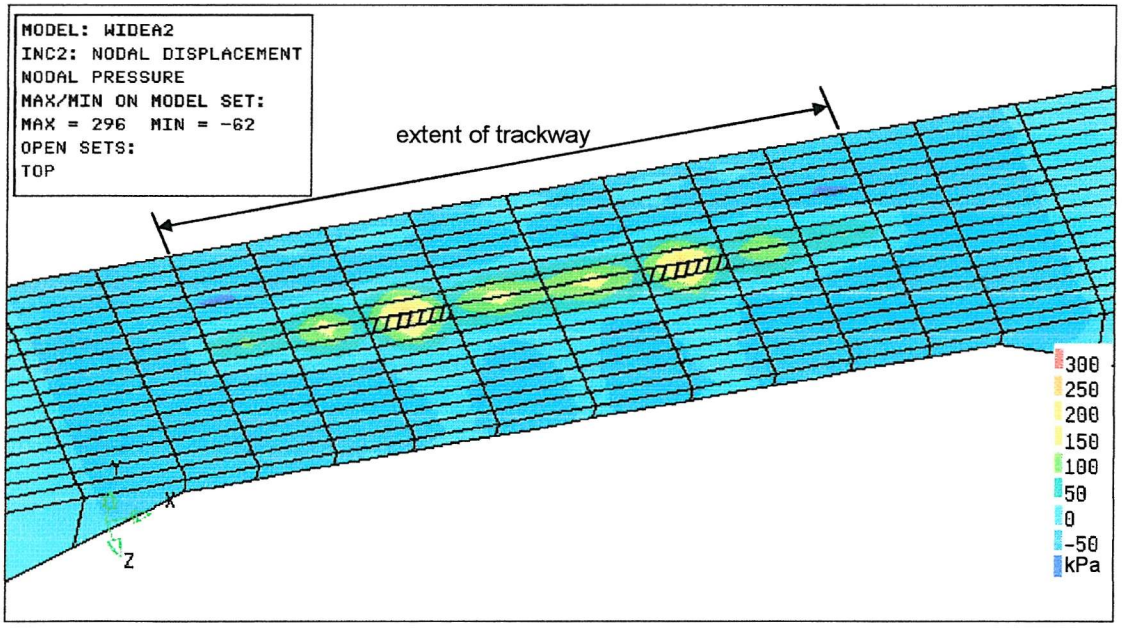

Figure 6.51: *Wide1.5*, joint load soil/trackway contact stress

The contact stresses for *wide1.5* shown in Figures 6.50 and 6.51 for a centrally applied and joint applied load respectively also show significant differences. The centrally applied load produced a peak contact stress of about 150kPa and distributed the stress more effectively in the longitudinal direction. The joint applied load produced a higher peak contact stress of about 250kPa and its distribution closely resembled that of *Test 4* shown in Figure 6.32. However, the $1^1/_2$ times wider panel did generally reduce contact stress along the panel by approximately 50kPa.

The deformed meshes at the end of the *wide2* analysis are shown in Figures 6.52 and 6.53. Since each panel now contained four rows of elements it was only possible to load the trackway adjacent to the centre of a panel, and this is shown by the shaded area in Figure 6.52. Since the applied load was off-centre there was a slight rotation of the trackway panels. When the applied load was applied adjacent to a joint, as shown in Figure 6.53, the panel rotation increased, but not to the same degree as *wide1.5* and *Test 4*, the trackway profile is notably flatter.

The contact stresses for *wide 2*, shown in Figures 6.54 and 6.55, also showed changes between them. For the off-centre applied load, the peak contact stress was about 150kPa, similar to the centrally applied load in *wide1.5*, with stresses well distributed in the longitudinal direction. For the joint applied load, shown in Figure 6.55, the contact stress pattern again resembles the joint applied loads in *wide1.5* and *Test 4* with a peak value of about 220kPa. This was a further reduction of about 30kPa from *wide1.5* and about an 80kPa overall reduction from *Test 4*.

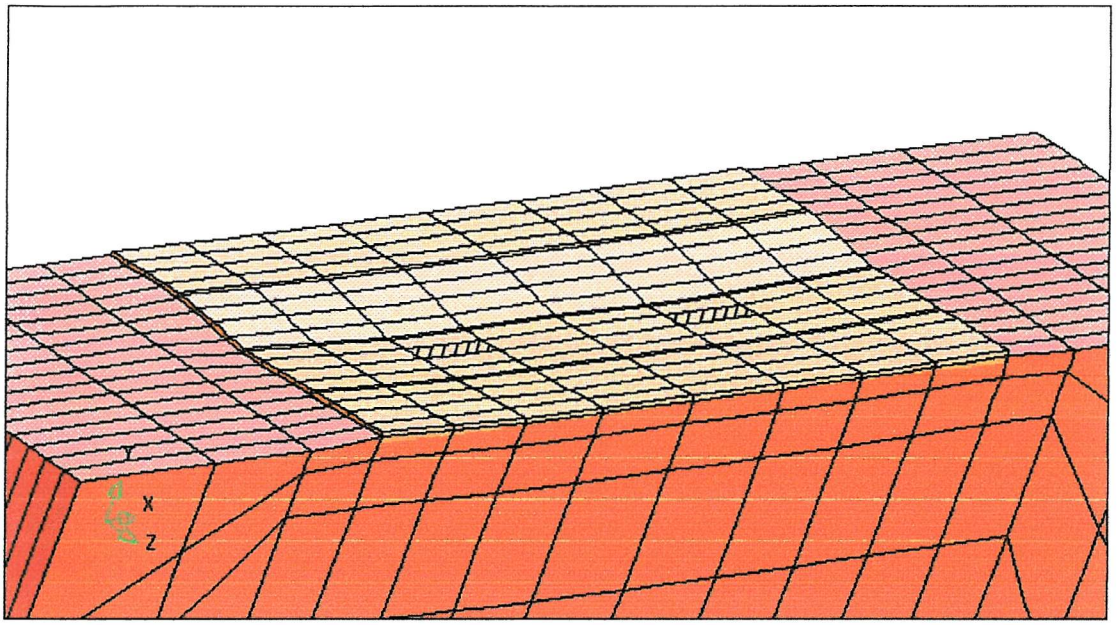

Figure 6.52: *Wide2*, off-centre load deformed mesh (actual deformed scale)

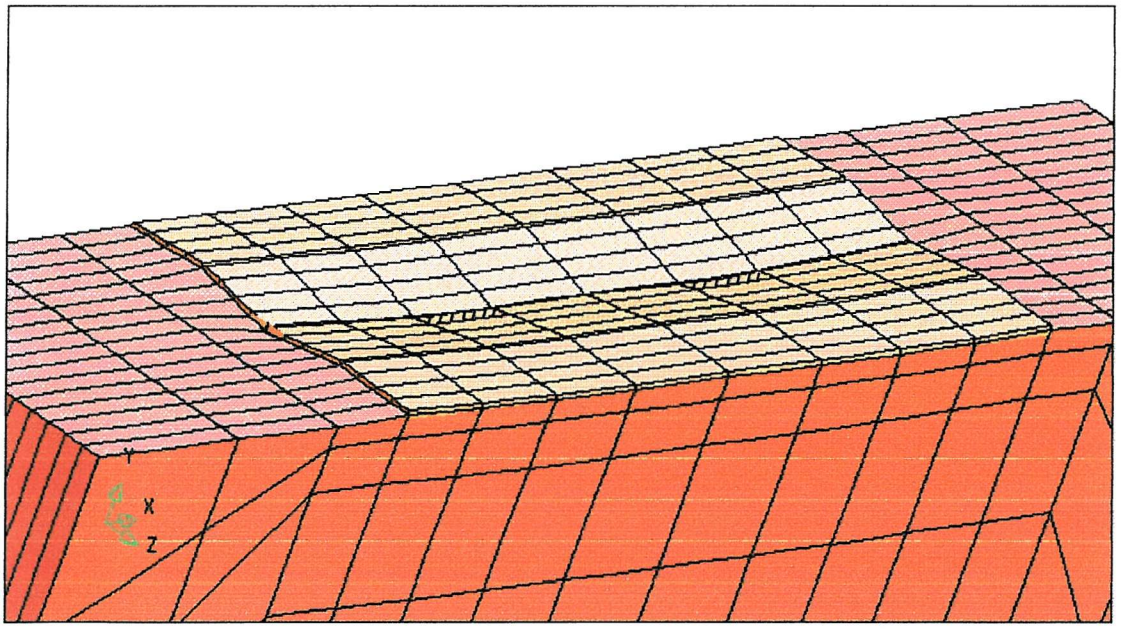

Figure 6.53: *Wide2*, joint load deformed mesh (actual deformed scale)

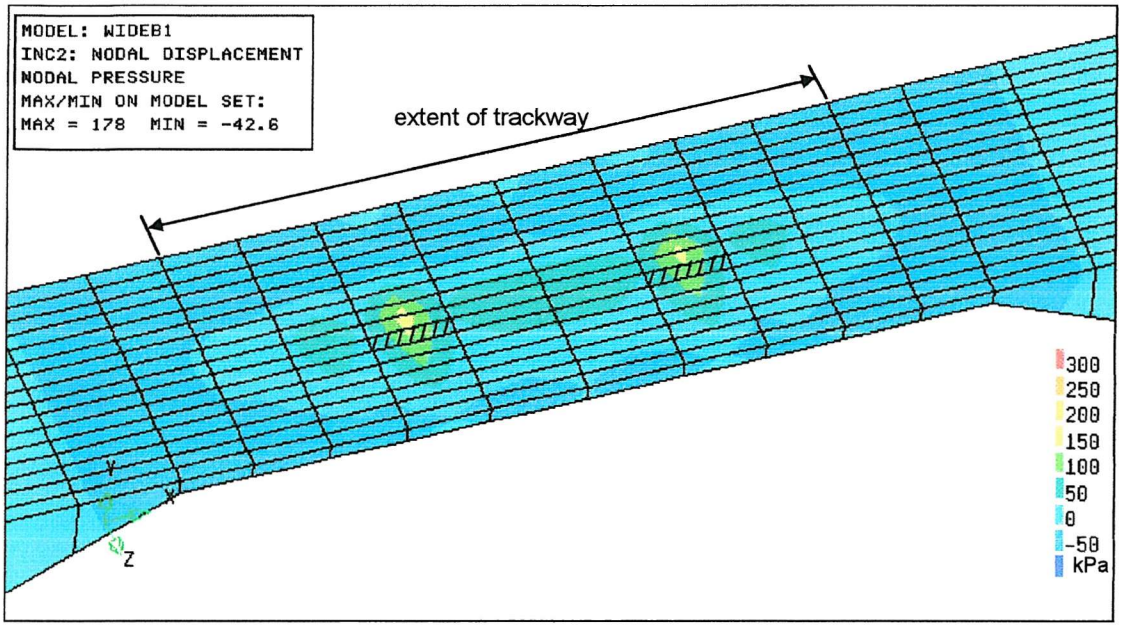

Figure 6.54: *Wide2*, off-centre load soil/trackway contact stress

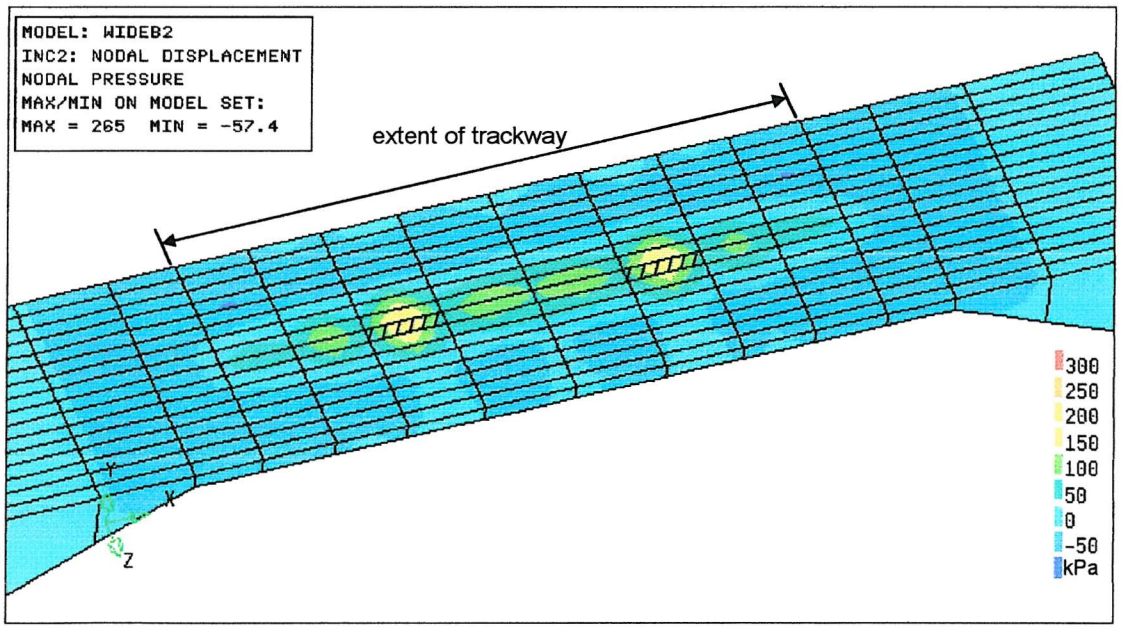

Figure 6.55: *Wide2*, joint load soil/trackway contact stress

The trackway profiles in the longitudinal direction across the panels for all of the three-dimensional analyses are shown in Figure 6.56. It provides a telling indication of the relative performance of each of the trackway configurations. The *Test 4* analysis replicated the original class 60 trackway and performed the worst with a maximum deflexion of 0.13m. The *Test 3* analysis with unjointed trackway performed the best with a maximum deflexion of only 0.03m. Between these two lie the various preliminary proposed modifications. When loaded on a joint, *wide1.5* reduced deflexions compared with class 60 by about 0.015m, *wide2* by 0.03m and *restrain* by 0.045m: a consistent improvement in performance with *restrain* the most effective. It is interesting to note the effect of loading the joint when comparing these values with the centrally loaded *wide1.5* and *wide2* whose maximum deflexions were only 0.06m, just over half their "on-joint" values. If the deflexion of trackway varies to this extent as a vehicle passes over each individual panel, a considerable pumping effect must be exerted on the underlying soil as evidenced in the centrifuge model tests reported in Chapter 4.

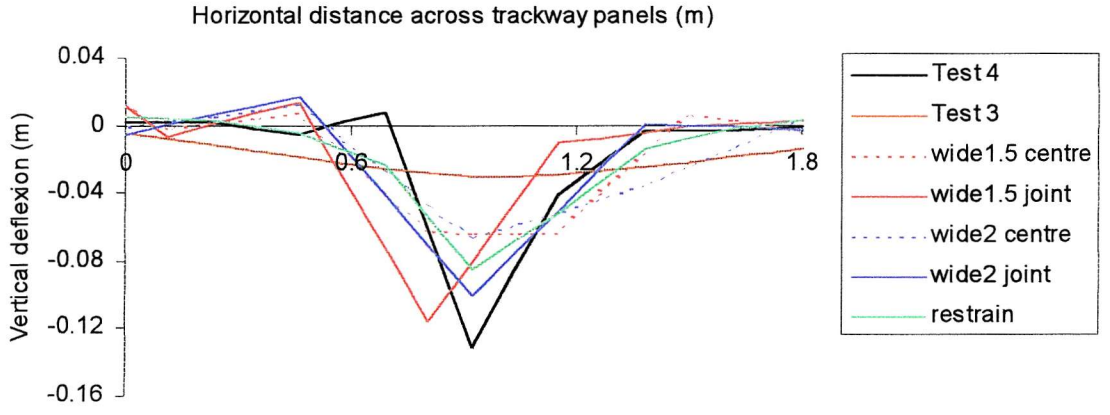

Figure 6.56: Comparison of longitudinal trackway profiles for all analyses

Chapter 7

Finite Element Analysis Results & Comparison with Centrifuge Test Data

7.0 Introduction

The results of the finite element analyses presented in the previous chapter are discussed with particular reference to trackway deflexions and soil/trackway contact stress. The results are compared with the centrifuge test data presented in chapter 4.

7.1 Trackway deflexions and strain

Figure 7.1 compares the applied stress/deflexion response of both plane strain centrifuge tests (test1 and test2) and FEA *test 1*. They show close agreement up to the applied stress of 115kPa, with maximum deflexions reaching, in all cases, approximately 100mm. When the applied stress was increased further, there was less agreement between the results. In centrifuge test 1 the applied stress was increased rapidly in small steps and small horizontal portions of the graph are visible at several values between 140 and 180kPa where the soil/trackway system appeared to yield, but hardened somewhat under consolidation, until eventually failing at about 180kPa. The "Cent test 1" graph has been truncated (deflexion continued to increase up to approximately 800mm). In centrifuge test 2 the mean applied stress was increased in three steps over periods of time to detect any deterioration of soil properties under a cyclic load. The clay did not fail but merely consolidated, although large deflexions in the trackway were evident. The applied stress in FEA *test 1* was increased more smoothly and thus produced a smoother line on the graph. It never achieved a horizontal profile, since finite element analyses can only approximate failure mechanisms. For this reason, it is difficult to determine failure stresses from finite element analyses. However, much of the data presented in Chapter 6 suggested failure of the soil/trackway system occurred at about 150kPa. The FEA predicted significantly lower deflections, at applied stresses above 115kPa, than the centrifuge test. A likely explanation for this is that as the trackway deformed in the centrifuge test, the applied stress could only be applied along knife-edges at the extreme edges of the loading platen, maximising the effective width of the trackway (see Figure 7.2). In the FEA, stresses were always applied across the full widths of the load strips, giving rise to a contact stress distribution more conducive to trackway deformation, as shown in Figure 7.2. The influence of contact stress distribution on trackway performance was discussed in Section 5.1 regarding the calculation of undrained bearing capacity.

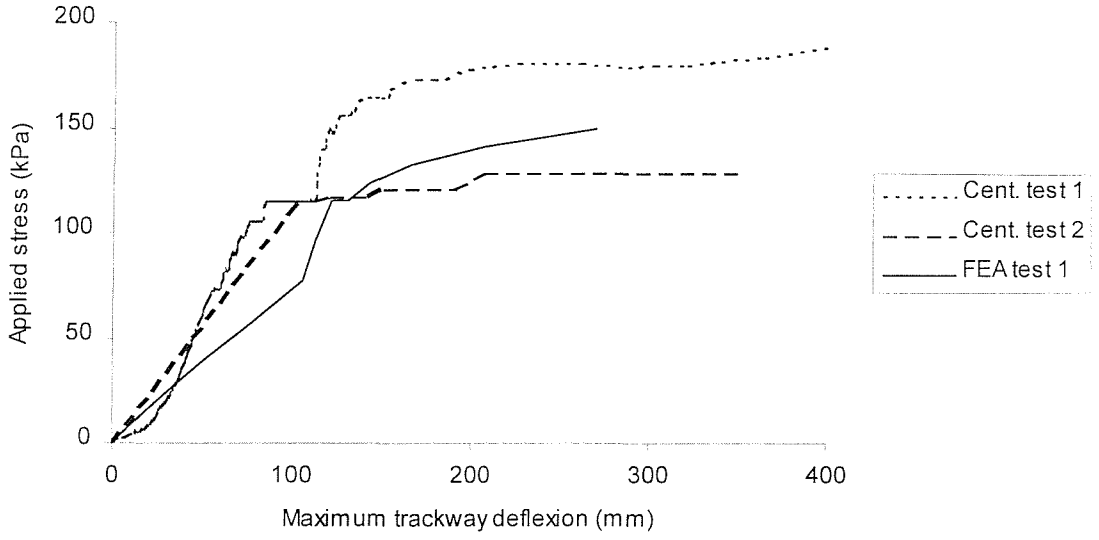

Figure 7.1: Stress/deflexion graphs for the plane strain models

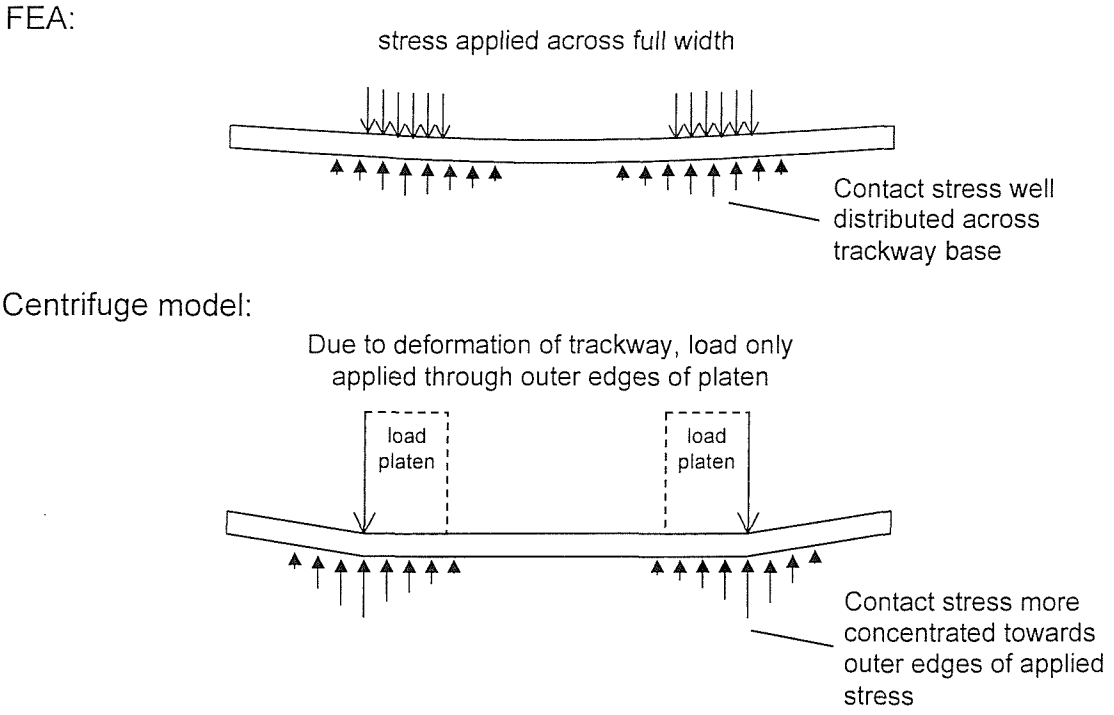

Figure 7.2: Comparison of contact stress distribution in centrifuge and FEA

This theory is borne out by the strain profiles for test 1 shown in Figure 7.3. There was very good agreement between the values of strain between the applied stresses but the centrifuge profile tended to concentrate strains on the outer edges of each applied stress region. This shows that trackway deformations in the centrifuge test were focused towards the ends of the trackway and suggested that it had a greater effective width than in the FEA. The FEA strain maxima and plastic hinges were positioned centrally beneath each of the applied stresses where most of the trackway deformations were concentrated. The centrifuge test strain maxima were much lower than in the FEA and it was significant that the strain gauge arrangement (marked with squares for the "180kPa" graph) skipped the peak in FEA strain. Had a strain gauge been mounted in this position, it is highly likely that larger strains would have been recorded, thus matching more closely the FEA maximum values.

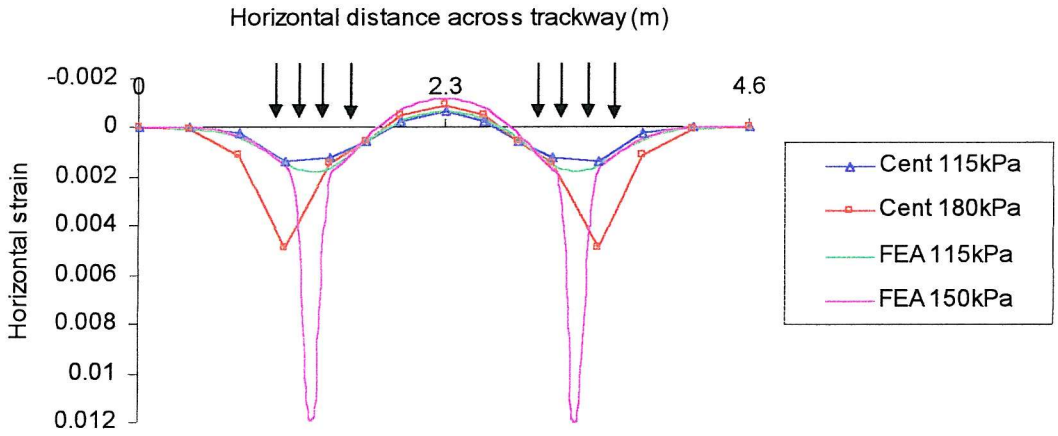

Figure 7.3: Comparison of transverse strain profiles in plane strain models

The graph shown in Figure 7.1 shows that the applied failure stress of Class 60 trackway on this particular clay, ignoring the effects of long-term consolidation, was in the region of 150 to 180kPa. This is significantly lower than the lowest estimate of bearing capacity of 209kPa given in Section 5.1. The flexible nature of the transverse Class 60 trackway section causes it to under-perform when compared with a rigid foundation of similar

dimensions. Thus the use of bearing capacity factors to predict soil/trackway failure would be inappropriate.

In addition, the occurrence of a bearing capacity failure in trackway beneath one heavy vehicle is inconsistent with field experience. While the plane strain methods of modelling, both in the centrifuge and with finite elements for tests 1 and 2 proved insufficient at re-creating the true nature of trackway failure, they nonetheless validated many of the FEA parameters and gave insight into the nature of transverse trackway bending.

One of the insights came with observations of the effect of plastic hinges forming in the trackway. In Figure 4.13, the transverse strain profiles in centrifuge test 2, the peak strain at the mean applied stress of 113kPa had already reached 0.002: approximately the estimated yield strain. The maximum strain increased further with higher applied stresses, reaching 0.009 at the end of the test, indicative of well-advanced plastic hinges in these regions. However, the soil/trackway system did not fail noticeably, certainly not at the mean applied stress of 121kPa when the strain reached 0.003, and trackway deflexions simply increased with the consolidation of the underlying clay.

In addition, in FEA *test1*, a plastic hinge was identified in the trackway in the stress state plot in Figure 6.18, at an applied stress of 123.75kPa. This was well below the approximate failure stress of 150kPa. In the analysis *test1 (elastic trackway)*, where plastic hinges could not occur in the trackway, although soil/trackway performance improved, the deflexion increase towards the end of the analysis suggested soil/trackway failure was still starting at 150kPa applied stress (Figures 6.19 and 6.20).

Although the formation of plastic hinges in the trackway have been shown to be detrimental to soil/trackway performance, they do not result in its immediate failure.

The second insight was the intrinsic nature of soil and trackway deformations observed in Figures 5.6 and 5.7. In both centrifuge tests 1 and 2, trackway deformations (i.e.

horizontal strains) increased concurrently with underlying soil settlement. Trackway deformations formed as a direct result of the soil displacement beneath. Since soil/trackway deflexions seem to be determined primarily by stress-induced soil displacements, the aim of improving soil/trackway performance may be most easily achieved through minimising the stresses applied to the soil, i.e. the soil/trackway contact stress.

In centrifuge tests 3 and 4, involving the moving axle, the accumulation of axle settlements (caused by trackway settlement) shown in Figure 5.4 were markedly different between the unjointed and jointed trackway cases. Axle settlements were greater in test 4 than in test 3 after the first pass and increased at a much higher rate. The appearance of clay slurry between the joints after only two passes in test 4 shown in Figure 4.25, suggested that a thin surface layer of the underlying clay failed on the first pass.

Finite element analyses *test3* and *test4* showed a similar contrast between jointed and unjointed trackway deflexions. Only one load case was analysed and the two longitudinal profiles were compared in Figure 6.38. The maximum jointed trackway deflexion was over four times the maximum unjointed deflexion. The FEA deflexion values were somewhat higher than the centrifuge test values, most likely because the FEA's used static vehicle loads. In the centrifuge tests the vehicle was rolling continuously, but smoothly, and any part of the underlying clay was subjected to very transient stresses which would not cause the same level of soil deflexions measured in the FEA's. In addition, by measuring axle settlement, the wheels of the axle, particularly on the jointed trackway, were somewhat isolated from the trackway and would have bridged the more extreme trackway deflexions.

The transverse trackway strain profiles for tests 3 and 4 in both the centrifuge tests and FEA's are compared in Figure 7.4. The test 3 profiles, as well as FEA *test4*, were very similar, with absolute strain values always below 0.001. The centrifuge test 4 strain values are slightly higher because these were the maximum values in the test after 80

vehicle passes. However, the trackway did not yield and the similarity between the jointed and unjointed trackway strain profiles showed that most of the jointed trackway deformations must have occurred through joint rotation, rather than in the transverse direction. It is interesting to note that soil failure in test 4 (centrifuge and FEA) was brought about without significant transverse trackway deflexions or yield. This shows that the transverse nature of trackway failure, observed in the field, occurs after the soil has failed beneath the joints. The degraded soil is driven aside or through the joints to form voids beneath, hence causing the transverse failure. This reaffirms the idea of intrinsic soil and trackway deformations in the plane strain tests described above: trackway deflexions reacting to soil displacements.

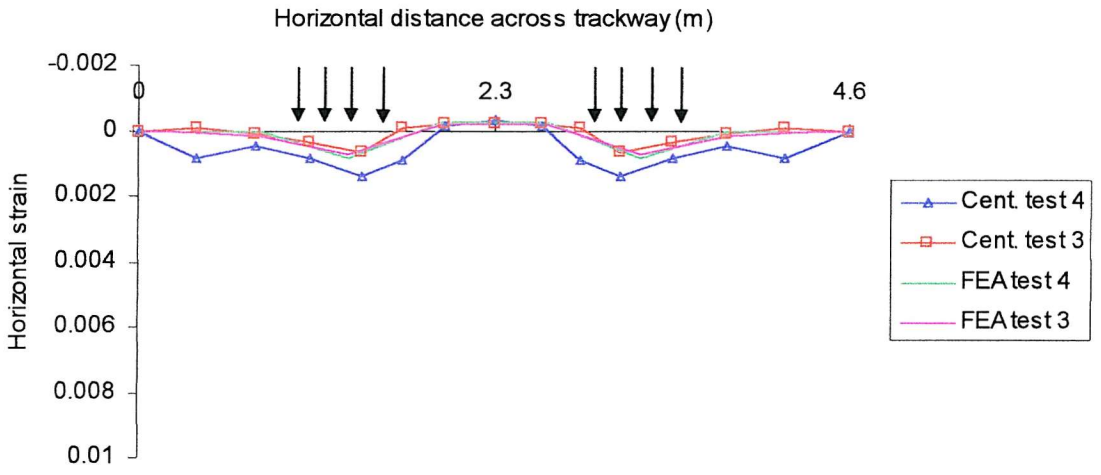

Figure 7.4: Comparison of transverse strain profiles in 3D models

7.2 Pore water pressure

Figure 6.11 showed the excess pore pressure in FEA *test1* under an applied stress of 115kPa, with a peak value of 33kPa about 0.5m below the trackway. There was also a bulb of pressure of 15-20kPa between 2 and 3m beneath the trackway. A similar plot for centrifuge test 1 was shown in Figure 4.7, which also displayed a 20kPa bulb of pressure at 2-3m depth beneath the trackway. However, the higher peak of 33kPa at 0.5m depth was not visible, simply because there were no pore pressure transducers close enough to the soil surface to register it. 0.5m depth at prototype scale was equivalent to 13mm depth at model scale and since the pore pressure transducers had 6mm diameters themselves, it was difficult to locate them very close to the surface without interfering with the soil/trackway interface and themselves experiencing large displacements.

The regions of negative excess pore pressure at either end of the trackway during soil failure extended to greater depths and were registered in centrifuge test 1 (Figure 4.8) and FEA *test1* (Figure 6.12), both showing a peak value of around –10kPa at 0-2m depth. This behaviour was characteristic of the shear zones in a bearing capacity failure, and the stress state plot in Figure 6.17 showed that the clay had a tendency to soften, or experience suction under partly drained conditions, when sheared in these regions.

In the contour plots of excess pore pressure for centrifuge tests 3 and 4 in Figures 4.19 and 4.24 respectively, particularly for test 4, only modest values were measured, out of proportion of the level of applied stress. It was suggested in Section 5.3 that very much higher values of excess pore pressure must have occurred near the surface of the clay, which could not be registered by the adopted transducer arrangement. The FEA pore pressure plots confirmed this, with *test3* in Figure 6.41 showing values in excess of 50kPa at soil depths of less than 0.25m, and *test4* in Figure 6.33 showing values in excess of 50kPa down to 0.7m depth and a maximum value at the surface of 327kPa.

This very high value of excess pore pressure seems feasible given the estimate of contact stress beneath trackway of 1200kPa, when using its longitudinal stiffness, in Figure

5.10. However, there was likely to be some exaggeration of pore pressure and contact stress beneath the joint since in the finite element mesh it was located at the base of the trackway and directly in contact with the underlying soil. In prototype trackway, the joint is located at the mid-depth of the section and is not in direct contact with the soil. Constraints on the number of elements available in each mesh would make such an arrangement prohibitive in the FEA's.

7.3 Soil/trackway contact stress

In Section 5.1 the relationship between contact stress and foundation slope, observed by Hemsley and Spence (1987), was discussed. They showed: a) as the deflected slope of a foundation increased, the contact stress increased as a continuous relationship; b) the deflected slope of the foundation depended on its relative stiffness with the underlying material.

These effects were also observed in the finite element trackway bending stiffness analysis in Section 6.6.8 and can be seen by comparing Figures 6.22 and 6.23. The deflected trackway slope of analysis *EI10 000* in Figure 6.23 was almost horizontal and, consequently, displayed the lowest contact stress (except at the extreme ends due to its rigid characteristics) in Figure 6.22. Analysis *EI13*, which had the highest contact stresses beneath the applied stresses, also had the steepest slopes in the vicinity of the applied stresses. Analysis *EI13* also possessed the lowest relative trackway/soil stiffness, thus following the inverse trend of increasing trackway slope with decreasing relative stiffness.

By comparing the longitudinal profiles of analyses *test3* and *test4* in Figure 6.38, trackway joints clearly have an influence on trackway slope in this direction. As a result, following the above trend, significant differences between their contact stresses would be expected. This is confirmed by comparing Figure 6.32 for jointed trackway where the peak contact stress beneath a joint was 327kPa, and Figure 6.40 for unjointed trackway

whose peak contact stress was only 88kPa. The negligible bending stiffness of the trackway joint caused deflexions to be concentrated there, generating steep trackway slopes and thus higher contact stresses.

A direct relationship between transverse trackway bending stiffness and deflexion in the two-dimensional FEA's was shown in Figure 6.24. The effect of bending stiffness became more significant at lower values of stiffness, particularly at values below the FEA Class 60 transverse bending stiffness value. Thus the influence of the reduced longitudinal trackway stiffness becomes important, when trackway deflexions change so markedly with trackway stiffness in this low stiffness region.

Since a continuous relationship between trackway slope and contact stress exists, as trackway deforms under increasing applied stresses, the contact stress beneath becomes doubly concentrated. To minimise contact stress and the likelihood of soil failure, trackway flexure must thus be kept as low as possible, by maximising its bending stiffness in both the transverse, and more particularly, the longitudinal directions.

7.4 Soil failure

When the contact stress to the soil becomes too high, it will fail. In analysis *test4*, high values of deviatoric stress (q) were recorded in a localised region beneath the trackway, as indicated by the stress paths in Figure 6.35 and contour plot in Figure 6.34. This caused rupture in a region of the clay 0.05 to 0.5m below the trackway. This is consistent with the clay slurry deposits in the top 3-4mm (equivalent to 0.11 to 0.15m at prototype scale) layer of clay beneath the trackway at the end of centrifuge test 4. The clay slurry had experienced a 14% increase in volume, characteristic of the rupture failure in over-consolidated soil described by Schofield and Wroth (1980) and discussed in Section 5.2.

Clearly, the stress path at 0.25m depth in Figure 6.35 achieved such a high stress ratio that it would cause yield and failure in many soil types. More particularly, a normally-consolidated clay, such as the Arun Valley alluvium, with a much smaller yield locus, would experience some hardening before failing quite rapidly.

The high q values and soil failure in test 4 were not observed under the unjointed trackway in centrifuge test 3 and FEA *test3*. The unjointed trackway formed a very effective support for the applied stresses and by preventing soil failure, succeeded in keeping trackway deflexions to a minimum.

Chapter 8

Conclusions

8.0 Introduction

A number of conclusions are drawn from the finite element analyses and centrifuge tests regarding the contribution of various factors to soil/trackway failure. On the basis of these, some recommendations for further research are made.

8.1 General conclusions

Two finite element models of soil and trackway were developed allowing the effects of various trackway geometries and traffic loads on different soil types to be assessed. One was two-dimensional, modelling the transverse trackway bending behaviour in plane strain conditions; the other was a three-dimensional model that considered the effects of both transverse and longitudinal trackway bending. These models can be used by other parties for the design of particular temporary roadways and for developing new, more effective trackway systems.

Two slip element models were successfully developed and tested:

- a two-dimensional slip element which is able to compute effective stresses across its boundaries, allowing the analysis of long-term soil/structure interaction problems, a process that had hitherto been unavailable
- a three-dimensional slip element using modified brick elements, allowing the analysis of three-dimensional soil/structure interaction problems, which was essential in this research and could also be used in other applications such as pile analyses or the corners of excavations.

The finite element models and, in particular, the newly developed slip elements and large strain formulation were verified using four centrifuge tests, between which there was good agreement. New centrifuge apparatus systems were developed:

- the application of vertical static and cyclic loads to the soil surface through an interchangeable platen, allowing virtually any "footprint" shape to be used across a broad range of load magnitudes
- the operation of a moving vehicle, applying its enhanced self-weight to the soil, in a straight line with the ability to reverse and with continuous control of speed. A very successful system which represents a significant advance in the modelling of vehicle/roadway interaction in a centrifuge.

In addition, the centrifuge tests helped in gaining a fuller understanding of the processes involved in soil/trackway failure and the effects of certain factors, such as cyclic vehicle loading or the trackway joints.

Both the finite element analyses and the centrifuge tests showed that the use of rigid foundation bearing capacity factors in the prediction of a trackway failure stress would be inappropriate. The flexibility of the trackway causes it to fail at average applied stresses significantly lower than those predicted in this way. However, the occurrence of a bearing capacity failure due to one heavy vehicle is inconsistent with anecdotal field experience, which refers to a build up of trackway deflexions with successive passes.

In centrifuge Test 2, cyclic "whole vehicle loads" were imposed on the trackway. These did not cause any degradation of the underlying soil or accumulation of trackway deflexions, even under applied loads well above those that would occur in the field. The gross weight of vehicles on their own was not the significant factor in the cause of soil/trackway failure. Rather it was the axle load and localised stress concentrations between vehicle wheels, trackway and the soil surface that led to premature failure.

Unjointed trackway with Class 60 transverse bending stiffness in both directions provides a very effective support for traffic on soft ground. Jointed Class 60 trackway provides a poor support and in centrifuge Test 4 the pattern of trackway failure matched the field experience of trackway deflexions building up over successive vehicle passes. The accumulation of clay slurry and the failure of the underlying soil near the surface began immediately on the first pass of the vehicle due to very high stresses beneath the trackway joints. It showed that the simplification of the trackway to a single panel, or to analyse the problem in plane strain, is insufficient to model, or explain, the nature of trackway failure. It is a three-dimensional problem with the effects of both the transverse and longitudinal trackway stiffnesses needing to be taken into account.

Soil displacement beneath trackway is determined by its strength and stiffness properties and the contact stress from the trackway. The contact stress is determined by the applied

vehicle stresses and the trackway slope. The trackway slope is determined by its elastic bending stiffness. Class 60 trackway is relatively stiff in the transverse direction and explains the good performance of the unjointed trackway. However, Class 60 trackway is very flexible in the longitudinal direction due to its corrugated section and, more particularly, its articulated joints, thereby explaining the poor performance during tests involving jointed trackway.

Trackway strength has a lesser influence on its performance. The development of a plastic hinge changes the deformed shape of trackway and increases the contact stress to the soil in its vicinity. However, plastic hinge formation does not necessarily lead to failure of the soil/trackway system and trackway yield will only occur after significant soil displacements beneath. Therefore, trackway failure will only occur after failure, or significant displacement, of the underlying soil. Indeed, soil failure in centrifuge Test 4 was caused without any yielding of the trackway. Trackway deformations and soil displacement are thus intrinsically linked together, with the former reacting to the latter.

The use of Class 60 trackway on a soft over-consolidated clay causes shallow-seated (~0.2m deep) bearing capacity failures beneath stress concentrations at the joints. The shear zones associated with each joint quickly merge to form a continuous shear zone beneath the trackway, which dilates in the presence of water to form a slurry. This slurry, which lubricates the soil/trackway interface and aids the movement of trackway, is easily driven away to the sides of the trackway or forced up through the joints. Successive layers of the underlying in-situ clay are degraded into a slurry in this manner and driven away, thereby causing an accumulation of trackway deflexions with successive vehicle passes, consistent with field experience. In centrifuge Test 4, slurry and trackway deflexions built up to such an extent that vehicle mobility was significantly compromised after 82 axle passes, or 20 DROPS vehicle passes.

Trackway performance can be greatly improved by increasing its bending stiffness, particularly when the existing bending stiffness is lower than the present Class 60 transverse value. Thus, increasing the Class 60 longitudinal bending stiffness values

would improve its performance, allowing more than 20 DROPS vehicle passes in Test 4, or heavier vehicles to use the trackway.

Finite element analyses of Class 60 trackway were carried out with their longitudinal stiffness values enhanced either by increasing the joint spacing or by restraining the ends of the panels against rotation. Some improvements to trackway performance were noted by increasing the joint spacing. The greatest improvement, using restrained trackway, reduced maximum deflexions by 36%. This could conceivably allow a 36% increase in vehicle passes, equivalent to 27 DROPS vehicle passes in Test 4, after only a minor modification to existing trackway stock.

8.2 Further research

As with any research project, during the course of the work it becomes apparent that further research will be needed to clarify and extend certain aspects of the work.

Using both centrifuge tests and finite element analyses, trackway performance on different soil types could be compared, together with different trackway bending stiffnesses. A method of incorporating joint spacing and stiffness into the panel bending stiffness would allow contact stresses beneath jointed trackway to be calculated. With further work, relationships between soil and trackway stiffnesses could be derived, perhaps using design factors based on soil/trackway relative stiffness.

New trackway geometries could be investigated, exploring the idea of enhancing the longitudinal stiffness of existing trackway: either by modifying the design of the joints to improve their rotational stiffness when trackway is laid on the ground, or by designing an entirely new trackway system to eliminate the detrimental effect of trackway joints altogether.

When carrying out physical model tests, larger scale, or full scale, field tests could be used to allow instrumentation to be placed closer to the soil/trackway interface, a significant shear zone that could not be instrumented in the small scale centrifuge tests. If further centrifuge test investigations were needed, a drum-type centrifuge may be more suitable since it would allow a longer length of vehicle pass without the need for continual reversing of the vehicle and would also allow a normally-consolidated clay sample to be prepared. Modifications to the existing centrifuge apparatus could allow the model vehicle to be driven along the long axis of the strongbox, giving $2^1/_2$ times the length of travel, since the perspex window and backplate would not encroach within the narrow zone of influence of the applied stresses.

In further finite element analyses, a rolling vehicle load could be applied to the trackway in successive increments to monitor trackway panel rotation and its interaction with the underlying soil as a vehicle moves. Dynamic loading capabilities and cyclic soil loading models could be incorporated into CRISP enabling analyses of the degradation of soil beneath trackway and the gradual build up of trackway deflexions.

Appendix A

Class 60 trackway transverse elastic bending stiffness values used in this thesis

	Bending stiffness, EI, per m width (kNm^2/m)	
	Measured experimentally	Calculated
Prototype trackway	69.2	78.2
Centrifuge model	48.0	67.9
Finite element analysis	48.0	38.0

Appendix B

Some properties of centrifuge model kaolin

$w^{(1)}$ (%)	48.6
$\rho_{bulk}^{(2)}$ (mg/mm^3)	1.70
$c_u^{(3)}$ (kPa)	22
$k_v^{(4)}$ (m/s)	1.0×10^{-9}
$k_h^{(4)}$ (m/s)	1.5×10^{-9}

1 - moisture content in accordance with BS 1377:Part2:1990, 2 - bulk density in accordance with BS 1377:Part 2:1990 specimen direct from sample tube, 3 - undrained shear strength by unconsolidated undrained triaxial test (Mohr circles shown below), 4 – permeability by falling head permeameter test.

Mohr circles (unconsolidated undrained triaxial tests):

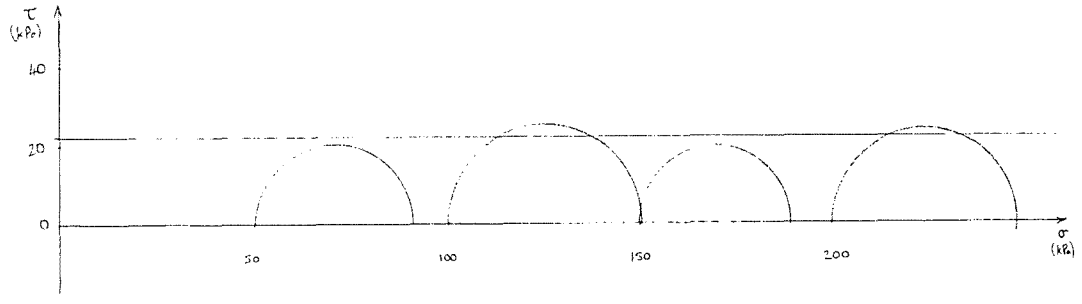

Particle size distribution:

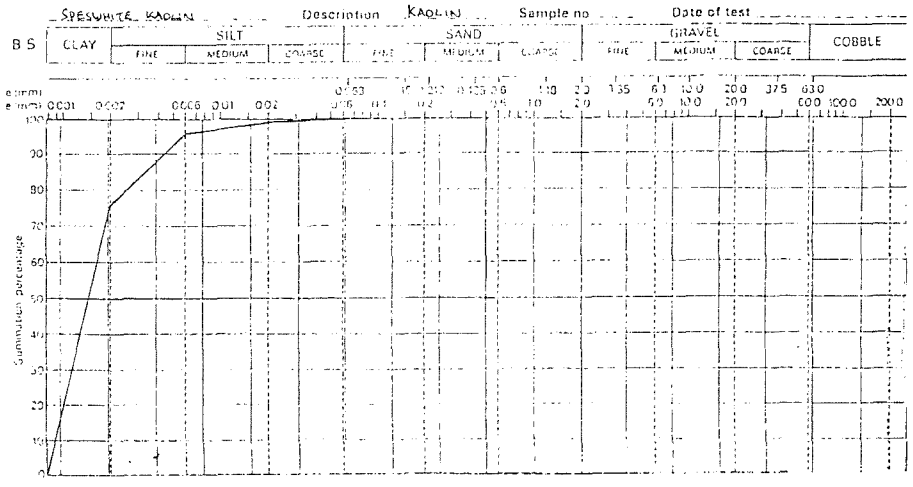

Appendix C

Centrifuge model vehicle motor control and pass counter Visual Basic program

Main window program within which motor control and pass counter programs operate:

```
VERSION 4.00
Begin VB.MDIForm MDIForm1
   BackColor       =   &H8000000C&
   Caption         =   "38g Roller Control Program"
   ClientHeight    =   6600
   ClientLeft      =   915
   ClientTop       =   1230
   ClientWidth     =   8130
   Height          =   6960
   Icon            =   "MDIForm1.frx":0000
   Left            =   855
   LinkTopic       =   "MDIForm1"
   Top             =   930
   Width           =   8250
End
Attribute VB_Name = "MDIForm1"
Attribute VB_Creatable = False
Attribute VB_Exposed = False

Private Sub MDIForm_Load()

    Width = Screen.Width * 0.75 ' Set width of form.
    Height = Screen.Height * 0.75   ' Set height of form.
    Left = (Screen.Width - Width) / 2   ' Center form horizontally.
    Top = (Screen.Height - Height) / 2  ' Center form vertically.

    Load frmCountTest
    Load frmSendAData

End Sub
```

Motor control program:

```
VERSION 4.00
Begin VB.Form frmSendAData
   Appearance      =   0  'Flat
   BackColor       =   &H80000005&
   Caption         =   "Motor Control"
   ClientHeight    =   3540
   ClientLeft      =   2670
   ClientTop       =   1620
```

```
ClientWidth     =   4905
BeginProperty Font {0BE35203-8F91-11CE-9DE3-00AA004BB851}
   Name            =   "MS Sans Serif"
   Size            =   8.25
   Charset         =   0
   Weight          =   700
   Underline       =   0   'False
   Italic          =   0   'False
   Strikethrough   =   0   'False
EndProperty
ForeColor       =   &H80000008&
Height          =   3900
Left            =   2610
MDIChild        =   -1  'True
ScaleHeight     =   3540
ScaleLeft       =   1000
ScaleMode       =   0  'User
ScaleTop        =   1000
ScaleWidth      =   4908
Top             =   1320
Width           =   5025
Begin VB.TextBox txtdelayval
   Height          =   372
   Left            =   2760
   TabIndex        =   8
   Text            =   "1000"
   Top             =   840
   Width           =   1212
End
Begin VB.CommandButton Command2
   Caption         =   "Stop"
   Height          =   375
   Left            =   2880
   TabIndex        =   7
   Top             =   2880
   Width           =   735
End
Begin VB.CommandButton Command1
   Caption         =   "Run"
   Height          =   372
   Left            =   1200
   TabIndex        =   6
   Top             =   2880
   Width           =   852
End
Begin VB.TextBox txtVoltsToSet
   Appearance      =   0  'Flat
   Height          =   375
   Left            =   840
   TabIndex        =   0
   Text            =   "0"
   Top             =   840
   Width           =   1215
End
Begin VB.Label lblShowVoltage
   Appearance      =   0  'Flat
   BackColor       =   &H80000005&
```

```
      ForeColor       =   &H00FF0000&
      Height          =   252
      Left            =   3600
      TabIndex        =   4
      Top             =   2280
      Width           =   1212
   End
   Begin VB.Label lblVoltage
      Appearance      =   0  'Flat
      BackColor       =   &H80000005&
      ForeColor       =   &H80000008&
      Height          =   252
      Left            =   240
      TabIndex        =   5
      Top             =   2280
      Width           =   3012
   End
   Begin VB.Label lblShowValue
      Appearance      =   0  'Flat
      BackColor       =   &H80000005&
      ForeColor       =   &H00FF0000&
      Height          =   252
      Left            =   3960
      TabIndex        =   3
      Top             =   1800
      Width           =   852
   End
   Begin VB.Label lblValueSent
      Appearance      =   0  'Flat
      BackColor       =   &H80000005&
      ForeColor       =   &H80000008&
      Height          =   252
      Left            =   360
      TabIndex        =   2
      Top             =   1800
      Width           =   3372
   End
   Begin VB.Label lblUseScroll
      Appearance      =   0  'Flat
      BackColor       =   &H80000005&
      Caption         =   "Enter a voltage within the DACs range:"
      ForeColor       =   &H80000008&
      Height          =   252
      Left            =   840
      TabIndex        =   1
      Top             =   360
      Width           =   3372
   End
End
Attribute VB_Name = "frmSendADData"
Attribute VB_Creatable = False
Attribute VB_Exposed = False
'ULAO01.MAK=============================================================
====

' File:                         ULAO01.MAK
```

```
' Library Call Demonstrated:    cbAOut%()

' Purpose:                      Writes to a D/A Output Channel.

' Demonstration:                Sends a digital output to D/A 1.

' Other Library Calls:          cbErrHandling%()

' Special Requirements:         Board 1 must have a D/A converter.

' (c) Copyright 1995, ComputerBoards, Inc.
' All rights reserved.
'=============================================================================
====

Const BoardNum = 1          ' Board number
Const Chan% = 1             ' output channel
Const Range% = 100
Dim out As Single
Dim target As Single
Dim delay As Double


Private Sub Command1_Click()

   target = Val(txtVoltsToSet.Text)
   delay = Val(txtdelayval.Text)

   For t = 1 To delay
        out = out + (t * (target - out) / delay)

        ' send the digital output value to D/A 0 with cbAOut%()

        EngUnits! = Val(out)

        ' Parameters:
        '   BoardNum    :the number used by CB.CFG to describe this
board
        '   Chan%       :the D/A output channel
        '   Range%      :ignored if board does not have programmable
rage
        '   DataValue%  :the value to send to Chan%


        ULStat% = cbFromEngUnits%(BoardNum%, Range%, EngUnits!,
datavalue%)
        If ULStat% <> 0 Then Stop

        ULStat% = cbAOut%(BoardNum%, Chan%, Range%, datavalue%)
        If ULStat% <> 0 Then Stop

   Next t


   lblValueSent.Caption = "The count sent to DAC channel " +
Format$(Chan%, "0") + " was:"
```

```
    lblVoltage.Caption = "The voltage at DAC channel " + Format$(Chan%,
"0") + " is:"
    lblShowValue.Caption = Format$(datavalue%, "0")
    lblShowVoltage.Caption = Format$(EngUnits!, "0.0##") + " Volts"

    Command1.Caption = "Change"

End Sub

Private Sub Command2_Click()

    EngUnits! = 0

    ULStat% = cbFromEngUnits%(BoardNum%, Range%, EngUnits!, datavalue%)
    If ULStat% <> 0 Then Stop

    ULStat% = cbAOut%(BoardNum%, Chan%, Range%, datavalue%)
    If ULStat% <> 0 Then Stop

    lblValueSent.Caption = "The count sent to DAC channel " +
Format$(Chan%, "0") + " was:"
    lblVoltage.Caption = "The voltage at DAC channel " + Format$(Chan%,
"0") + " is:"
    lblShowValue.Caption = Format$(datavalue%, "0")
    lblShowVoltage.Caption = Format$(EngUnits!, "0.0##") + " Volts"
    txtVoltsToSet.Text = "0"
    Command1.Caption = "Run"

     End Sub

Private Sub Form_Load()

    ' declare revision level of Universal Library

    ULStat% = cbDeclareRevision(CURRENTREVNUM)

    ' Initiate error handling
    '  activating error handling will trap errors like
    '  bad channel numbers and non-configured conditions.
    '  Parameters:
    '    PRINTALL    :all warnings and errors encountered will be
printed
    '    DONTSTOP    :if an error is encountered, the program will not
stop,
    '                 errors must be handled locally


    ULStat% = cbErrHandling%(PRINTALL, DONTSTOP)
    If ULStat% <> 0 Then Stop

    ' If cbErrHandling% is set for STOPALL or STOPFATAL during the
program
    ' design stage, Visual Basic will be unloaded when an error is
encountered.
    ' We suggest trapping errors locally until the program is ready for
compiling
```

```
    ' to avoid losing unsaved data during program design.  This can be
done by
    ' setting cbErrHandling options as above and checking the value of
ULStat%
    ' after a call to the library. If it is not equal to 0, an error has
occurred.

    out = 0

End Sub
```

Pass counter program:

```
VERSION 4.00
Begin VB.Form frmCountTest
   Appearance      =   0  'Flat
   BackColor       =   &H80000005&
   Caption         =   "Cycle Counter"
   ClientHeight    =   2295
   ClientLeft      =   2955
   ClientTop       =   5505
   ClientWidth     =   4290
   BeginProperty Font {0BE35203-8F91-11CE-9DE3-00AA004BB851}
      Name            =   "MS Sans Serif"
      Size            =   8.25
      Charset         =   0
      Weight          =   700
      Underline       =   0   'False
      Italic          =   0   'False
      Strikethrough   =   0   'False
   EndProperty
   ForeColor       =   &H80000008&
   Height          =   2655
   Left            =   2895
   LinkMode        =   1  'Source
   LinkTopic       =   "Form1"
   MDIChild        =   -1  'True
   ScaleHeight     =   2295
   ScaleWidth      =   4290
   Top             =   5205
   Width           =   4410
   WindowState     =   2  'Maximized
   Begin VB.Timer Timer1
      Interval        =   100
      Left            =   480
      Top             =   1680
   End
   Begin VB.Timer tmrReadCount
      Interval        =   100
      Left            =   1800
      Top             =   1680
   End
   Begin VB.Label lblShowCountRead
```

```
      Appearance      =   0  'Flat
      BackColor       =   &H80000005&
      ForeColor       =   &H00FF0000&
      Height          =   252
      Left            =   2880
      TabIndex        =   3
      Top             =   840
      Width           =   972
   End
   Begin VB.Label lblCountRead
      Appearance      =   0  'Flat
      BackColor       =   &H80000005&
      Caption         =   "Value read from counter:"
      ForeColor       =   &H80000008&
      Height          =   252
      Left            =   240
      TabIndex        =   1
      Top             =   840
      Width           =   2172
   End
   Begin VB.Label lblShowLoadVal
      Appearance      =   0  'Flat
      BackColor       =   &H80000005&
      ForeColor       =   &H00FF0000&
      Height          =   252
      Left            =   3120
      TabIndex        =   2
      Top             =   240
      Width           =   972
   End
   Begin VB.Label lblCountLoaded
      Appearance      =   0  'Flat
      BackColor       =   &H80000005&
      ForeColor       =   &H80000008&
      Height          =   252
      Left            =   360
      TabIndex        =   0
      Top             =   240
      Width           =   2652
   End
End
Attribute VB_Name = "frmCountTest"
Attribute VB_Creatable = False
Attribute VB_Exposed = False
'ULCT01.MAK=============================================================
====

' File:                         ULCT01.MAK

' Library Call Demonstrated:    8254 Counter Functions
'                               cbC8254Config%()
'                               cbCLoad%()
'                               cbCIn%()

' Purpose:                      Operate the counter.
```

```
' Demonstration:                Configures, loads and reads the
counter.

' Other Library Calls:          cbErrHandling%()

' Special Requirements:         Board 0 must have an 8254 Counter.

' (c) Copyright 1995, ComputerBoards, Inc.
' All rights reserved.
'==============================================================================
====

Const BoardNum = 0              ' Board number

Const CounterNum% = 1           ' number of counter used
Const RegName% = LOADREG1       ' register name of counter 1
Const PortNum% = AUXPORT
Dim datavalue%
Private Sub cmdStopRead_Click()

   'End

End Sub

Private Sub Form_Load()

   ' declare revision level of Universal Library

   ULStat% = cbDeclareRevision(CURRENTREVNUM)

   ' Initiate error handling
   '  activating error handling will trap errors like
   '  bad channel numbers and non-configured conditions.
   '  I love Skevi.
   '  Parameters:
   '    PRINTALL    :all warnings and errors encountered will be
printed
   '    DONTSTOP    :if an error is encountered, the program will not
stop,
   '                  errors must be handled locally


   ULStat% = cbErrHandling%(PRINTALL, DONTSTOP)
   If ULStat% <> 0 Then Stop

   ' If cbErrHandling% is set for STOPALL or STOPFATAL during the
program
   ' design stage, Visual Basic will be unloaded when an error is
encountered.
   ' We suggest trapping errors locally until the program is ready for
compiling
   ' to avoid losing unsaved data during program design.  This can be
done by
   ' setting cbErrHandling options as above and checking the value of
ULStat%
   ' after a call to the library. If it is not equal to 0, an error has
occurred.
```

```
    ' Configure the counter for desired operation
    '  Parameters:
    '    BoardNum    :the number used by CB.CFG to describe this board
    '    CounterNum% :the counter to be setup
    '    Config%     :the operation mode of counter to be configured


    Config% = HIGHONLASTCOUNT

    ULStat% = cbC8254Config%(BoardNum, CounterNum%, Config%)
    If ULStat% <> 0 Then Stop

    ' Send a starting value to the counter with cbCLoad%()
    '  Parameters:
    '    BoardNum    :the number used by CB.CFG to describe this board
    '    RegName%    :the counter to be loading with the starting value
    '    LoadValue%  :the starting value to place in the counter

    LoadValue% = 2
    datavalue% = 0
    ULStat% = cbCLoad%(BoardNum, RegName%, LoadValue%)
    If ULStat% <> 0 Then Stop

    lblCountLoaded.Caption = "Counter starting value loaded:"

    lblShowLoadVal.Caption = Format$(LoadValue% - 2, "0")

End Sub

Private Sub lblDemoFunction_Click()

End Sub

Private Sub Timer1_Timer()

    ' write the value to AUXPORT
    '  Parameters:
    '    BoardNum    :the number used by CB.CFG to describe this board
    '    PortNum%    :the output port
    '    DataValue%  :the value written to the port

    'If DataValue% = 1 Then DataValue% = 0 Else DataValue% = 1

   datavalue% = Abs(datavalue% - 1)

   ULStat% = cbDOut%(BoardNum, PortNum%, datavalue%)
   If ULStat% <> 0 Then Stop

End Sub

Private Sub tmrReadCount_Timer()

    ' Parameters:
    '   BoardNum        :the number used by CB.CFG to describe this
board
```

```
    '   CounterNum%      :the counter to be setup
    '   CBCount%         :the count value in the counter

    ULStat% = cbCIn%(BoardNum, CounterNum%, CBCount%)
    If ULStat% <> 0 Then Stop

    lblShowCountRead.Caption = Format$(Abs(CBCount% / 4), "0")

End Sub
```

References

Al-Tabbaa, A. (1987) Permeability & stress-strain response of speswhite kaolin. PhD dissertation, University of Cambridge.

Anon. (1987) BS 18: 1987. *Method for tensile testing of metals.* British Standards Institute, London.

Anon. (1990) BS 1377: 1990. *Methods of test for soils for civil engineering purposes.* British Standards Institute, London.

Ansal, A.M. and Erken, A (1989) Undrained behaviour of clay under cyclic shear stresses. *Journal of Geotechnical Engineering*, Vol. 115, No. 7, pp 968-982. ASCE.

Bjerrum, L. (1972) Embankments on soft ground, *Performance of Earth & Earth Supported Structures*. Proc. ASCE Speciality Conference, Vol. 2, pp.1-54.

Bolton, M.D., Britto, A.M., Powrie, W. and White, T.P. (1989) Finite element analysis of a centrifuge model of a retaining wall embedded in a heavily overconsolidated clay, *Computers and Geotechnics*, Vol. 7, pp.289-318.

Britto, A.M. and Gunn, M.J. (1987) Critical state soil mechanics via finite elements. Ellis Horwood, Chichester.

Chen, J., Robson, S., Cooper, M.A.R. & Taylor, R.N. (1996) An evaluation of three different image capture methods for measurement and analysis of deformation within a geotechnical centrifuge. *International Archives of Photogrammetry and Remote Sensing* XXXI (B5):70-75.

Croney, D. and Croney, P. (1991) The Design and performance of road pavements. McGraw-Hill, London.

Ghaboussi, J., Wilson, E.L. and Isenberg, J. (1973) Finite element for rock joints and interfaces, *Proceedings of the American Society of Civil Engineers: Journal of the Soil Mechanics and Foundation Division*, Vol. 99, n. SM10, pp.833-848.

Georgiadis, M. (1979) Flexible landing mats on clay, PhD thesis, University of Southampton.

Hemsley, J.A. and Spence, D.A. (1987) Elastostatic plane strain flexure of a finite strip foundation in frictionless contact with a half-plane. *Proc. Instn. Civ. Engrs. (Structural Engineering Group)*, Part 2, **83**, pp 517-540.

Hvorslev, M.J. (1937) Uber die festigkeitseigenschaften gestorter bindiger boden. (The properties of ruptured soil). Igeniorvidenskabelige Skrifter A No. 45, Kobenhaven.

Jaky, J. (1944) Magyar mernok es epitesz egylet kozloyne. (The Coefficient of earth pressure at rest). Hungary.

Jardine, R.J., Potts, D.M., St John, H.D. and Hight, D.W. (1991) Deformation of soils and displacements of structures, *Proc. 10th Eur. Conf. Soil Mech.*, Florence, Italy.

Kinner, E.B. and Ladd, C.C. (1973) Undrained bearing capacity of footing on clay, *Proc. 8th ICSMFE*, Moscow, Vol. 1, pp.209-215.

Konig, D., Jessberger, H.L., Bolton, M., Phillips, R., Bagge, G., Renzi, R. and Garnier, J. (1994) Pore pressure measurement during centrifuge model tests: experience of five laboratories. *Proc. Int. Conf. Centrifuge '94*, Singapore, pp 101-108. Balkema, Rotterdam.

Li, E.S.F. (1990) On the Analysis of Singly-Propped Diaphragm Walls. PhD dissertation, University of London (King's College).

Mayne, P.W. and Kulhawy, M. (1982) K_0-OCR relationships in soil, *Proceedings of the American Society of Civil Engineers: Journal of the Geotechnical Engineering Division*, Vol. 108, pp.851-872.

Ohta, H., Nishihara, A. and Morita,Y. (1985) Undrained stability of K_0 consolidated clays. *Proc. 11th ICSMFE*, San Francisco, Vol. 2, pp.613-617.

Powrie, W. (1986) The behaviour of diaphragm walls in clay. PhD dissertation, University of Cambridge.

Rahim, A. (1998) Joint interface (slip) elements in CRISP in 2D and 3D space, *CRISP Development Report*, No. 9801, The CRISP Consortium.

Rahim, A. (1998a) Large deformation formulation in CRISP98, *CRISP Development Report*, The CRISP Consortium.

Richards, D.J. (1995) Centrifuge & Numerical Modelling of Twin-Propped Retaining Walls. PhD dissertation, University of London (Queen Mary & Westfield College).

Schofield, A.N. (1980) Cambridge geotechnical centrifuge operations. 20th Rankine Lecture. *Geotechnique* 20(2), pp.129-170.

Schofield, A.N. and Taylor, R.N. (1988) Development of standard geotechnical centrifuge operations. *Proc. Int. Conf. Centrifuge '88*, (ed. J-F Corte), pp 29-32. Balkema, Rotterdam.

Schofield, S. and Wroth, P. (1968) *Critical State Soil Mechanics,* McGraw-Hill.

Schumm, S.A., Mosley, M.P. and Weaver, W.E. (1987) *Experimental fluvial geomorphology*, Wiley, New York.

Selvadurai, A. P. S. (1979) *Elastic Analysis of Soil-Foundation Interaction,* Elsevier Scientific.

Sharma, J. (1994) Behaviour of reinforced embankments on soft clay. PhD dissertation, University of Cambridge.

Simpson, B. (1992) Retaining structures: displacement and design. 32nd Rankine Lecture, *Geotechnique* 42(4), pp.541-576.

Sokolovskii, V.V. (1959) *Statics of Soil Media.* Oxford Pergamon.

Sokolovskii, V.V. (1965) *Statics of Granular Media.* Oxford Pergamon.

Stallebrass, S.E. (1990) Modelling the effect of recent stress history on the deformation of overconsolidated soils. PhD dissertation, City University, London.

Steedman, R.S. and Zeng, X. (1995) Dynamics. *Geotechnical Centrifuge Technology*, ed. R.N.Taylor, pp 168-195. Blackie Academic, Glasgow.

Sun, H.W. (1990) Ground deformation mechanisms for soil-structure interaction. PhD dissertation, University of Cambridge.

Taylor, R.N. (1995) Centrifuges in modelling: principles and scale effects. *Geotechnical Centrifuge Technology*, ed. R.N.Taylor, pp 19-33. Blackie Academic, Glasgow.

Timoshenko, S.P. (1959) *Theory of Plates and Shells*. McGraw-Hill, London.

Wood, D.M. (1982) Laboratory investigations of the behaviour of soils under cyclic loading: a review, in *Soil mechanics transient and cyclic loads*, (eds. Pande, G.N. & Zienkiewicz, O.C.), pp 513-582. Wiley, New York.

Zienkiewicz, O.C. (1967) The Finite Element Method in Structural and Continuum Mechanics. London: McGraw-Hill.

Bibliography

Anon. (1965) Planning and design of rapid airfield construction in the theatre of operations. *Department of Army Technical Manual*, Ministry of Defence.

Bowler, S.B. and Prescott, P.F. (1978) Predicted performance characteristics of the Class 60 trackway and the PSA (prefabricated surfacing aluminium) ground surfacing equipments. Test report XTE/581/03, Military Vehicles and Engineering Establishment, Christchurch.

Britto, A.M. and Gunn, M.J. (1987) Critical state soil mechanics via finite elements. Ellis Horwood, Chichester.

Britto, A.M. and Gunn, M.J. (1990) CRISP90 – Users' and Programmers' Guide, Vol. 1 & 3, Cambridge University Engineering Department.

Brown, S.F. (1996) Soil mechanics in pavement engineering. 36th Rankine Lecture. *Geotechnique*, **46**, No.3, pp 383-426.

Clark, R (1990) A study in the use of Class 30 and Class 60 trackways by tracked vehicles of less than Class 80 load classification. Report No. 61621, Laird (Anglesey) Ltd.

Craig, W.H., James, R.G. and Schofield, A.N. (Eds.) (1988) Centrifuges in Soil Mechanics. Balkema, Rotterdam.

Foss, C.F. and Gander, T.J. (1995) *Jane's Military Vehicles and Logistics '95-'96.* Jane's, London.

Foss, C.F. (1995) *Jane's Armour and Artillery '95-'96.* Jane's, London.

Little, P.H. (1992) The design of unsurfaced roads using geosynthetics, PhD thesis, University of Nottingham.

Muir Wood, D. (1990) Soil behaviour and critical state soil mechanics. Cambridge University Press.

Nath, B. (1974) Fundamentals of Finite Elements for Engineers. The Athlone Press.

Powrie, W. (1997) *Soil Mechanics: Concepts and Applications*. E & FN Spon, London.

Prescott, P.F. (1986) Load trolley testing of Class 60 trackway over weak soil. Test report XAD/HW/3165, Royal Armament Research and Development Establishment, Christchurch.

Schofield, A.N. (1980) Cambridge geotechnical centrifuge operations. 20th Rankine Lecture. *Geotechnique* 20(2), pp.129-170.

Schofield, A.N. and Taylor, R.N. (1988) Development of standard geotechnical centrifuge operations. *Proc. Int. Conf. Centrifuge '88*, (ed. J-F Corte), pp 29-32. Balkema, Rotterdam.

Schofield, S. and Wroth, P. (1968) *Critical State Soil Mechanics,* McGraw-Hill.

Sokolovskii, V.V. (1959) *Statics of Soil Media*. Oxford Pergamon.

Taylor, R.N. (Ed.) (1995) *Geotechnical Centrifuge Technology*. Blackie Academic, Glasgow.

Terzaghi, K. and Peck, R.B. (1967) *Soil Mechanics in engineering practice*, 2nd edition. Riley, New York.

Wheeler, P.N. (1997) Investigation into distortion characteristics of trackway vehicle support roadway. Restricted document.